

---

# Applied Research Laboratory

## Technical Report

**Effects of Surface Roughness and Aging on  
the Electrical Contact Resistance and Residual  
Stress In Gold-Nickel-Copper Connector Materials**

by

Nan E. Butler and Dr. Douglas E. Wolfe

Approved for public release, distribution unlimited.

PENNSTATE

---



**The Pennsylvania State University  
The Applied Research Laboratory  
P.O. Box 30  
State College, PA 16804**

**Effects of Surface Roughness and Aging on the Electrical Contact Resistance and Residual  
Stress In Gold-Nickel-Copper Connector Materials**

**By  
Nan Butler and Dr. Douglas E. Wolfe**

**Technical Report No. TR 14-006  
December 2014**

**Supported By:**

**Sandia Master's Fellowship program**

**Approved for public release, distribution unlimited**

REPORT DOCUMENTATION PAGE				Form Approved OMB No. 0704-0188	
<p>The public reporting burden for this collection of information is estimated to average 1 hour per response, including the time for reviewing instructions, searching existing data sources, gathering and maintaining the data needed, and completing and reviewing the collection of information. Send comments regarding this burden estimate or any other aspect of this collection of information, including suggestions for reducing the burden, to the Department of Defense, Executive Service Directorate (0704-0188). Respondents should be aware that notwithstanding any other provision of law, no person shall be subject to any penalty for failing to comply with a collection of information if it does not display a currently valid OMB control number.</p> <p><b>PLEASE DO NOT RETURN YOUR FORM TO THE ABOVE ORGANIZATION.</b></p>					
1. REPORT DATE (DD-MM-YYYY) 06-18-15		2. REPORT TYPE Technical Report		3. DATES COVERED (From - To) December 14-June 2015	
4. TITLE AND SUBTITLE Effects of Surface Roughness and Aging on the Electrical Contact Resistance and Residual Stress In Gold-Nickel-Copper Connector Materials				5a. CONTRACT NUMBER	
				5b. GRANT NUMBER	
				5c. PROGRAM ELEMENT NUMBER	
6. AUTHOR(S) Nan Butler Douglas E. Wolfe				5d. PROJECT NUMBER	
				5e. TASK NUMBER	
				5f. WORK UNIT NUMBER	
7. PERFORMING ORGANIZATION NAME(S) AND ADDRESS(ES) Applied Research Laboratory The Pennsylvania State University PO Box 30 State College, PA 16804				8. PERFORMING ORGANIZATION REPORT NUMBER  TR 14-006	
9. SPONSORING/MONITORING AGENCY NAME(S) AND ADDRESS(ES) Defense Advance Research Projects Agency Tactical Technology Office 675 N. Randolph Street Arlington, VA 22203-2114 Attn: Kevin Massey				10. SPONSOR/MONITOR'S ACRONYM(S)  DARPA	
				11. SPONSOR/MONITOR'S REPORT NUMBER(S)	
12. DISTRIBUTION/AVAILABILITY STATEMENT Approved for Public Release: distribution unlimited					
13. SUPPLEMENTARY NOTES					
14. ABSTRACT See attached					
15. SUBJECT TERMS					
16. SECURITY CLASSIFICATION OF:			17. LIMITATION OF ABSTRACT  UU	18. NUMBER OF PAGES  155	19a. NAME OF RESPONSIBLE PERSON Douglas E. Wolfe
a. REPORT Unclassified	b. ABSTRACT Unclassified	c. THIS PAGE Unclassified			19b. TELEPHONE NUMBER (include area code) 814-865-0316

20151210105

The Pennsylvania State University  
The Graduate School  
Materials Science and Engineering Intercollege Graduate Degree Program

**EFFECTS OF SURFACE ROUGHNESS AND AGING ON THE ELECTRICAL CONTACT  
RESISTANCE AND RESIDUAL STRESS IN GOLD-NICKEL-COPPER CONNECTOR  
MATERIALS**

A Thesis in  
Materials Science and Engineering  
by  
Nan Butler

© 2014 Nan Butler

Submitted in Partial Fulfillment  
of the Requirements  
for the Degree of

Master of Science

December 2014

Approved for public release;  
distribution unlimited



The thesis of Nan Butler was reviewed and approved\* by the following:

Douglas E. Wolfe  
Associate Professor of Materials Science and Engineering  
Associate Professor of Engineering Science and Mechanics  
Thesis Advisor

Barbara A. Shaw  
Professor of Engineering Science and Mechanics

Todd A. Palmer  
Associate Professor of Materials Science and Engineering

Suzanne E. Mohney  
Professor of Materials Science and Engineering  
Professor of Electrical Engineering  
Intercollege Graduate Degree Program in Materials Science and Engineering Chair

\*Signatures are on file in the Graduate School

## ABSTRACT

The purpose of this research is to investigate the effects of surface roughness and aging environment on the electrical contact resistance and residual stress in nickel and nickel/gold coated copper. In order to accomplish these research objectives, oxygen free copper coupons were prepared to a variety of average surface roughnesses ( $R_a$  ranging from 0.05  $\mu\text{m}$  to 2.5  $\mu\text{m}$ ) prior to coating application. Three coating systems were investigated: Au/Ni plating, Ni plating, and Ni sputtering. The majority of this research focuses on the Au/Ni plated samples, with Ni plated and Ni sputtered data included for comparison.

Nickel, gold, and copper are commonly used in electrical components, such as electrical contacts, in which component reliability is of great importance. As there are a wide variety of environments to which electrical components could be exposed to during service, the coated samples were aged for up to nine weeks in one of three aging environments: mixed flowing gas/atmospheric corrosion (MFG), elevated temperature and relative humidity (TRH), and thermal cycling (TC). The mixed flowing gas/atmospheric corrosion environment was created by using a Battelle Class 2 environment with the following conditions: 30 °C, 70 % relative humidity, 200 ppb  $\text{NO}_2$ , 10 ppb  $\text{H}_2\text{S}$ , and 10 ppb  $\text{Cl}_2$ . The elevated temperature and relative humidity environment maintained samples at a constant temperature and relative humidity of 40 °C and 85%, respectively. Samples in the thermal cycling environment were cycled between temperatures of -40 °C and 60 °C with a 15 minute dwell time and an approximately 4.5 °C/minute ramp rate.

Characterization using optical profilometry, optical microscopy (OM), scanning electron microscopy (SEM), energy dispersive x-ray spectroscopy (EDS), x-ray diffraction (XRD), and electrical contact resistance (ECR) measurements allowed for the determination of changes in the coupons due to the coating system, surface preparation, and environmental exposure.

For the unexposed samples, the surface roughness effects on the residual stress varied depending on the coating material and deposition technique utilized. The residual stress in the gold

coating of the Au/Ni plated coupons was tensile and decreased in magnitude with increasing substrate surface roughness. The Ni plated coupons exhibited a compressive stress for the smoothest set of samples, while the rougher samples were nearly stress free. The Ni sputtered samples retained an approximately constant residual stress regardless of the substrate surface roughness. On the other hand, the surface roughness had little to no effect on the electrical contact resistance for the as received samples. All measured electrical contact resistance values for these samples were observed to be within approximately 1 m $\Omega$  of each other, with values on the order of 10-12 m $\Omega$ .

Characterization after environmental exposure revealed aging effects on the residual stress and electrical contact resistance to vary depending on the surface roughness and aging environment. Samples exposed to the atmospheric corrosion/mixed flowing gas (MFG) environment exhibited the largest change in electrical contact resistance. ECR values increased from the as received condition of 10-12 m $\Omega$  to over 1000 m $\Omega$ . The extent of the sample surface with increased ECR values increased with increasing roughness and amount of corrosion product present. In comparison, little to no changes in the electrical contact resistance were observed in the thermal cycled and elevated temperature and relative humidity aged samples.

The tensile residual stresses observed in the Au/Ni plated samples remained approximately constant or decreased in magnitude with aging time (depending on the aging environment), with the largest change resulting from thermal cycle aging. The tensile stresses found in the Au/Ni plated coatings were observed to decrease in magnitude two to three times more for the thermal cycled samples (~60-120 MPa depending on the substrate surface roughness) as compared to the MFG aged samples (~10-50 MPa). Little to no changes were observed as a result of TRH exposure.

## TABLE OF CONTENTS

List of Figures .....	vii
List of Tables .....	xvi
Acknowledgements.....	xviii
Chapter 1 Introduction .....	1
Objectives.....	2
Chapter 2 Literature Search/Background.....	4
2.1 Electrical Connectors .....	4
2.1.1 Failure Mechanisms in Electrical Contacts .....	5
2.1.2 Materials in Electrical Connectors .....	8
2.2 Coating Processes .....	10
2.2.1 Electroplating .....	11
2.2.2 Sputtering .....	20
2.3 Aging Studies .....	26
2.3.1 Atmospheric Corrosion/Mixed Flowing Gas (MFG) .....	27
2.3.2 Thermal Cycling (TC) .....	29
2.3.3 Elevated Temperature and Relative Humidity (TRH).....	30
2.4 Electrical Contact Resistance (ECR) .....	31
2.5 Residual Stress .....	38
2.5.1 Residual Stress Measurement Techniques .....	39
2.5.2 Residual Stress Calculations with X-ray Diffraction (XRD) .....	40
Chapter 3 Experimental Procedure .....	49
3.1 Substrate Materials.....	49
3.2 Surface Roughness Preparation.....	50
3.3 Coatings .....	51
3.3.1 Electroplating .....	52
3.3.2 Sputtering .....	53
3.4 Aging Studies .....	54
3.4.1 Atmospheric Corrosion/Mixed Flowing Gas (MFG) .....	57
3.4.2 Elevated Temperature and Relative Humidity (TRH).....	58
3.4.3 Thermal Cycling (TC) .....	59
3.5 Characterization .....	61
3.5.1 Optical Profilometry.....	61
3.5.2 Scanning Electron Microscopy (SEM) / Energy Dispersive Spectroscopy (EDS) .....	61
3.5.3 Optical Microscopy (OM).....	62
3.5.4 X-Ray Diffraction (XRD) .....	63
3.5.5 Electrical Contact Resistance .....	64
Chapter 4 Results and Discussion.....	67

4.1	Characterization of As Received (Week 0) Coated Samples Prior to Aging .....	67
4.1.1	Surface Morphology.....	67
4.1.2	Coating Thickness .....	76
4.1.3	Electrical Contact Resistance (ECR).....	81
4.1.4	Residual Stress .....	88
4.1.5	As Received Results Summary .....	95
4.2	Characterization of Environmentally Exposed/Aged Coated Samples (Week 3, 6, 9) .....	97
4.2.1	MFG Aged Samples.....	97
4.2.2	Elevated Temperature and Relative Humidity (TRH) Aged Samples .....	113
4.2.3	Thermal Cycled (TC) Aged Samples .....	118
4.2.4	Aging Environment Effects on Surface Roughness .....	127
	Chapter 5 Conclusions and Future Work.....	135
5.1	Summary and Conclusions.....	135
5.2	Future Work .....	138
	References.....	139
	Appendix Raw Data .....	144
	Optical Profilometry .....	144

## LIST OF FIGURES

Figure 2-1. Digital images showing example electrical connectors: (a) VGA (video graphics array) connector and USB (universal serial bus) flash drive and (b) side view of a laptop showing (i) connection for a power connector, (ii) network cable, (iii) VGA, and (iv) HDMI (high definition multimedia interface) cable input, respectively. ....	4
Figure 2-2. Schematic of pore corrosion nucleation and growth in nickel and gold plated copper aged in a Battelle Class II atmospheric corrosion MFG environment: (a) initiation of corrosion site with pollutant gases reacting with the less noble nickel underlayer through a pore/defect in the gold top coating, (b) propagation of corrosion further into the nickel layer, with corrosion products traveling through the pore to the surface, and (c) corrosion reaches/corrodes the copper (with corrosion products still migrating through the pore to the surface creating a void at the nickel to copper interface). Source: Enos [6]. ....	6
Figure 2-3. Schematic of the nickel electroplating process depicting the nickel target (anode) and the substrate (cathode). Nickel is oxidized and removed from the target material and goes into solution, is attracted to the negatively biased substrate material, and reduces back to nickel metal on the substrate surface creating the nickel coating. ....	12
Figure 2-4. Microthrowing power/leveling effects during electroplating. (a) Neutral microthrow, i.e., even coating thickness across peaks and valleys, (b) negative microthrow, i.e., predominate plating on peaks resulting in increased surface roughness, and (c) positive microthrow, i.e., leveling effects resulting in decreased surface roughness. ....	14
Figure 2-5. Example of the effects the operating conditions can have on electroplated nickel from Watts and sulfamate solutions. Source: Di Bari [32]. ....	16
Figure 2-6. Schematic depicting the effect cathode/anode geometries can have on the coating uniformity. (a) Single anode located on one side of the substrate resulting in a thicker coating on the surfaces nearer the target material and (b) four anode system allowing for improved coating uniformity. ....	17
Figure 2-7. Image of gold plated copper with spherical nanoparticles incorporated into the coating producing a spherically structured surface. Source: Song [21]. ....	19
Figure 2-8. SEM images of gold plated oxygen free high conductivity (OFHC) copper, from P. Misra and J. Nagaraju, showing the differences in surface topography based on the thickness of the gold coating applied with (a) bare copper, followed by copper with (b) 0.1 $\mu\text{m}$ thick gold plating, (c) 0.3 $\mu\text{m}$ thick gold plating, and (d) 0.5 $\mu\text{m}$ thick gold plating. Source: Misra & Nagaraju [38]. ....	20
Figure 2-9. Schematic depicting the ionization of the inert gas (argon) used during sputtering upon colliding with an electron, as well as the subsequent collision of the ionized gas particle with the target surface ejecting target atoms. Source: Oxford Vacuum Science [22]. ....	21

Figure 2-10. Schematic of the fundamental sputtering process depicting the ionized gas particles ( $\text{Ar}^+$ ) colliding with the target material causing target atoms to be ejected and deposited on the substrate. Source: Reade [39].	21
Figure 2-11. Schematic of the magnetron sputtering process depicting the magnetic field used to retain electrons near the target surface. Ionized gas particles ( $\text{Ar}^+$ ) colliding with the target material causing target atoms to be ejected and deposited on the substrate. Source: Maraca Coating Technologies, LLC [47].	22
Figure 2-12. Schematic depicting the three growth modes observed in thin film deposition: (a) Volmer-Weber or Island, (b) Frank van der Merwe or layer, and (c) Stranksi-Krastanov. Source: Ohring [43].	23
Figure 2-13. Schematic depicting the “effects of bombarding ions on the surface atoms: (a) adsorbate removal or chemical activation, (b) lateral displacement, (c) surface vacancy created by sputtering, (d) surface vacancy created by displacement to an adatom position, (e) knock-on implantation of an impurity atom, (f) knock-on implantation of a film atom, (g) crevice filling by ion-enhanced surface mobility, (h) crevice filling by forward sputtering, and (i) breakup of 3D nucleus”. Source: Smith [31].	24
Figure 2-14. “Types of atomic displacements produced in the collision cascade. The heavy line is the path of the impinging ion. (a) Frenkel-pair creation, (b) replacement collision, (c) sputtering, and (d) ion mixing”. Source: Smith [31].	24
Figure 2-15. Structure Zone Model schematic describing the microstructure of sputtered coatings as a function of substrate/melting point temperature, argon pressure, and ion energy. Source: Stelmack [46].	25
Figure 2-16. Schematic of two conductive surfaces in contact. Due to the limited number of actual points in contact between the two surfaces where the current can pass between the surfaces, the overall electrical resistance is increased.	32
Figure 2-17. Schematic comparing smooth versus rough surfaces when in contact under a load. Source: Braunović [50].	32
Figure 2-18. Example of change in electrical contact resistance with applied load for a nickel and gold plated copper contact using a gold plated beryllium copper probe.	33
Figure 2-19. Example cumulative distribution function plot (CDF) showing that about 85% of the example resistance data has a resistance of 17 m $\Omega$ or less for the aged samples while 100% of the resistance data for the unaged samples falls within 10-11 m $\Omega$ .	34
Figure 2-20. Example of a Battelle Class II aged Au/Ni plated copper sample showing the typical corrosion bloom and product halo created during the pore corrosion of the surface.	35



Figure 2-21. Experimental (data points) and numerical (solid/dashed lines) electrical contact resistance for gold coated copper using a gold plated beryllium copper probe. Source: Moffat et al. [52].	35
Figure 2-22. Experimental electrical contact resistance for nickel and gold plated copper as a function of gold plating thickness. Source: Misra & Nagaraju [38].	36
Figure 2-23. Basic x-ray diffraction setup. Source: Brundel et al. [64].	41
Figure 2-24. Miller indices are used to describe specific planes. A few examples are shown in (a) $(hkl) = (hkl)$ , (b) $(hkl) = (110)$ , and (c) $(hkl) = (102)$ . Source: Cullity [63].	42
Figure 2-25. XRD stress measurement based on shifts in the lattice spacing $d$ with changing surface orientation $\psi$ . $D$ is the x-ray detector, $S$ is the x-ray source, $N$ is normal to the surface, and $\psi$ describes the surface orientation, where (a) $\psi = 0$ and (b) $\psi = \psi$ . Source: Prevey [14, 15].	42
Figure 2-26. Plane-stress elastic model depicting various variables used in the stress calculations, where $\phi$ and $\psi$ are angles defining the orientation of the sample, $\sigma_1$ and $\sigma_2$ are principal stresses, and $\epsilon_{\phi\psi}$ , $d_{\phi\psi}$ , and $\sigma_{\phi\psi}$ are the strain, lattice spacing, and stress, respectively for a given $\phi$ and $\psi$ orientation (i.e., $\sigma_{\phi}$ is the stress in the plane where $\psi = 0$ ). Source: Prevey [14, 15].	43
Figure 2-27. Example XRD results showing the required linear correlation between $d$ and $\sin^2\psi$ as required for the two angle and $\sin^2\psi$ residual stress analysis techniques.	46
Figure 2-28. General plot of lattice spacing versus the diffraction angle, based on Bragg's Law (Equation 2.11), depicting the potential variability in $d$ for the same step size in $\theta$ .	47
Figure 3-1. Schematic of the panel layout prepared, N01, including the numbering for the individual coupons.	50
Figure 3-2. (a) Digital image of Bosch sputtering system used to nickel sputter coat select panels of samples, (b) digital image of the deposition chamber interior where surface prepared and cleaned samples were mounted for sputter coating (note that the panels, along with a few witness coupons, were mounted with kapton tape), and (c) digital image of sample panels after sputter deposition.	54
Figure 3-3. Schematic of a panel (N14 for example) depicting the sample designation within the panel and which samples were removed at what increments during the aging study. Samples in each column are duplicates, i.e., there are a total of three duplicates for each specific condition/aging time.	55
Figure 3-4. Flow chart depicting the coupon assignment for the nickel and gold plated samples. Note that the number of coupons for each division is listed in the brackets.	56
Figure 3-5. Schematic of mixed flowing gas system set up and testing chamber. Source: Enos [76].	57



Figure 3-6. (a) Digital image of coupons mounted in MFG chamber for aging and (b) Close-up view of samples in MFG chamber showing plating tape (green tape) on the back of samples.....	58
Figure 3-7. (a) Digital image of coupons mounted in TRH chamber for aging and (b) Close-up view of samples in TRH chamber showing plating tape (green tape) covering exposed edges of copper. ....	58
Figure 3-8. (a) Digital image of the thermal cycle chamber used (EC-2 Sigma Climatic Chamber), (b) Digital image of coupons mounted in TC chamber for aging, and (c) Close-up view of samples in TC chamber. ....	59
Figure 3-9. Excerpt from the complete thermal cycle profile showing upper and lower temperature bounds, as well as the 15 minute dwell time during the thermal cycle testing.....	60
Figure 3-10. Example images depicting coating thickness determination with Clemex Analytical software. One hundred columns per image were created for each coating and measured to obtain thickness data. Shown above are the images for a Group 1 Au/Ni plated sample where (a) focuses on the thickness of the gold coating and (b) on the nickel underlayer. ....	62
Figure 3-11. Theta-2Theta diffraction pattern for a Group 1 Au/Ni plated copper sample using chromium radiation source. ....	64
Figure 3-12. Electrical contact resistance equipment with four wire resistance measurement set up depicting the location of the stationary lead, coupon location, and the probe.....	65
Figure 3-13. Schematic of measurement orientation on sample with arrows indicating measurement direction. Note that for spot check work, only 20 measurements were taken per sample with the same orientation/direction of measurement, but instead of ten measurements per row, there were only five.....	66
Figure 4-1. Average $R_a$ surface roughnesses for select samples from each of the four roughness groups before coatings were applied.....	68
Figure 4-2. Examples of stitched optical profilometry scans for the as received samples. Each image represents a total of 27 scans as it is comprised of a 3 x 3 stitch, averaged three times. (a) Group 1 sample with $R_a = 0.05 \mu\text{m}$ , (b) Group 2 sample with $R_a = 0.47 \mu\text{m}$ , (c) Group 3 sample with $R_a = 0.82 \mu\text{m}$ , and (d) Group 4 sample with $R_a = 2.50 \mu\text{m}$ . ....	69
Figure 4-3. Optical images of Group 1 Ni sputtered copper samples showing the visual variations in the appearance of the coating based on the deposition run: Run #1 (left), Run #2 (middle), Run #3 (right). ....	70
Figure 4-4. Optical images of Groups 1, 2, and 3 for the unaged Au/Ni plated samples. ....	71

- Figure 4-5. SEM images of unaged Au/Ni plated samples. Each image is for a different surface roughness group: (a) Group 1 samples with average  $R_a$  of 0.06  $\mu\text{m}$ , (b) Group 2 with an  $R_a$  of 0.55  $\mu\text{m}$ , (c) Group 3 with an  $R_a$  of 0.83  $\mu\text{m}$ , and (d) Group 4 with an  $R_a$  of 2.83  $\mu\text{m}$ . Note that Group 2, 3, and 4 samples have embedded grit from the surface preparation stages (circled above).....72
- Figure 4-6. SEM image of Group 4 Au/Ni plated sample showing the presence of a contaminant in the coating. EDS mapping shows the presence of (i) gold and (ii) silicon confirming that the contaminant is silicon based, i.e., the silicon carbide grit. Note that in the EDS maps (i) and (ii), white is used to represent where a particular element is present (relative concentration) while everything else remains black. ....73
- Figure 4-7. SEM image of a cross section of a Group 4 Au/Ni plated sample showing the presence of embedded grit. EDS mapping shows the presence of (i) silicon and (ii) gold, which confirms the elemental composition of the grit as silicon based, i.e., silicon carbide. Note that in (i) and (ii) the yellow and blue show where the element is present (relative concentration), while everything else remains black.....73
- Figure 4-8. SEM image of a cross section of an unaged Group 3 Au/Ni plated sample revealing embedded grit. EDS mapping shows the presence of (i) aluminum, (ii) oxygen, (iii) nickel, and (iv) gold, which confirms the elemental composition of the grit as aluminum and oxygen based (i.e., aluminum oxide) instead of silicon carbide. Note that in (i) – (v) the various colors (yellow, green, and blue) show where the element is present (relative concentration), while everything else remains black. ....74
- Figure 4-9. SEM image of a cross section of an unaged Group 4 Au/Ni plated sample revealing embedded grit that is exposed (i.e., visible from the surface) and unexposed (i.e., grit that has been plated over or is embedded deeper into the substrate). ....75
- Figure 4-10. SEM images of Week 0 Group 1, 3, and 4 samples for the Ni plated and Ni sputtered samples. ....76
- Figure 4-11. Optical images of select cross sections of Au/Ni plated as received samples: (a) Group 1, (b) Group 2, (c) Group 3, and (d) Group 4. Note that there is a significant amount of embedded grit present in the Group 3 and 4 samples. There also appears to be a higher porosity concentration in the Au coating for the Group 2 samples.....77
- Figure 4-12. Optical images of select cross sections of Ni plated as received samples: (a) Group 1, (b) Group 3, and (c) Group 4. ....77
- Figure 4-13. Optical images of select cross sections of Ni sputtered as received samples: (a) Group 1, (b) Group 3, and (c) Group 4.....78
- Figure 4-14. Cross sectional SEM images of Group 1 Ni sputtered copper samples at a couple of locations. ....78

Figure 4-15. Cross sectional SEM images of Group 1 Au/Ni plated copper samples. The image on the left is at a lower magnification to provide a wider view regarding the size and depth of embedded grit.....	79
Figure 4-16. Cross sectional SEM images of Group 3 Au/Ni plated copper samples. The image on left is at a lower magnification to provide a wider view regarding the size and depth of embedded grit.....	79
Figure 4-17. Cross sectional SEM images of Group 4 Au/Ni plated samples. Image on left is at a lower magnification to provide a wider view regarding the size and depth of embedded grit. ....	79
Figure 4-18. Example cross sectional image showing the coating thickness for the individual nickel and gold layers in a Group 1 Au/Ni plated sample. ....	80
Figure 4-19. Cumulative distribution plot of the electrical contact resistance (ECR) for unexposed, Week 0, Au/Ni plated coupons under a load of 200g. ....	81
Figure 4-20. (a) Cumulative distribution plot of the electrical contact resistance (ECR) for unexposed, Group 1 Week 0, Au/Ni plated, Ni plated, and Ni sputtered coupons under a load of 200g, and (b) close-up of (a) providing a better depiction of the difference in ECR values for the Au/Ni plated and Ni sputtered samples. ....	82
Figure 4-21. (a) Schematic depicting exposed embedded grit in one surface preventing contact between two electrical conductive surfaces and (b) showing the same surface set but with an additional larger piece of embedded grit to emphasize the effect grit size can have on the number of electrical contacts between surfaces. ....	84
Figure 4-22. Total area of contact area between the probe tip and sample surface decreases with increasing surface roughness. ....	85
Figure 4-23. Electrical contact resistance data for Week 0 Au/Ni plated Group 1, 3, and 4 samples showing the resistance vs. load relationship. ....	85
Figure 4-24. Electrical contact resistance data for as received Au/Ni plated Group 1, 3, and 4 samples under various loads. Note that as the load increases for a given sample, the resistance decreases. ....	86
Figure 4-25. Cumulative distribution plot of the electrical contact resistance (ECR) for unexposed, Week 0, Group 1 and Group 4 Au/Ni plated coupons under a load of 200g from the two data collection periods.....	87
Figure 4-26. Residual stress in the gold coating of the Au/Ni plated samples for each of the four different surface roughness sets without exposure to the aging environments.....	89
Figure 4-27. Residual stress in the Ni sputtered coating for each of the four different surface roughness sets without exposure to the aging environments (i.e., Week 0/as received samples). Samples show increased standard deviations. ....	90

Figure 4-28. Residual stress in the Ni plated coating for each of the four different surface roughness sets without exposure to the aging environments (i.e., Week 0/as received samples). .....	91
Figure 4-29. Raw XRD data for Ni sputter coated sample #1 on panel N23 depicting the texturing present (i.e., note that the intensity for the $\psi = 0^\circ$ peak is drastically higher than for the other $\psi$ angles). .....	92
Figure 4-30. Residual stress in the Week 0 (as received) Ni sputtered samples separated based on the deposition run (i.e., Run #1, #2, or #3). .....	93
Figure 4-31. Residual stress in the Week 0 (as received) Ni and Au/Ni plated samples. Note that the residual stresses reported for the Au/Ni plated samples are for the Au layer, not the Ni underlayer. ....	94
Figure 4-32. Residual stress for the Week 0 (as received) Ni plated samples including typical stress values reported by Di Bari [32] based on electroplating bath type and presence of co-deposited sulfur. ....	95
Figure 4-33. (a) Digital images of as received Groups 1, 3, and 4 samples and (b) Optical images of MFG Week 9 samples for Groups 1, 3, and 4 showing easily identifiable changes in the surface with aging, including corrosion sites and changes in observed surface color. ....	98
Figure 4-34. (a) SEM images of MFG Week 0 samples (Groups 1 through 4 going from left to right) at, (b) SEM images at the same magnification but after nine weeks of aging to show corrosion sites/product on the surface, and (c) SEM images of areas shown in (b) but at a higher magnification to allow a closer view of the corrosion sites/product on the surface. ....	99
Figure 4-35. Optical images for Ni plated and Ni sputtered coupons after nine weeks of MFG aging. The majority of the sample surfaces do not appear to show signs of corrosion/ changes in the surface with a few exceptions. ....	100
Figure 4-36. SEM images of the Ni plated and Ni sputtered Week 9 MFG samples showing the differences in the coating morphology based on the coating process and surface roughness. ....	101
Figure 4-37. Optical profilometry data for MFG aged Au/Ni plated coupons depicting the percent change in the Ra surface roughness from the unaged (Week 0) condition. ....	102
Figure 4-38. SEM image of part of the product halo around a corrosion site on a Au/Ni plated sample after aging in the MFG environment. EDS mapping was completed to show the presence of (i) gold, (ii) nickel, (iii) copper, (iv) sulfur, and (v) oxygen in the corrosion products. Note that in the EDS maps, white is used to represent where a particular element is present (relative concentration) while everything else remains black. ....	103
Figure 4-39. (a) Optical image of a region on a Group 1 Au/Ni plated MFG Week 9 aged coupon and (b) optical image of region with corrosion sites/product halos	



highlighted in Clemex. The area of the highlighted regions was compared to the total area of the image in Clemex in order to determine the percent area covered by corrosion sites/products.....	104
Figure 4-40. Optical images of Group 1 Au/Ni plated MFG coupons after three, six, and nine weeks of aging, respectively. Note that the corrosion sites are not necessarily uniformly distributed over the surface and that they are not all the same size. ....	105
Figure 4-41. (a) Depiction of a corrosion site for atmospheric degradation in a nickel and gold plated copper system (Source: Enos [6]) and (b) SEM surface image of a corrosion site on a Group 1 MFG sample exhibiting the same general components as those found in the literature including the corrosion product bloom and halo, as well as the cracks in the gold layer. ....	106
Figure 4-42. Residual stress in the gold coating for each of the atmospheric corrosion/mixed flowing gas (MFG) sample sets. Each point represents the averaged residual stress from the three duplicate samples.....	107
Figure 4-43. Electrical contact resistance data under a 200g load for the Au/Ni plated samples (Groups 1, 2, 3, and 4) after nine weeks of exposure to the Battelle Class II environment (MFG). ....	108
Figure 4-44. Electrical contact resistance data under a 200g load for the Au/Ni plated Group 1 samples as a function of aging time in the MFG environment. ....	109
Figure 4-45. Electrical contact resistance data under a 200g load for the Au/Ni plated Group 2 samples as a function of aging time in the MFG environment. ....	110
Figure 4-46. Electrical contact resistance data under a 200g load for the Au/Ni plated Group 4 samples as a function of aging time in the MFG environment. ....	110
Figure 4-47. Electrical contact resistance data comparison between current research and data from Sandia (SNL). Source: Moffat et al. [52]. Note that the SNL data is for a Au plated copper sample with no Ni underlayer, thus the values vary to a degree.....	111
Figure 4-48. (a) Electrical contact resistance data for Ni plated and Ni sputtered Group 1 Week 0 and Week 3 samples and (b) close-up of (a) providing a better depiction of the changes in the electrical contact resistance for the Ni sputtered samples. ....	112
Figure 4-49. Optical surface mapping of Au/Ni plated TRH samples after nine weeks of aging. No noticeable changes in the surface are observed. ....	113
Figure 4-50. SEM images of the Au/Ni plated TRH samples before and after aging (i.e., Week 0 and Week 9). No obvious changes in the surface were observed. ....	114
Figure 4-51. Optical images of the Ni plated and Ni sputtered TRH samples after nine weeks of aging. No noticeable changes in the surface are observed. ....	114
Figure 4-52. SEM images of the Ni sputtered Group 1 and 4 TRH samples after nine weeks of aging. No noticeable changes in the surface are observed. ....	115

Figure 4-53. SEM images of the Ni plated Group 1 and 4 TRH samples after nine weeks of aging. No noticeable changes in the surface are observed.....	115
Figure 4-54. Residual stress in the gold coating for each of the elevated temperature and relative humidity (TRH) samples. Each point represents the averaged residual stress from the three duplicate samples.....	116
Figure 4-55. Week 0 ECR data for Group 1, 3, and 4 Au/Ni plated TRH samples as a function of load. ....	117
Figure 4-56. Week 9 ECR data for Group 1, 3, and 4 Au/Ni plated TRH samples as a function of load. ....	117
Figure 4-57. Electrical contact resistance data under a 200g load for the Au/Ni plated TRH as received and nine weeks aged samples.....	118
Figure 4-58. Optical surface mapping of Au/Ni plated TC samples after nine weeks of aging. No noticeable changes in the surface are observed. ....	119
Figure 4-59. Optical images of Ni sputtered and Ni plated samples after nine weeks of thermal cycling.....	119
Figure 4-60. SEM surface images of Week 0 and Week 9 Au/Ni plated TC samples for (a) Group 1, (b) Group 3, and (c) Group 4.....	120
Figure 4-61. SEM surface images of Week 9 Ni plated and Ni sputtered Groups 1 and 4 TC samples.....	121
Figure 4-62. Residual stress in the gold coating for each of the thermal cycled (TC) samples. Each point represents the averaged residual stress from the three duplicate samples.....	124
Figure 4-63. Electrical contact resistance data as a function of load for Group 1, 3, and 4 Au/Ni plated Week 0 TC samples.....	125
Figure 4-64. Electrical contact resistance data as a function of load for Group 1, 3, and 4 Au/Ni plated Week 9 TC samples.....	125
Figure 4-65. Electrical contact resistance data under a 200g load for the Au/Ni plated thermal cycled samples after nine weeks of cycling. Note that the Group 1 Week 9 data appears to be tri-modal. ....	126
Figure 4-66. Electrical contact resistance data under a 200g load for the Au/Ni plated thermal cycled samples after nine weeks of cycling. Note that the Group 1 Week 9 data appears to be tri-modal. ....	127
Figure 4-67. Residual stress data for all Group 1 Au/Ni plated samples. Note that the magnitude of the residual stress remains approximately constant/decreases slightly for the MFG and TRH aged samples, while decreasing more significantly for the TC aged samples. ....	128

Figure 4-68. Residual stress data for all Group 3 Au/Ni plated samples. Note that the magnitude of the residual stress decreases slightly.....	128
Figure 4-69. Residual stress data for all Group 4 Au/Ni plated samples. Note that the magnitude of the residual stress decreases slightly.....	129
Figure 4-70. Electrical contact resistance data for Group 1 Au/Ni plated samples before and after aging in the MFG environment, showing the effect of localized corrosion in the data distributions for (a) ECR data as a function of load before aging (i.e., Week 0), (b) ECR data as a function of load after nine weeks of aging, and (c) CDF plot of ECR data under a load of 200g.....	130
Figure 4-71. Electrical contact resistance data for Group 4 Au/Ni plated samples before and after aging in the MFG environment, showing the effect of extensive localized corrosion in the data distributions for (a) ECR data as a function of load before aging (i.e., Week 0), (b) ECR data as a function of load after nine weeks of aging, and (c) CDF plot of ECR data under a load of 200g.....	131
Figure 4-72. (a) Electrical contact resistance data for Week 9 Au/Ni plated Group 1 samples and (b) close-up of data in (a) showing the differences in ECR values as a function of the aging environment.....	132
Figure 4-73. (a) Electrical contact resistance data for Week 9 Au/Ni plated Group 3 samples and (b) close-up of data in (a) showing the differences in ECR values as a function of the aging environment.....	133
Figure 4-74. (a) Electrical contact resistance data for Week 9 Au/Ni plated Group 4 samples and (b) close-up of data in (a) showing the differences in ECR values as a function of the aging environment.....	134

## LIST OF TABLES

Table 2-1. Summary of various electrical connector types and applications [50, 59, 60].	5
Table 2-2. Brief description of wear failure mechanism for electrical contacts [7].	7
Table 2-3. Electrical resistivity and conductivity for commonly used metals in electrical connector applications [24].	8
Table 2-4. Summary of the various coating systems used in electrical connector applications with a few of the advantages and disadvantages of each [7, 21, 24 - 28].	9
Table 2-5. Summary of bath compositions and operating conditions for the Watts nickel and nickel sulfamate plating solutions. Source: Di Bari [32].	16
Table 2-6. Summary of various plating operating parameters and their effects on the resulting coating [26, 32, 34, 35, 36, 37].	19
Table 2-7. Summary of the advantages and disadvantages of various sputtering techniques [26].	22
Table 2-8. Listing of the four Battelle Class test environments. Note that no information is provided for the Class 1 environment as data showed no environmental concerns for reliability issues. Source: CALCE [75].	28
Table 2-9. Corrosion mechanisms and product chemistries for nickel and gold plated copper contact materials aged in the Battelle Class test environments. Source: Abbott [1].	29
Table 2-10. Linear thermal expansion coefficients for various materials for temperatures between roughly 20 °C and 300 °C [3, 77].	29
Table 2-11. Summary of various ECR values found in the literature for unaged samples [38, 52, 71-74].	36
Table 2-12. Summary of various techniques used to determine residual stress with their advantages and disadvantages [14-17, 20].	40
Table 2-13. Example of peak location shifts for a few nickel and copper diffraction peaks based on the use of different radiation sources. Change in separation between the nickel and copper peaks is also provided [62].	48
Table 3-1. Chemical composition range provided by M. Vincent & Associates for their C101 oxygen free copper [23].	49
Table 3-2. Substrate surface roughness processing conditions and average resulting $R_a$ surface roughnesses. Samples from Group 1 prepared by LAPCO using proprietary conditions. Samples from Group 2, 3, and 4 were prepared by Micro Lapping & Grinding using various grits of silicon carbide and listed pressures.	51



Table 3-3. Sample matrix overview detailing the prepared surface roughness group and coating system for each specific panel of coupons. Note that each panel consists of twelve coupons, resulting in a total of 432 coupons prepared and aged. ....	52
Table 3-4. Sample matrix detailing the prepared surface roughness group, coating system, and aging environment for each specific panel of coupons tested. ....	55
Table 3-5. Battelle Class II MFG environment [1]. ....	57
Table 3-6. Number of thermal cycles completed for the various aging times. ....	60
Table 4-1. Average surface roughness, $R_a$ , for the unaged samples based on the coating system for Groups 1, 2, 3, and 4 samples. ....	68
Table 4-2. Average surface roughness, $R_a$ , for the unaged Ni sputtered samples grouped based on the deposition run in which the panels were coated for Groups 1, 2, 3, and 4 samples. ....	70
Table 4-3. Coating thickness summary for the Ni plate, Ni sputtered, and Au/Ni plated samples, as well as the targeted coating thicknesses. ....	80
Table 4-4. Summary of Clemex results regarding the area of the sample surface covered by visibly distinguishable corrosion products. ....	104
Table 4-5. Optical profilometry results for the Group 1, 3, and 4 TRH Au/Ni plated samples listing the roughness before and after aging, as well as the percent difference. ....	116
Table 4-6. Optical profilometry results for the Group 1, 3, and 4 TC Au/Ni plated samples listing the surface roughness before and after aging, as well as the percent difference. ....	121
Table 4-7. Linear thermal expansion coefficients (for temperatures between roughly 20 °C and 300 °C) [3, 77]. ....	122
Table 5-1. Summary of trends in residual stress based on surface roughness and aging environment for the Au/Ni plated samples. Note that all residual stress numbers refer to the amount of decrease in tensile residual stress observed. ....	136
Table 5-2. Summary of trends in electrical contact resistance values based on surface roughness and aging environment for the Au/Ni plated samples. Note that all ECR values refer to the increase in ECR observed. ....	137
Table A-1. Optical profilometry data for select samples prior to coating. ....	145
Table A-2. Optical profilometry data for unexposed Au/Ni plated samples. ....	147
Table A-3. Optical profilometry data for unexposed Ni plated samples. ....	149
Table A-4. Optical profilometry data for all unexposed Ni sputtered samples. ....	151
Table A-5. Optical profilometry data for all MFG aged Au/Ni plated samples. ....	153

Table A-6. Optical profilometry data for all TRH aged Au/Ni plated samples .....	154
--	-----

Table A-7. Optical profilometry data for all TC aged Au/Ni plated samples .....	155
---	-----

## ACKNOWLEDGEMENTS

There are many people I would like to thank for their support during my time at Penn State. First, I would like to thank my advisor, Dr. Douglas Wolfe, for his patience and support as I transitioned from my chemical engineering and mathematics background to materials science, as well as for all that he has taught me as a teacher and advisor. In addition, I would like to thank the staff members and fellow students in my research group for their technical assistance and advice for my research.

I would also like to thank my manager, Jill Glass, and mentors, Rob Sorensen and David Enos, at Sandia National Laboratories for their continued technical support and for all of the time they spent talking with me and providing valuable suggestions and insight to my research. In addition, I would like to thank another member of our organization at Sandia, Sam Lucero, for his help in preparing and mounting my samples into the various aging chambers as well as keeping tabs on them during the entire aging study while I was back at Penn State. I would also like to thank Sandia National Laboratories in general for their support through the Master's Fellowship Program.

Last, but not least, I would like to thank my family for their unfailing love and support, as well as my very close friends in State College, Michelle, Steve, Mikala, and Bailey Hursh, who have become like a second family to me with all of the support and kindness they have bestowed.



Sandia National Laboratories is a multi-program laboratory managed and operated by Sandia Corporation, a wholly owned subsidiary of Lockheed Martin Corporation, for the U.S. Department of Energy's National Nuclear Security Administration under contract DE-AC04-94AL85000.



## **Chapter 1**

### **Introduction**

Over the course of the last century, the field of electronics has exploded becoming a fast growing and important area of science and engineering, as well as being increasingly incorporated into our daily lives. The use of computers, internet, cell phones, radios, and television has greatly changed our lives, especially in terms of conveniences and capabilities. As a result, the reliability of electronics has also become of great concern as various electrical components play a crucial role in many systems in which a failure could result in catastrophe.

In order to improve the reliability and performance of a component, coatings are often applied to the component's surface to help protect against and prevent degradation or failure from the service environment, such as wear and corrosion, which can be detrimental to the component's functionality. As such, a component's service life can be closely related to the coating condition and performance. If the coating fails (i.e., cracking, delamination, etc.) the life of the component is reduced, sometimes dramatically, as the component is then exposed to the service environment.

The type of coating used (i.e., coating material and process) depends on the application. In general, the applied coating is chosen in order to improve specific properties of the component such as corrosion resistance, wear resistance or thermal resistance [24]. For instance, electrical contacts are typically coated with a metal/metal alloy as they are electrically conductive. On the other hand, the same metal coatings utilized on electrical contacts are completely inadequate for protecting substrate metals in high temperature engines, as metals are good conductors of heat and would not be able to protect the substrates from the excessive engine operating temperatures (ceramic thermal barrier coatings are used in this particular application).

For electrical connector applications there are a range of metals/metal alloys and coating processes that have been examined and/or used. A few of the coating materials that have been investigated include nickel, silver, palladium, platinum, and gold [7, 21, 24-28]. One of the most common, particularly for high reliability applications, is electroplated gold over nickel because of its high corrosion resistance [7, 24] and the ease of coating complex objects by the electroplating process.

There are many factors that can affect the performance of a coating beyond its intrinsic material properties including. For example substrate cleaning (i.e., potential impurities on the surface), surface roughness, adhesion, residual stresses (magnitude and type, i.e., compressive versus tensile), coating microstructure, hardness, and service environment need to be considered. Of course, several of these factors can be tailored, at least to some degree, based on the sample preparation and deposition parameters/processes utilized. Previous research on coatings for electrical connectors has focused on either the change in electrical contact resistance in a Battelle Class II (or similar) environment (more detail in Section 2.3.1) or the study of unaged coating properties, such as hardness and residual stress work. However, much of the earlier work has been completed with limited selection of surface roughnesses, if at all, that does not represent the full range of surfaces roughnesses found on electrical contacts and connectors. Therefore, this work seeks to examine the effect of connector material surface roughness on electrical contact resistance under different environmental conditions.

## **Objectives**

The primary objective of this research was to determine how the electrical contact resistance of gold and nickel coated copper connector materials is affected by various aging environments including: elevated temperature and relative humidity (TRH), thermal cycling (TC), and atmospheric corrosion/mixed flowing gas (MFG). Additional secondary objectives are:

- To determine the effect of surface roughness on the electrical contact resistance before and after aging.
- To determine how the surface roughness affects the residual stress of the gold plated coating.
- To determine how the coating residual stress is affected by aging in the environments previously mentioned (i.e., TRH, TC, and MFG).

## Chapter 2

### Literature Search/Background

Electrical connectors are an important part in electrical systems, which are widely used in today's world. Whether it be an alarm clock, a cell phone, or a computer, most people interact with, and in some cases depend on, equipment requiring the use of some sort of electrical connector. In addition, with the level of dependency that many systems have on the functionality of the electrical contacts, it is important to know what may affect their performance.

#### 2.1 Electrical Connectors

As the name suggests, an electrical connector connects various parts of an electrical circuit, to provide an uninterrupted electrical current across the electrical contact interface [50]. There are many applications for connectors ranging from simple connections between small electronics (see Figure 2-1) to network connections, to large connections for utility/transmission power lines.

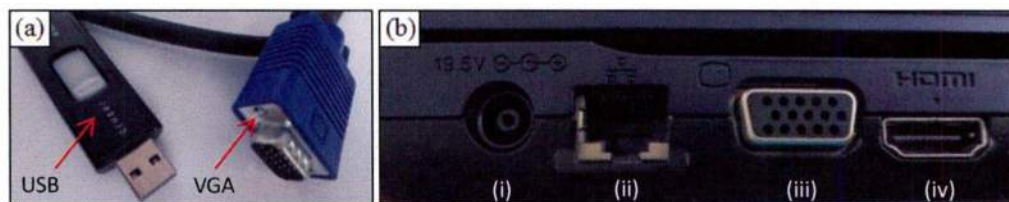


Figure 2-1. Digital images showing example electrical connectors: (a) VGA (video graphics array) connector and USB (universal serial bus) flash drive and (b) side view of a laptop showing (i) connection for a power connector, (ii) network cable, (iii) VGA, and (iv) HDMI (high definition multimedia interface) cable input, respectively.

The design of a connector is dependent on the specific application and system requirements.

A few of the most common connector types include: plug-and-socket, wire, bolted, insulated-



piercing, and sliding. Each of which is listed along with a brief description of their particular application in Table 2-1[50, 59, 60].

Table 2-1. Summary of various electrical connector types and applications [50, 59, 60].

Connector Type	Description	Application	Common Design Styles
Plug-and-Socket	Stationary/fixed contact	Quick electrical connection/disconnections	Jacks, pins, rack-and-panel connectors, integrated-circuit sockets, printed-circuit edge connector, etc.
Wire	Stationary/fixed contact	Connecting wires/cables to connection sites for electronic equipment	Weld bond, crimped bond, solder joint, screwed joint, etc.
Compression	Stationary/fixed contact	Power network	Bolted connector
Insulation-Piercing	Stationary/fixed contact	Hermetically sealed contacts	Jaw clamp
Sliding	Moving contact	Instrumentation/controls	Crossed rod, pin on disc, cartridge brush, etc.

### 2.1.1 Failure Mechanisms in Electrical Contacts

The functionality of electrical connectors is often reliant on the contact resistance of the contact surface. There are six common failure mechanisms observed that cause an increase in the contact resistance for electrical contacts: corrosion, wear, interference, mechanical, thermal acceleration, and thermal expansion [7].

Corrosion failure is caused by a chemical reaction between the contact and its surroundings, which can leave the surface of the connector covered in corrosion products and insulating films, thus increasing the contact resistance. The main types of corrosion observed in electrical contacts include creep corrosion (i.e., reactive base metal corrosion products creep over the noble metal coating), pore corrosion (corrosion product from the base metal moves to the surface through pores in the coating), and dry corrosion (i.e., oxidation). Several factors including temperature, presence of corrosive gases, dust, and air velocity can influence the corrosion of an electrical contact by altering the rate/extent of corrosion. Increased temperatures and air flow can increase the kinetics with added heat and improved circulation of corrosive species [7, 24]. Pore corrosion is typically observed for



nickel and gold coated contacts exposed to a Battelle Class II atmospheric corrosion mixed flowing gas (MFG) environment and is depicted for this specific system in Figure 2-2 [6, 13, 24] .

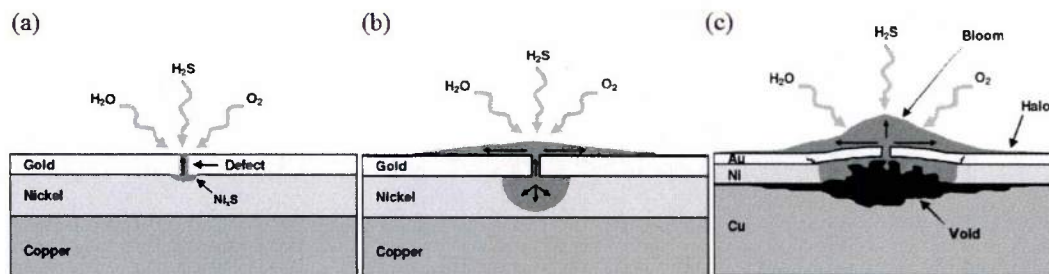


Figure 2-2. Schematic of pore corrosion nucleation and growth in nickel and gold plated copper aged in a Battelle Class II atmospheric corrosion MFG environment: (a) initiation of corrosion site with pollutant gases reacting with the less noble nickel underlayer through a pore/defect in the gold top coating, (b) propagation of corrosion further into the nickel layer, with corrosion products traveling through the pore to the surface, and (c) corrosion reaches/corrodes the copper (with corrosion products still migrating through the pore to the surface creating a void at the nickel to copper interface). Source: Enos [6].

Wear failure occurs when excessive motion causes damage to the connector interface, such as from vibrations or sliding. Wear failure can take place by one or more of a range of mechanisms including adhesive wear, abrasive wear, delamination, brittle fracture, and fretting. Table 2-2 provides a brief description of the common wear mechanisms. Lubrication can aid in reducing wear in electrical contacts in some situations, though it does not prevent all wear mechanisms. Instead, careful decisions regarding surface roughnesses, coating materials, and deposition processes and parameters, particularly those affecting the residual stresses in the coating (i.e., tensile versus compressive), are more influential factors that can be addressed to reduce wear failure. It should also be noted that in many wear failure mechanisms, debris is formed which then can cause abrasive wear degradation [7].

Table 2-2. Brief description of wear failure mechanism for electrical contacts [7].

Wear Mechanism	Description
Adhesive	Damage to contact surface caused by adhesion, decohesion, or reduced adhesion at the contact surface interface
Abrasive	Damage caused to contact surface by contact with a harder and rougher surface or by particles coming in between moving contact surfaces
Delamination	Subsurface cracking and crack coalescence causing delamination from cyclic movement
Brittle Fracture	Development of cracks in brittle materials due to sliding at the contact surface
Fretting	Damage caused by small cyclic movements

Interference and mechanical failure mechanism are interrelated. Interference failure is based on particles, such as dust, coming in between contact surfaces causing a variety of issues, including preventing or reducing electrical contact. Mechanical failure of connectors encompasses a larger range of failure mechanisms from interference of particles to actual physical damage to the contact surfaces via mishandling or even disfigured components due to poor connector designs [7].

The last two failure mechanisms are temperature based. Thermal expansion failure is caused by a mismatch in the thermal expansion coefficients for the materials within the connectors or the motion that might occur at the contact interface as a result of thermal cycling. The last of the six main connector failure mechanisms, thermally accelerated failure, occurs when connectors are exposed to elevated temperatures which in turn accelerate certain mechanisms, including diffusion, stress relaxation, and creep [7].

In many cases, damage caused by each of the latter five main failure mechanisms (i.e., wear, interference, mechanical, thermal expansion, and thermal acceleration) can lead to additional damage by corrosion, as any damage sustained by the protective coating on the surface of the connector could leave the more active nickel or copper exposed to the service environment. In general, the failure mechanism type observed often depends on the connector type. For instance, wear failure

mechanisms are a larger concern for sliding connector applications rather than for stationary or permanently mated connectors [7].

### 2.1.2 Materials in Electrical Connectors

The failure mechanisms observed in electrical connectors are based in part on the application and service environment of the connector. As such, the substrate and coating materials used in electrical connectors can vary slightly based on their application. The connector substrate material is chosen, predominately, based on electrical conductivity and cost. As such, copper and copper alloys are typically used due to their high electrical conductivity (see Table 2-3), though aluminum has also been used in some cases [7, 24].

Table 2-3. Electrical resistivity and conductivity for commonly used metals in electrical connector applications [24].

Material	Resistivity at 20°C $\mu\Omega\text{cm}$	Electrical Conductivity at 20°C $\text{m}\Omega^{-1}\text{mm}^{-2}$
Silver	1.59	63.0
Copper	1.65	59.9
Gold	2.19	45.7
Aluminum	2.65	37.7
Nickel	6.84	14.6
Platinum	10.6	9.5
Palladium	10.8	9.3

Based on the failure mechanisms discussed in the previous section, electrical connectors typically have a coating or coating system applied to the base substrate material in order to help prevent/delay failure and thus extend the life and reliability of the connector. Several different coatings have been investigated in the literature to identify coating materials that can maintain a relatively stable and low electrical resistance while in the various service environments. Table 2-4

provides a summary of some of the advantages and disadvantages for each [7, 21, 24-28]. Most coatings are produced by electroplating processes due to their low costs and the ease of coating complex components. As such, limited work has been completed with silver, gold, and nickel sputtered coatings [24]. Some previous work has investigated the possibility of using a nickel sputtered coating instead of a nickel plated coating due to the more environmental friendly nature of sputtering as opposed to electroplating (which utilizes solutions that must often undergo hazardous waste treatment prior to disposal) and the possibility of improved barrier related properties. However, little aging work has been completed [28].

Table 2-4. Summary of the various coating systems used in electrical connector applications with a few of the advantages and disadvantages of each [7, 21, 24 - 28].

Coating Material	Coating Process	Advantages	Disadvantages
Pure Gold	Electroplating	<ul style="list-style-type: none"> <li>• Very high corrosion resistance</li> <li>• Very high electrical conductivity</li> </ul>	<ul style="list-style-type: none"> <li>• Low wear resistance</li> <li>• Expensive</li> </ul>
Hard Gold/Nickel	Electroplating	<ul style="list-style-type: none"> <li>• Very high corrosion resistance</li> <li>• Very high electrical conductivity</li> <li>• Good wear resistance</li> </ul>	<ul style="list-style-type: none"> <li>• Gold is expensive</li> </ul>
Silver	Electroplating	<ul style="list-style-type: none"> <li>• Very high electrical conductivity</li> <li>• Less expensive than gold</li> </ul>	<ul style="list-style-type: none"> <li>• Low wear resistance</li> <li>• Lower corrosion resistance</li> </ul>
Tin, Tin-Lead Alloys	Electroplating	<ul style="list-style-type: none"> <li>• Less expensive than gold</li> </ul>	<ul style="list-style-type: none"> <li>• Low wear resistance</li> <li>• Lower corrosion resistance</li> </ul>
Palladium, Palladium Alloys (with or without Au flash)	Electroplating	<ul style="list-style-type: none"> <li>• Good wear resistance</li> <li>• Less expensive than gold</li> </ul>	<ul style="list-style-type: none"> <li>• Lower corrosion resistance</li> </ul>
Gold Alloys	Cladding	<ul style="list-style-type: none"> <li>• Good corrosion resistance</li> </ul>	<ul style="list-style-type: none"> <li>• Low wear resistance</li> </ul>
Nickel	Electroplating	<ul style="list-style-type: none"> <li>• Inexpensive</li> <li>• Ease of coating complex objects</li> </ul>	<ul style="list-style-type: none"> <li>• Lower corrosion resistance</li> <li>• Contaminations in coating</li> </ul>
Nickel	Sputtering	<ul style="list-style-type: none"> <li>• Finer microstructure</li> </ul>	<ul style="list-style-type: none"> <li>• Difficult to coat complex objects</li> </ul>

The most commonly used coating system is a plated gold layer over a nickel underlayer. Gold is the preferred top coating for electrical connectors, particularly for high reliability applications, as it has a very high resistance to corrosion in addition to being very electrically conductive [6, 7, 13, 25]. The nickel underlayer acts as a barrier layer, preventing the diffusion

between the base metal and gold, as well as increasing the wear resistance and durability of the gold coating [27, 29].

While gold is the best choice in terms of corrosion resistance, it is also very expensive. As such, thinner gold layers or alternative coatings are often pursued for electrical contacts. The issue with reducing the gold coating thickness is that there is a tradeoff between decreasing costs and increasing porosity in the coating (which leads to lower corrosion resistance as more of the underlying materials are exposed to the environment) [7, 24, 29]. In efforts to balance these concerns, coating thicknesses used vary depending on the application. In cases where highly corrosive environments are present or high reliability is required thicker gold coatings are used. Gold coating thicknesses tend to range from roughly 0.4  $\mu\text{m}$  to 1.3  $\mu\text{m}$  with a nickel underlayer of at least 1.3  $\mu\text{m}$ . Gold coatings with thicknesses under 0.8  $\mu\text{m}$  are used in benign environments [21, 29]. In addition, recent research investigating the possibility of adding a 1  $\mu\text{m}$  sealant layer of either pure silver or pure tin underneath the nickel and gold coatings to aid with the possibility of reducing the amount of gold without sacrificing any of the corrosion resistance of the system has been pursued [27].

## **2.2 Coating Processes**

There are many different coating processes available, including electroplating, sputtering, evaporation, and cladding. Each process is different and has its own advantages and disadvantages. There are six main steps that can be used to help determine a suitable coating for a specific application. These steps include:

1. Identify and understand the final application
2. Identify the desired properties that are believed to be the most important for the application
3. Perform a materials selection to identify the best coating candidate material

4. Choose the proper deposition technique based on fabrication methods
5. Coat the component with the chosen process while optimizing the deposition technique
6. Characterize, analyze, and measure properties/performance [26].

For this research, the application is electrical contacts/connectors, thus the primary desired properties include low electrical resistance (high electrical conductivity), high corrosion resistance, and good wear resistance. The current state of the art coating system for electrical contacts and connectors is a combination of nickel and gold layers deposited via electroplating. As electroplating is not a line-of-sight process, complex components can be coated with more ease. In addition, electroplating is a relatively inexpensive technique [7, 24, 26]. As such, the majority of samples prepared for this research were prepared via electroplating. However, a subset of coupons was prepared with a nickel sputtered coating to act as a comparison.

### ***2.2.1 Electroplating***

Electroplating is an aqueous process that involves the oxidation of the target material at the anode, creating cations in the electrolyte plating solution. The cations are then attracted to the negatively biased substrate at the cathode where they are reduced at the substrate surface creating the coating. This process is depicted for nickel electroplating in Figure 2-3 where the anode is the nickel target material, the cathode is the substrate material (i.e., copper for the purposes of this research), with the following fundamental oxidation (Equation 2.1a)/reduction (Equation 2.1b) reactions occurring.





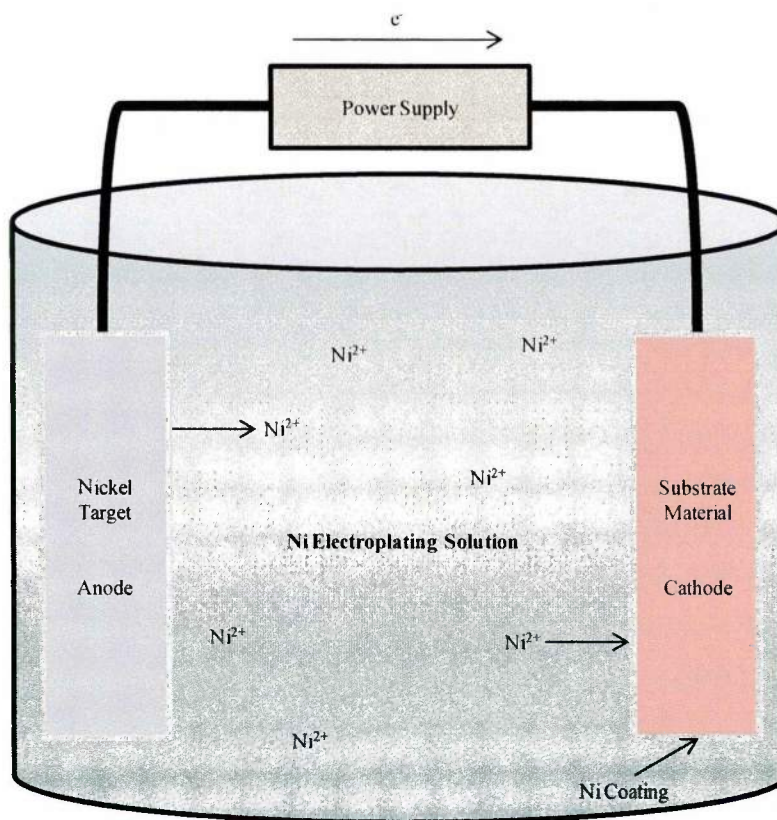


Figure 2-3. Schematic of the nickel electroplating process depicting the nickel target (anode) and the substrate (cathode). Nickel is oxidized and removed from the target material and goes into solution, is attracted to the negatively biased substrate material, and reduces back to nickel metal on the substrate surface creating the nickel coating.

The amount of material removed from the target and deposited on the substrate is related to the current density and plating time via Faraday's Law (shown in Equation 2.2) [34, 35, 36].

$$m = \frac{ItM}{nF} \quad (\text{Eq 2.2})$$

where  $m$  = mass lost by target, g

$I$  = current, A

$t$  = time, s

$M$  = molecular weight, g/mol

$n$  = charge of dissolved ions, equivalent/mol

$F$  = Faraday's constant, C/equivalent

The complete plating process, however, is more complicated than described earlier, with several important parameters that influence the plating process and quality of the coating include the electrolyte solution, applied current, temperature, pH, circulation, anode/cathode configurations, deposition time, and substrate cleaning/activation. In addition, each of the listed parameters can affect more than just one aspect of the plating process.

The composition of the electroplating solution is very important in the plating process. In order for electroplating to occur, the anode and cathode must be electrically connected. Thus, the plating solution, as well as the anode and cathode materials, must be electrically conductive, which limits the materials that can be electroplated. Major components in the plating bath include metal ions/compounds supplying ions for coating, support ions (such as salts that help increase the conductivity of the plating solution), and additives. The metal ions/compounds supplying metal ions are used to create the actual coating and the support ions are added to help improve the conductivity of the plating solution. A variety of additives can be included in the plating solution to help control the coating properties, including, but not limited to, brighteners, stress relievers, and levelers. The name of each additive describes its effect on the coating/deposit. For example, stress relievers are added to help reduce the stresses in the coating and brighteners are added to help improve the optical reflectivity of the plated surface. Levelers (often organic additives) create a smoother surface by causing preferential plating in the recesses/valleys in the surface, see Figure 2-4c. Peaks and valleys can be the result of scratches in the substrate or surface preparations such as grinding [26, 32, 34, 35, 36, 67].



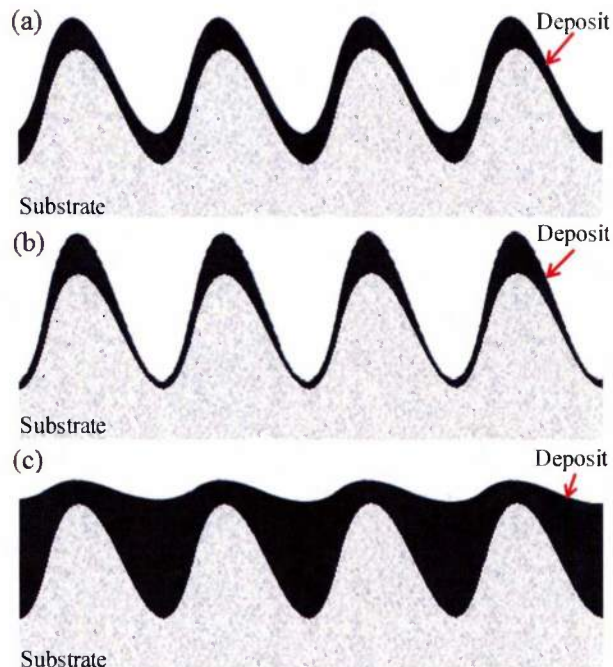


Figure 2-4. Microthrowing power/leveling effects during electroplating. (a) Neutral microthrow, i.e., even coating thickness across peaks and valleys, (b) negative microthrow, i.e., predominate plating on peaks resulting in increased surface roughness, and (c) positive microthrow, i.e., leveling effects resulting in decreased surface roughness.

In addition to decreasing the surface roughness via the use of levelers, the plating solution composition can also increase the surface roughness if the peaks are preferentially plated instead of the recesses/valleys. In general, the uniformity of the coating deposition based on the plating solution, is referred to as the throwing power. The throwing power can be separated into macro and micro throwing power, where macro throwing power refers to the thickness uniformity of a plating on a substrate with macroscopic surface features [35]. Similarly, but on a smaller scale (i.e., irregularities/surface features roughly 10  $\mu\text{m}$  to 1 cm in size), the micro throwing power plating solution describes the coating uniformity to one of three possible categories: neutral micro throw, positive micro throw, or negative microthrow (see Figure 2-4). A plating solution producing a coating with uniform thickness over surface features is referred to as having a neutral micro throw. If the peaks of the features have a larger coating thickness than the recesses, the plating solution has a

negative microthrow, while a plating solution with a leveling effect on the coating has a positive microthrow [26, 27, 32, 34, 35].

The composition of the plating solution can also affect the porosity, coating composition, and various mechanical properties (such as hardness, tensile strength, etc.). Many of these properties are influenced by the presence of impurities in the plating solution which can be co-deposited along with the intended metal. For example, sulfur deposited with nickel coatings can result in compressive stresses, and the deposition of gold with small amounts of cobalt increase the coating hardness/wear resistance, and an increased pH can cause metal hydroxides to be co-deposited [32, 34, 35, 37]. Di Bari (Figure 2-5) shows qualitatively how a few of the various operating parameters can influence properties of electroplated nickel for the commonly used, Watts nickel and nickel sulfamate plating solutions. Compositions and typical operating conditions for each plating solution are detailed in Table 2-5 [32].

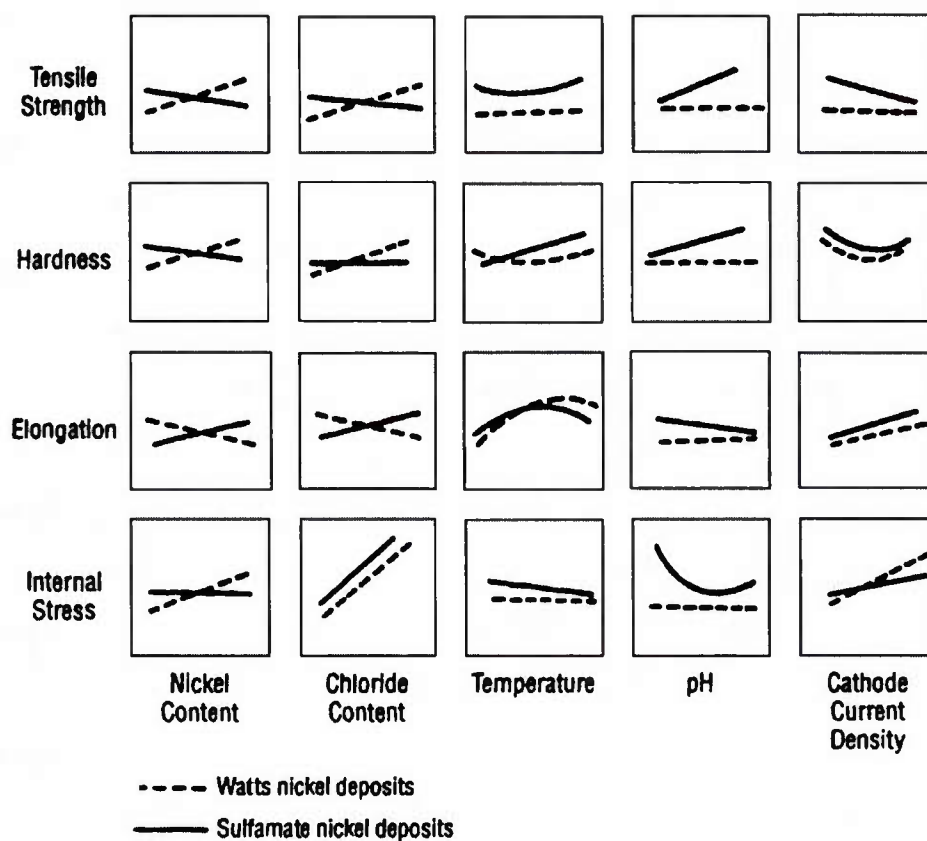


Figure 2-5. Example of the effects the operating conditions can have on electroplated nickel from Watts and sulfamate solutions. Source: Di Bari [32].

Table 2-5. Summary of bath compositions and operating conditions for the Watts nickel and nickel sulfamate plating solutions. Source: Di Bari [32].

	Parameter / Bath Component	Watts Bath	Nickel Sulfamate Bath
Bath Composition (g/L)	Nickel sulfate, $\text{NiSO}_4 \cdot 6\text{H}_2\text{O}$	225-400	---
	Nickel sulfamate, $\text{Ni}(\text{SO}_3\text{NH}_2)_2$	---	30-45
	Nickel chloride, $\text{NiCl}_2 \cdot 6\text{H}_2\text{O}$	30-60	300-450
	Boric acid, $\text{H}_3\text{BO}_3$	30-45	0-30
Operating Conditions	Temperature ( $^{\circ}\text{C}$ )	44-66	32-60
	Cathode current density ( $\text{A}/\text{dm}^2$ )	3-11	0.5-30
	pH	2-4.5	3.5-5.0

The current density and deposition time are two of the parameters that govern the coating thickness. If the current density is not distributed properly, the coating thickness will vary, with thicker coatings produced in the areas with higher current densities. As such, the geometry and arrangement of the anode (target material) and cathode (substrate) can influence the coating uniformity by adjusting the current density distribution at the cathode [35]. Figure 2-6 depicts this principle for the example of electroplating nickel onto a copper substrate. Additional parameters that influence the current distribution include: plating solution composition, conductivity/composition of the anode/cathode, and surface condition of the cathode [26].

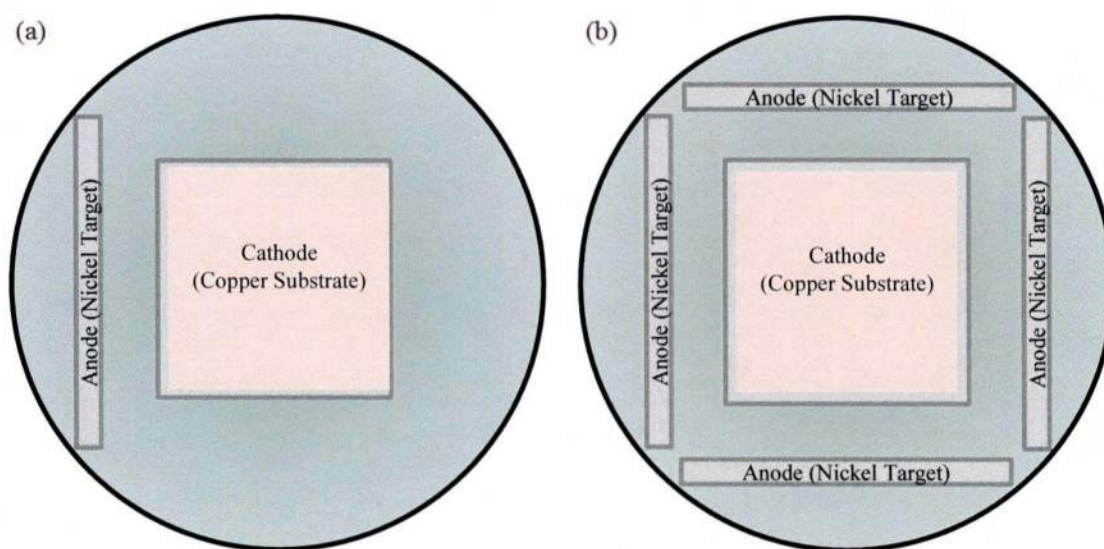


Figure 2-6. Schematic depicting the effect cathode/anode geometries can have on the coating uniformity. (a) Single anode located on one side of the substrate resulting in a thicker coating on the surfaces nearer the target material and (b) four anode system allowing for improved coating uniformity.

Substrate preparation and cleaning is another aspect of the plating process that can have a large influence on the quality of the coating produced. If the substrates are not properly cleaned prior to coating, impurities (such as dirt, oils, etc.) will remain on the surface and can negatively impact the coating adhesion. In addition, impurities on the substrate surface can also increase the porosity of the

coating, as they may not necessarily be electrically conductive, and thus will not be plated [26, 37]. Substrate surface roughnesses can further affect the coating thickness, as the coating thickness on a rough sample can be thinner as compared to a smooth sample plated under the same condition. As x-ray fluorescence is a commonly used technique to examine electroplated coatings, based on its quick and non-destructive nature, the mass of coating material is evaluated. As such, for a given mass of coating material deposited on the surface, the coating thickness will not be the same for a rough sample versus a smooth one due to the fact that the amount of surface area to be coated increases with increasing surface roughness [37].

The resulting surface morphology of an electrodeposited coating can vary depending on many of the aforementioned electroplating processing parameters. For instance, the surface topography in general will follow the topography of the underlying substrate. Depending on the size of the surface features, coating thickness, and presence of leveling agents in the plating solution, the resulting surface could be smoother or rougher than the substrate surface (see Figure 2-7 and Figure 2-8) [35, 38]. A brief summary of a few of the processing parameters along with the various aspects of the plating process that they influence are provided in Table 2-6.

Table 2-6. Summary of various plating operating parameters and their effects on the resulting coating [26, 32, 34, 35, 36, 37].

Parameter	Process Influence
Temperature	• Deposition rate
pH	• Coating composition
Agitation	• Deposition rate • Coating uniformity
Current Density	• Deposition rate • Coating uniformity • Coating composition • Coating microstructure • Coating adherence
Deposition Time	• Coating thickness
Electrolyte Composition	• Deposition rate • Coating composition • Stress in coating • Porosity • Corrosion resistance • Throwing power/coating roughness
Substrate Preparation	• Porosity • Coating microstructure • Coating adherence • Coating uniformity • Throwing power/coating roughness
Anode/Cathode Geometry	• Coating uniformity

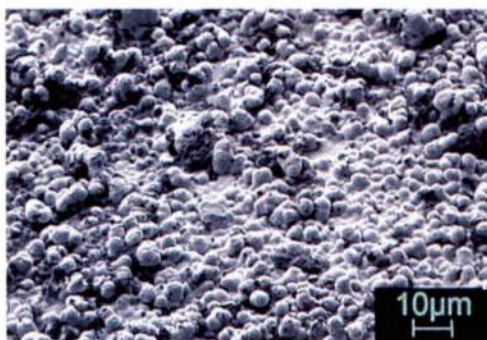


Figure 2-7. Image of gold plated copper with spherical nanoparticles incorporated into the coating producing a spherically structured surface. Source: Song [21].



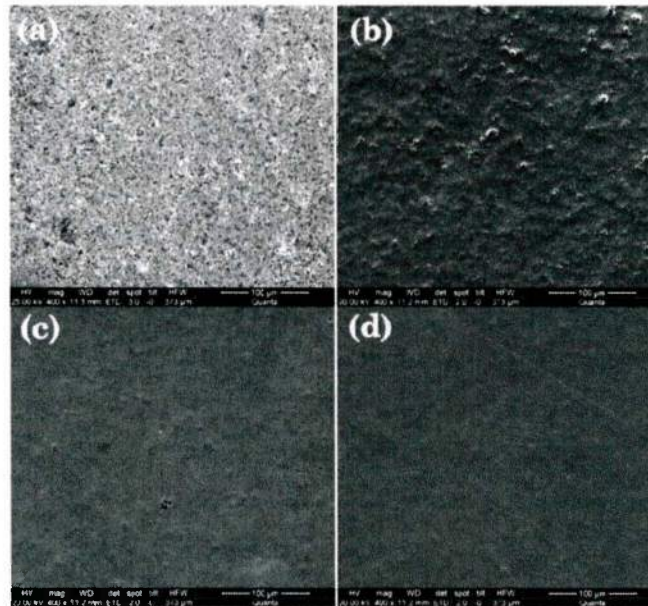


Figure 2-8. SEM images of gold plated oxygen free high conductivity (OFHC) copper, from P. Misra and J. Nagaraju, showing the differences in surface topography based on the thickness of the gold coating applied with (a) bare copper, followed by copper with (b) 0.1  $\mu\text{m}$  thick gold plating, (c) 0.3  $\mu\text{m}$  thick gold plating, and (d) 0.5  $\mu\text{m}$  thick gold plating. Source: Misra & Nagaraju [38].

### 2.2.2 Sputtering

There are several different types of sputtering processes, including diode, triode, direct current (DC), radio frequency (RF), balanced magnetron, unbalanced magnetron, and high power impulse magnetron (HIPIMS). Each varies from the fundamental process to enhance efficiency or to allow for added capabilities (see Table 2-7). In the basic sputtering process (also known as diode sputtering), an inert gas is ionized via a collision with a high energy electron (see Figure 2-9). The ionized gas particles are then accelerated toward the target material which has a negative voltage applied to it. When the ionized gas particles collide with the target material, momentum is transferred causing atoms of the target material to be ejected from the surface and deposit on the negatively charged substrate, as depicted in Figure 2-10 [26, 40-42].

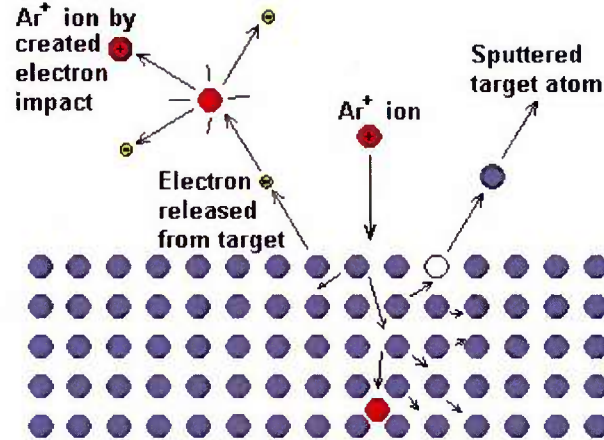


Figure 2-9. Schematic depicting the ionization of the inert gas (argon) used during sputtering upon colliding with an electron, as well as the subsequent collision of the ionized gas particle with the target surface ejecting target atoms. Source: Oxford Vacuum Science [22].

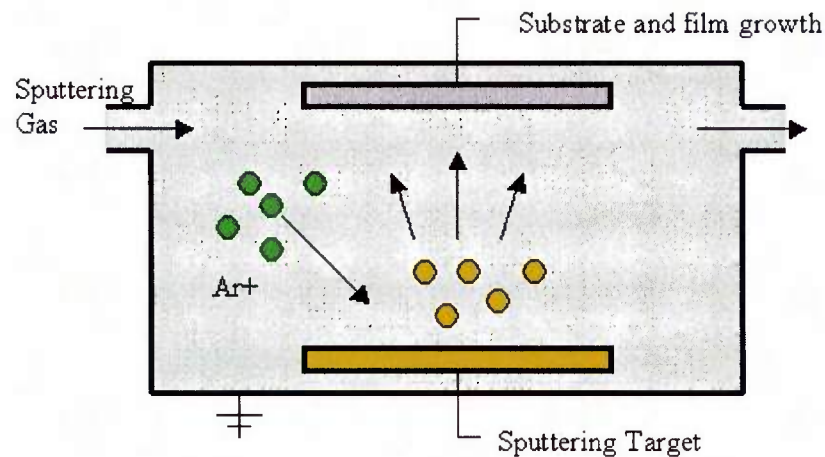


Figure 2-10. Schematic of the fundamental sputtering process depicting the ionized gas particles ( $\text{Ar}^+$ ) colliding with the target material causing target atoms to be ejected and deposited on the substrate. Source: Reade [39].

While diode sputtering is simple, it also can have low deposition rates. Magnetron sputtering addresses this issue by using a magnet and the creation of a magnetic field to retain the electrons near the target surface, thus creating a higher electron density and an increased number of collisions between the electrons and inert gas particles (Figure 2-11). Since increased sputtering and deposition rates are achieved, magnetron sputtering is among the most commonly used sputtering techniques.

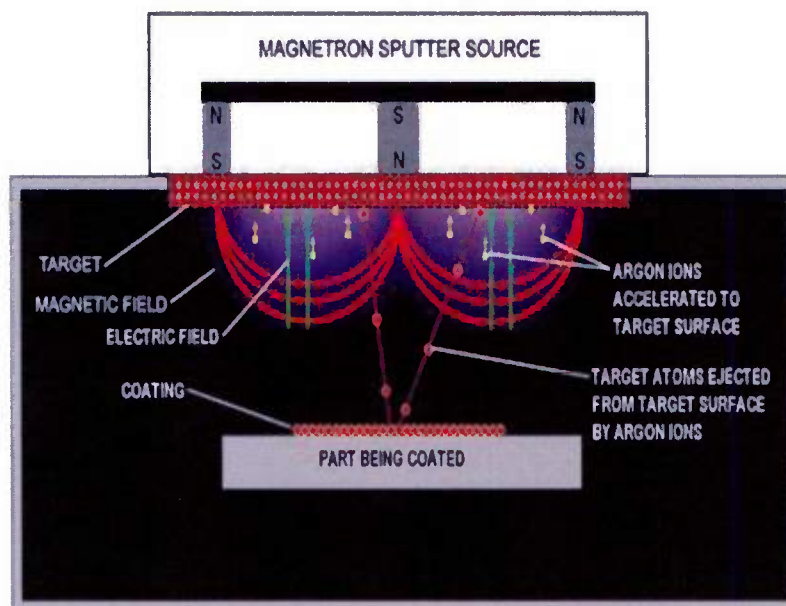


Figure 2-11. Schematic of the magnetron sputtering process depicting the magnetic field used to retain electrons near the target surface. Ionized gas particles ( $\text{Ar}^+$ ) colliding with the target material causing target atoms to be ejected and deposited on the substrate. Source: Maraca Coating Technologies, LLC [47].

Table 2-7. Summary of the advantages and disadvantages of various sputtering techniques [26].

Sputtering Method	Advantages	Disadvantages
Diode	<ul style="list-style-type: none"> <li>Simple design</li> <li>RF or DC</li> </ul>	<ul style="list-style-type: none"> <li>Low deposition rates</li> <li>Hard to deposit uniformly on complex components</li> <li>Residual stresses prevent the creation of thick coatings</li> </ul>
Triode	<ul style="list-style-type: none"> <li>Lower pressure required</li> </ul>	
Magnetron	<ul style="list-style-type: none"> <li>Increased sputtering/deposition rates</li> <li>Decreases impurities in coatings</li> <li>Lower pressure required</li> <li>Higher efficiencies</li> <li>RF or DC</li> <li>Direct or reactive sputtering</li> <li>Higher target utilization (such as with unbalanced magnetron)</li> </ul>	<ul style="list-style-type: none"> <li>Difficult to sputter magnetic materials</li> <li>Difficult to coat complex objects</li> </ul>
HIPIMS	<ul style="list-style-type: none"> <li>Improved adhesion</li> <li>Improved microstructures</li> <li>Improved coverage of complex objects</li> </ul>	<ul style="list-style-type: none"> <li>Lower deposition rates as compared to magnetron sputtering</li> </ul>

There are several deposition parameters (pressure, temperature, ion energy, etc.) that have an impact on the coating properties. Qualities such as adhesion, purity, structure, coating growth modes, and coating microstructure are amongst the most important influenced by the operating conditions.

The three primary growth modes are Volmer-Weber, Frank van der Merwe, and Stanski-Krastavnov. The Volmer-Weber mode (i.e., island mode) can be described by the formation of individual islands of coating material that grow to form the coating. Island growth is typical when stronger bonding is formed between the coating materials rather than between the coating material and the substrate. Frank van der Merwe growth (i.e., layer-by-layer mode) is observed for systems where the bond strength between film and substrate atoms is greater than or equal to the bond between coating atoms. As most systems do not strictly correspond to either of the two aforementioned growth modes, the most common mode observed is the Volmer-Weber mode. This mode is a “mixed-mode” in that the coating is formed by a combination of the previous two methods with some layer-by-layer aspects as well as island formations [26, 43]. Each growth mode is depicted in Figure 2-12.

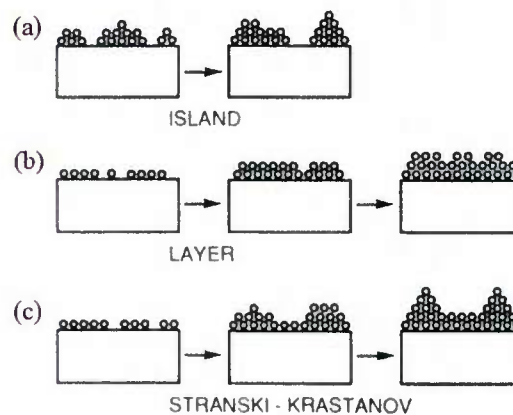


Figure 2-12. Schematic depicting the three growth modes observed in thin film deposition: (a) Volmer-Weber or Island, (b) Frank van der Merwe or layer, and (c) Stranski-Krastanov. Source: Ohring [43].

Ion bombardment can be used to improve coating properties during deposition. Depending on the bombarding ion energy, several phenomena can occur. Nine different surface effects are depicted in Figure 2-13, including removal of surface impurities, removal of surface atoms via sputtering, creation of surface vacancies, incorporation of impurities, and crevice filling [31]. The subsurface effects from ion bombardment, i.e., the creation of vacancies, intermixing of atom, and re-sputtering of atoms, are further illustrated in Figure 2-14, depicting the specific types of vacancies formed. Depending on the system needs, many of these effects are beneficial and can result in smoother coatings with increased density, step coverage, and adhesion [26, 31].

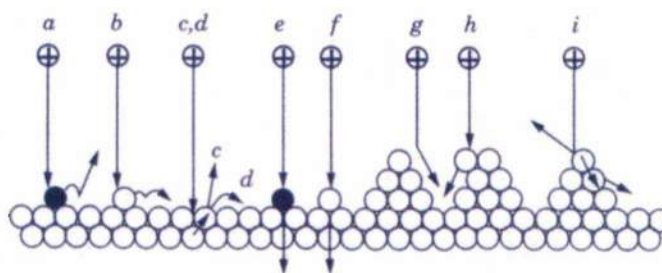


Figure 2-13. Schematic depicting the “effects of bombarding ions on the surface atoms: (a) adsorbate removal or chemical activation, (b) lateral displacement, (c) surface vacancy created by sputtering, (d) surface vacancy created by displacement to an adatom position, (e) knock-on implantation of an impurity atom, (f) knock-on implantation of a film atom, (g) crevice filling by ion-enhanced surface mobility, (h) crevice filling by forward sputtering, and (i) breakup of 3D nucleus”. Source: Smith [31].

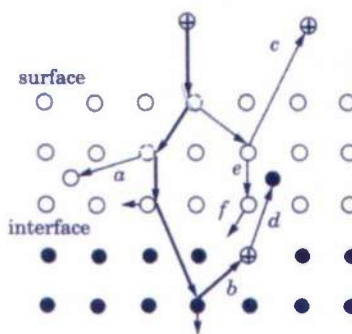


Figure 2-14. “Types of atomic displacements produced in the collision cascade. The heavy line is the path of the impinging ion. (a) Frenkel-pair creation, (b) replacement collision, (c) sputtering, and (d) ion mixing”. Source: Smith [31].



In addition to these surface/subsurface effects, the overall microstructure of the coating can be modeled as a function of the bombarding ion energy, substrate temperature, and the argon pressure as shown in Figure 2-15. A total of five zones are depicted (Zone 1, Zone M, Zone T, Zone 2, and Zone 3) in the structure zone models. Zone 1 is characterized by a low density packing of tapered columns. Zones M and T are part of a region called a transition region in earlier versions of the model [43, 45], though now separated with Zone T remaining a transition region and Zone M a region with a domed topped columnar structure [46]. Zone 2 is characterized by columnar grains with a faceted surface, and Zone 3 has a higher density recrystallized grain structure [26, 46].

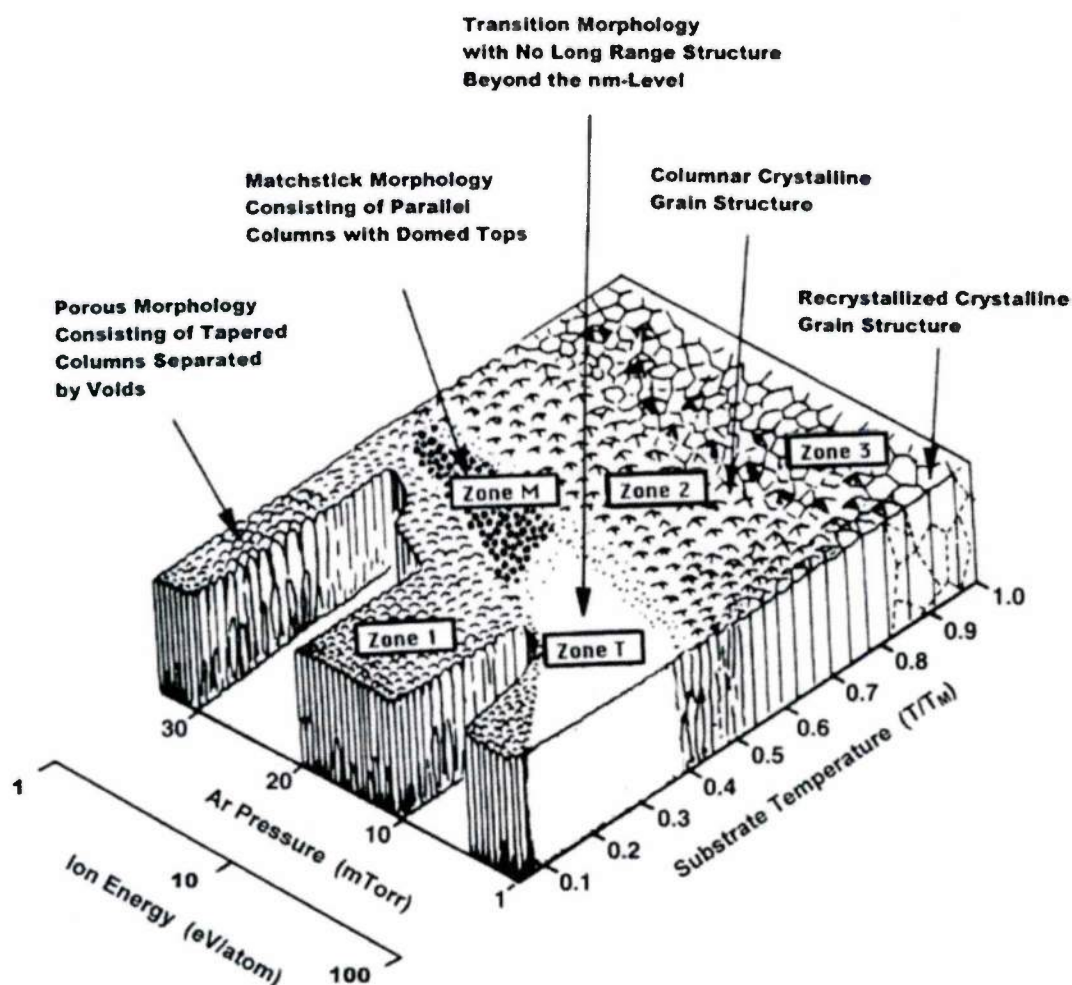


Figure 2-15. Structure Zone Model schematic describing the microstructure of sputtered coatings as a function of substrate/melting point temperature, argon pressure, and ion energy. Source: Stelmack [46].



One disadvantage associated with magnetron sputtering is that magnetic materials can be difficult to deposit. This creates a challenge for sputtering nickel as it is a magnetic metal. In the literature, there are a few different approaches to allow for the sputter deposition of magnetic materials including: doping the target (i.e., nickel doped with vanadium, typically on the order of 7-9% [19]) to the point that it is no longer magnetic, heating the target material and depositing at a temperature above the Curie temperature, or reducing the target thickness in order to increase the magnetic field strength [5, 10, 19]. The issue with magnetron sputtering magnetic materials is that the magnetic material blocks/interferes with the magnetic field used during the sputtering process to help increase the density of electrons near the target surface. The use of thin targets for magnetic materials allows the magnetic field generated by the magnetron system to penetrate the target and work as intended, though the field may not be quite as strong as it normally would be with a non-magnetic target. Similarly, stronger magnets can be used with the magnetron system to help extend the magnetic field past the target material [10]. For the purposes of this research, a reduced thickness target was utilized for nickel sputtering.

### **2.3 Aging Studies**

Aging studies are completed to observe how a particular system will react to a given environment over time. There are a few different types of aging studies, the most accurate of which is a long term field test, where the components or coupons are placed in the actual environment and allowed to remain there for years. However, in some cases, the time and resources are not always available for such a test, and shorter accelerated tests are performed. One issue to be concerned with accelerated tests is that you must be careful that the “enhanced” environment will accelerate the various aging mechanisms as they normally would occur and not additional side reactions. For instance, during the atmospheric corrosion aging of nickel and gold plated copper contacts, the corrosion products and films created are dependent on the environment. If the test environment used

is not representative of the actual field environment, such as by obtaining extremely high concentrations of pollutants or including pollutants that are not observed in the actual environment, they can produce results that have little significance by obtaining different corrosion product chemistries and mechanisms (more detail provided in Section 2.3.1) [1, 48]. The state of the art accelerated aging test for electrical connectors is an atmospheric corrosion/mixed flowing gas (MFG) exposure, though there are many different types of aging environments. As such, this research will focus on atmospheric corrosion/mixed flowing gas (MFG), with additional elevated temperature and relative humidity (TRH) and thermal cycling (TC) studies as well.

### ***2.3.1 Atmospheric Corrosion/Mixed Flowing Gas (MFG)***

The mixed flowing gas (MFG) test environments were created to allow for realistic accelerated aging of electrical components based on the combination of temperature, humidity, and pollutant gases ( $\text{H}_2\text{S}$ ,  $\text{Cl}_2$ ,  $\text{NO}_2$ , and  $\text{SO}_2$ ) that would be found in the normal working environment of the components. Each testing condition is based on data collected over time in the actual service environments [1, 2, 30]. Several different MFG test methods have been created, with the most commonly used test being designed by Battelle Labs. In addition, a few of the other MFG test methods were directly based on the Battelle work (including test methods from Electronic Industries Association and International Electrotechnical Commission). Each MFG test consists of a range of environments (i.e., Class I, II, III, etc.) meant to represent the service environment. Even though the test methods have differing numbers of environments (Battelle MFG has four environments and Electronic Industries Associations has six environments), they each have the same basic components (i.e.,  $\text{H}_2\text{S}$ ,  $\text{Cl}_2$ ,  $\text{NO}_2$ , and occasionally  $\text{SO}_2$  pollutant gases, temperature, and relative humidity). However, exact concentrations vary slightly [30, 75]. Since the Battelle Class II MFG environment is one of the most commonly used test environment involving nickel and/or gold plated connectors [1,

2, 6, 11, 13, 18], this research used a Battelle Class II MFG environment to allow for better comparison with previous studies.

There are four Battelle test environments (Classes I, II, III, and IV) used to represent a variety of service environments. With each class, the corrosive nature of the environment increases, ranging from Class I to Class IV. Each of the classes are described in terms of industrial environments, where Class I refers to a well-controlled office environment, Class II is a light industrial environment (i.e., office environment with moderate environmental control), Class III is a moderate industrial environment (i.e., areas with little environmental control), and Class IV is a heavy industrial environment (i.e., areas with elevated pollutant levels with little to no environmental control) [30, 75]. Based on which test environment is chosen, the test concentrations of the pollutant gases, the temperature, and the relative humidity levels change. Table 2-8 shows the conditions used for each of the four Battelle environments. The choice of class environment depends on the final application.

Table 2-8. Listing of the four Battelle Class test environments. Note that no information is provided for the Class I environment as data showed no environmental concerns for reliability issues. Source: CALCE [75].

Class	Temperature, °C	Relative Humidity, %	NO <sub>2</sub> , ppb	H <sub>2</sub> S, ppb	Cl <sub>2</sub> , ppb
I	---	---	---	---	---
II	30 ± 2	70 ± 2	200 ± 25	10 +0/-4	10 +0/-2
III	30 ± 2	75 ± 2	200 ± 25	100 ± 10	20 ± 5
IV	50 ± 2	75 ± 2	200 ± 25	200 ± 10	50 ± 5

Creep, pore, and dry (i.e., oxidation) corrosion are typical failure mechanisms observed in electrical connectors. Due to the fact that the nickel underlayer acts as a barrier/inhibitor for creep corrosion and gold does not oxidize, pore corrosion (discussed in more detail in Section 2.1.1) is the primary corrosion mechanism observed for the nickel and gold plated copper system in the Battelle Class II environment. As the testing environment changes, and higher concentrations of pollutant gases are utilized, the mechanism and primary corrosion products vary to an extent, see Table 2-9 [1, 48].

Table 2-9. Corrosion mechanisms and product chemistries for nickel and gold plated copper contact materials aged in the Battelle Class test environments. Source: Abbott [1].

Class	Mechanism	Chemistry
I	--	Cu <sub>2</sub> O
II	pore	Cu <sub>2</sub> O, Cu <sub>x</sub> O <sub>y</sub> Cl <sub>z</sub>
III	pore & creep	Cu <sub>2</sub> S, Cu <sub>2</sub> O
IV	creep	Cu <sub>2</sub> S, Cu <sub>2</sub> O

### 2.3.2 Thermal Cycling (TC)

Thermal cycling aging is based on differences in the expansion coefficients and potential shock/vibrations that may be observed at the coating/substrate interface. It is typically a more significant issue for systems in which the materials have large differences in their thermal expansion coefficient, or CTE. Table 2-10 lists linear thermal expansion coefficients for several materials, including nickel, gold, and copper, for temperatures between roughly 20 °C to 300 °C [3, 77].

Table 2-10. Linear thermal expansion coefficients for various materials for temperatures between roughly 20 °C and 300 °C [3, 77].

Material	Thermal Expansion Coefficient ppm/°C
Oxygen-Free Copper	17.7
Nickel	13.3
Gold	14.2
Aluminum	23.6
Iron	11.7
Silicon	5.0

When a material cannot freely expand/contract as it is heated or cooled, thermal residual stresses are induced and can be expressed as:

$$\sigma = E\alpha_1(T_f - T_o) = E\alpha_1\Delta T \quad (\text{Eq 2.3})$$

where  $E$  is the modulus of elasticity,  $\alpha_1$  is the linear thermal expansion coefficient, and  $\Delta T$  is the change in the temperature (i.e., final temperature,  $T_f$ , minus initial,  $T_o$ ) [26]. When working with a coating/substrate system, the residual stress due to mismatched expansion coefficients can be expressed as:

$$\sigma_{CTE} = \frac{E_c}{1-\nu_c} \int_{T_1}^{T_2} (\alpha_s - \alpha_c) dT = \frac{E_c}{1-\nu_c} (\alpha_s - \alpha_c) (T_2 - T_1) \quad (\text{Eq 2.4})$$

where  $\sigma_{CTE}$  = residual stress due to mismatched CTE's, MPa  
 $E_c$  = modulus of elasticity for the coating material, GPa  
 $\nu_c$  = Poisson's ratio for the coating  
 $\alpha_c$  = thermal expansion coefficient for coating,  $\mu\text{m}/\mu\text{m}^\circ\text{C}$  or  $\mu\text{m}/\mu\text{m}^\circ\text{F}$   
 $\alpha_s$  = thermal expansion coefficient for the substrate,  $\mu\text{m}/\mu\text{m}^\circ\text{C}$  or  $\mu\text{m}/\mu\text{m}^\circ\text{F}$   
 $T_1$  = initial temperature,  $^\circ\text{F}$  or  $^\circ\text{C}$   
 $T_2$  = final temperature,  $^\circ\text{F}$  or  $^\circ\text{C}$

For example, in order to calculate the residual stress due to mismatched CTE's in association with the cooling of a sample after deposition,  $T_1$  would be the deposition temperature, and  $T_2$  would be the final temperature [26]. For metal to metal interfaces between nickel, copper, and gold, it is not expected that there will be a dramatic change based on thermal cycling alone as their thermal expansion coefficients are relatively similar in magnitude.

### 2.3.3 Elevated Temperature and Relative Humidity (TRH)

While investigating atmospheric corrosion environments, Abbott compiled a list of the various parameters important for corrosion in connector materials in order of importance including:

- 1) relative humidity
- 2) reactive chlorides
- 3) reduced sulfides (i.e.,  $\text{H}_2\text{S}$ )
- 4) air exchange rate

- 5) humidity cycling
- 6) linear velocity
- 7) oxidizers (i.e., NO<sub>2</sub>, O<sub>3</sub>)
- 8) sulfur dioxide
- 9) temperature.

While Abbott lists relative humidity amongst the most important variables for corrosion, he also notes that in and of itself, relative humidity environments are benign in regards to electrical contact systems [48]. In the absence of additional corrosive species, any of the nickel underlayer that is exposed to the environment through pore/defects in the gold coating will act as a barrier to corrosion and forms a passive oxide film [29].

## **2.4 Electrical Contact Resistance (ECR)**

One of the primary methods for assessing the functionality of an electrical connector is to examine the electrical contact resistance of the contact surfaces. The electrical contact resistance is the total resistance between two contact surfaces which can greatly affect the performance of the connector and potentially the entire device. As no surface is completely flat when observed at the microscopic level, there are a finite number of points of contact between two surfaces. Therefore, the current flow between materials is restricted to passing through the limited number of contact sites, as depicted in Figure 2-16, which results in an increase in the electrical resistance. If the electrical resistance is too high, a sufficient electrical current will not be able to flow across the contact to allow the component to work properly, if at all [38, 49, 51].



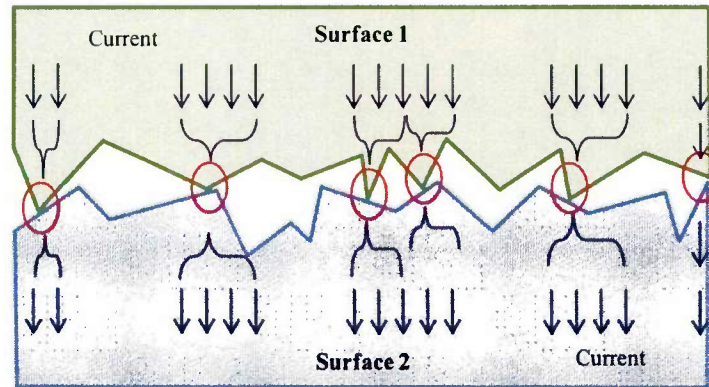


Figure 2-16. Schematic of two conductive surfaces in contact. Due to the limited number of actual points in contact between the two surfaces where the current can pass between the surfaces, the overall electrical resistance is increased.

There are a variety of conditions that can influence the observed electrical contact resistance of a system, including surface roughness, hardness, and load [37, 38]. It is expected that with increasing surface roughness, a decrease in the electrical contact resistance should be observed due to an increase in the area actually in contact between the two surfaces. In addition, rough surfaces are better able to penetrate surface oxide films than smooth surfaces, as depicted in Figure 2-17 [37, 50].

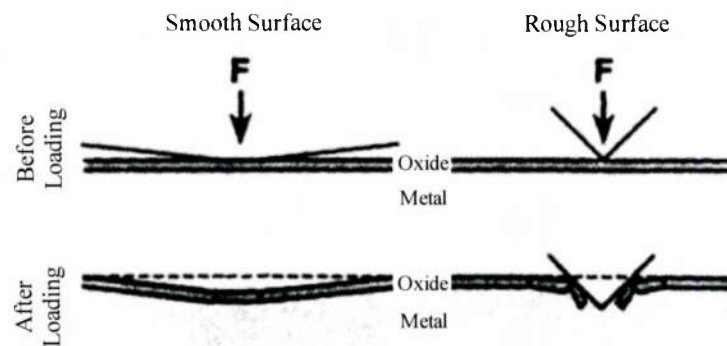


Figure 2-17. Schematic comparing smooth versus rough surfaces when in contact under a load. Source: Braunović [50].

The electrical contact resistance decreases with increasing load, as shown in Figure 2-18, due to an increased extent of contact between two surfaces as the two surfaces are brought closer together, as well as the fact that features on the surface can begin to deform [49]. As the hardness of the materials influences their ability to deform under load, it also affects the electrical contact resistance. For example, softer materials (such as pure gold) are easier to deform than harder materials, but often a trade-off must be made as increased hardness in the coating materials improves the wear resistance [38].

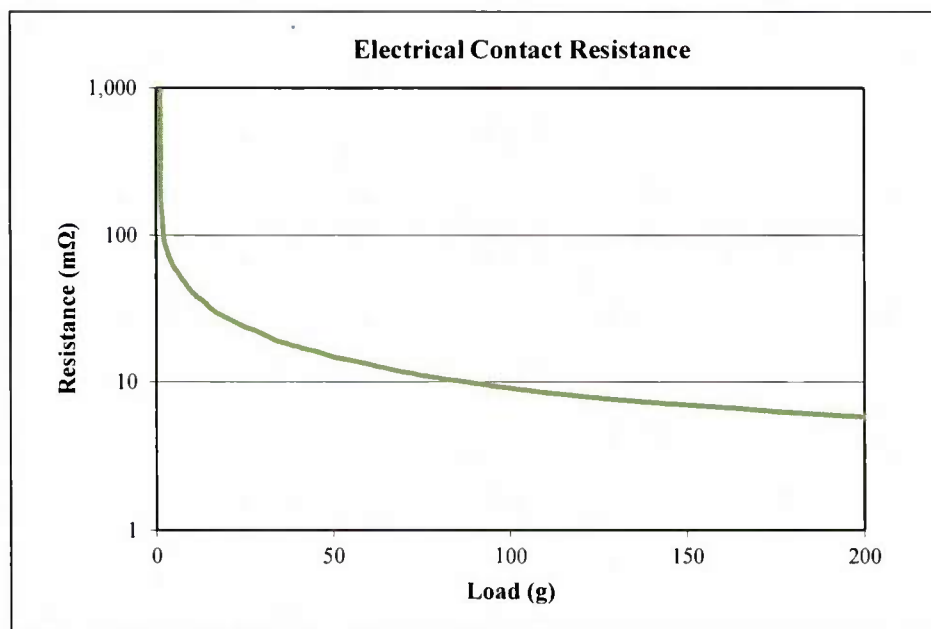


Figure 2-18. Example of change in electrical contact resistance with applied load for a nickel and gold plated copper contact using a gold plated beryllium copper probe.

Cumulative distribution function plots (CDF) are used to aid in the analysis of ECR data. A general CDF plot shows percentage (or fraction) versus some specified parameter. The parameter used is typically the parameter of interest, i.e., for this research the parameter is electrical contact resistance, while the percentage (or fraction) refers to the percentage (or fraction) of the data that are less than or equal to a specific value for the parameter used on the x-axis. For example, if we had a

CDF plot that looked like the one shown in Figure 2-19, we observe that approximately 85% of the data is for a resistance of 17 mΩ or less for the Battelle Class II aged sample, while 100% of the data for the unaged sample falls within the 10-11 mΩ range.

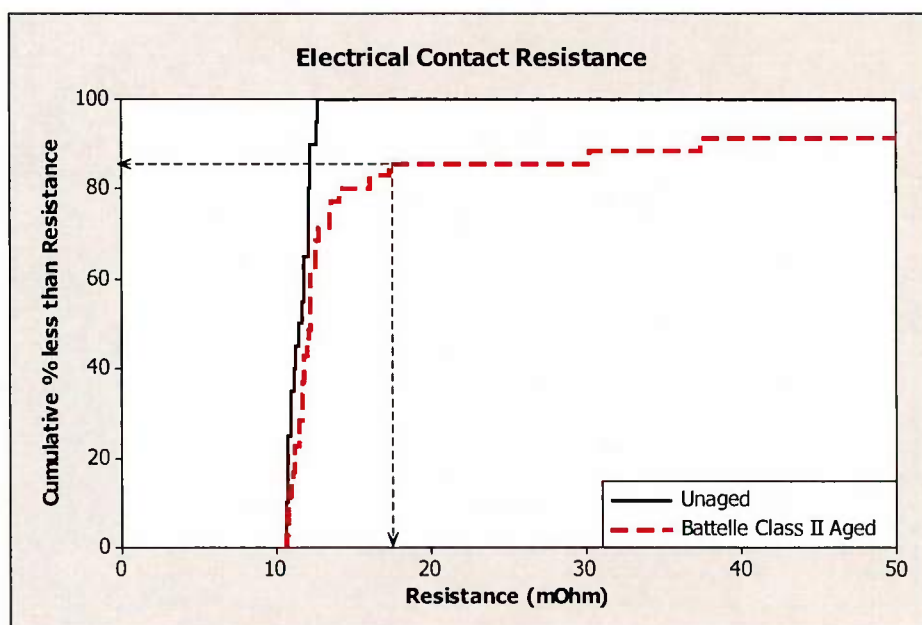


Figure 2-19. Example cumulative distribution function plot (CDF) showing that about 85% of the example resistance data has a resistance of 17 mΩ or less for the aged samples while 100% of the resistance data for the unaged samples falls within 10-11 mΩ.

The CDF plots can be particularly useful for analyzing ECR data for systems undergoing pore corrosion, such as nickel and gold plated copper exposed to a Battelle Class II environment [6, 13], as the data can be displayed without being skewed due to a few data points with dramatically increased resistances corresponding to the localized areas of corrosion that do not uniformly cover the surface (see Figure 2-20).

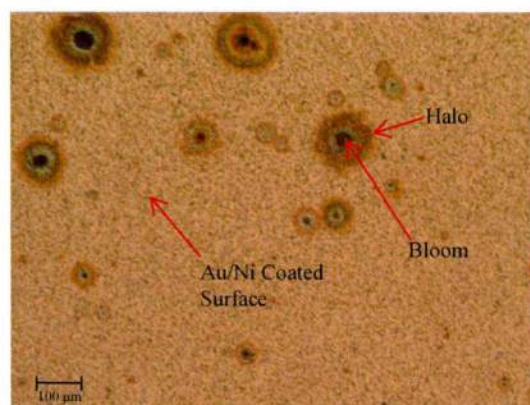


Figure 2-20. Example of a Battelle Class II aged Au/Ni plated copper sample showing the typical corrosion bloom and product halo created during the pore corrosion of the surface.

Electrical contact resistances for unexposed/clean contacts are typically on the order of 1 m $\Omega$  or less depending on the applied load, materials system, and probe used during data collection [37, 38, 49, 52]. A few authors, however, acquired data at roughly 10 m $\Omega$  which is an order of magnitude larger [13, 52]. The difference in magnitude of observed resistances is based on variations in the actual measurement set up and technique, specifically between dynamic and static data collection. See Figure 2-21 and Figure 2-22, as well as Table 2-11, for examples and a summary of electrical contact resistance values observed in the literature.

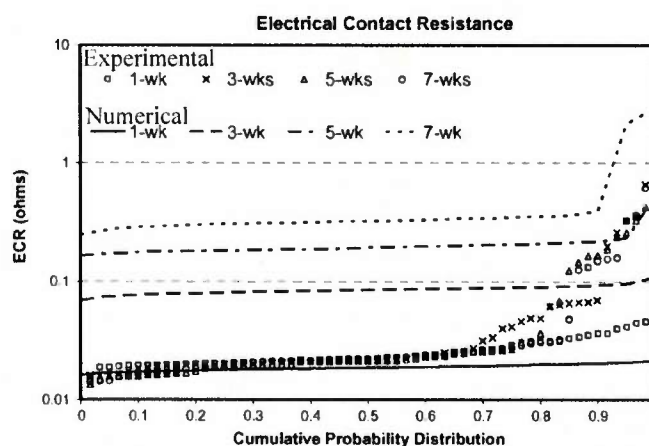


Figure 2-21. Experimental (data points) and numerical (solid/dashed lines) ECR values for gold coated copper using a gold plated beryllium copper probe. Source: Moffat et al. [52].

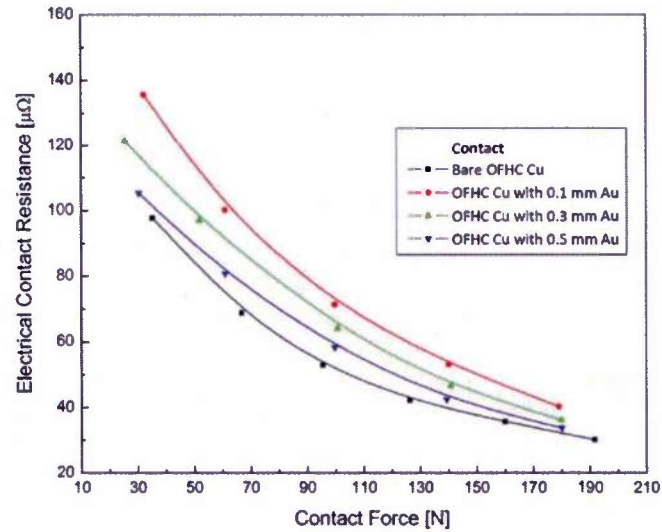


Figure 2-22. Experimental electrical contact resistance for nickel and gold plated copper as a function of gold plating thickness. Source: Misra & Nagaraju [38].

Table 2-11. Summary of various ECR values found in the literature for unaged samples [38, 52, 71-74].

Substrate Material	Coating System	Load	ECR (mΩ)	Probe diameter (mm)	Probe material	Reference
Cu	Au plated	200 g	~ 10	3	Au plated BeCu	52
Cu	Copper	50 g	0.8 - 1.5	---	---	70
		200 g	0.8 - 1	---	---	
Ag	Au plated	10 g	2 - 4	---	---	74
CA 725	Au flash, Pd plated	50 g	~ 3 - 7	---	---	71
	Au plated	100 g	1.3 - 2	1.6	Gold	
Alloy 511 Phosphor Bronze	Ni + Au plated	25 g	2.9 - 4.5	1	---	72
		50 g	2 - 3		---	
		75 g	1.4 - 2.2		---	
Alloy 511 Phosphor Bronze	Ni + Au plated	25 g	5.3 - 6.5	6.36	---	72
		50 g	1.5 - 2		---	
		75 g	1 - 1.1		---	
Cu	Au plated	40 - 190 g	~ 0.04 - 0.14	---	---	38

There are several different models that have been used to describe and model the contact resistance. Most are based on the works of Holm and Greenwood with modifications made to

improve the model based on variations in surface features/sizes or aging products/films on the surface [13, 38, 49, 51-57]. For instance, in the work completed by Sun et al. and Moffat et al. on Battelle Class II aged nickel and gold plated copper contact materials, the authors used a slightly modified version of Malucci's model based on Greenwood's work [13, 52]. Malucci defined the electrical contact resistance as the sum of two contributing resistance factors, i.e., the resistance due to the points of true contact created between asperities on the surface (Equation 2.6) and the apparent resistance (Equation 2.7) [13, 52, 54-56].

$$ECR = R_{spots} + R_{int} \quad (\text{Eq 2.5})$$

with

$$R_{spots} = \frac{1}{\sum_{i=1}^N \frac{1}{R_i}} = \frac{\rho}{\sum_{i=1}^N \frac{d_i^2 \sqrt{X_i X'_i}}{(d_i - C) \sqrt{X_i X'_i} + C}} \quad (\text{Eq 2.6})$$

$$R_{int} = \frac{\rho}{D} \quad (\text{Eq 2.7})$$

$$D = 2.2 \left( \frac{FR_{probe}}{E} \right)^{1/3} \quad (\text{Eq 2.8})$$

where ECR = electrical contact resistance  
 $R_{spots}$  = ECR contribution due to resistance at spots of true contact  
 $R_{int}$  = ECR contribution due to the apparent contact area  
 $\rho$  = resistivity  
 $D$  = diameter of cluster of surface feature in actual contact  
 $d_i$  = diameter of  $i^{th}$  true contact  
 $N$  = total number of true contact points  
 $X_i, X'_i$  = fraction of exposed metal before and after  $i^{th}$  contact  
 $F$  = applied force  
 $R_{probe}$  = probe radius  
 $E$  = elastic modulus  
 $C$  = 4/3

Sun et al. and Moffat et al. extended this model by adding to the  $R_{spots}$  term in order to account for the differences in the resistances of large corrosion blooms, small corrosion blooms, and other asperities on the surface. They defined the resistance of the large blooms as:



$$R_{BB} = \frac{\rho_{bloom}}{\sqrt{\pi A_{bloom}}} \quad (\text{Eq 2.9})$$

and added to the  $R_{spots}$  term providing the expression

$$R_{spots} = \frac{1}{\sum N_i \frac{1}{R_{spots}} + \sum N_{BB} \frac{1}{R_{BB}}} \quad (\text{Eq 2.10})$$

where  $R_{BB}$  = resistance of the large bloom  
 $\rho_{bloom}$  = resistivity of bloom material  
 $A_{bloom}$  = area of bloom

This particular method was able to model the electrical contact resistance data for unaged samples. However it over predicted the resistances for aged samples, see Figure 2-21 [13].

## 2.5 Residual Stress

Residual stress by definition is stress within a material that remains after the original stress has been removed. Residual stress is sometimes referred to as internal stress and can be divided into two main types, extrinsic and intrinsic stresses. Extrinsic stresses are typically caused by high temperature processing with mismatched thermal expansion coefficients for the substrate and coating materials (such as those described in Section 2.3.2) or, in the case of epitactic stresses, due to structural mismatches between the substrate and film. These stresses are typically less than 1GPa. Intrinsic residual stresses, on the other hand, are caused by a variety of factors, including changes in volume and displacement of atoms, and can be very difficult to measure, though they can be much higher in magnitude (1-10 GPa) as compared to the extrinsic stresses [26].

There are several sources of residual stresses in materials. Residual stresses can be introduced to a system at one of many steps during processing, whether it is due to grinding or rolling of the substrate material or the various coating processing conditions which influence the coating

microstructure and composition (i.e., coating density, texturing, grain size, surface morphology/roughness, and incorporated impurities). If residual stresses become too large (whether compressive or tensile) they can cause immediate damage to the coating, and thus influence the functionality of the coating. In order to relieve large compressive stresses, coatings will buckle. Likewise, cracks can form to relieve tensile stresses [26].

A variety of residual stresses has been observed for nickel and gold plated copper, as well as nickel sputtered copper. For electroplated nickel coatings, Di Bari lists possible tensile residual stresses ranging from 0-185 MPa in magnitude depending on the plating solution/condition. For example, additive free Watts nickel platings range from roughly 125-185 MPa, and 0-55 MPa for sulfamate nickel coatings. Nickel coatings can also have a compressive stress instead of a tensile one, which is typically observed when sulfur is co-deposited with nickel [32]. Various additives can be incorporated in the plating bath to influence various aspects of the process, including stress relievers.

As with the electroplated nickel, the residual stresses observed in electroplated gold can vary depending on the plating conditions. Kohl examines a gold electroplating solution containing thallium and how depending on the temperature and the current density used during deposition, the residual stress ranges from a compressive stress of approximately 25 MPa up to a 150 MPa tensile stress [33]. In addition, Lille et al. reports an initial residual stress ranging from approximately 180 MPa to 400 MPa depending on the current density and coating thickness for brush-plated gold coatings [8, 9].

### ***2.5.1 Residual Stress Measurement Techniques***

There are many different techniques that can be used to determine the residual stresses present in a material. The particular technique selected will depend on several factors including information needed (i.e., stresses in the surface versus subsurface) and technique requirements versus system specifications (i.e., there may limitations for certain techniques based on observable materials

or substrate to coating thickness ratios). A brief summary of a few select residual stress measurement techniques, along with a few of their respective advantages and disadvantages, are listed in Table 2-12. For the purpose of this research, x-ray diffraction was used to determine the residual stress present in the coatings based on its ability to determine residual stresses in thin coatings non-destructively.

Table 2-12. Summary of various techniques used to determine residual stress with their advantages and disadvantages [14-17, 20].

Technique	Advantages	Disadvantages
X-Ray Diffraction (XRD)	<ul style="list-style-type: none"> <li>• Non-destructive</li> <li>• Commonly available</li> <li>• Large range of materials observable</li> <li>• Surface stresses (can be combined with other techniques to obtain subsurface stresses)</li> </ul>	<ul style="list-style-type: none"> <li>• Predominantly lab-based systems</li> <li>• Small coupons required</li> <li>• Expensive</li> </ul>
Synchrotron X-Ray Diffraction	<ul style="list-style-type: none"> <li>• Non-destructive</li> <li>• Deeper penetration depths as compared to XRD</li> </ul>	<ul style="list-style-type: none"> <li>• Very expensive – specialty labs only</li> <li>• Unable to analyze thin films</li> <li>• Poor resolution</li> </ul>
Neutron Diffraction	<ul style="list-style-type: none"> <li>• Non-destructive</li> <li>• Deeper penetration depths as compared to XRD</li> </ul>	<ul style="list-style-type: none"> <li>• Very expensive – specialty labs only</li> <li>• Unable to analyze thin films</li> </ul>
Hole Drilling	<ul style="list-style-type: none"> <li>• Inexpensive</li> <li>• Can be used to obtain residual stress vs. depth for large depths (upto ~ 1 m below the surface)</li> </ul>	<ul style="list-style-type: none"> <li>• Semi-destructive</li> <li>• Complex data analysis</li> <li>• Limited resolution and sensitivity</li> <li>• Not practical for thin/brittle coatings</li> </ul>
Curvature Method	<ul style="list-style-type: none"> <li>• Can be used to observe residual stresses during coating or after coating</li> </ul>	<ul style="list-style-type: none"> <li>• Requires thin substrates/coatings</li> </ul>
Raman	<ul style="list-style-type: none"> <li>• Non-destructive</li> </ul>	<ul style="list-style-type: none"> <li>• Limited materials observable</li> </ul>

### 2.5.2 Residual Stress Calculations with X-ray Diffraction (XRD)

The basic XRD process involves an incident x-ray beam that irradiates a sample with x-rays and diffract off of an atomic plane within the crystal structure of the material, as depicted in Figure 2-23. This phenomenon is characterized by Bragg's Law of diffraction:

$$n\lambda = 2d\sin\theta$$

41  
(Eq 2.11)

where  $d$  is the lattice spacing between atomic planes,  $\theta$  is the angle of diffraction,  $\lambda$  is the wavelength of the x-rays used, and  $n$  is the order of diffraction. As such, the angle of diffraction will be different when different radiation sources (i.e., copper or chromium, which have different  $\lambda$  values) are used.

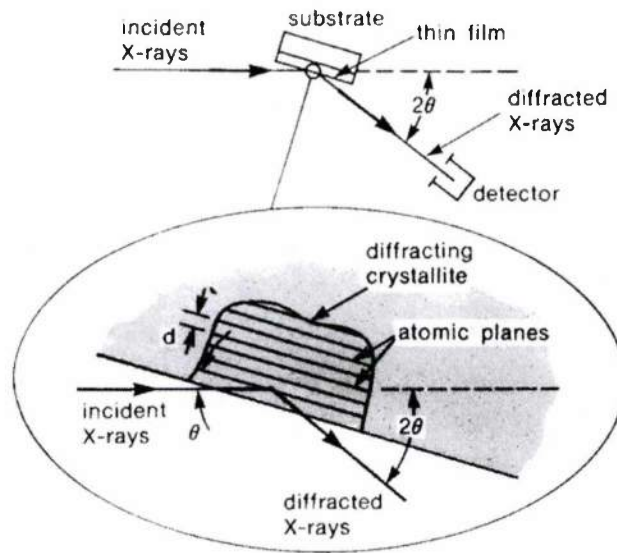


Figure 2-23. Basic x-ray diffraction setup. Source: Brundel et al. [64].

The atomic planes observed in a crystalline material can be described via Miller indices ( $h$   $k$   $l$ ), where  $h$ ,  $k$ , and  $l$  are the inverse of the axis intercepts in a unit cell. As such, if the Miller indices for a plane were (110), the plane would intercept the  $a$ -axis at  $1/1=1$ , the  $b$ -axis at  $1/1=1$ , and the  $c$ -axis at  $1/0=\infty$  (i.e., the plane intersects with the axis at all points), see Figure 2-24 [63].

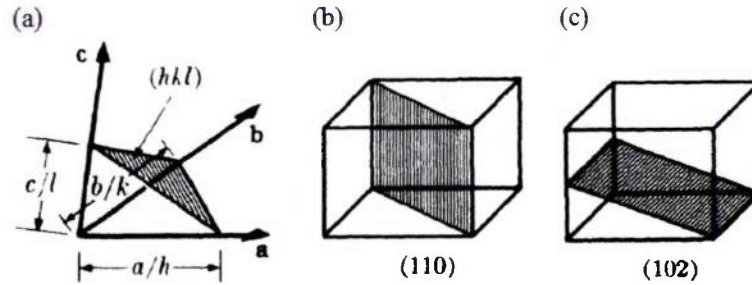


Figure 2-24. Miller indices are used to describe specific planes. A few examples are shown in (a)  $(hkl) = (hkl)$ , (b)  $(hkl) = (110)$ , and (c)  $(hkl) = (102)$ . Source: Cullity [63].

In order to calculate the residual stresses present in a particular diffraction plane, the lattice spacing is determined for various surface orientations, as defined by the angle  $\psi$ . By taking measurements at different  $\psi$  angles, a shift in the lattice spacing can be measured (see Figure 2-25), which is used to calculate the residual stress.

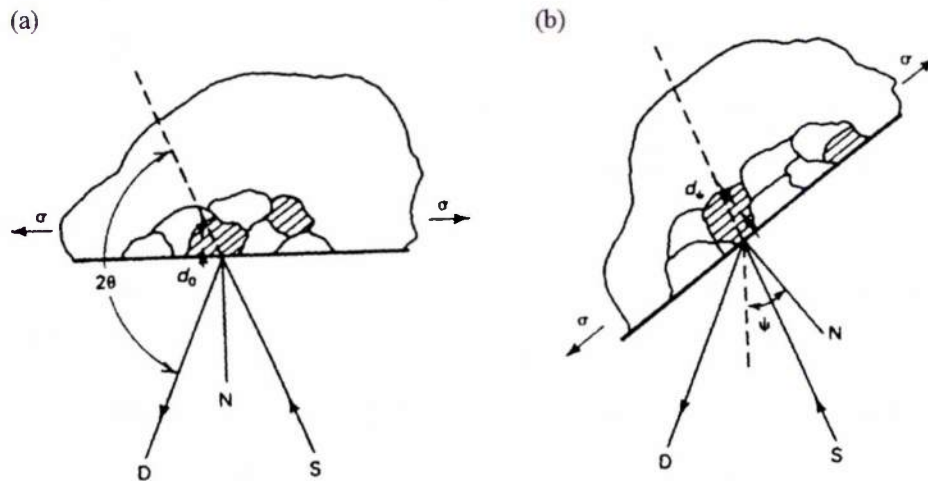


Figure 2-25. XRD stress measurement based on shifts in the lattice spacing  $d$  with changing surface orientation  $\psi$ . D is the x-ray detector, S is the x-ray source, N is normal to the surface, and  $\psi$  describes the surface orientation, where (a)  $\psi = 0$  and (b)  $\psi = \psi$ . Source: Prevey [14, 15].

As listed in Table 2-12, XRD is limited in determining residual stresses present in the sample surface and subsurface depending on the irradiated volume of the XRD beam and experimental

equipment parameters. Additional techniques can be applied, in conjunction with XRD, to allow for subsurface residual stress determination, such as removing surface layers via electropolishing.

Within XRD measurements, there are several analysis techniques available for calculating residual stress. Two of the commonly used techniques include the double angle and  $\sin^2 \psi$  techniques which utilize the plane-stress elastic model. The plane-stress elastic model is used to calculate surface residual stress. Figure 2-26 is a schematic depicting the variables and components involved in the surface stress calculations. The plane-stress elastic model assumes that the stress in the plane is expressed as a function of the principal stresses,  $\sigma_1$  and  $\sigma_2$  (the model assumes there is no perpendicular principal stress,  $\sigma_3 = 0$ , as that would cause the stress to be out of the surface plane). In addition, it is assumed that there is no significant texturing in the sample (i.e., random orientation within the coating) and that the sample is infinitely wide in comparison to the irradiated area in order to eliminate edge effects. If these assumptions do not hold, the residual stress calculated via this method will have increased error and may not be accurate [14, 15].

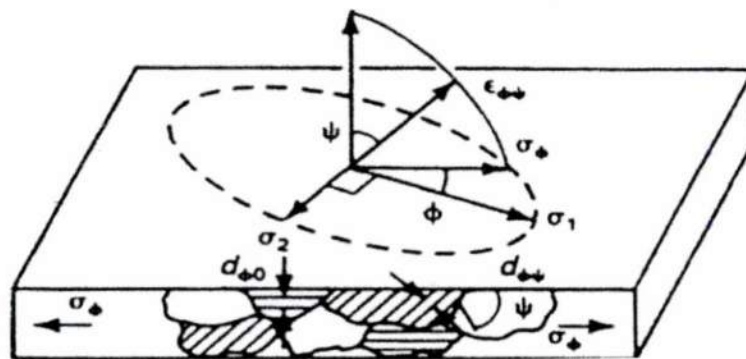


Figure 2-26. Plane-stress elastic model depicting various variables used in the stress calculations, where  $\phi$  and  $\psi$  are angles defining the orientation of the sample,  $\sigma_1$  and  $\sigma_2$  are principal stresses, and  $\epsilon_{\phi\psi}$ ,  $d_{\phi\psi}$ , and  $\sigma_{\phi\psi}$  are the strain, lattice spacing, and stress, respectively for a given  $\phi$  and  $\psi$  orientation (i.e.,  $\sigma_{\phi}$  is the stress in the plane where  $\psi = 0$ ). Source: Prevey [14, 15].

Stress itself cannot be directly measured, but is calculated from the measured strain, i.e., the change in the lattice spacing,  $d$ . As such, to determine the stress in a shallow volume near the surface



(i.e., the irradiated volume) one must first start with the general strain equation for the plane-stress model:

$$\epsilon_{\phi\psi} = \left[ \frac{1+\nu}{E} (\sigma_1 \cos^2 \phi \sin^2 \psi + \sigma_2 \sin^2 \phi \sin^2 \psi) \right] - \frac{\nu}{E} (\sigma_1 + \sigma_2) \quad (\text{Eq 2.12})$$

where  $\phi$  and  $\psi$  are the angles describing the orientation of the sample,  $\sigma_1$  and  $\sigma_2$  are the principal stresses,  $\nu$  is Poisson's ratio, and  $E$  is the modulus of elasticity [14,15]. Equation 2.12 can be simplified to Equation 2.13 as shown below:

$$\epsilon_{\phi\psi} = \left[ \frac{1+\nu}{E} (\sigma_1 \cos^2 \phi + \sigma_2 \sin^2 \phi) \sin^2 \psi \right] - \frac{\nu}{E} (\sigma_1 + \sigma_2) \quad (\text{Eq 2.13})$$

The stress in the plane of interest when  $\psi = 0$ , is given by:

$$\sigma_{\phi} = \sigma_1 \cos^2 \phi + \sigma_2 \sin^2 \phi \quad (\text{Eq 2.14})$$

which can be substituted into Equation 2.13 to form an expression for the strain as a function of  $\sigma_{\phi}$  as shown by Equation 2.15 [14,15]:

$$\epsilon_{\phi\psi} = \left[ \frac{1+\nu}{E} \sigma_{\phi} \sin^2 \psi \right] - \frac{\nu}{E} (\sigma_1 + \sigma_2) \quad (\text{Eq 2.15})$$

An equation relating the lattice spacing to the stress can be formed by substituting the definition for strain (Equation 2.16) into Equation 2.15, see Equation 2.17.

$$\epsilon_{\phi\psi} = \frac{\Delta d}{d_0} = \frac{d_{\phi\psi} - d_0}{d_0} \quad (\text{Eq 2.16})$$

where  $d_0$  = the stress free lattice spacing  
 $d_{\phi\psi}$  = the lattice spacing in the direction defined by  $\phi$  and  $\psi$

$$\frac{d_{\phi\psi} - d_0}{d_0} = \sigma_{\phi} \sin^2 \psi \left( \frac{1+\nu}{E} \right)_{hkl} - (\sigma_1 + \sigma_2) \left( \frac{\nu}{E} \right)_{hkl} \quad (\text{Eq 2.17})$$

Solving Equation 2.17 for  $d_{\phi\psi}$  results in a linear  $y = mx + b$  type expression between  $d_{\phi\psi}$  and  $\sin^2 \psi$  (Equation 2.18), which can be plotted having a slope as listed in Equation 2.19 below:

$$d_{\phi\psi} = \left[ d_0 \sigma_{\phi} \left( \frac{1+\nu}{E} \right)_{hkl} \right] \sin^2 \psi + \left[ d_0 - d_0 (\sigma_1 + \sigma_2) \left( \frac{\nu}{E} \right)_{hkl} \right] \quad (\text{Eq 2.18})$$

$$\frac{\partial d_{\phi\psi}}{\partial \sin^2 \psi} = d_0 \sigma_{\phi} \left( \frac{1+\nu}{E} \right)_{hkl} \quad (\text{Eq 2.19})$$

Equation 2.19 can be solved for the stress in the plane of interest, as shown in Equation 2.20.

$$\sigma_{\phi} = \frac{1}{d_0} \left( \frac{\partial d_{\phi\psi}}{\partial \sin^2 \psi} \right) \left( \frac{E}{1+\nu} \right)_{hkl} \quad (\text{Eq 2.20})$$

If the stress free lattice spacing,  $d_0$ , is unknown, it can be approximated by  $d_{\phi 0}$ , i.e.,  $d_{\phi\psi}$  when  $\psi = 0$  via Equation 2.18. Due to the fact that the modulus of elasticity is much larger than the sum of the two principal stresses, i.e.,  $E \gg \sigma_1 + \sigma_2$ ,  $d$  typically only differs from  $d$  by 1% or less as demonstrated by Equations 2.21 and 2.22 [14, 15].

$$d_{\phi 0} = \left[ d_0 \sigma_{\phi} \left( \frac{1+\nu}{E} \right)_{hkl} \right] \sin^2 0 + \left[ d_0 - d_0 (\sigma_1 + \sigma_2) \left( \frac{\nu}{E} \right)_{hkl} \right] \quad (\text{Eq 2.21})$$

$$d_{\phi 0} = d_0 - d_0 (\sigma_1 + \sigma_2) \left( \frac{\nu}{E} \right)_{hkl} = d_0 \left( 1 - \frac{(\sigma_1 + \sigma_2) \nu_{hkl}}{E_{hkl}} \right) \cong d_0 \quad (\text{Eq 2.22})$$

As such, the residual stress can be calculated using the  $d_{\phi 0}$  approximation as shown in Equation 2.23.

$$\sigma_{\phi} = \frac{1}{d_{\phi 0}} \left( \frac{\partial d_{\phi \psi}}{\partial \sin^2 \psi} \right) \left( \frac{E}{1+\nu} \right)_{hkl} \quad (\text{Eq 2.23})$$

The two angle and  $\sin^2 \psi$  techniques are both based on the plane-stress model with the stress calculated via Equation 2.20 or 2.23. In fact, the two techniques are identical with the exception that the two angle technique only requires XRD measurements to be taken for two  $\psi$  angles, thus obtaining the lattice spacing for the two angles, while the  $\sin^2 \psi$  technique involves determining  $d_{\phi \psi}$  for two or more angles. One reason to use the  $\sin^2 \psi$  technique rather than the faster two angle technique is that by determining the lattice spacing for more than two  $\psi$  angles, one is able to show that the relationship between  $d$  and  $\sin^2 \psi$  is indeed linear as required for the use of the equations previously described, see Figure 2-27.

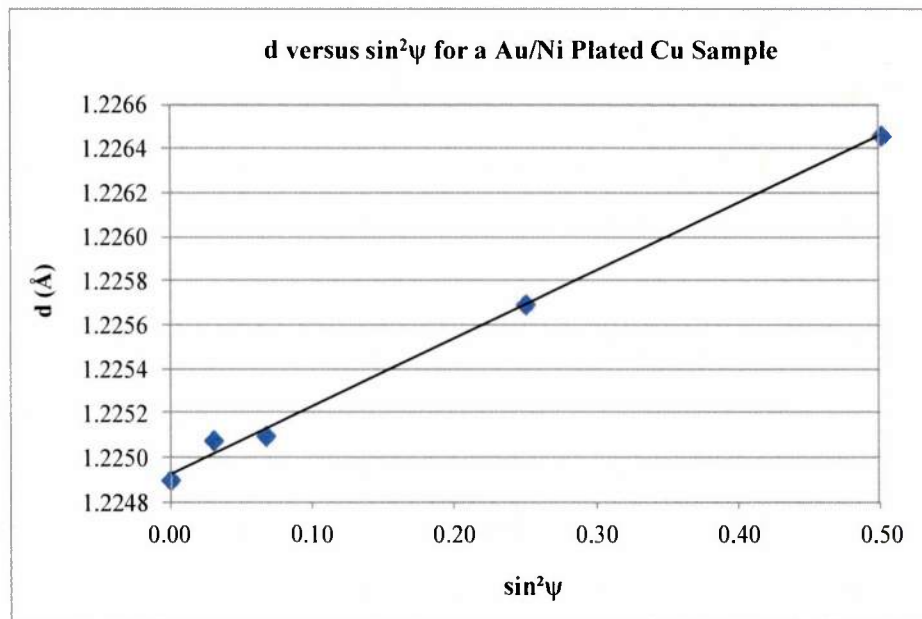


Figure 2-27. Example XRD results showing the required linear correlation between  $d$  and  $\sin^2 \psi$  as required for the two angle and  $\sin^2 \psi$  residual stress analysis techniques.

Typically when using XRD for residual stress calculations, measurements should be performed using the higher diffraction angles (above roughly  $120^\circ$ ). The primary reason for doing this is that higher diffraction angles provide better precision in the determination of the change in lattice spacing as compared to lower diffraction angles. Figure 2-28 demonstrates this by showing that for the same angular step size the potential variability in  $d$  is much smaller for the higher angles.

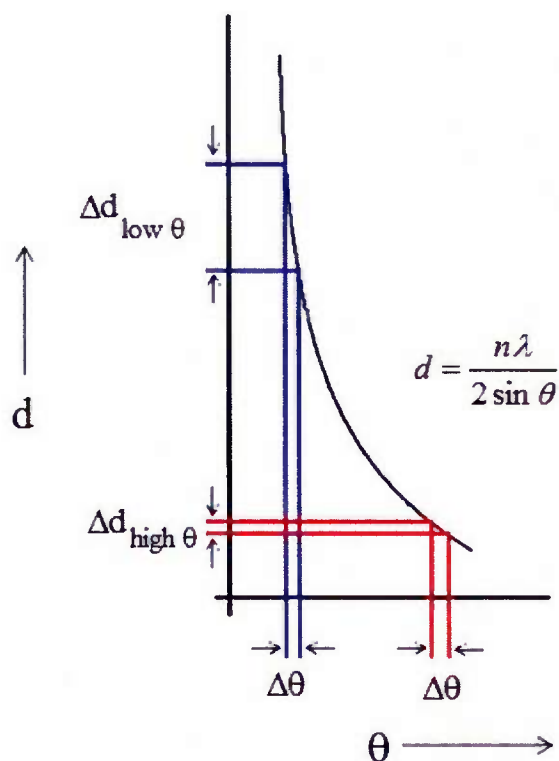


Figure 2-28. General plot of lattice spacing versus the diffraction angle, based on Bragg's Law (Equation 2.11), depicting the potential variability in  $d$  for the same step size in  $\theta$ .

One of the most common sources of radiation used for XRD is copper radiation. However, as was previously discussed, the use of different radiation sources cause changes in the observed diffraction angle for a given system (as described in Equation 2.11). As such, the use of different radiation sources can improve the residual stress calculations by shifting the diffraction peaks to higher angles, allowing for increased precision, as well as increasing the separation between

diffraction peaks. The increased peak separation can be specifically beneficial when there are peaks for multiple materials near each other. For example, this research looks at the residual stress in the coating of nickel and nickel/gold coated copper coupons. However, nickel and copper have several diffraction peaks that are very close to one another. Table 2-13 lists a few of the diffraction peaks for nickel and copper for both copper and chromium radiation (the wavelength for copper and chromium radiation is  $\lambda_{Cu} = 1.5406 \text{ \AA}$  and  $\lambda_{Cr} = 2.2898 \text{ \AA}$  respectively [62]). Thus, we can see that the separation between the nickel and copper peaks is larger for the chromium radiation, and even more so when looking at higher angle diffraction peaks.

Table 2-13. Example of peak location shifts for a few nickel and copper diffraction peaks based on the use of different radiation sources. Change in separation between the nickel and copper peaks is also provided [62].

	Diffraction Plane	Peak Location, $^{\circ}2\theta$		$\Delta^{\circ}2\theta$
		Ni	Cu	
Cu Radiation	(111)	44.508	43.298	1.21
	(200)	51.847	50.434	1.413
	(220)	76.372	74.133	2.239
Cr Radiation	(111)	68.509	66.503	2.006
	(200)	81.047	78.578	2.469
	(220)	133.515	127.232	6.283

## Chapter 3

### Experimental Procedure

#### 3.1 Substrate Materials

The sample substrates were made from two sheets of oxygen free copper (C101) from M. Vincent & Associates Ltd. Specialty Metals<sup>1</sup>. The panel thickness was 1.6 mm with a chemical composition detailed in Table 3-1.

Table 3-1. Chemical composition range provided by M. Vincent & Associates for their C101 oxygen free copper [23].

Element	Minimum %	Maximum %
Copper	99.99	---
Antimony	---	0.0004
Arsenic	---	0.0005
Oxygen	---	0.0005
Phosphorus	---	0.0003
Tellurium	---	0.0002

Sample substrates were prepared into 2.5 cm x 2.5 cm coupons in a 12 sample panel layout (see Figure 3-1) from the sheets of copper via water jet cutting. Each panel consisted of twelve 2.5 cm x 2.5 cm coupons, and was assigned an ID number, N01 through N48. Preparing the samples in this manner allowed for better uniformity between samples during subsequent sample preparation processes. The use of the sample panel format was specifically important for electroplating deposition, as it allowed a larger group of samples to be prepared simultaneously versus individually, which helped reduce coating variations due to differences in the electroplating bath.

---

<sup>1</sup> M. Vincent & Associates Ltd. Specialty Metals, 9341 Penn Ave S, Minneapolis, MN 55431



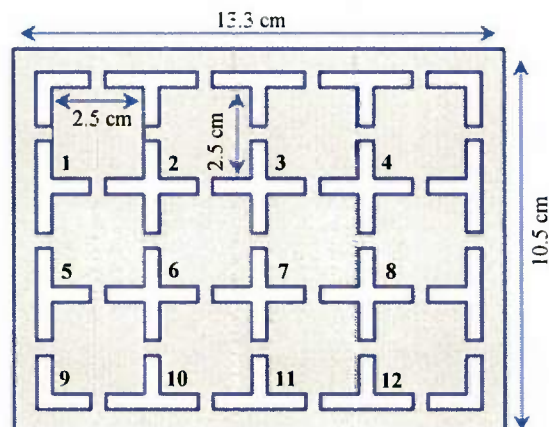


Figure 3-1. Schematic of the panel layout prepared, N01, including the numbering for the individual coupons.

### 3.2 Surface Roughness Preparation

In order to study the surface roughness effects, samples were prepared to one of four surface roughnesses prior to coating by LAPCO LLC<sup>2</sup> and Micro Lapping & Grinding Co.<sup>3</sup> via grinding and lapping processes. Initial targeted average surface roughnesses,  $R_a$ , were 0.05  $\mu\text{m}$ , 0.4  $\mu\text{m}$ , 0.8  $\mu\text{m}$ , and 2.5  $\mu\text{m}$  (referred to as Group 1 through 4 respectively from this point forward). These values were provided to the vendors as guidelines in order to make sure the final substrate surface roughnesses would provide a range of roughnesses from a near mirror finish (Group 1), to a value that would be considered very rough for the application (Group 4). The two intermediate roughnesses were chosen to be near the actual surface roughnesses found in some electrical contacts. LAPCO prepared the two smoother surfaces (Groups 1 and 2) and Micro Lapping & Grinding the two rougher surfaces (Groups 3 and 4).

Once the panels were returned from the vendors, optical profilometry was performed to provide a check regarding the actual surface roughnesses obtained before they were shipped back out

<sup>2</sup> LAPCO LLC, 1 Kenwood Circle, Franklin, MA 02038

<sup>3</sup> Micro Lapping & Grinding Co., 2330 N. 17th Ave., Franklin Park, IL 60131

for coating at Red Sky Plating<sup>4</sup>. Unfortunately, the Group 2 panels, which should have had a surface roughness near 0.4  $\mu\text{m}$ , came back with an average roughness of approximately 0.76  $\mu\text{m}$ , which was too close to the roughness of the Group 3 samples. As such, the Group 2 samples were sent to Micro Lapping & Grinding for further surface processing in order to obtain a surface roughness closer to the targeted value. More extensive optical profilometry was completed after the substrates were nickel and gold coated with the resulting average  $R_a$  surface roughnesses for each group listed in Table 3-2, along with the processing conditions used by Micro Lapping & Grinding. No specific information was provided for the work LAPCO completed as their processes are proprietary.

Table 3-2. Substrate surface roughness processing conditions and average resulting  $R_a$  surface roughnesses. Samples from Group 1 prepared by LAPCO using proprietary conditions. Samples from Group 2, 3, and 4 were prepared by Micro Lapping & Grinding using various grits of silicon carbide and listed pressures.

Group #	Uncoated $R_a$ , $\mu\text{m}$	Coated $R_a$ , $\mu\text{m}$	Processing Conditions		
			Grit	Pressure	Vendor
Group 1	$0.05 \pm 0.01$	$0.06 \pm 0.01$	---	---	LAPCO
Group 2	$0.62 \pm 0.02$	$0.55 \pm 0.04$	400 grit SiC	10 lb	MicoLapping & Grinding
Group 3	$0.94 \pm 0.06$	$0.83 \pm 0.06$	240 grit SiC	10 lb	MicoLapping & Grinding
Group 4	$2.53 \pm 0.09$	$2.38 \pm 0.11$	180 grit SiC	10 lb	MicoLapping & Grinding

### 3.3 Coatings

After the substrate sample surface roughness preparations were completed, the samples were coated. The coupon panels were separated into four groups: one set to be set aside as spares (i.e., no coating applied), one set to be nickel plated, one set to be nickel and gold plated, and the last set to be nickel sputtered. Each set included three full panels (i.e., thirty-six 2.5 cm x 2.5 cm coupons) from each of the four surface roughness groups, as detailed in Table 3-3, resulting in a total of 432 coupons prepared and aged.

<sup>4</sup> Red Sky Plating, 630 Oak St SE, Albuquerque, NM 87106

Table 3-3. Sample matrix overview detailing the prepared surface roughness group and coating system for each specific panel of coupons. Note that each panel consists of twelve coupons, resulting in a total of 432 coupons prepared and aged.

Coating	Surface Roughness			
	Group 1 (0.06 $\mu\text{m}$ )	Group 2 (0.55 $\mu\text{m}$ )	Group 3 (0.83 $\mu\text{m}$ )	Group 4 (2.38 $\mu\text{m}$ )
Ni+Au Plated	N14	N02	N26	N38
	N18	N06	N30	N42
	N22	N10	N34	N46
Ni Plated	N13	N01	N25	N37
	N17	N05	N29	N41
	N21	N09	N33	N45
Ni Sputtered	N19	N07	N31	N43
	N16	N04	N28	N40
	N23	N11	N35	N47
None	N15	N03	N27	N39
	N20	N08	N32	N44
	N24	N12	N36	N48

### 3.3.1 Electroplating

The nickel and gold electroplated coatings were applied by Red Sky Plating. Upon receipt, Red Sky Plating cleaned and activated the sample surface of the coupons via electrocleaning and an acid dip prior to coating. The panels were electrocleaned for 0.5-1 minute at 4-5 V and 140-150 °F in Sparkleen 366 electrocleaning solution, followed by the acid dip in Pickleen AS-10 solution for 1-2 minutes. Both cleaning/activating solutions were obtained from A-Bright Company<sup>5</sup>.

The total thickness of the electroplated coatings was targeted to be approximately 3.8  $\mu\text{m}$ . Thus, for the panels that were only nickel plated, the nickel layer was approximately 3.8  $\mu\text{m}$ . For the panels that were nickel and gold plated, approximately 2.5  $\mu\text{m}$  of nickel was applied, followed by about 1.3  $\mu\text{m}$  of gold, for a total coating thickness of 3.8  $\mu\text{m}$ . The specific details of the actual plating processes are considered propriety. However, the nickel coating met ASTM B689 standards and the

<sup>5</sup> A-Brite Company, 3217 Wood Dr, Garland, TX 75041

gold coating met ASTM B488 Type I Code C. After plating, the samples were rinsed and air dried. Before starting the aging studies, optical profilometry was completed for the coated panels.

Prior to aging, the samples were cleaned one last time to remove any residues remaining on the surface from the plating process. The cleaning procedure involved seven steps: 1) surface was gently wiped with cotton ball supersaturated with isopropanol, 2) rinsed with isopropanol, 3) nitrogen blow dried, 4) dipped in 10% HCl for 20 s, 5) rinsed with DI water, 6) final rinse in isopropanol, and 7) nitrogen blow dried.

### ***3.3.2 Sputtering***

The nickel sputter coatings were applied at Penn State using a magnetron sputtering system. Prior to mounting the coupon panels in the deposition chamber, they were cleaned through a series of five steps: 1) surface was gently rubbed with a Spec wipe while in a 1% solution of Alconox detergent, 2) rinsed with DI water, 3) dipped in 25% HCl (no dwell time), 4) rinsed in DI water, and 5) nitrogen blow dried. Samples were then mounted to the platens in the deposition chamber with Kapton tape (as shown in Figure 3-2) and the chamber was subsequently pumped down to a pressure of at least  $2.0 \times 10^{-5}$  Torr and heated to 200 °C.

Before the coating deposition was started, the samples underwent RF sputter cleaning for ten minutes with 43.3 sccm Argon, 1.5 mTorr, and 300 W to remove dirt, oils, and the thin native oxides to promote coating adhesion. The nickel coating was then deposited with 140 sccm Argon, 16 mTorr, 0.8 kW, at 200 °C for 270 minutes in order to achieve a coating thickness of approximately 3.8  $\mu\text{m}$ . Once the deposition was completed, the chamber was allowed to cool to room temperature before venting and removing samples.

As with the electroplated samples, optical profilometry was completed for all sputtered samples prior to the start of the aging studies.





Figure 3-2. (a) Digital image of Bosch sputtering system used to nickel sputter coat select panels of samples, (b) digital image of the deposition chamber interior where surface prepared and cleaned samples were mounted for sputter coating (note that the panels, along with a few witness coupons, were mounted with kapton tape), and (c) digital image of sample panels after sputter deposition.

### 3.4 Aging Studies

After the samples were coated, they were aged in one of three different environments: atmospheric corrosion/mixed flowing gas (MFG), elevated temperature and relative humidity (TRH), or thermal cycle (TC) for up to nine weeks. In order to allow for characterization as a function of time, samples were removed every three weeks. Individual panels were designated to a specific aging environment such that each environment had one full panel of samples for each of the four roughnesses, as listed in the sample matrix in Table 3-4. Each of the panels was cut into the strips of three duplicate samples, as indicated in Figure 3-3, to allow for easy removal of the samples at the designated times throughout the course of the aging study. Figure 3-4 provides a visual overview of the coupon assignment breakdown for the coupons within one of the three coating system sets. The

same flow chart can be used for each of the coating systems (nickel and gold plated, nickel plated, and nickel sputtered), but Figure 3-4 is labeled for the nickel and gold plated samples as an example.

Table 3-4. Sample matrix detailing the prepared surface roughness group, coating system, and aging environment for each specific panel of coupons tested.

Coating	Aging Environment	Surface Roughness			
		Group 1 (0.06 $\mu\text{m}$ )	Group 2 (0.55 $\mu\text{m}$ )	Group 3 (0.83 $\mu\text{m}$ )	Group 4 (2.38 $\mu\text{m}$ )
Ni+Au Plated	MFG	N14	N02	N26	N38
	T/RH	N18	N06	N30	N42
	TC	N22	N10	N34	N46
Ni Plated	MFG	N13	N01	N25	N37
	T/RH	N17	N05	N29	N41
	TC	N21	N09	N33	N45
Ni Sputtered	MFG	N19	N07	N31	N43
	T/RH	N16	N04	N28	N40
	TC	N23	N11	N35	N47

Panel N14

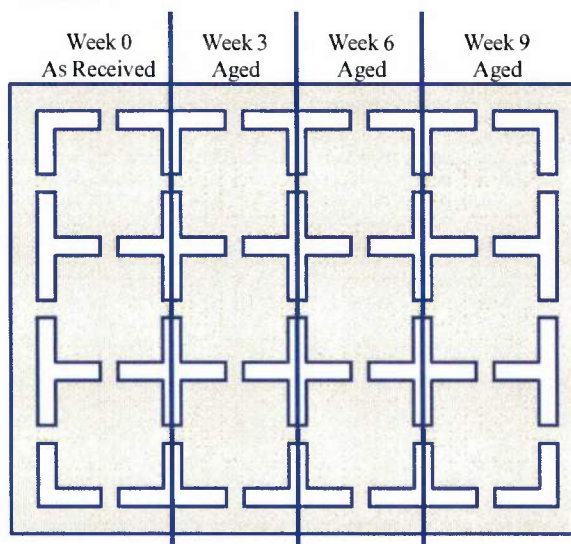


Figure 3-3. Schematic of a panel (N14 for example) depicting the sample designation within the panel and which samples were removed at what increments during the aging study. Samples in each column are duplicates, i.e., there are a total of three duplicates for each specific condition/aging time.



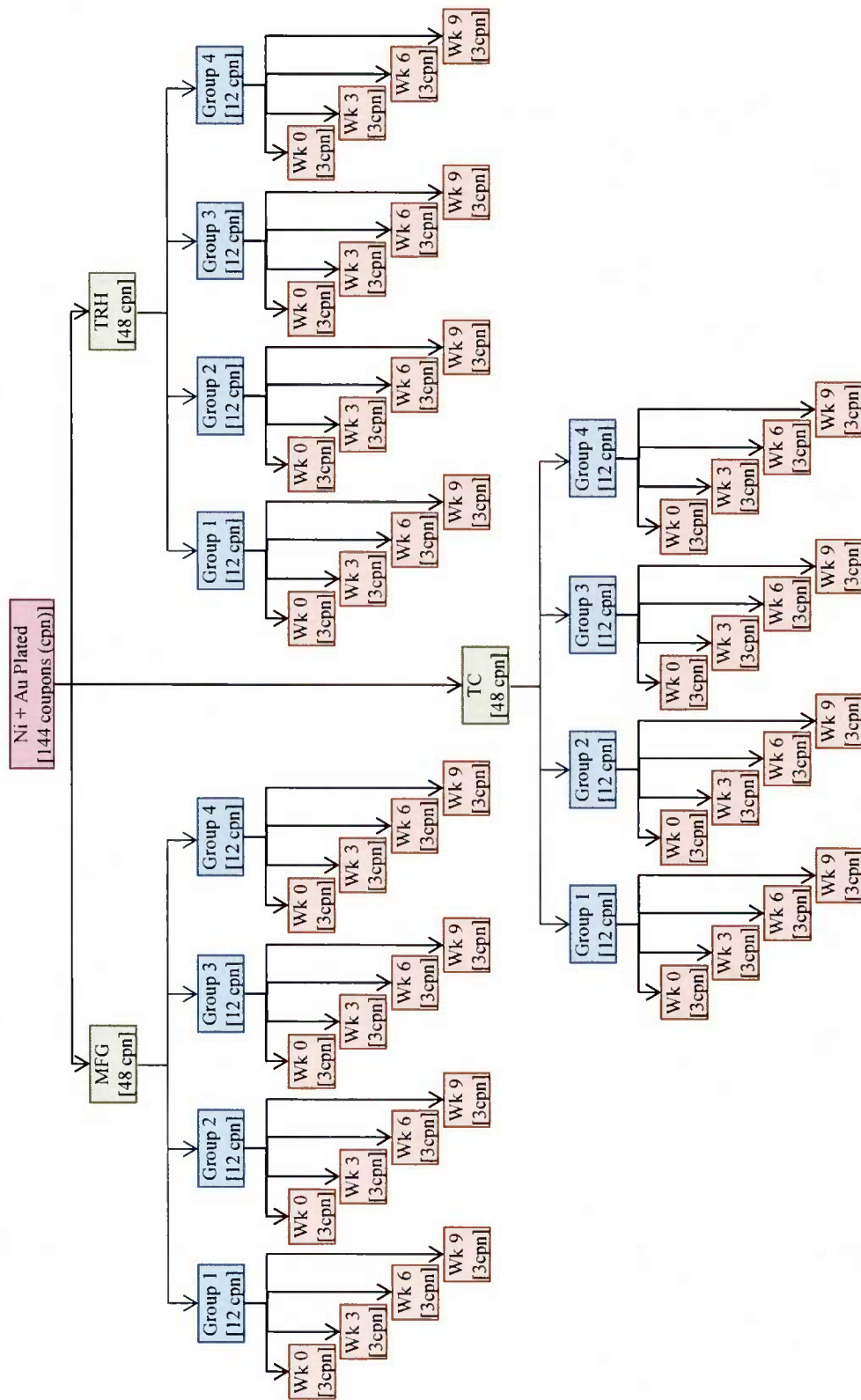


Figure 3-4. Flow chart depicting the coupon assignment for the nickel and gold plated samples. Note that the number of coupons for each division is listed in the brackets.

### 3.4.1 Atmospheric Corrosion/Mixed Flowing Gas (MFG)

The atmospheric corrosion/mixed flowing gas environment consisted of a Battelle Class II environment with exposure parameters as listed in Table 3-5. A schematic of the system used to create the environment is also depicted, in Figure 3-5, showing the various mass flow controllers and gas analyzers used to control the environment, as well as the permeation tubes supplying the contaminants.

Table 3-5. Battelle Class II MFG environment [1].

Temperature	Relative Humidity	NO <sub>2</sub>	H <sub>2</sub> S	Cl <sub>2</sub>
30 ± 2°C	70 ± 2%	200 ± 25 ppb	10 +0/-4 ppb	10 +0/-2 ppb

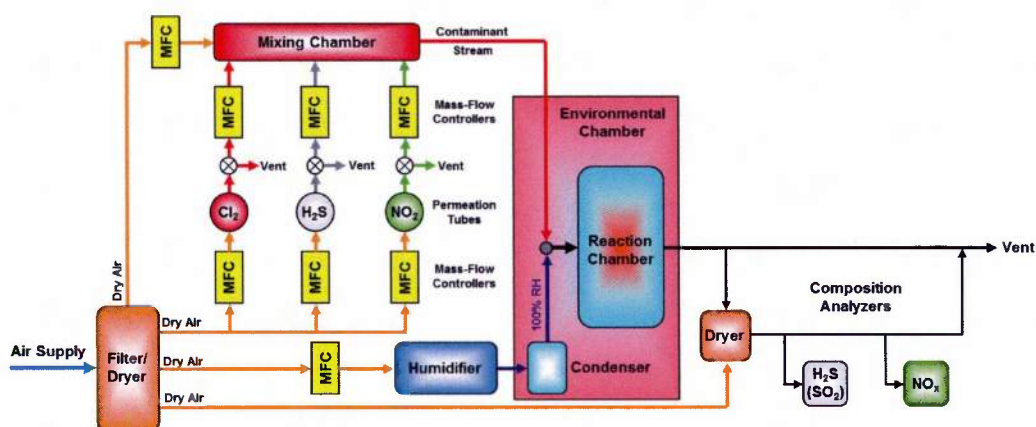


Figure 3-5. Schematic of mixed flowing gas system set up and testing chamber. Source: Enos [76].

Since the sample panels were cut prior to aging to allow for easy removal, there was a small amount of exposed copper at the cut sites. These areas were sealed off from the environment using a stop-off lacquer (MicroStop lacquer from Pyramid Plastics, Inc.) or plating tape (circuit plating tape 851L from 3M). In addition, the back side of the MFG samples was covered with plating tape to help prevent excessive consumption of the contaminants in the environment, as shown in Figure 3-6. Samples were mounted in the MFG chamber via covered wire ties.

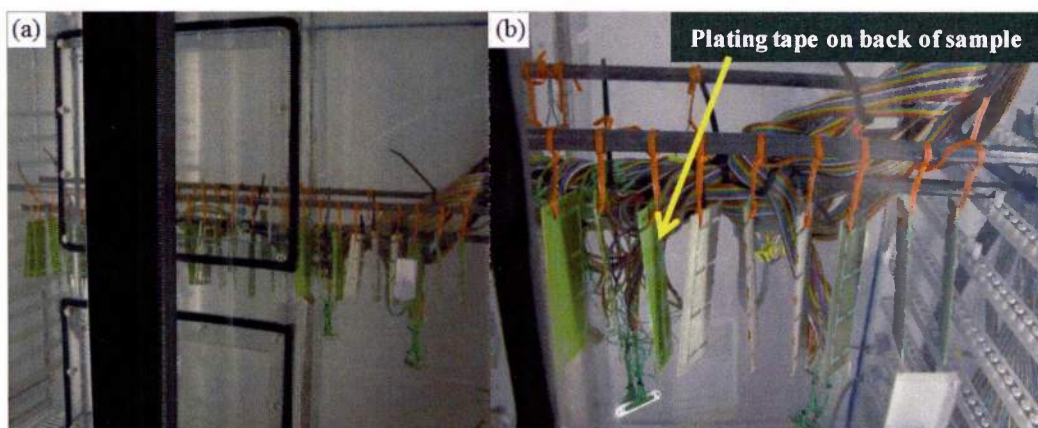


Figure 3-6. (a) Digital image of coupons mounted in MFG chamber for aging and (b) Close-up view of samples in MFG chamber showing plating tape (green tape) on the back of samples.

### 3.4.2 Elevated Temperature and Relative Humidity (TRH)

For the elevated temperature and relative humidity aging study, samples were mounted in an oven at 40°C with a relative humidity of 85%, see Figure 3-7. In order to prevent condensation from forming on the samples upon insertion in the chamber, samples were pre-heated to temperature in a separate oven which was flowing nitrogen and also contained a desiccant.

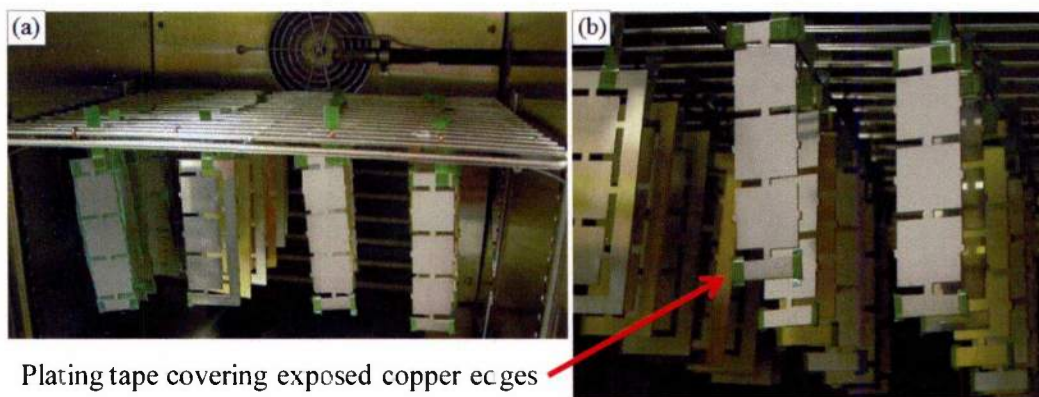


Figure 3-7. (a) Digital image of coupons mounted in TRH chamber for aging and (b) Close-up view of samples in TRH chamber showing plating tape (green tape) covering exposed edges of copper.



### 3.4.3 Thermal Cycling (TC)

Once mounted within the thermal cycle chamber (EC-2 Sigma Climatic Chamber, see Figure 3-8), the coupons were cycled between temperatures of  $-40^{\circ}\text{C}$  and  $60^{\circ}\text{C}$ . Since the thermal cycle environment did not include high humidity levels or contaminant gases, the stop-off lacquer and plating tape were not used to cover the exposed copper on the samples.



Figure 3-8. (a) Digital image of the thermal cycle chamber used (EC-2 Sigma Climatic Chamber), (b) Digital image of coupons mounted in TC chamber for aging, and (c) Close-up view of samples in TC chamber.

The thermal profile for the test is shown in Figure 3-9. Each cycle was 75 minutes with a hold time of 15 minutes at the end point temperatures before the next phase of the cycle was

continued. Due to the maintenance requirements of the thermal cycling system associated with the use of liquid nitrogen (used during thermal cycling to achieve the lower temperature endpoint), cycling could only be performed during the work week and was suspended over weekends. As such, the total number of cycles each set of samples completed was dependent on the number of weeks cycled. Table 3-6 lists the number of thermal cycles completed for each of the sample sets based on their designated aging time.

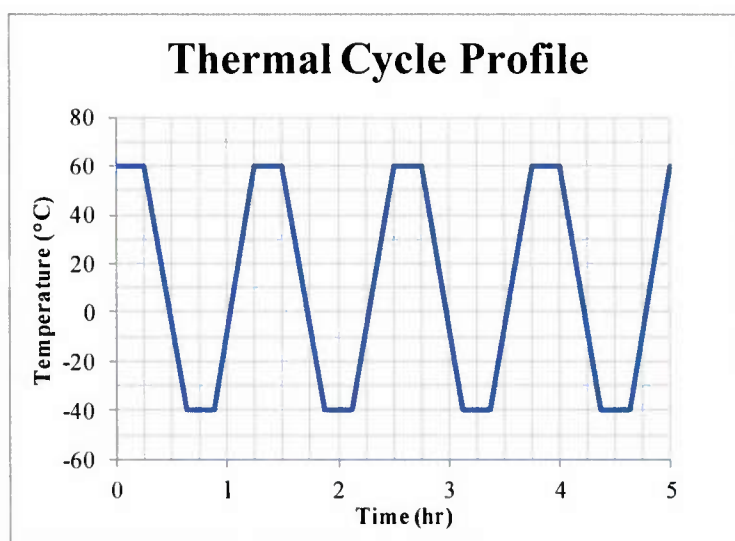


Figure 3-9. Excerpt from the complete thermal cycle profile showing upper and lower temperature bounds, as well as the 15 minute dwell time during the thermal cycle testing.

Table 3-6. Number of thermal cycles completed for the various aging times.

Aging Time	Number of Thermal Cycles Completed
Week 0	0
Week 3	325
Week 6	675
Week 9	1000

### 3.5 Characterization

Several analytical characterization techniques were implemented into this research, including optical profilometry, optical microscopy (OM), scanning electron microscopy/energy dispersive spectroscopy (SEM/EDS), x-ray diffraction (XRD), and electrical contact resistance (ECR) to aid in the characterization of the samples.

#### 3.5.1 *Optical Profilometry*

Optical profilometry was used to determine the surface roughness of the samples. Before all of the optical profilometry was completed, an initial set of trial measurements was collected for a range of scan sizes, or fields of view (FOV), in order to optimize the conditions used for the sample measurements. As a result, all optical profilometry was completed for a field of view of 0.64 mm x 0.48 mm with a 50x objective, 0.5x zoom, and with three averaged scans per site. In order to obtain the selected field of view, nine individual scans were stitched together via a 3 FOV x 3 FOV stitch with a 20% overlap. Final measurements were completed on a select subset of samples prior to coating, and on all of the samples after coating both before and after their respective environmental exposures. Measurements taken immediately before the aging studies (i.e., after the coupons were coated, but before environmental exposure) were completed at Sandia National Laboratories on a Veeco Wyko NT1100, and all other measurements were collected at Penn State on a Zygo NV7300.

#### 3.5.2 *Scanning Electron Microscopy (SEM) / Energy Dispersive Spectroscopy (EDS)*

Scanning electron microscopy was used for visual analysis of the sample surface for differences in surface morphology due to the various surface roughnesses, as well as to examine corrosion sites. In addition, energy dispersive spectroscopy was used with SEM to obtain chemical



information for the corrosion products (predominately for the atmospheric corrosion/mixed flowing gas samples). SEM imaging was completed for every set of samples.

Cross sectioning was also completed for a select set of samples, and examined in the SEM, to determine coating thickness for the nickel and gold layers, as well as to observe any larger subsurface defects that may have been present, such as embedded grit. A total of at least 300 measurements were made per cross section, using Clemex Analytical software, to determine the coating thickness (one hundred measurements per SEM image examined as depicted in Figure 3-10). Cross sections were created via mounting and polishing a section of a selected sample.

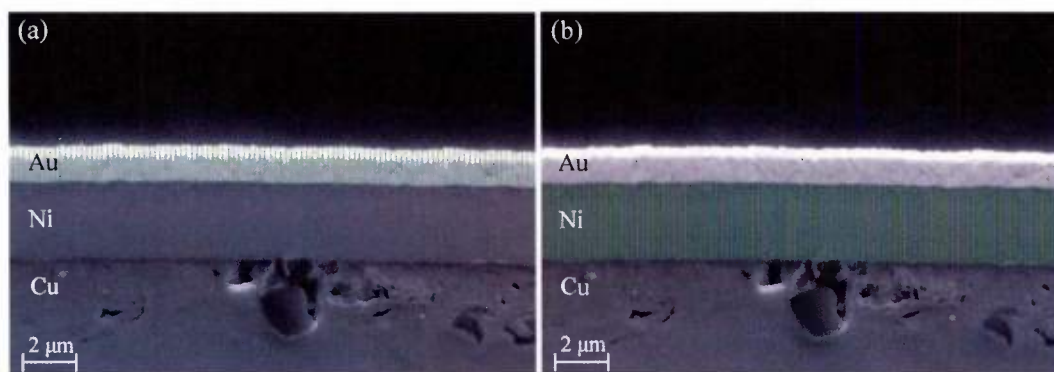


Figure 3-10. Example images depicting coating thickness determination with Clemex Analytical software. One hundred columns per image were created for each coating and measured to obtain thickness data. Shown above are the images for a Group 1 Au/Ni plated sample where (a) focuses on the thickness of the gold coating and (b) on the nickel underlayer.

### 3.5.3 Optical Microscopy (OM)

Optical microscopy was used for additional visual analysis. The larger fields of view possible with optical microscopy allowed for a larger scale examination of the surface than what could be completed via SEM, such as obtaining corrosion site density information. Single field of view images and/or surface mapping were completed for samples and analyzed with Clemex to

acquire an approximate percent of area covered with corrosion sites/products. For the samples analyzed based on single field of view images, the percent area was approximated by averaging the results from 20 images collected randomly across the surface with a magnification of 100x. Similarly for samples analyzed based on surface maps, the sample surface was divided into four regions, each analyzed with Clemex Analytical software and the results averaged for the overall approximated area percent. This data, however, are only an approximation, particularly for the rougher samples, as the ability to distinguish between features of interest, i.e., corrosion/defect sites, and the base surface morphology/heterogeneities became increasingly difficult with increasing substrate surface roughness.

#### 3.5.4 X-Ray Diffraction (XRD)

X-ray diffraction was used to determine the residual stress in the gold coating utilizing a PANalytical X'Pert MRD system. Preliminary theta-2theta diffraction patterns were collected to determine which peak to focus on for the residual stress measurements. Based on Figure 3-11, it was decided to focus on the (311) plane, with a diffraction peak at approximately  $138^\circ 2\theta$ , due to its higher diffraction angle and intensity (recall from previous discussion that for residual stress measurements, it is best to use a peak with a diffraction angle of  $2\theta \geq 120^\circ$  to help improve the precision of the results) [14, 15]. Measurements were completed for all samples using a chromium radiation source ( $\lambda_{Cr} = 2.2898 \text{ \AA}$ ), a 3mm x 3mm slit size, five psi scans at  $\Psi = 0^\circ, 10^\circ, 15^\circ, 30^\circ$ , and  $45^\circ$ , a  $2\theta$  step size of  $0.02^\circ$ , and a step time of 25s for the entire  $2\theta$  range of  $136.5^\circ \leq 2\theta \leq 140.5^\circ$  surrounding the peak of interest.

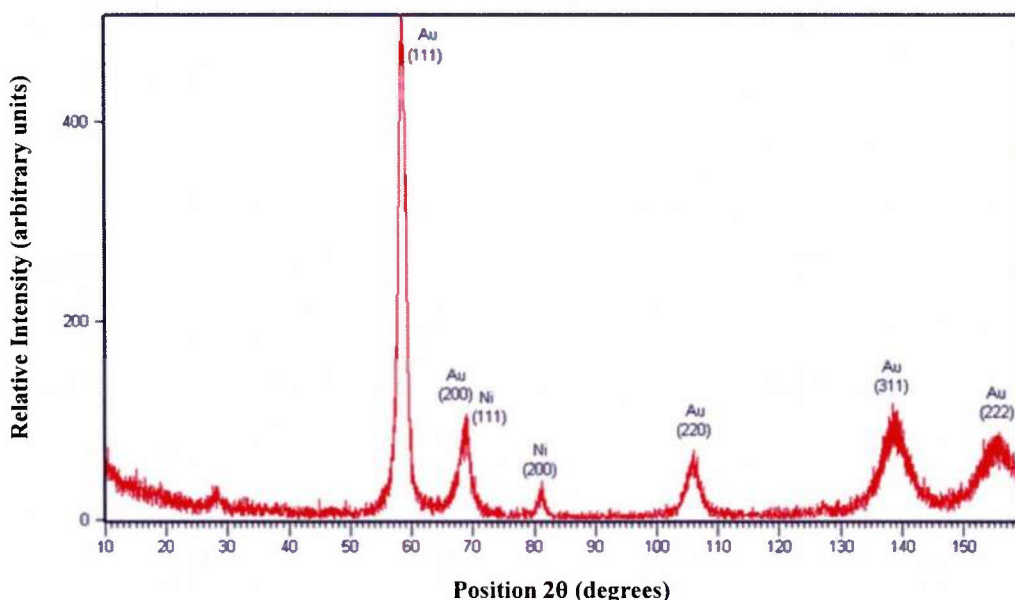


Figure 3-11. Theta-2Theta diffraction pattern for a Group 1 Au/Ni plated copper sample using chromium radiation source.

Residual stress calculations were completed with PC Stress software via the  $\sin^2\Psi$  method using a modulus of elasticity and a Poisson's ratio of 79 GPa and 0.42, respectively, for gold [65] and 232 GPa and 0.31 for nickel [12, 69]. Note, however, that the moduli of elasticity and Poisson's ratios used are not specifically for the (311) plane, but rather bulk material. As such, the calculated residual stress will be off by a factor (N), where  $N = \left( \frac{E}{1+\nu} \right)_{hkl} / \left( \frac{E}{1+\nu} \right)_{bulk}$ , and will not represent the absolute stress present in the coating. However, this should not present a large issue as this research is focused on the change in stress between environments, aging times, and surface preparation.

### 3.5.5 Electrical Contact Resistance

The electrical contact resistance was determined for loads ranging from 0 – 200g using the system set up depicted in Figure 3-12. A load cell and stage were used to load the sample during

testing, and a Keithley 580 micro-Ohm meter was used to determine corresponding resistances. Measurements were made dynamically, meaning that the load was gradually applied for the entire range (via vertical travel of the stage at  $0.75\mu\text{m/s}$ ) while the resistance data was collected for a single site. The probe used for these measurements was nickel and gold plated beryllium copper with a 3 mm hemispherical tip. The orientation and direction for which measurements were collected is depicted in Figure 3-13, starting with M1 to M40. Data collected were analyzed with the aid of cumulative distribution plots created in Minitab.

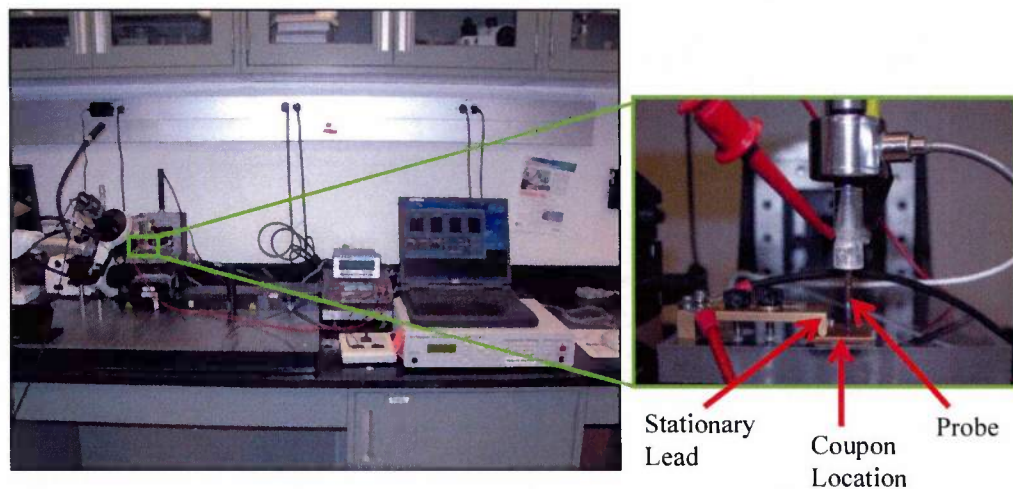


Figure 3-12. Electrical contact resistance equipment with four wire resistance measurement set up depicting the location of the stationary lead, coupon location, and the probe.

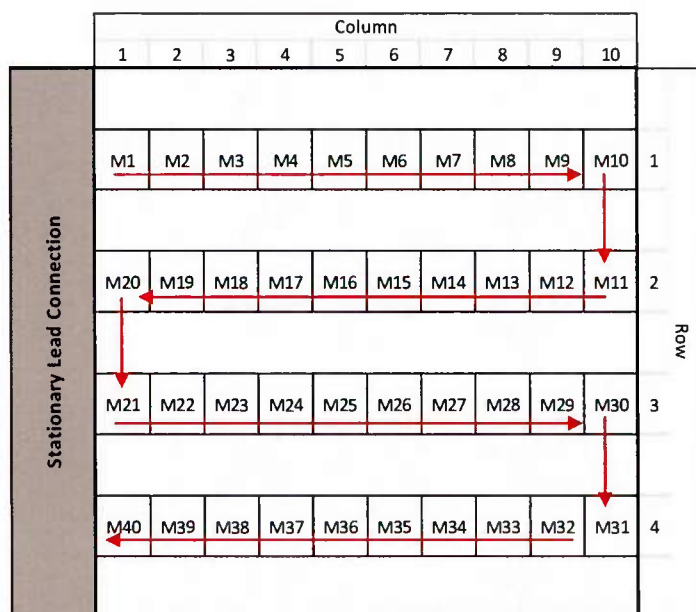


Figure 3-13. Schematic of measurement orientation on sample with arrows indicating measurement direction. Note that for spot check work, only 20 measurements were taken per sample with the same orientation/direction of measurement, but instead of ten measurements per row, there were only five.

## Chapter 4

### Results and Discussion

Various analytical characterization techniques, such as SEM, OM, XRD, optical profilometry, and ECR measurements were performed to identify correlations and determine the effects of surface roughness on ECR and residual stress as a function of aging condition. Within Chapter 4, results for the as received (i.e., unexposed) will be presented followed by the results and discussion for the aged samples exposed to atmospheric corrosion/mixed flowing gas (MFG), elevated temperature and relative humidity (TRH), and thermal cycled (TC) environments. The reported results focus predominately on the Au/Ni plated samples with additional data from the Ni plated or the Ni sputtered samples for comparison.

#### 4.1 Characterization of As Received (Week 0) Coated Samples Prior to Aging

##### 4.1.1 *Surface Morphology*

The beginning stages of this research involved preparing the copper substrates to various surface roughnesses and applying Au/Ni plated, Ni plated, or Ni sputtered coatings. Optical profilometry was completed at three different stages: prior to coating, after coating but before environmental exposure, and after environmental exposure. The final averaged surface roughness values of the samples prior to coating are shown in Figure 4-1. Average surface roughness values for the coupons after coating are listed in Table 4-1 based on the coating system. In addition, a few examples of the stitched images acquired via optical profilometry for the coated samples are shown in Figure 4-2.



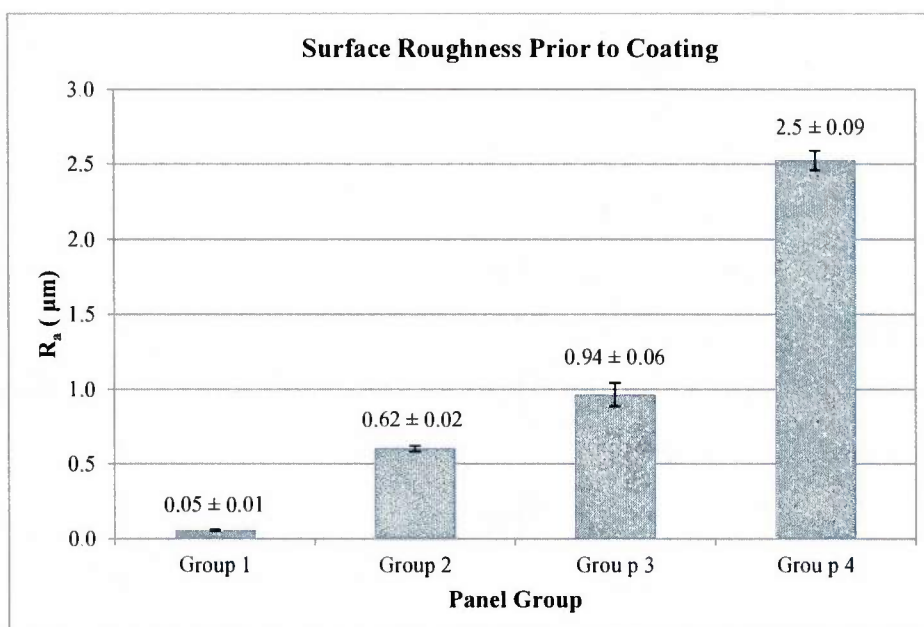


Figure 4-1. Average  $R_a$  surface roughnesses for select samples from each of the four roughness groups before coatings were applied.

Table 4-1. Average surface roughness,  $R_a$ , for the unaged samples based on the coating system for Groups 1, 2, 3, and 4 samples.

Week 0 Average $R_a$ ( $\mu\text{m}$ )				
Coating	Group 1	Group 2	Group 3	Group 4
Ni + Au Plated	$0.04 \pm 0.01$	$0.56 \pm 0.04$	$0.88 \pm 0.07$	$2.72 \pm 0.17$
Ni Plated	$0.04 \pm 0.01$	$0.49 \pm 0.05$	$0.73 \pm 0.04$	$2.57 \pm 0.12$
Ni Sputtered	$0.11 \pm 0.01$	$0.59 \pm 0.02$	$0.87 \pm 0.05$	$2.63 \pm 0.08$

The surface roughness values before and after coating are all relatively close, which suggests that there are no significant leveling or roughening effects due to the coating processes/conditions used, with one exception. The average surface roughness of the Group 1 Ni sputtered samples is  $0.11 \pm 0.01 \mu\text{m}$ , as listed in Table 4-1, which is significantly rougher than the  $0.05 \pm 0.01 \mu\text{m}$  of the uncoated Group 1 samples. Upon further investigation of the three panels of nickel sputter coated Group 1 samples, two panels (i.e., 24 of the 36 Group 1 Ni sputtered samples) had average surface

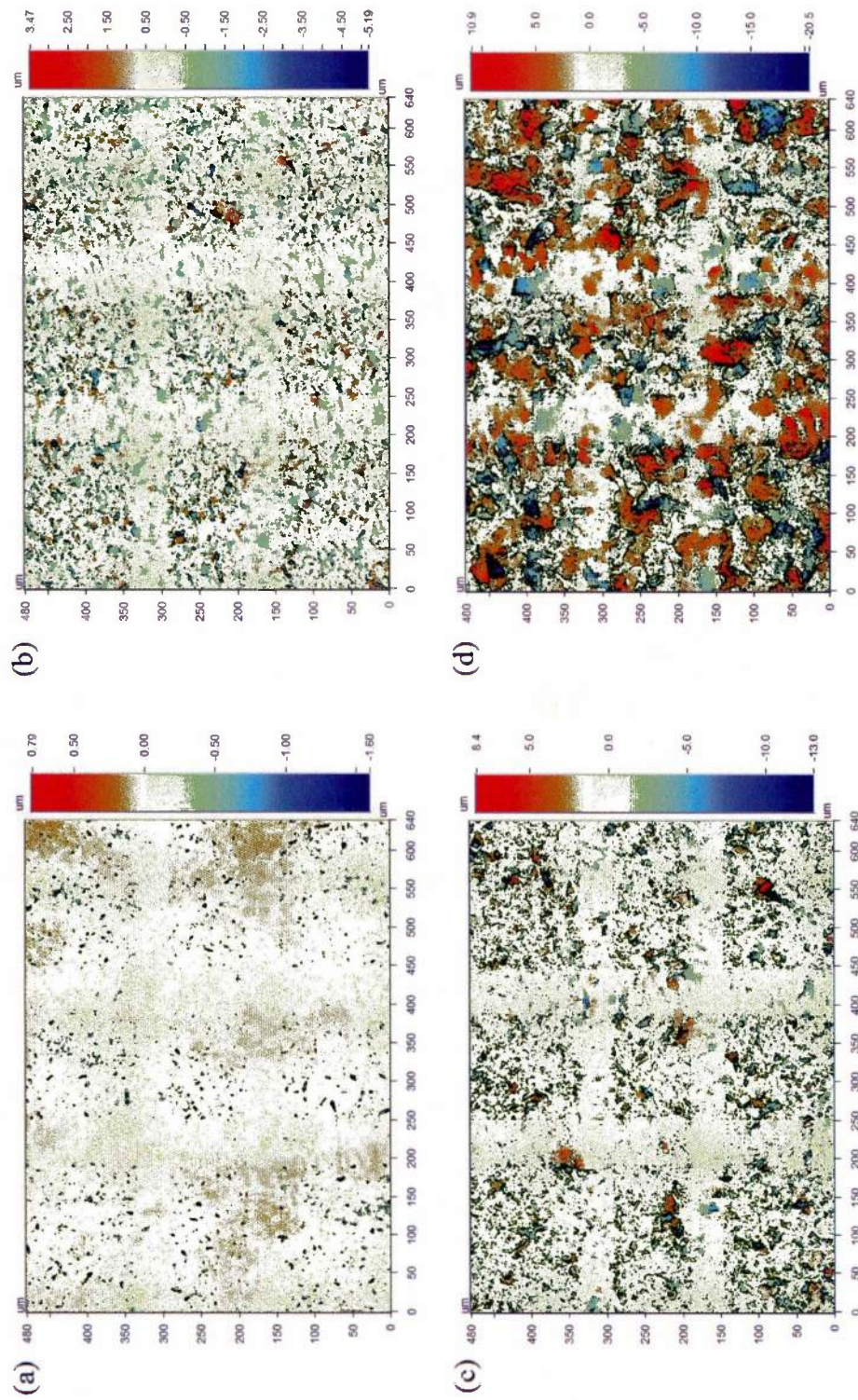


Figure 4-2. Examples of stitched optical profilometry scans for the as received samples. Each image represents a total of 27 scans as it is comprised of a 3 x 3 stitch, averaged three times. (a) Group 1 sample with  $R_a = 0.05 \mu\text{m}$ , (b) Group 2 sample with  $R_a = 0.47 \mu\text{m}$ , (c) Group 3 sample with  $R_a = 0.82 \mu\text{m}$ , and (d) Group 4 sample with  $R_a = 2.50 \mu\text{m}$ .



roughnesses of  $0.06 \pm 0.01 \mu\text{m}$  and  $0.07 \pm 0.01 \mu\text{m}$ , while the remaining panel had an average surface roughness of  $0.2 \pm 0.01 \mu\text{m}$ . Each of the three panels was coated in a separate deposition batch run (see Table 4-2), which may suggest that there were variations in the deposition conditions in the second deposition run. In fact, from Table 4-2 we can see that all of the panels coated during the second sputter deposition run had higher average surface roughnesses than the panels from the other deposition runs. This increase in surface roughness may be attributed to a higher pressure or variation in the deposition rate. The samples from the second deposition run also appear to be significantly darker in appearance, see Figure 4-3.

Table 4-2. Average surface roughness,  $R_a$ , for the unaged Ni sputtered samples grouped based on the deposition run in which the panels were coated for Groups 1, 2, 3, and 4 samples.

Ni Sputtered - Week 0 Average $R_a$ ( $\mu\text{m}$ )				
Deposition Run	Group 1	Group 2	Group 3	Group 4
1	$0.06 \pm 0.01$	$0.58 \pm 0.02$	$0.85 \pm 0.40$	$2.58 \pm 0.07$
2	$0.20 \pm 0.01$	$0.63 \pm 0.03$	$0.90 \pm 0.01$	$2.68 \pm 0.06$
3	$0.07 \pm 0.01$	$0.56 \pm 0.01$	$0.88 \pm 0.06$	$2.62 \pm 0.12$



Figure 4-3. Optical images of Group 1 Ni sputtered copper samples showing the visual variations in the appearance of the coating based on the deposition run: Run #1 (left), Run #2 (middle), Run #3 (right).

Optical microscopy and SEM images were obtained after the samples were coated to observe the differences in the surface morphology based on the substrate roughness. Figure 4-4 shows select

optical images for Groups 1, 2, and 3 Au/Ni unaged samples. Due to the surface roughnesses, it was difficult to obtain fully focused optical images at higher magnifications, particularly for Groups 3 and 4. As such, a large portion of the sample imaging completed was with SEM. Figure 4-5 shows SEM surface morphology images at the same magnification (5000x) for each of the surface roughness groups. Samples from Groups 2 through 4 show the presence of embedded grit in the coating, as identified by the red circles in the images.

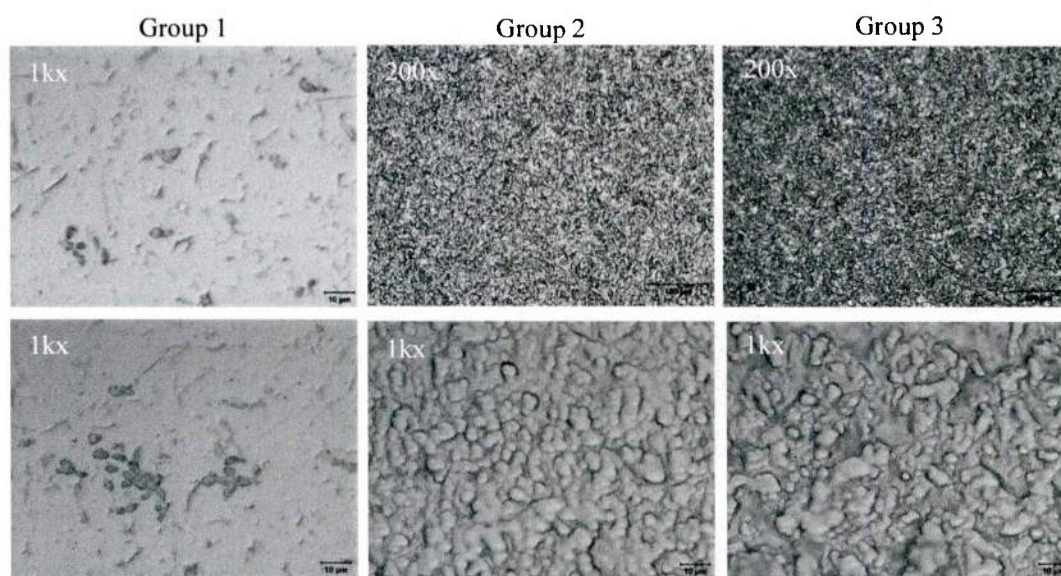


Figure 4-4. Optical images of Groups 1, 2, and 3 for the unaged Au/Ni plated samples.

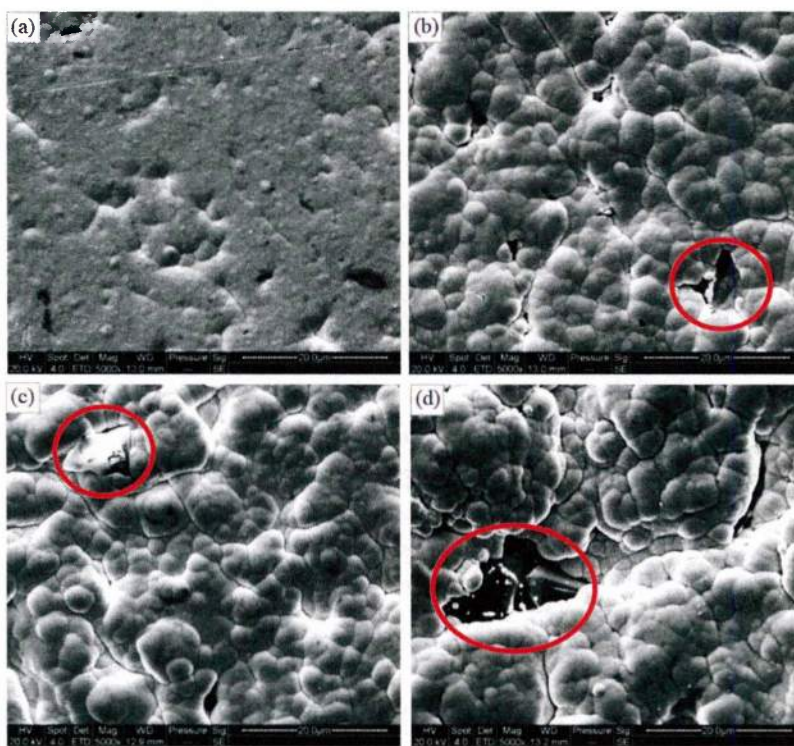


Figure 4-5. SEM images of unaged Au/Ni plated samples. Each image is for a different surface roughness group: (a) Group 1 samples with average  $R_a$  of  $0.06\ \mu\text{m}$ , (b) Group 2 with an  $R_a$  of  $0.55\ \mu\text{m}$ , (c) Group 3 with an  $R_a$  of  $0.83\ \mu\text{m}$ , and (d) Group 4 with an  $R_a$  of  $2.83\ \mu\text{m}$ . Note that Group 2, 3, and 4 samples have embedded grit from the surface preparation stages (circled above).

Spot EDS and EDS mapping were performed to confirm the elemental composition of the embedded grit. Figure 4-6 through Figure 4-8 show EDS mapping from Group 3 and 4 Au/Ni plated samples. EDS confirmed the presence of silicon carbide in the Group 4 samples, which is consistent with the grit Micro Lapping & Grinding reported using during the surface roughness preparations. In comparison, Group 2, and some Group 3, samples had aluminum oxide embedded in the surface (see Figure 4-8) in addition to silicon carbide. This could potentially be due to either some aluminum oxide contamination in the process used by Micro Lapping & Grinding (particularly for the Group 3 samples) or the aluminum oxide could be a result of the work LAPCO completed on the Group 2 samples before they were sent to Micro Lapping & Grinding to be reprocessed.



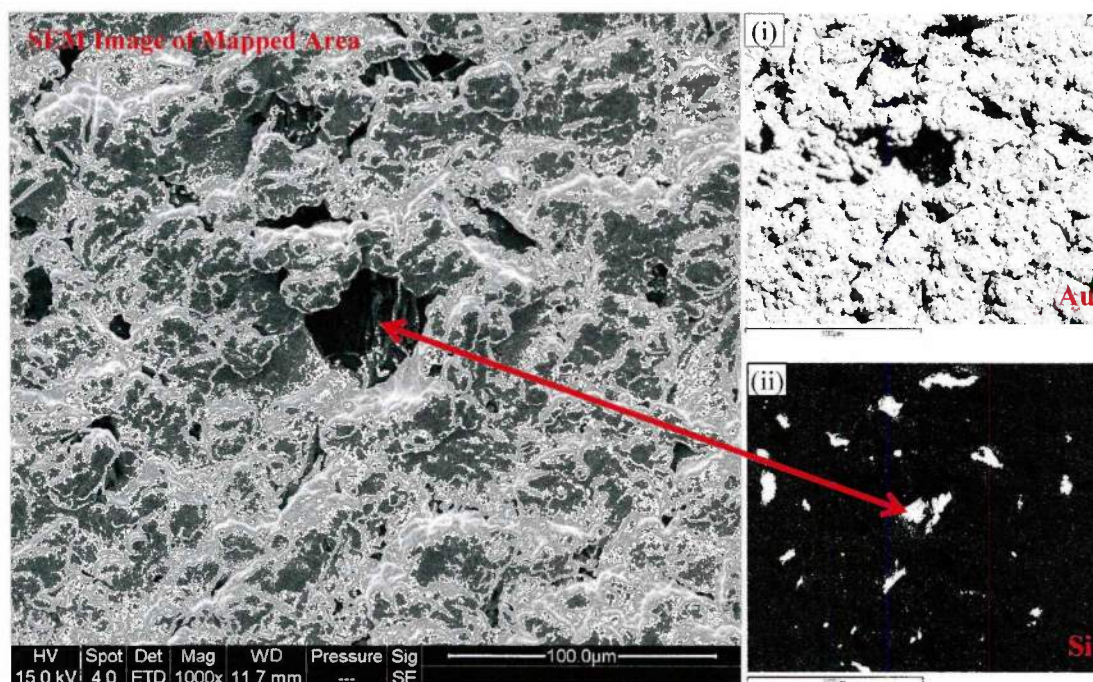


Figure 4-6. SEM image of Group 4 Au/Ni plated sample showing the presence of a contaminant in the coating. EDS mapping shows the presence of (i) gold and (ii) silicon confirming that the contaminant is silicon based, i.e., the silicon carbide grit. Note that in the EDS maps (i) and (ii), white is used to represent where a particular element is present (relative concentration) while everything else remains black.

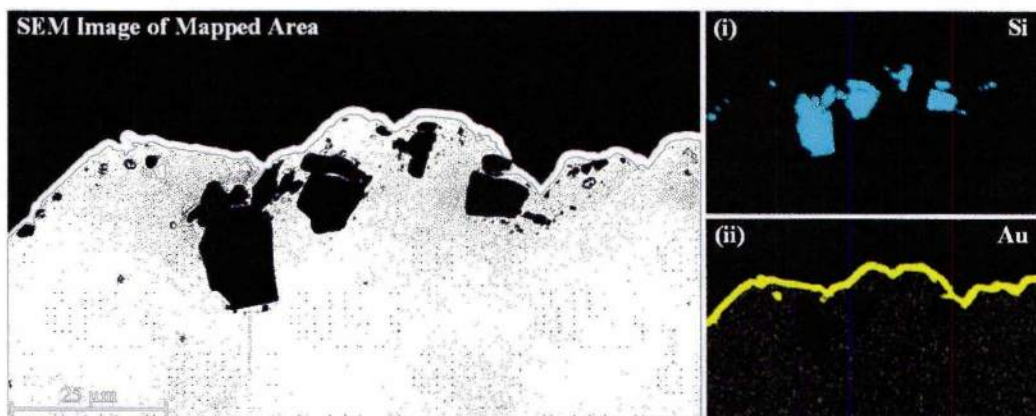


Figure 4-7. SEM image of a cross section of a Group 4 Au/Ni plated sample showing the presence of embedded grit. EDS mapping shows the presence of (i) silicon and (ii) gold, which confirms the elemental composition of the grit as silicon based, i.e., silicon carbide. Note that in (i) and (ii) the yellow and blue show where the element is present (relative concentration), while everything else remains black.



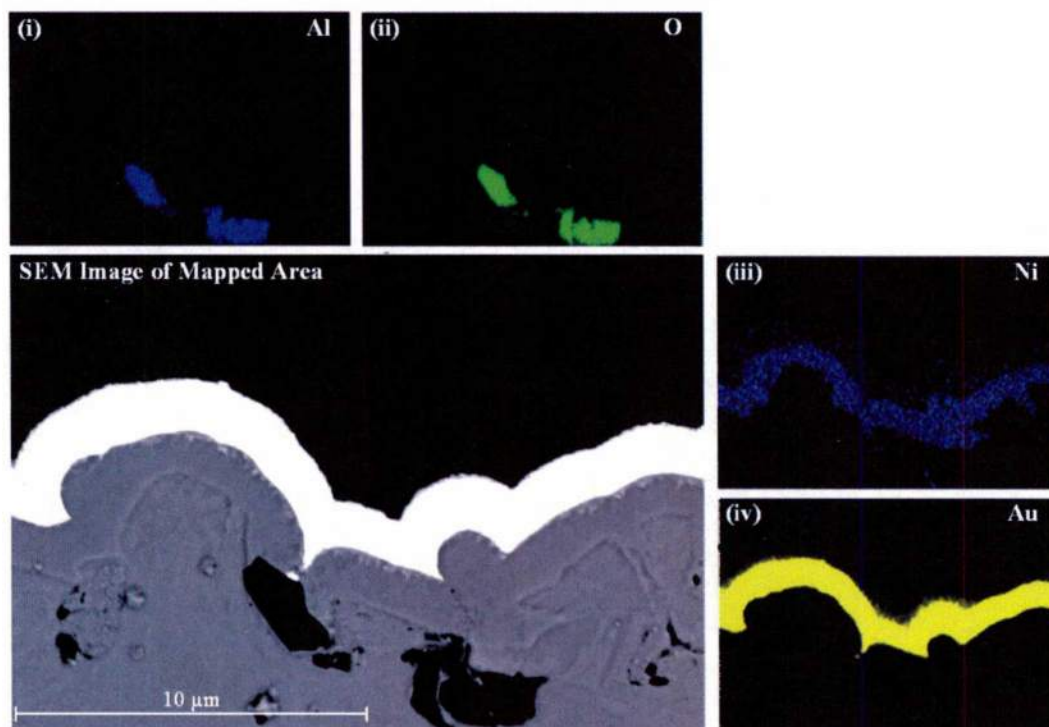


Figure 4-8. SEM image of a cross section of an unaged Group 3 Au/Ni plated sample revealing embedded grit. EDS mapping shows the presence of (i) aluminum, (ii) oxygen, (iii) nickel, and (iv) gold, which confirms the elemental composition of the grit as aluminum and oxygen based (i.e., aluminum oxide) instead of silicon carbide. Note that in (i) – (iv) the various colors (yellow, green, and blue) show where the element is present (relative concentration), while everything else remains black.

The embedded grit was incorporated into the copper substrate surface during the surface roughness preparation (i.e., lapping and grinding processes). As copper is a relatively soft metal, it is much easier for grit to become embedded as compared to other metals such as stainless steels or titanium. From a visual inspection of the coupons, a larger amount of embedded grit is observed in the Group 3 and Group 4 samples as compared to the Group 1 and 2 samples. It would be difficult to quantify the amount of embedded grit from surface images due to the surface roughness, as it becomes increasingly difficult to distinguish features on the surface with increasing surface roughness, and the fact that not all of the embedded grit is visible from the surface, see Figure 4-9. It

can also be noted that larger pieces of grit are embedded in the Group 3 and 4 samples, as the larger grits sizes are used to aid in the production of rough surfaces as compared to smooth surfaces.

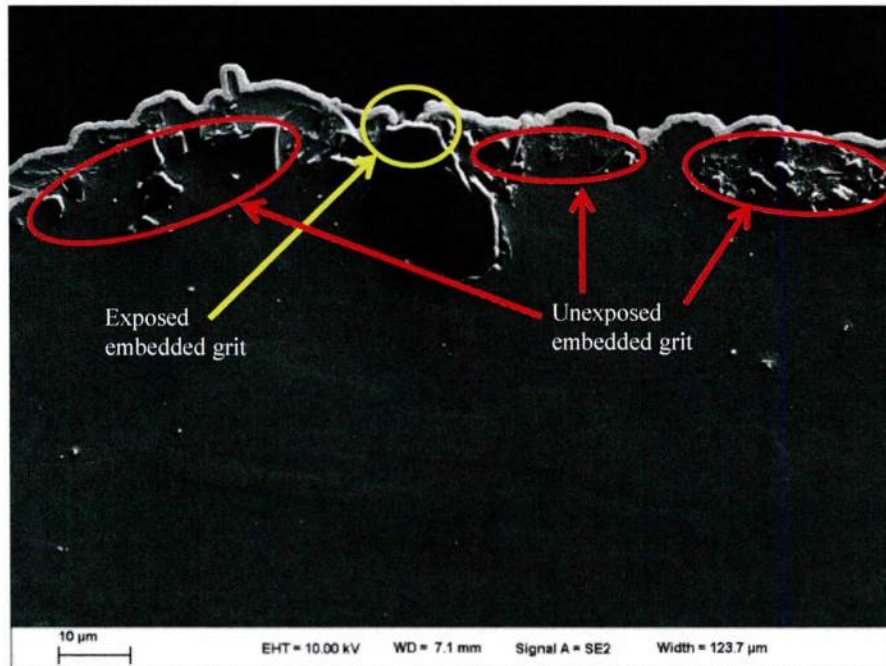


Figure 4-9. SEM image of a cross section of an unaged Group 4 Au/Ni plated sample revealing embedded grit that is exposed (i.e., visible from the surface) and unexposed (i.e., grit that has been plated over or is embedded deeper into the substrate).

Based on the coating mechanism of the sputtering process, it would be expected that less embedded grit would be observable from the surface for the Ni sputtered samples as compared to the Au/Ni plated and Ni plated samples, see Figure 4-10. As the embedded grit is not electrically conductive, they are not necessarily coated over in the electroplating process, while they would be in a sputtering process which relies on momentum transfer for material deposition.

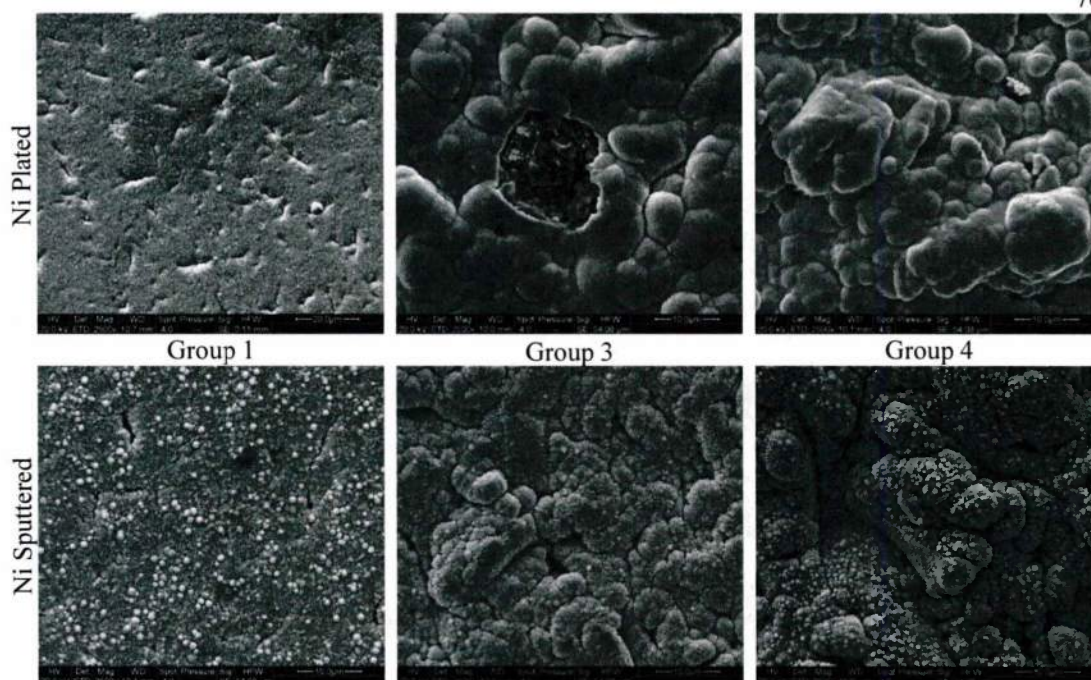


Figure 4-10. SEM images of Week 0 Group 1, 3, and 4 samples for the Ni plated and Ni sputtered samples.

#### 4.1.2 Coating Thickness

The targeted total coating thickness for all samples was 3.8  $\mu\text{m}$ . Cross sections were taken of select Au/Ni plated, Ni plated, and Ni sputtered samples. Optical images of the cross sections are shown in Figure 4-11 through Figure 4-13. In addition, SEM images for Group 1, 3, and 4 Au/Ni plated samples, as well as the Group 1 Ni sputtered sample, are shown in Figure 4-14 through Figure 4-17. As shown by arrows in several of the figures, the embedded grit noted in the surface images can also be observed in the cross sectional images.



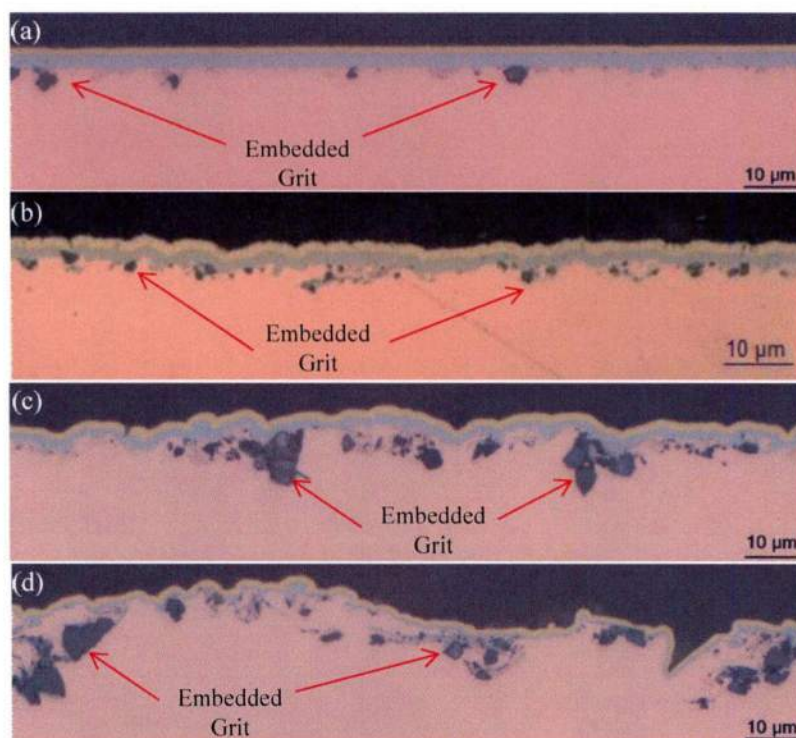


Figure 4-11. Optical images of select cross sections of Au/Ni plated as received samples: (a) Group 1, (b) Group 2, (c) Group 3, and (d) Group 4. Note that there is a significant amount of embedded grit present in the Group 3 and 4 samples. There also appears to be a higher porosity concentration in the Au coating for the Group 2 samples.

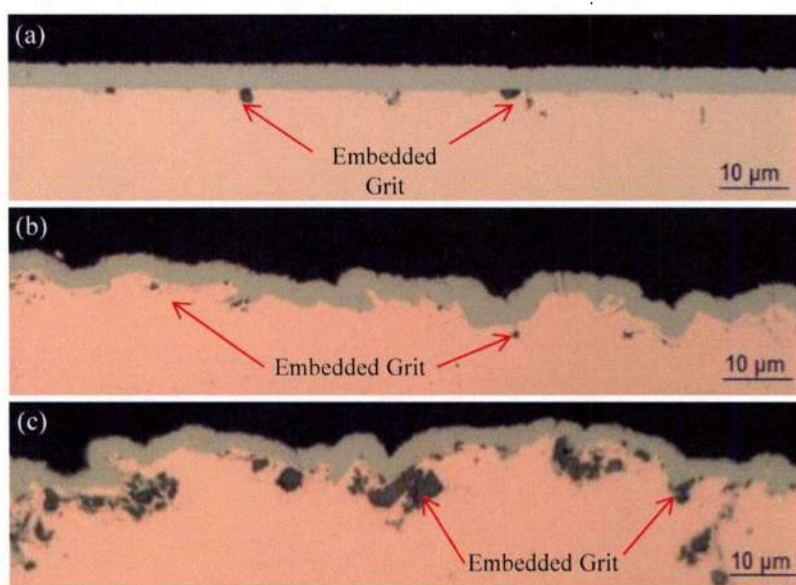


Figure 4-12. Optical images of select cross sections of Ni plated as received samples: (a) Group 1, (b) Group 3, and (c) Group 4.

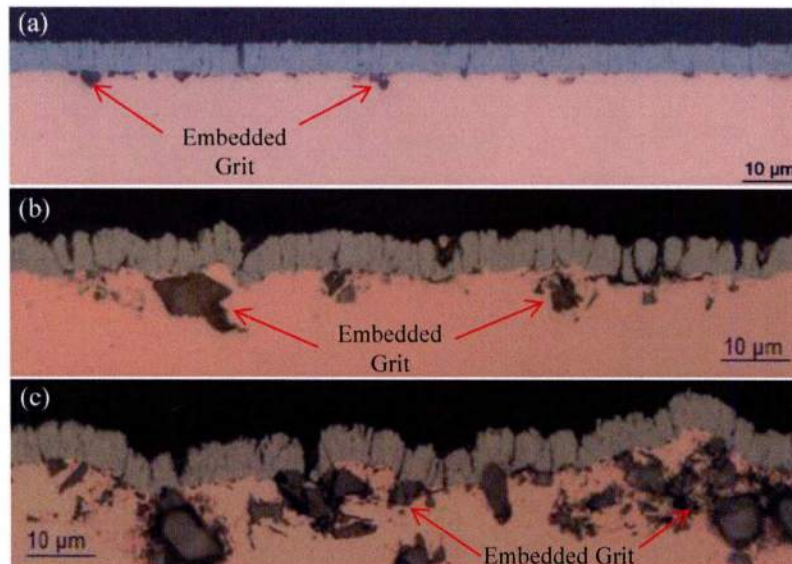


Figure 4-13. Optical images of select cross sections of Ni sputtered as received samples: (a) Group 1, (b) Group 3, and (c) Group 4.

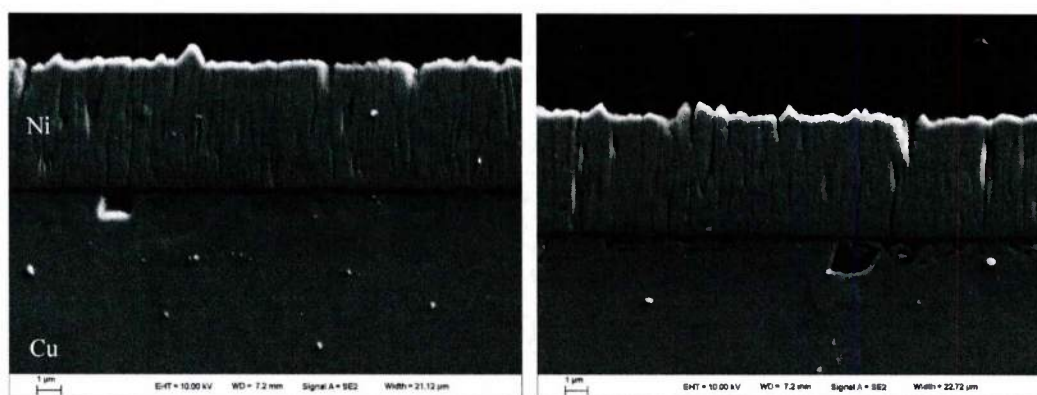


Figure 4-14. Cross sectional SEM images of Group 1 Ni sputtered copper samples at a couple of locations.

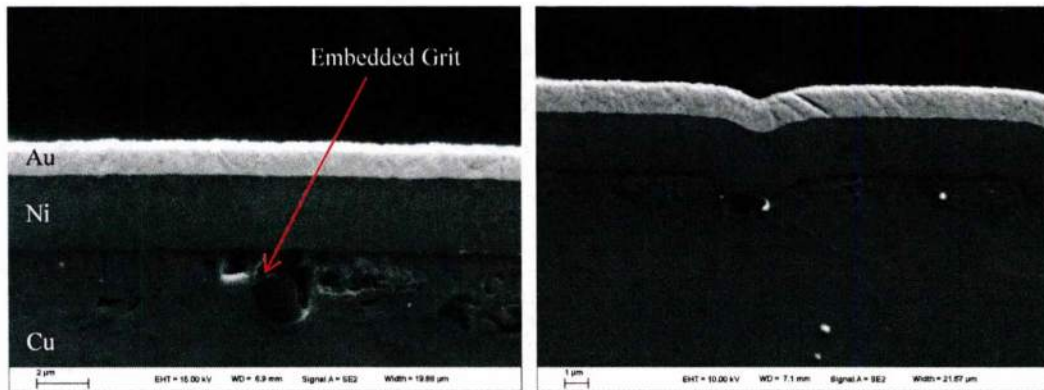


Figure 4-15. Cross sectional SEM images of Group 1 Au/Ni plated copper samples. The image on the left is at a lower magnification to provide a wider view regarding the size and depth of embedded grit.

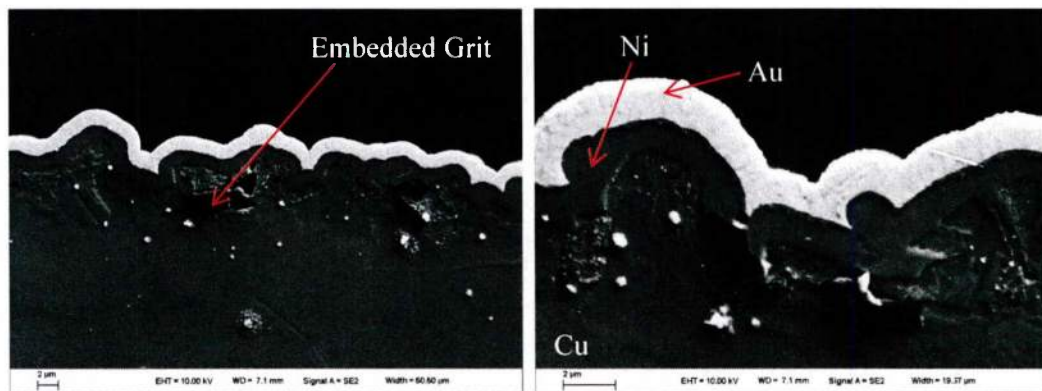


Figure 4-16. Cross sectional SEM images of Group 3 Au/Ni plated copper samples. The image on left is at a lower magnification to provide a wider view regarding the size and depth of embedded grit.

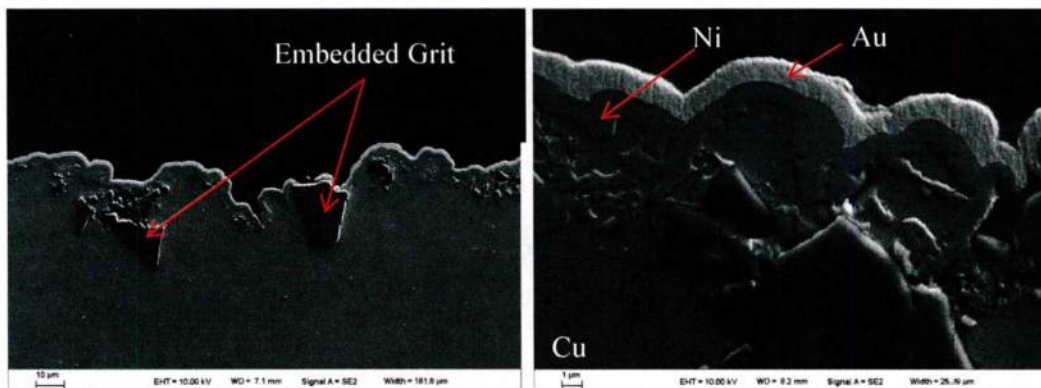


Figure 4-17. Cross sectional SEM images of Group 4 Au/Ni plated samples. Image on left is at a lower magnification to provide a wider view regarding the size and depth of embedded grit.



Detailed examination of the SEM cross section images of the Au/Ni plated samples reveals that the targeted ratio of nickel to gold coating thicknesses was not acquired for the rougher samples (Groups 3 and 4). The targeted 2.5  $\mu\text{m}$  of nickel to the 1.3  $\mu\text{m}$  of gold should result in a nickel coating approximately two times thicker than the gold. However, for the Group 3 and 4 samples there appears to be an approximately equal coating thickness for both nickel and gold. This observation was further quantified by measuring the coating thickness in several places using Clemex Analytical software, as exemplified in Figure 4-18, with the results summarized in Table 4-3. It can also be observed that the final coating thickness for the sputtered Ni coating is on the order of one to two microns thicker than the plated coatings.

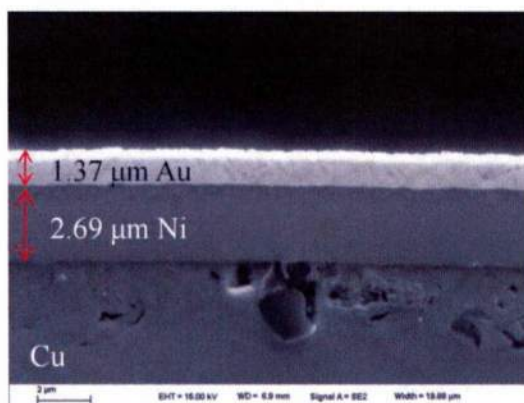


Figure 4-18. Example cross sectional image showing the coating thickness for the individual nickel and gold layers in a Group 1 Au/Ni plated sample.

Table 4-3. Coating thickness summary for the Ni plate, Ni sputtered, and Au/Ni plated samples, as well as the targeted coating thicknesses.

Coating Thickness ( $\mu\text{m}$ )					
Coating	Targeted	Group 1	Group 2	Group 3	Group 4
Ni Plated	3.8	3.53 $\pm$ 0.26	----	3.83 $\pm$ 0.9	4.1 $\pm$ 1.62
Ni Sputtered	3.8	5.55 $\pm$ 0.18	----	5.34 $\pm$ 0.77	5.18 $\pm$ 1.27
Ni Plated*	2.7	2.69 $\pm$ 0.14	1.84 $\pm$ 0.38	1.51 $\pm$ 0.57	1.49 $\pm$ 0.43
Au Plated*	1.3	1.37 $\pm$ 0.06	1.73 $\pm$ 0.27	1.55 $\pm$ 0.35	1.54 $\pm$ 0.35

\* Individual Ni or Au layers for the Au/Ni plated samples

### 4.1.3 Electrical Contact Resistance (ECR)

The electrical contact resistance for similar materials systems (i.e., gold plated copper, with or without a nickel underlayer) was reported to be on the order of approximately 1 m $\Omega$ , with some sources reporting slightly lower resistances. One set of sources for work completed at Sandia National Laboratories observed ECR values in the 10 – 20 m $\Omega$  range for unexposed samples [13, 52]. The results reported for this research are similar to the work completed at Sandia with the unaged electrical contact resistances shown in Figure 4-19 with observed ECR values in the range of 5 – 15 m $\Omega$ . Figure 4-20 shows that the ECR values for the Ni coated samples are significantly higher than for the Au/Ni plated samples, as would be expected.

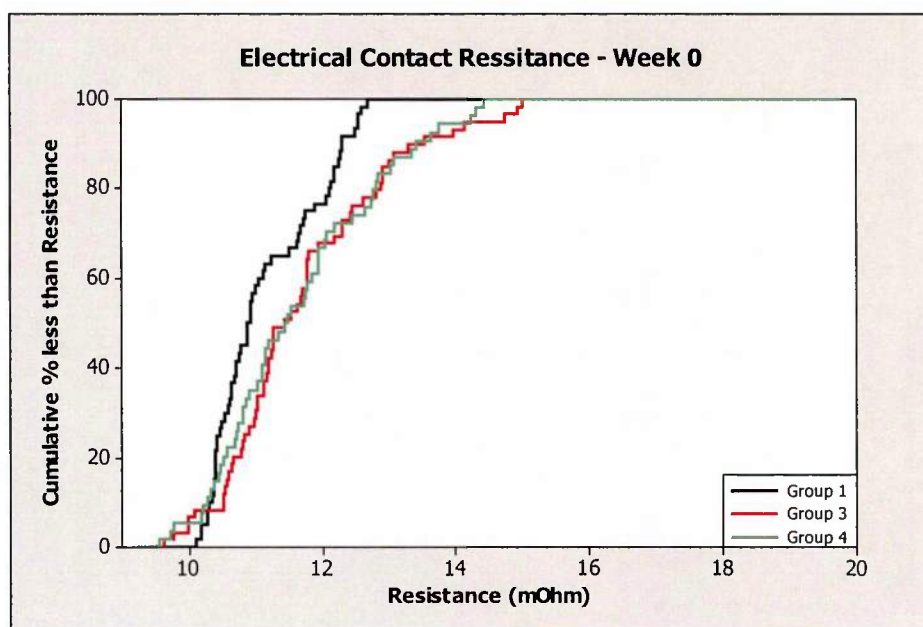


Figure 4-19. Cumulative distribution plot of the electrical contact resistance (ECR) for unexposed, Week 0, Au/Ni plated coupons under a load of 200g.

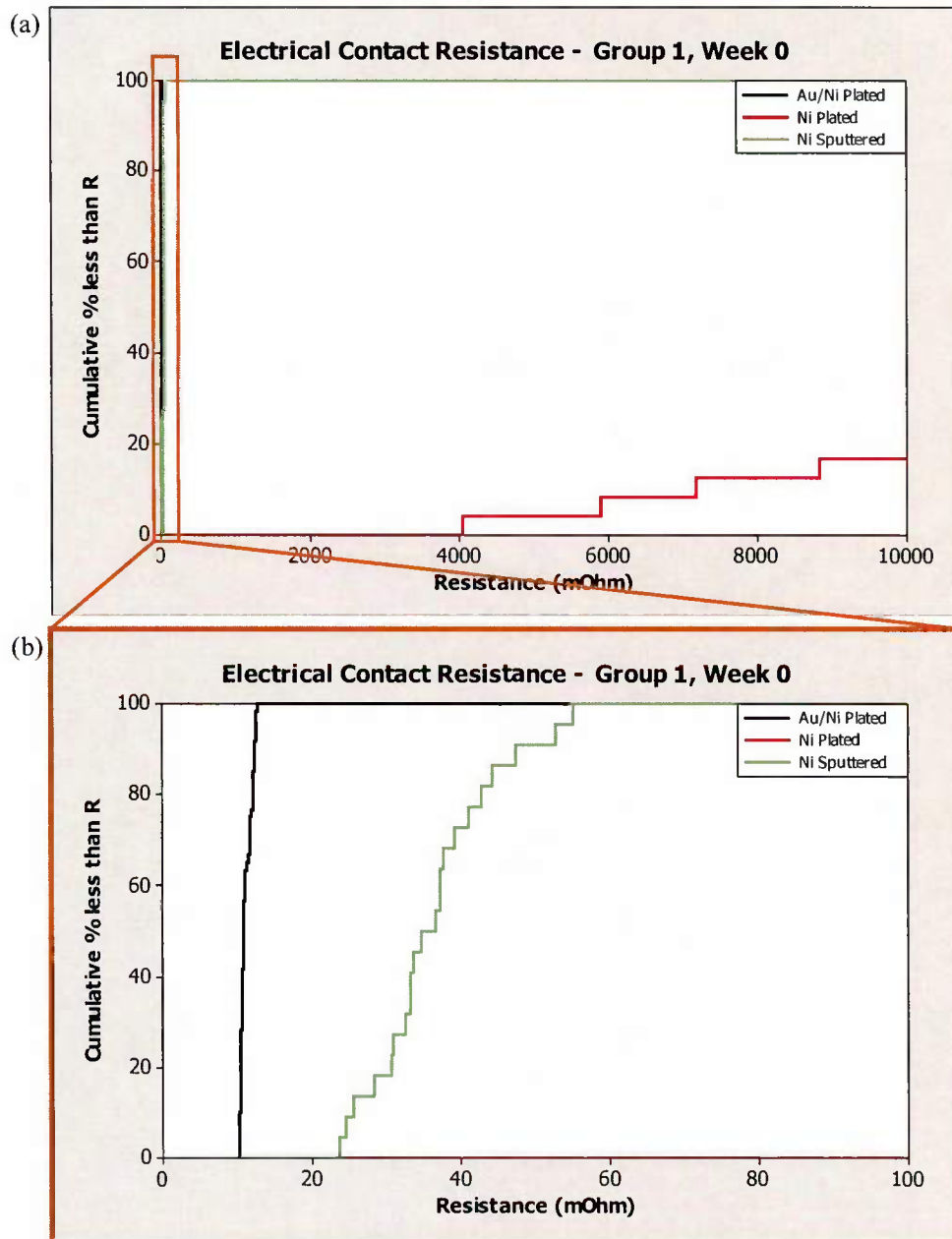


Figure 4-20. (a) Cumulative distribution plot of the electrical contact resistance (ECR) for unexposed, Group 1 Week 0, Au/Ni plated, Ni plated, and Ni sputtered coupons under a load of 200g, and (b) close-up of (a) providing a better depiction of the difference in ECR values for the Au/Ni plated and Ni sputtered samples.

From Figure 4-19, it can be observed that the electrical contact resistance is slightly lower for the smoothest samples (i.e., Group 1) versus the two rougher samples (Groups 3 and 4), which are

almost identical. This result is reverse from what was expected based on the literature search results where it was said that, at least for unaged coupons, electrical contact resistance should decrease with increasing surface roughness as the rougher samples would have more points of contact that could break through any oxide layers that may be present on the surface [37]. As mentioned in the previous section, there is grit embedded in the surface of the coupons from the surface preparation process. This grit could be one of the contributing factors leading to the electrical contact resistance of the rougher samples to be higher than expected as the grit is not electrically conductive itself. In addition, before it can be concluded that the electrical contact resistance above a cut-off point are nearly identical (as it appears in Figure 4-19 where Groups 3 and 4 data are nearly identical), additional work must be completed to help determine the possible contribution of the embedded grit to the electrical contact resistance. For instance, it may be expected that the Group 4 unaged samples would have a lower contact resistance than the Group 3 samples; however, based on surface imaging, there is also a larger degree of embedded grit in the Group 4 samples. The size, type, and amount of grit present (particularly grit exposed at the surface) are several of the factors associated with embedded grit that can all affect the observed electrical contact resistance.

Of the two grit materials observed in the samples, alumina has the higher electrical resistivity (i.e., lower electrical conductivity). The electrical resistivity of alumina and silicon carbide are on the order of  $10^{14} \Omega\text{cm}$  and  $10^8$ , respectively [68]. As such, it would be expected that samples with comparable amounts of alumina grit rather than silicon carbide, would have higher electrical contact resistances. As the amount of embedded grit increases, the area fraction of the surface that is not electrically conductive increases, causing the electrical contact resistance to increase as well. Whether or not the difference in the two grits are responsible for the Group 3 and Group 4 unaged samples having nearly identical electrical contact resistances is unclear at this point. Additional investigation must be completed as the amount of total embedded grit in these samples have not be quantified, let alone the amount of a specific grit. With respect to the size of the individual pieces of embedded grit,

the larger the exposed embedded grit is, the more it prevents contact between the conductive surfaces, see Figure 4-21.

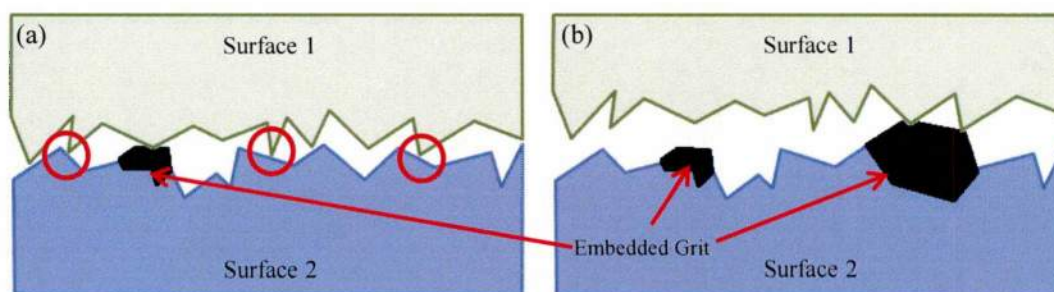


Figure 4-21. (a) Schematic depicting exposed embedded grit in one surface preventing contact between two electrical conductive surfaces and (b) showing the same surface set but with an additional larger piece of embedded grit to emphasize the effect grit size can have on the number of electrical contacts between surfaces.

Another possible explanation as to why the observed electrical contact resistance increased with increasing roughness rather than decreasing is due to the lack of an insulating oxide/surface film present on the unaged samples. The decrease in electrical contact resistance with increasing surface roughness was based on the increased ability of rougher surfaces to penetrate surface oxides that act as an insulating barrier between the surfaces, thus increasing the area of electrical contact. As gold is a noble metal and does not readily form a surface oxide as compared to the more active metals, the area of electrical contact between the sample surface and the probe is based more predominately on the total area of contact between the surfaces. Thus the area of electrical contact decreases with increasing surface roughness as demonstrated in Figure 4-22.



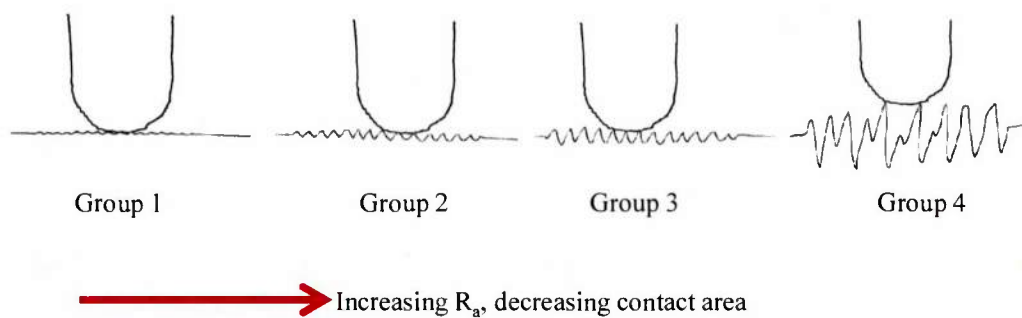


Figure 4-22. Total area of contact area between the probe tip and sample surface decreases with increasing surface roughness.

While the observed relationship between surface roughness and electrical contact resistance was not as initially expected, the electrical contact resistance versus load closely followed the literature, as shown in Figure 4-23. The decrease in resistance with increasing load is in part due to better contact between the two conductive surfaces. In fact, if the load is large enough, small amounts of plastic deformation can occur further increasing the area of electrical contact, and thus decreasing the resistance.

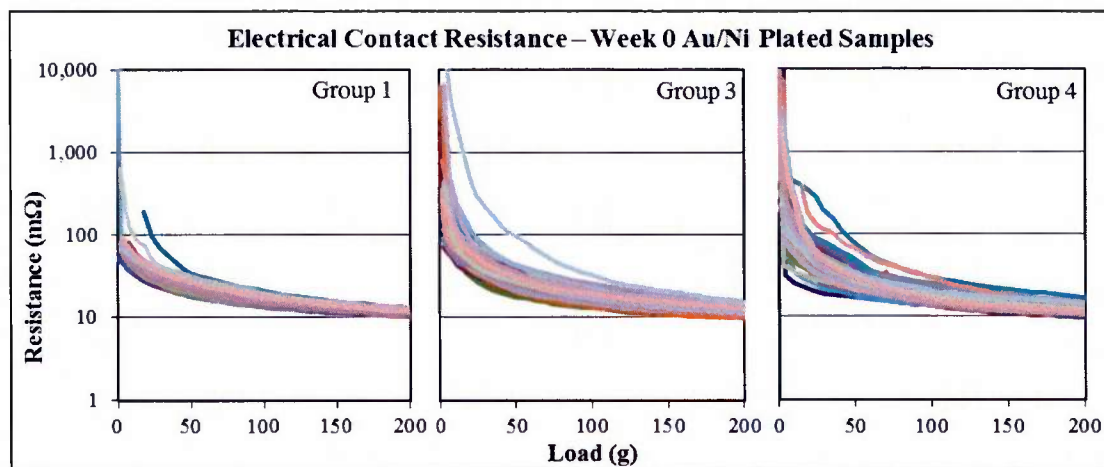


Figure 4-23. Electrical contact resistance data for Week 0 Au/Ni plated Group 1, 3, and 4 samples showing the resistance vs. load relationship.



From Figure 4-23, it is a little easier to see the distribution of the electrical contact resistance for each of the 60 measurements per group. Note that the data is relatively tightly grouped for the Group 1 samples, while more variations (while slight) are observed in the Group 3 and Group 4 Au/Ni plated samples. The variation is likely to be due in part to the surface roughness effects, but also to the presence of the embedded grit in the surface.

The effects of the load can also be observed in Figure 4-24, which reveals that for the as received (Week 0) Au/Ni plated samples, as the load increases, the separation between the Group 1 ECR and the Groups 3 and 4 ECR also decreases. The decrease in separation is potentially due to elastic/plastic deformation of the Au/Ni plated surface as the load increases causing the area of contact for the rougher surfaces to increase.

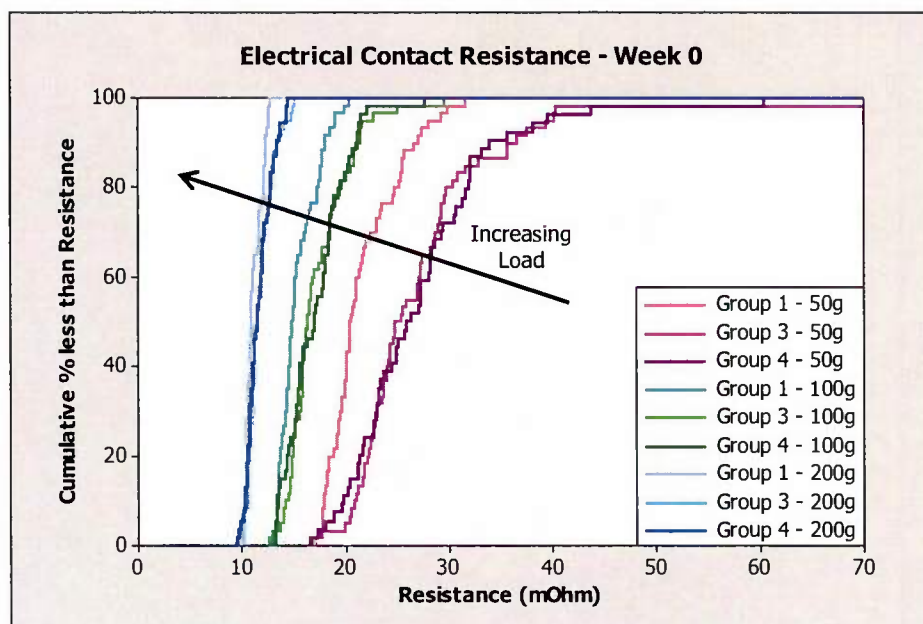


Figure 4-24. Electrical contact resistance data for as received Au/Ni plated Group 1, 3, and 4 samples under various loads. Note that as the load increases for a given sample, the resistance decreases.

Additional investigation of the electrical contact resistance revealed that the ECR values for the unexposed samples increased over time while in the lab waiting for characterization. The bulk of the electrical contact resistance data was collected during two main collection times roughly four months apart. Figure 4-25 shows that the initial data collected for Group 1 and Group 4 Au/Ni plated samples in May/June, as well as the data collected for the same samples four months later in October. A 5 m $\Omega$  shift in the electrical contact resistance was observed. This increase in resistance is most likely due to further aging, as the coupons were stored and analyzed in a lab/office and not in a dry/inert atmosphere.

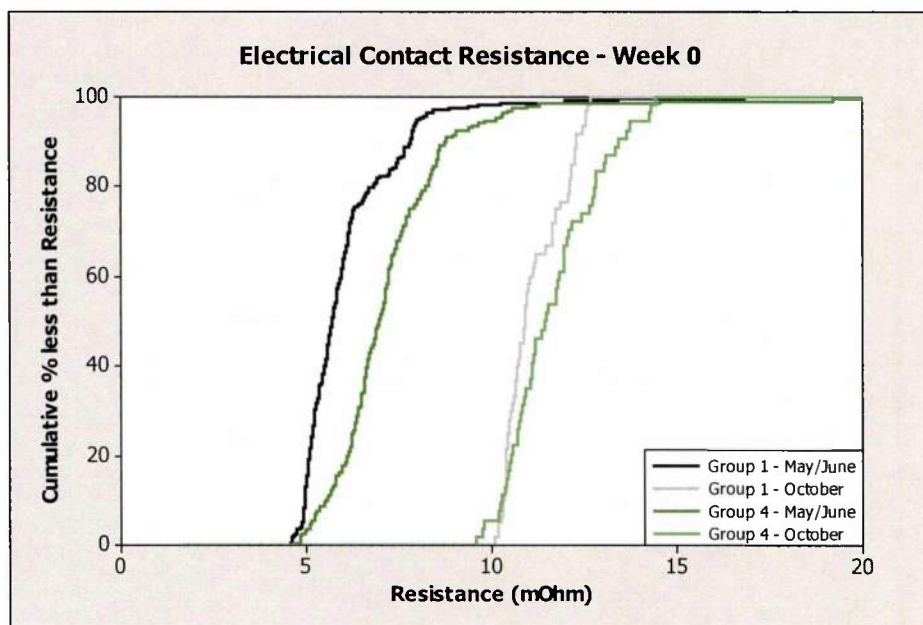


Figure 4-25. Cumulative distribution plot of the electrical contact resistance (ECR) for unexposed, Week 0, Group 1 and Group 4 Au/Ni plated coupons under a load of 200g from the two data collection periods.

#### 4.1.4 Residual Stress

The residual stress in the coatings was determined by x-ray diffraction (XRD) using the  $\sin^2\Psi$  method with the aid of PC Stress software using a modulus of elasticity and a Poisson's ratio of 79 GPa and 0.42, respectively, for gold [65] and 232 GPa and 0.31 for nickel [12, 69]. It should be noted that the residual stress values reported here are not the absolute residual stresses present in the coatings, but differ by a factor (N), defined in Equation 4.2 below, due to the use of the bulk rather than plane specific values for the modulus of elasticity and Poisson's ratio. Residual stress can be calculated via:

$$\sigma_{\phi} = \frac{1}{d_{\phi 0}} \left( \frac{\partial d_{\phi \psi}}{\partial \sin^2 \psi} \right) \left( \frac{E}{1+\nu} \right)_{hkl} \quad (\text{Eq 4.1})$$

where the  $\left( \frac{E}{1+\nu} \right)_{hkl}$  term is a constant. Thus, an expression can be written correlating the plane specific term to one calculated with bulk values as shown in Equation 4.2:

$$N = \left( \frac{E}{1+\nu} \right)_{hkl} / \left( \frac{E}{1+\nu} \right)_{\text{bulk}} \quad (\text{Eq 4.2})$$

The residual stress data from the as received (i.e., Week 0) samples, allow for a better observation of the effects of the surface roughness on the residual stress without the added influence of the various aging environments. Residual stress measurements for the unaged samples were only completed on three samples per panel that were designated as Week 0 samples rather than for the entire panel prior to aging. As such, an assumption was made that the residual stress would be similar across the entire panel. While the residual stress measurements were close for Au/Ni plated Group 3 and 4 samples, Figure 4-26 shows there is a larger degree of variation in the residual stress for the

Group 1 Au/Ni plated samples. Such a variation prevents us from being able to determine more regarding the manner in which the residual stress decreases with surface roughness (i.e., linearly, logarithmic, etc.) with very high degree of confidence from our data alone. Additional investigation is needed to confirm the findings.

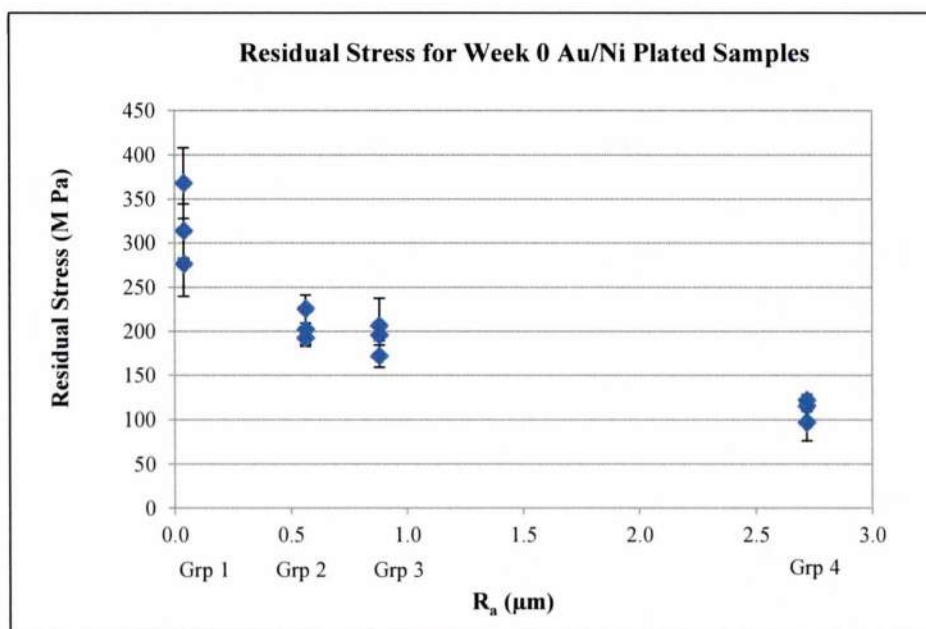


Figure 4-26. Residual stress in the gold coating of the Au/Ni plated samples for each of the four different surface roughness sets without exposure to the aging environments.

Initially, stress relaxation effects were considered as a possible explanation for some of the variability between residual stress measurements within a single roughness group due to the time differences between measurements (Group 1 as received data was collected over the course of two to three months due to the volume of XRD measurements to be completed and the time required per run). However, upon further consideration, it was determined that this was probably not the major contributor to the observed differences, but rather due to variations between the panels themselves. For instance, consider the residual stress data for the Au/Ni plated samples shown in Figure 4-26. While there was a delay between measurements, the data was not collected until roughly four to five

months after the coatings were applied (as many of the measurements for the nickel sputtered and nickel plated samples were completed first), and significant changes due to stress relaxation typically occur within the first month or so after coating, depending on the coating system and the conditions in which the samples are stored [8, 9].

The bulk of the residual stress analysis work completed for this research focused on the Au/Ni plated samples (i.e., residual stress in the gold coating, as subsurface techniques were not utilized to determine the stress of the underlying nickel layer). This is in part due to the amount of uncertainty/standard deviations associated with the residual stress calculations for the nickel sputtered and plated coatings (as seen in Figure 4-27 and Figure 4-28).

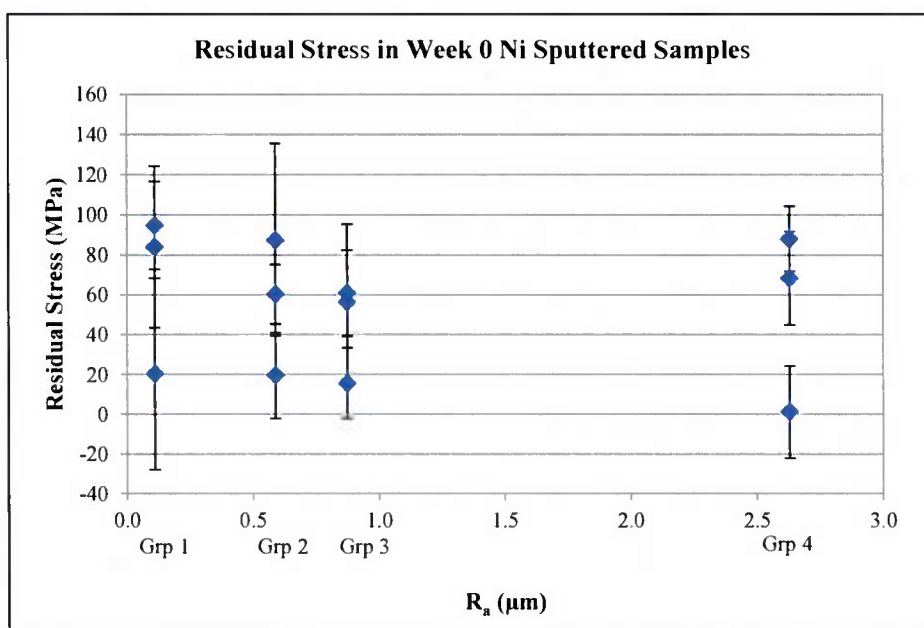


Figure 4-27. Residual stress in the Ni sputtered coating for each of the four different surface roughness sets without exposure to the aging environments (i.e., Week 0/as received samples). Samples show increased standard deviations.



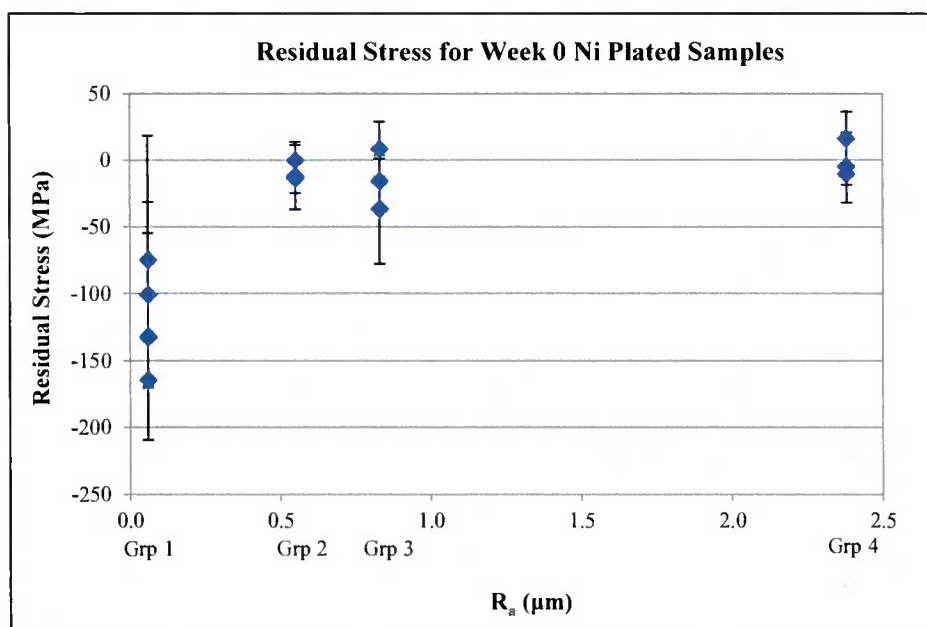


Figure 4-28. Residual stress in the Ni plated coating for each of the four different surface roughness sets without exposure to the aging environments (i.e., Week 0/as received samples).

There are several possible sources of error associated with the XRD measurements/ residual stress calculations, including sample setup, data analysis (i.e., peak location identification), and texturing (preferred orientation) in the sample. When setting up the sample for a XRD data collection run, one of the most important steps is to set the height location of the surface to be examined. Deviations in the location of the surface can cause variations in the resulting XRD data. Once the raw XRD spectra have been collected, errors can be introduced during data analysis. Typically a software program (such as PC Stress) is utilized to identify the peak locations; however, some of the older versions of such software can occasionally have difficulty distinguishing between overlapping peaks when working in their automatic identification mode. In addition, certain aspects of the sample itself can cause errors. For instance, the presence of extensive texturing, as observed in some of the Ni sputtered samples (see Figure 4-29), can cause errors in the residual stress calculations.

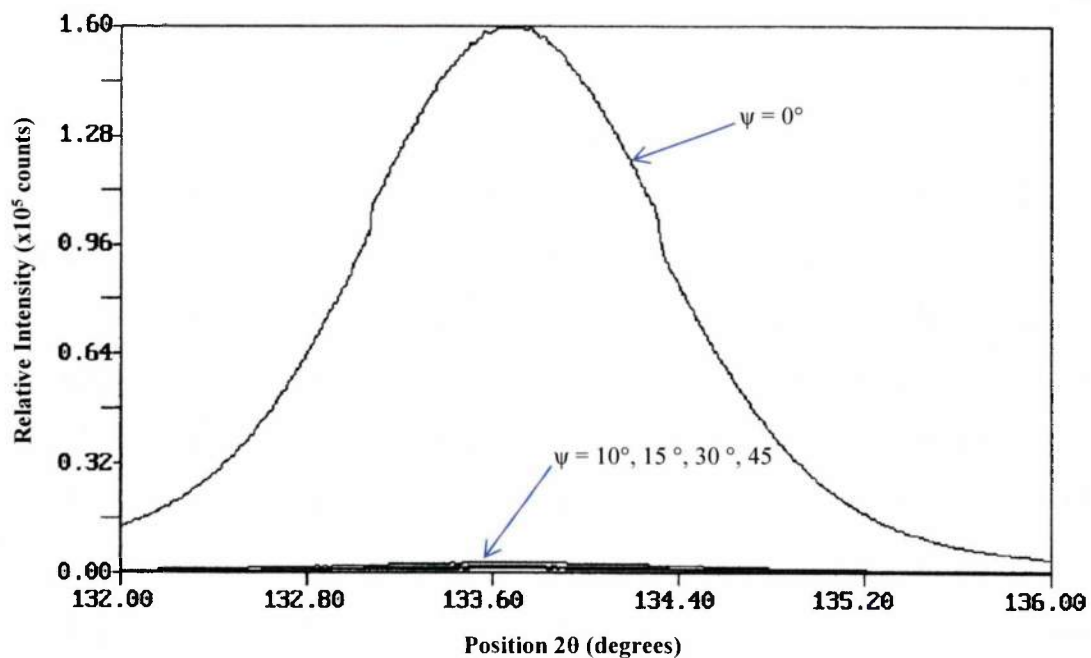


Figure 4-29. Raw XRD data for Ni sputter coated sample #1 on panel N23 depicting the texturing present (i.e., note that the intensity for the  $\psi = 0^\circ$  peak is drastically higher than for the other  $\psi$  angles).

Variations in coating depositions parameters can also cause variations in residual stress data. The Ni sputtered samples were coated in three separate depositions runs one of which (deposition run #2), produced samples with higher average surface roughnesses as compared to the panels from the other two runs (Table 4-2). As with the surface roughness, the samples from the second sputter deposition run also display a significant difference in residual stress value as compared to the rest of the Ni sputtered samples, see Figure 4-30. For the Ni sputtered samples, the residual stress data appear to be relatively consistent within an individual deposition run, but with some variation between runs (particularly for Run #2 due to a higher deposition pressure).

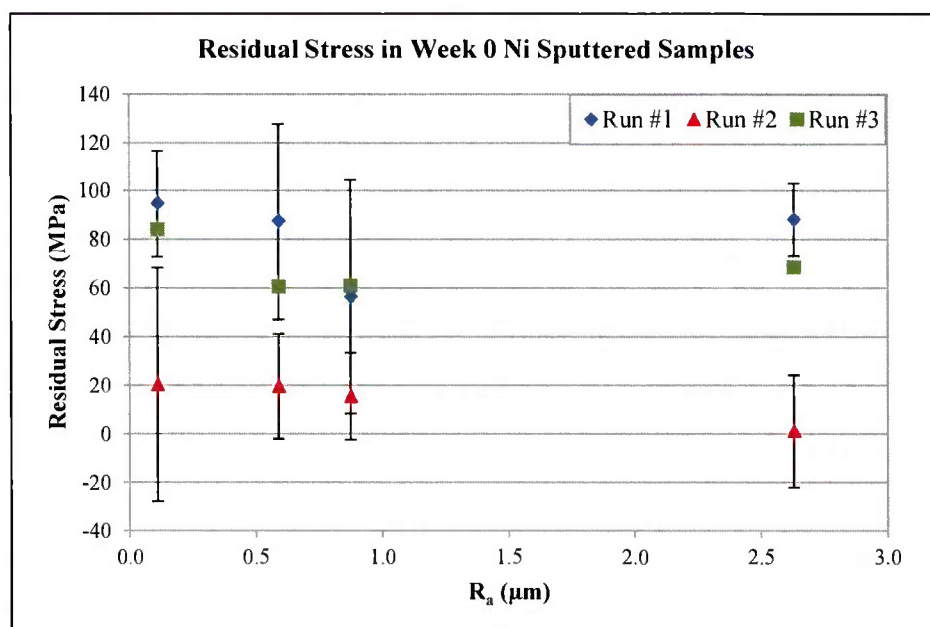


Figure 4-30. Residual stress in the Week 0 (as received) Ni sputtered samples separated based on the deposition run (i.e., Run #1, #2, or #3).

While the uncertainty may prevent a more quantitative look at the effects of surface roughness and aging on the residual stress in the Ni plated coatings, general differences (i.e., compressive versus tensile stresses) based on the deposition techniques and/or coating materials can still be observed. For instance, from Figure 4-31 it can be observed that the residual stress in the nickel coating for the Ni plated samples is compressive for the Group 1 samples and nearly unstressed for Groups 2, 3, and 4 Ni plated samples, while the residual stress in the gold for the Au/Ni plated samples is tensile. In addition, for the Ni sputtered samples, the samples in Run #2 appear to be nearly unstressed, while the other Ni sputtered samples have a slightly tensile residual stress present in the coating. The tensile nature of the stress is potentially due to the trace amount of argon revealed in the coating via EDS.

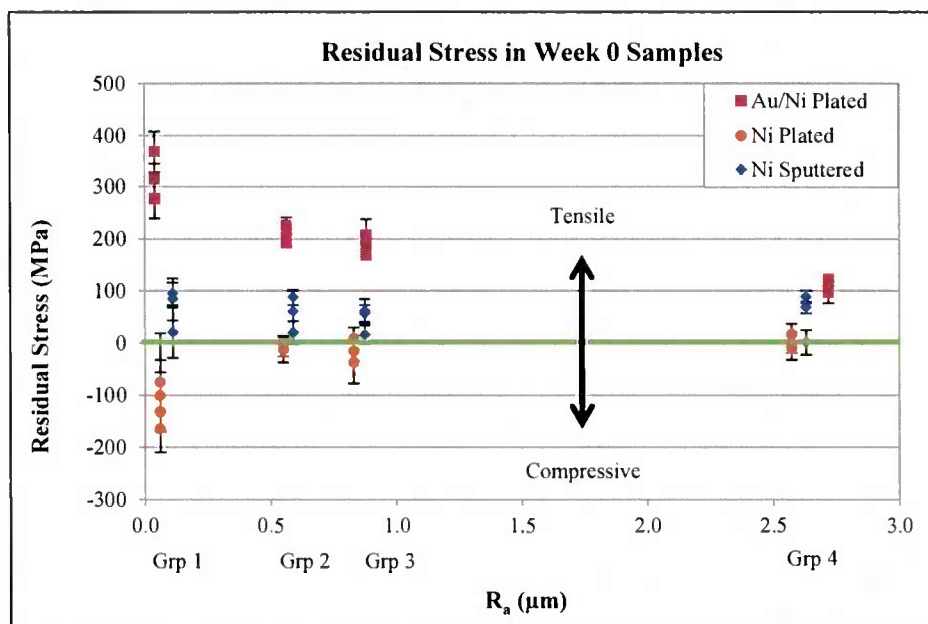


Figure 4-31. Residual stress in the Week 0 (as received) Ni and Au/Ni plated samples. Note that the residual stresses reported for the Au/Ni plated samples are for the Au layer, not the Ni underlayer.

It can be observed from Figure 4-31 that for the Ni plated coupons, the residual stress in nickel becomes less compressive with increasing surface roughness while the reverse is true for the gold coating of the Au/Ni plated coupons. In both cases, regardless of the type of stress, i.e., compressive versus tensile, the magnitude of the stress decreases with increasing surface roughness. The change in residual stress magnitude with surface roughness is based on the amount of interfacial contact area present. Increased contact areas have lower stress levels versus surfaces with little contact area. In contrast, from Figure 4-30 and Figure 4-31 it appears that the substrate surface roughness has little to no effect on the residual stresses in the Ni sputtered coupons. This is primarily the result of the sputtering processing parameters contributing more towards the value of the residual stress than the substrate surface roughness.

Di Bari states that the residual stress in electroplated nickel typically varies from roughly 0-185 MPa (tensile), depending on the plating conditions (such as bath composition) with most compressive stresses arising from sulfur contamination in the coating [32]. The residual stress values

reported for this research for the as received Ni plated samples correspond with the lower end of the stress values Di Bari lists with Groups 2, 3, and 4 Ni plated samples having residual stress values at approximately 0 MPa (i.e., stress free), though with more of a compressive tendency rather than tensile. This fact, along with the compressive stresses observed in the Group 1 Ni plated samples, suggests that sulfur may have been co-deposited to some degree. Additional investigation for the Ni plated samples would be needed to confirm. Di Bari does not provide the surface roughness values for the Ni plated samples associated with his work, which prevents more direct comparisons of the residual stress for nickel plating (see Figure 4-32 below).

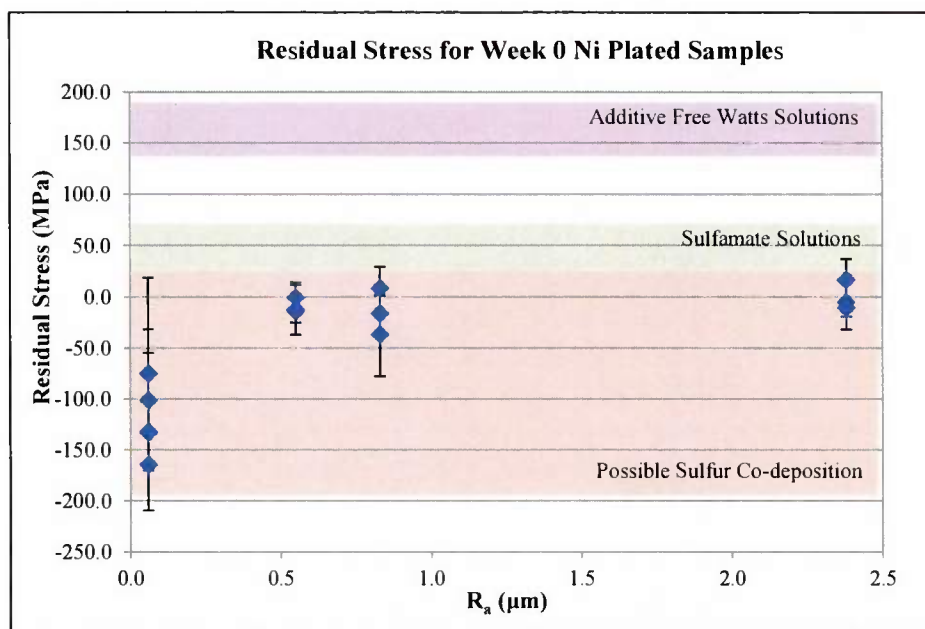


Figure 4-32. Residual stress for the Week 0 (as received) Ni plated samples including typical stress values reported by Di Bari [32] based on electroplating bath type and presence of co-deposited sulfur.

#### 4.1.5 As Received Results Summary

Below is a brief summary of the findings from the characterization of the as received samples.



- Optical profilometry data showed that the coatings exhibited no significant leveling effects, i.e., the surface roughness before and after coating is approximately constant.
- Optical/SEM imaging revealed the presence of embedded grit remaining from the surface preparation, particularly for the Group 3 and 4 samples. EDS data confirmed the grit as being alumina and/or silicon carbide.
- Cross sections showed that the nickel layer thickness in the Au/Ni plated samples was nearly half of the targeted thickness for the Group 3 and 4 samples. In addition, the Ni sputtered coating was nearly 1.5 times thicker than the targeted thickness for the Group 1 samples.
- The ECR of the Au/Ni plated samples decreased with increasing surface roughness due to decreasing area of contact with the rougher surfaces, with Group 3 and 4 ECR data as nearly identical.
- The magnitude and type of residual stress present depended on the coating material/process as well as the surface roughness/amount of interfacial area.
  - The residual stress in the gold of the Au/Ni plated samples was tensile, with the magnitude decreasing with increasing surface roughness.
  - The residual stress in the Ni plated samples was compressive for the Group 1 samples and nearly stress free for Groups 2, 3, and 4.
  - The residual stress in the Ni sputtered coatings is tensile, though approximately constant regardless of the surface roughness.

## **4.2 Characterization of Environmentally Exposed/Aged Coated Samples (Week 3, 6, 9)**

After coupons were exposed to their respective environments for three, six, or nine weeks, data was collected to be compared with the as received results to determine what sort of changes occurred based on aging time and environment (MFG, TC, or TRH).

### **4.2.1 MFG Aged Samples**

#### *4.2.1.1 Surface Morphology*

Even after only three weeks of aging, noticeable changes in the surface could easily be identified by visual inspection for the Au/Ni plated MFG samples, such as clusters of corrosion sites and changes in color on the surface. Figure 4-33 shows a few of the MFG samples before exposure and after the full nine weeks of aging. Upon closer inspection via SEM, the corrosion sites were further analyzed. Figure 4-34 presents SEM images showing the differences between the unaged and aged MFG samples, as well as a few of the corrosion sites from each of the roughness groups. Samples from Groups 1 through 3 all exhibit corrosion site structures like those found and described in similar experiments [6, 13], i.e., with a corrosion bloom and a halo of corrosion product surrounding it. However, no noticeable/distinct bloom and halo corrosion site formations were found during SEM surface imaging of the Group 4 samples. Instead, smaller clusters of corrosion product were found across the surface of the Group 4 samples, such as that shown in Figure 4-34. Figure 4-34 also demonstrates how distinguishing corrosion sites/products become increasingly difficult with increasing surface roughness.

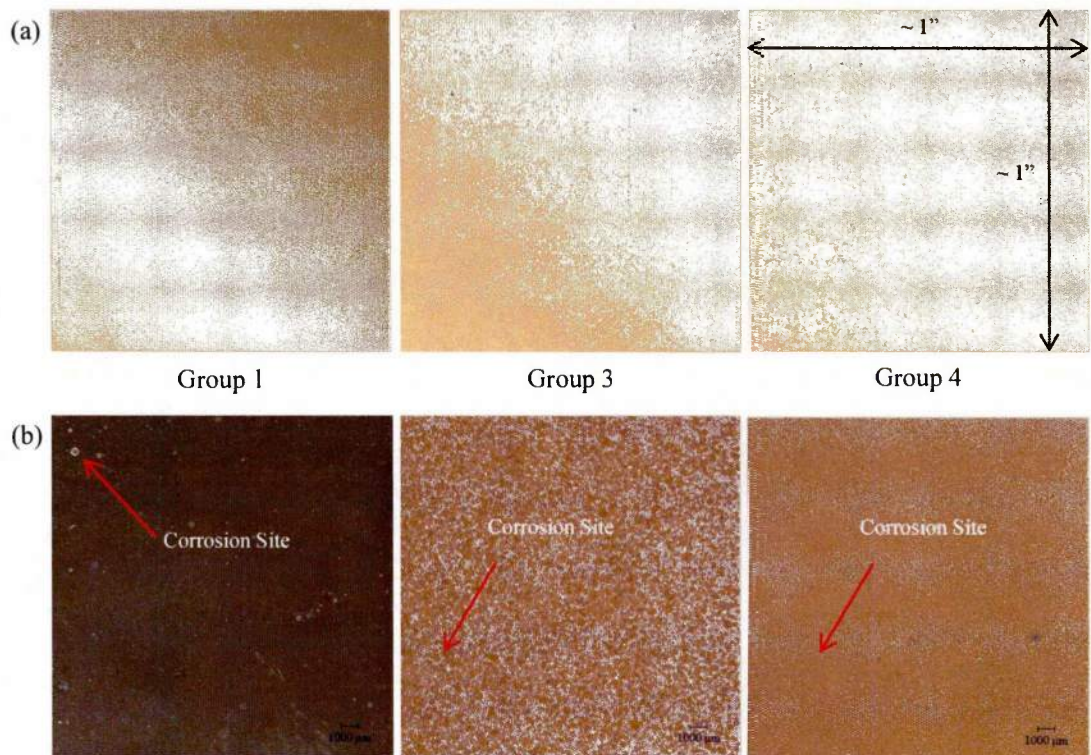


Figure 4-33. (a) Digital images of as received Groups 1, 3, and 4 samples and (b) Optical images of MFG Week 9 samples for Groups 1, 3, and 4 showing easily identifiable changes in the surface with aging, including corrosion sites and changes in observed surface color.



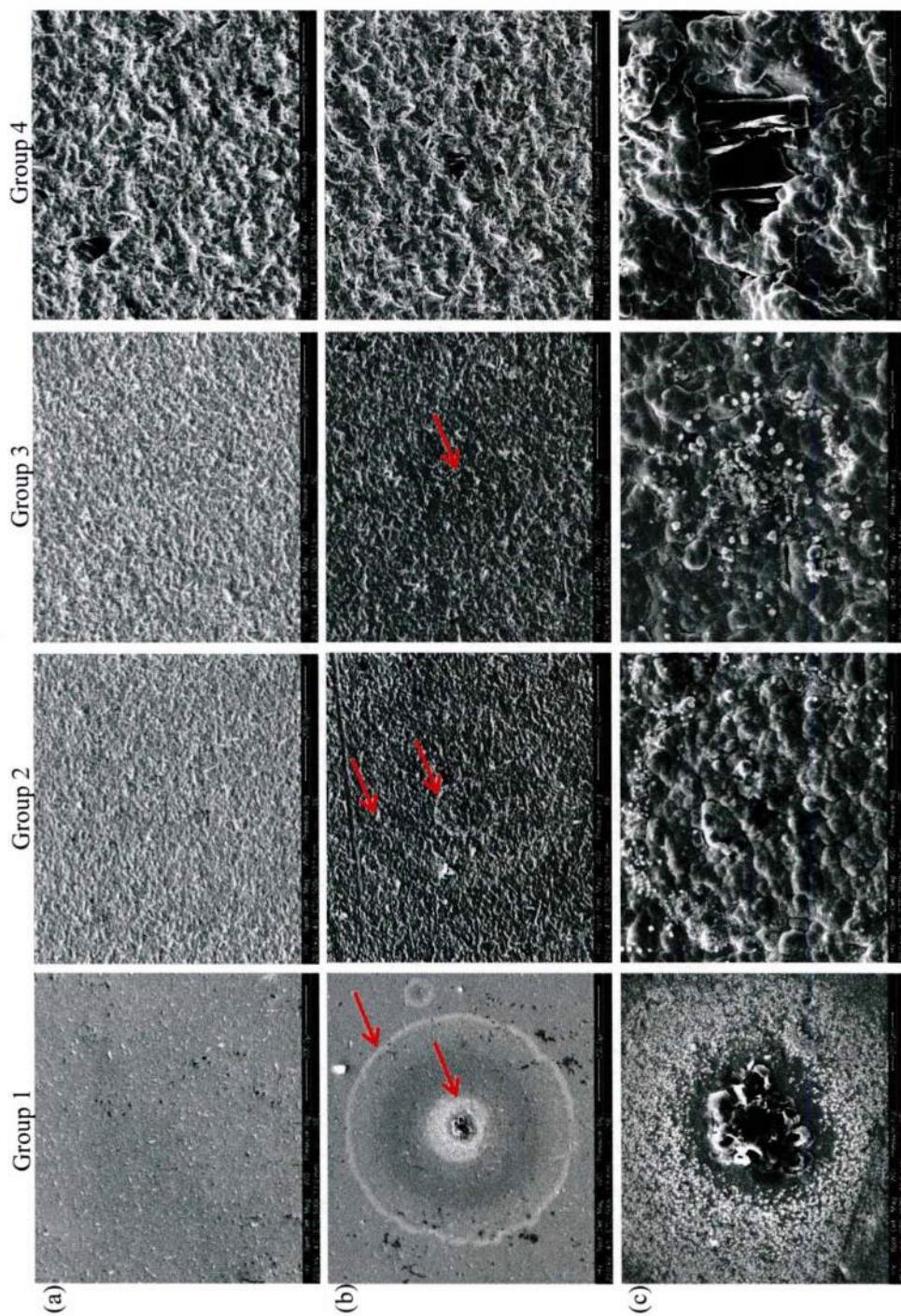


Figure 4-34. (a) SEM images of MFG Week 0 samples (Groups 1 through 4 going from left to right) at, (b) SEM images at the same magnification but after nine weeks of aging to show corrosion sites/product on the surface, and (c) SEM images of areas shown in (b) but at a higher magnification to allow a closer view of the corrosion sites/product on the surface.

Unlike the Au/Ni plated coupons, the same corrosion bloom/halo formation was not as visibly apparent in the Ni plated and Ni sputtered samples except for a few isolated exceptions shown in Figure 4-35 and Figure 4-36. It would be expected that the Ni samples would have undergone a larger extent of corrosion without a noble gold layer to act as a barrier between the environment and the more active nickel and copper. EDS confirmed that the surface of the samples is covered with nickel oxide, but little corrosion of the underlying copper layer was observed.

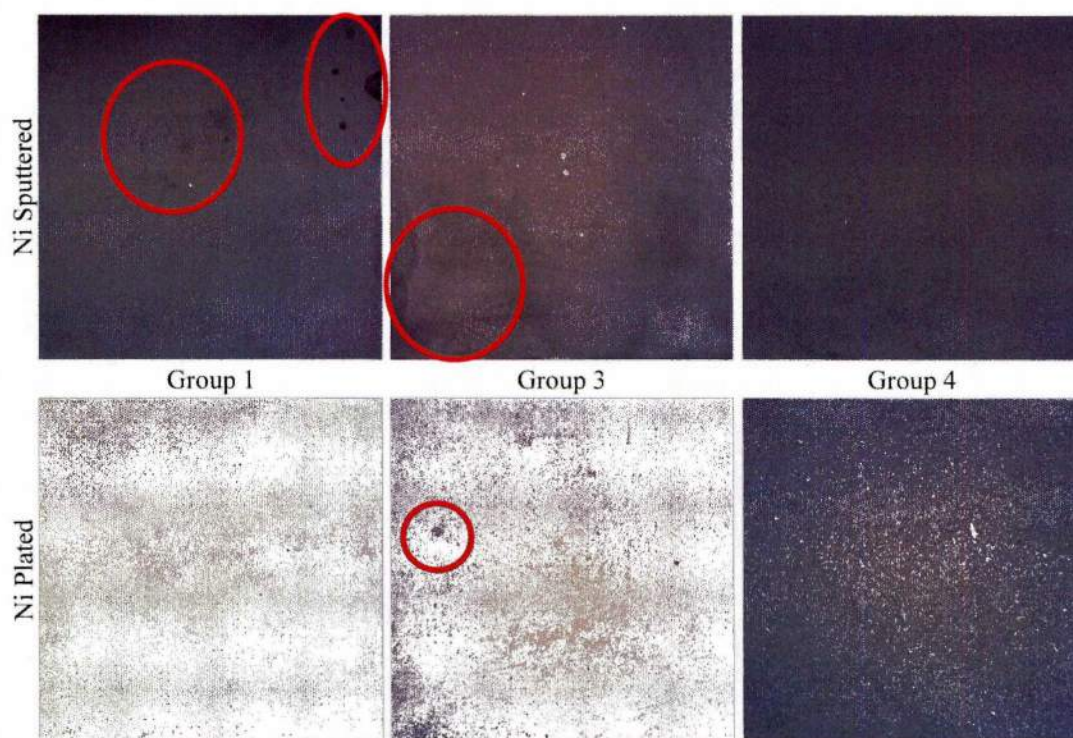


Figure 4-35. Optical images for Ni plated and Ni sputtered coupons after nine weeks of MFG aging. The majority of the sample surfaces do not appear to show signs of corrosion/ changes in the surface with a few exceptions.



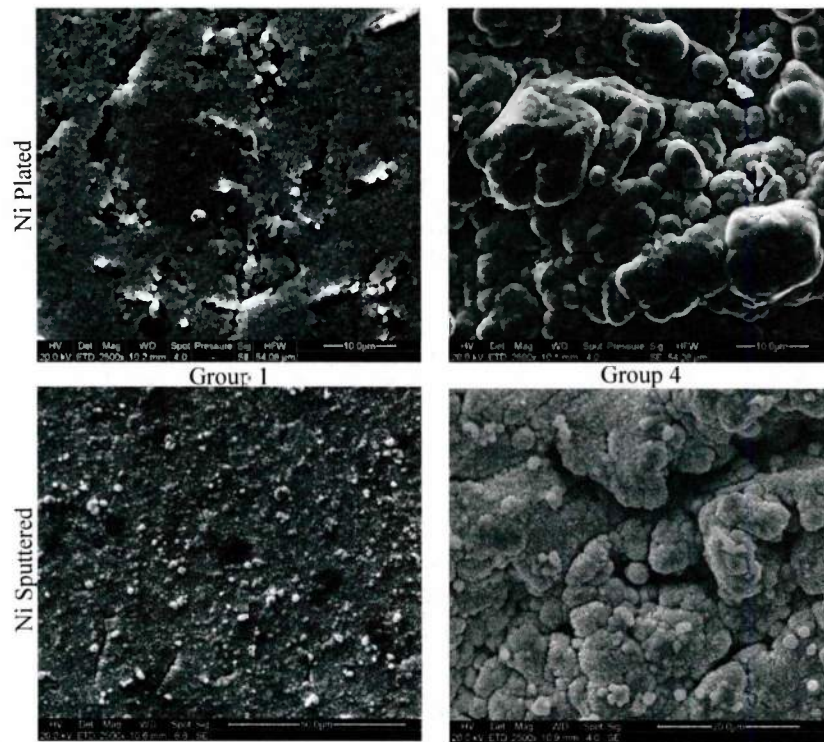


Figure 4-36. SEM images of the Ni plated and Ni sputtered Week 9 MFG samples showing the differences in the coating morphology based on the coating process and surface roughness.

Optical profilometry completed after environmental exposure showed a slight increase in roughness for the Group 1 samples, as expected with the formation of the corrosion sites, while the Group 3 and 4 samples remained approximately the same or decreased in roughness, as shown in Figure 4-37. The apparent decrease in roughness could potentially be the result of the corrosion blooms and products “filling” the surface and making it appear to be less. Since the corrosion products/blooms are relatively small in comparison to the size of the surface features, especially for the Group 4 samples, it is more likely that the apparent decrease in roughness not statistically significant as the change in surface roughness falls within the standard deviation associated with the initial roughness measurements.

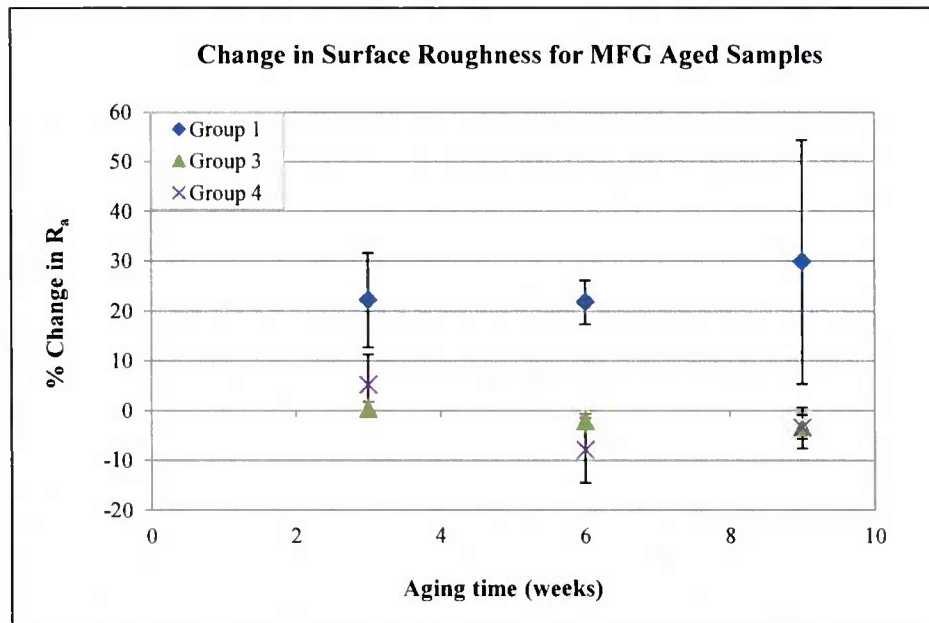


Figure 4-37. Optical profilometry data for MFG aged Au/Ni plated coupons depicting the percent change in the  $R_a$  surface roughness from the unaged (Week 0) condition.

#### 4.2.1.2 Corrosion Sites

Au/Ni plated electrical contacts in atmospheric corrosion environments (such as Battelle Class II) typically corrode via a pore corrosion mechanism with various copper oxide and copper sulfide corrosion products. SEM/EDS mapping of several corrosion sites confirmed that the primary corrosion products observed on the Au/Ni plated samples in this research are also copper oxides and copper sulfides (see example in Figure 4-38).

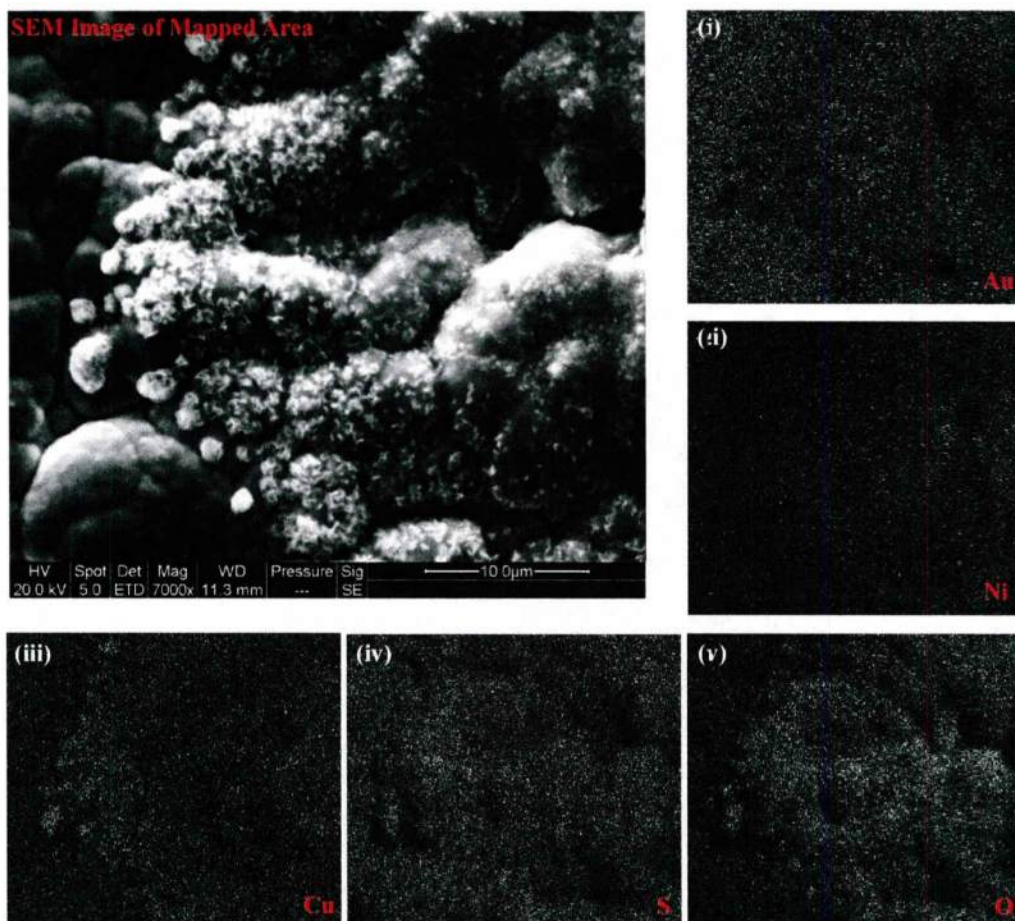


Figure 4-38. SEM image of part of the product halo around a corrosion site on a Au/Ni plated sample after aging in the MFG environment. EDS mapping was completed to show the presence of (i) gold, (ii) nickel, (iii) copper, (iv) sulfur, and (v) oxygen in the corrosion products. Note that in the EDS maps, white is used to represent where a particular element is present (relative concentration) while everything else remains black.

Corrosion site density data was collected using Clemex Analytical software. It becomes increasingly difficult to distinguish corrosion sites/defects with increasing surface roughness. As such, no corrosion site density data was collected for the Group 4 samples. The data collected for Groups 1 and 3 is better described as the percent area of the surface covered in corrosion sites/products, as the software could not distinguish between overlapping corrosion sites/product halos. Figure 4-39 shows an example of how the area percent was determined with Clemex and results for Group 1 and 3 are listed in Table 4-4.



The standard deviation for the percent area covered by corrosion for the Group 1 samples appears to be rather higher, since the corrosion sites occur where there are defects in the coating, and not necessarily uniformly across the surface. As such, some areas have multiple corrosion sites clustered together while other regions may not have any corrosion sites. Figure 4-39 depicts the process followed, however that is only for one image. A total of 20 images were taken randomly across the surface, analyzed, and averaged to obtain the data presented in Table 4-4. No data was collected for the percent area covered by corrosion for the Group 4 samples as it was too difficult to distinguish between the base surface roughness and the corrosion product in the optical images.

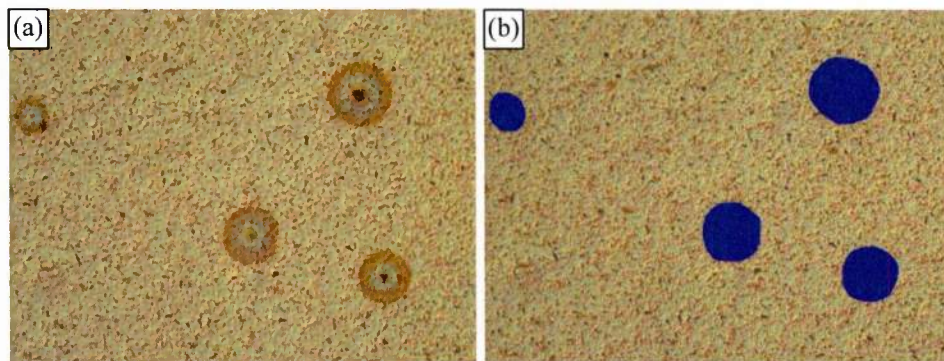


Figure 4-39. (a) Optical image of a region on a Group 1 Au/Ni plated MFG Week 9 aged coupon and (b) optical image of region with corrosion sites/product halos highlighted in Clemex. The area of the highlighted regions was compared to the total area of the image in Clemex in order to determine the percent area covered by corrosion sites/products.

Table 4-4. Summary of Clemex results regarding the area of the sample surface covered by visibly distinguishable corrosion products.

Group	%Area Covered by Corrosion
1	10 ± 12
4	56 ± 7
4	----

Higher standard deviations can also be attributed to the fact that the size of individual sites (bloom + halo) varies depending on where it is in its life cycle. Not all corrosion sites will “activate” at the same time. As the sites become active and corrosion product is formed, the product halo will expand. Eventually the sites will die (i.e., they are no longer actively corroding) [6]. Thus, for samples that have the same number of corrosion sites, the area covered by corrosion product can vary. This concept may be more easily observed by comparing the size of the corrosion sites after various weeks of aging (i.e., Week 3 vs. Week 6 vs. Week 9), see Figure 4-40.

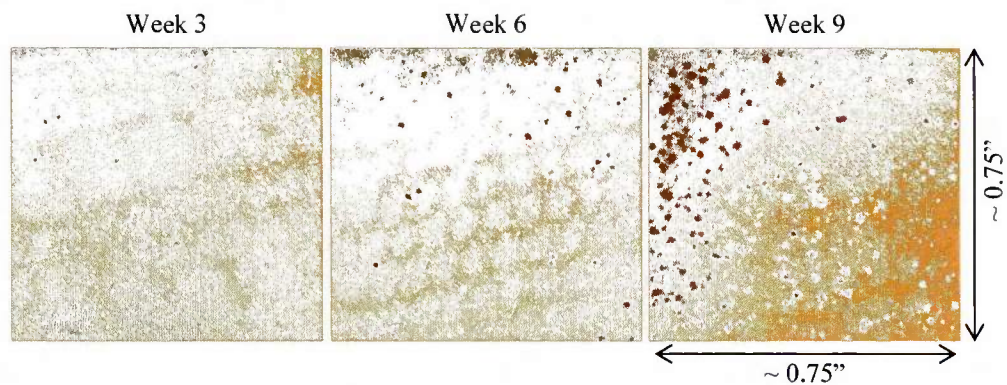


Figure 4-40. Optical images of Group 1 Au/Ni plated MFG coupons after three, six, and nine weeks of aging, respectively. Note that the corrosion sites are not necessarily uniformly distributed over the surface and that they are not all the same size.

The Clemex analysis also allows for a more quantitative comparison between Groups 1 and 3 in terms of the amount of corrosion product present. From Table 4-4, it should be noted that the percent area of the Group 3 samples covered by corrosion product is roughly five to six times that of the Group 1 samples. The significant increase in area covered by corrosion products in the Group 3 samples is likely due to the increased amount of porosity/defects in the coatings associated with the increased roughness, embedded grit, and thinner coatings. Additional analysis would need to be completed if the corrosion density (i.e., number of sites/area), rather than just percent area covered



could be compared. Due to overlapping halos of corrosion product, this data could not be collect via Clemex in a timely fashion.

#### 4.2.1.3 Residual Stress

From the corrosion site level, Enos comments on how the residual stress in the gold first becomes more tensile as the corrosion product formation under the gold coating forms a blister, pushing up on the gold layer, and then reduces in magnitude as the gold cracks and the blister collapses [6]. We can see the evidence of this process, as shown in Figure 4-41, though it is not completely reflected in the XRD residual stress measurements for all samples. Figure 4-42 shows the residual stress data for the Au/Ni plated samples at Week 0, 3, 6, and 9. For Group 1 and 2 samples we can see a slight decrease in the residual stress with aging while the Group 4 samples maintain an approximately constant residual stress level.

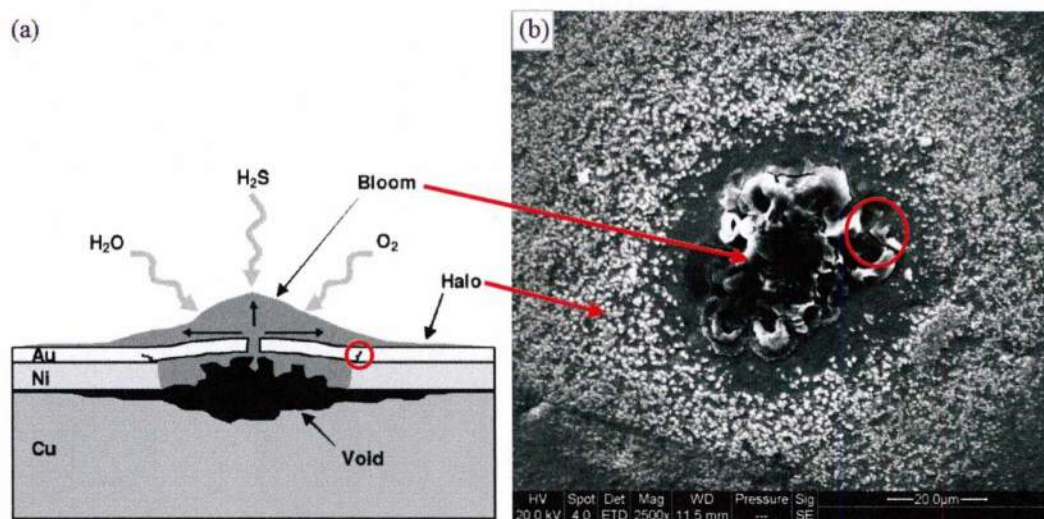


Figure 4-41. (a) Depiction of a corrosion site for atmospheric degradation in a nickel and gold plated copper system (Source: Enos [6]) and (b) SEM surface image of a corrosion site on a Group 1 MFG sample exhibiting the same general components as those found in the literature including the corrosion product bloom and halo, as well as the cracks in the gold layer.

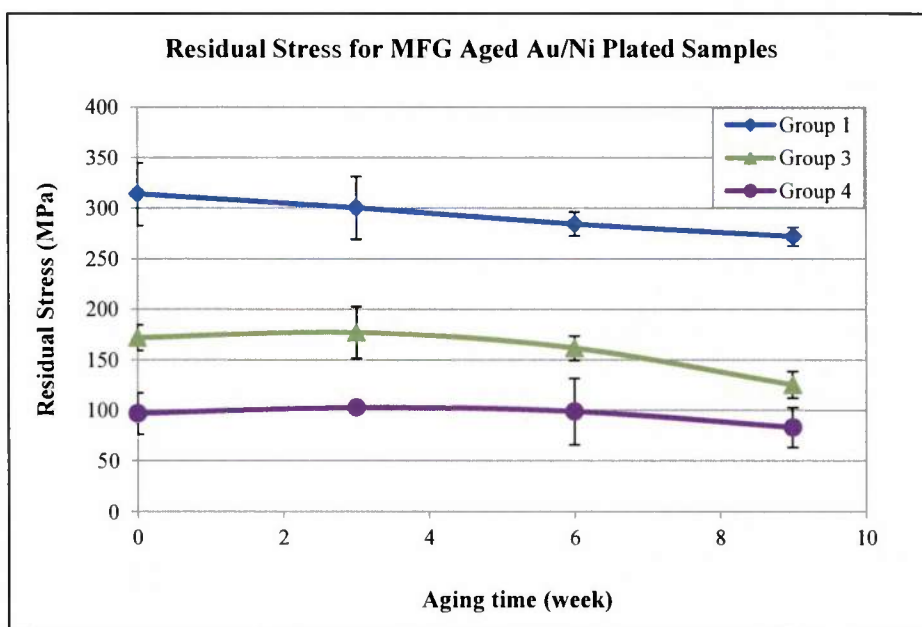


Figure 4-42. Residual stress in the gold coating for each of the atmospheric corrosion/mixed flowing gas (MFG) sample sets. Each point represents the averaged residual stress from the three duplicate samples.

The expected increase in tensile residual stress at the beginning of the pore corrosion process was not observed. As not all of the corrosion sites become active at the same time, it is likely that at the time XRD was performed, some of the sites were going through the initial stages exhibiting increased tensile stresses, while other sites were further along in development. The presence of sites at various stages of development could cause a cancellation effect when looking at the average residual stress levels across a larger section of the surface. In addition, the corrosion sites occur on such a localized scale in comparison to the area observed during XRD. As such, in order to capture the initial increase in tensile stress in the gold coating, XRD residual stress data may need to be collected more often, particularly towards the beginning of the aging study, and potentially over a smaller area.

#### 4.2.1.4 Electrical Contact Resistance

As expected from the literature, an increase in the electrical contact resistance was observed with aging due to the presence of the corrosion sites/products on the surface, as shown in Figure 4-43. While Group 2 and Group 3 are similar in roughness and may be expected to behave similarly, the Group 2 samples exhibited a substantially increased extent of corrosion as compared to any of the other groups. This may be due to some effect of the double processing of the samples during the sample preparation steps, but additional analysis will need to be completed to confirm this. As such, this research focuses on Groups 1, 3, and 4 with additional analysis of the Group 2 samples completed with future work.

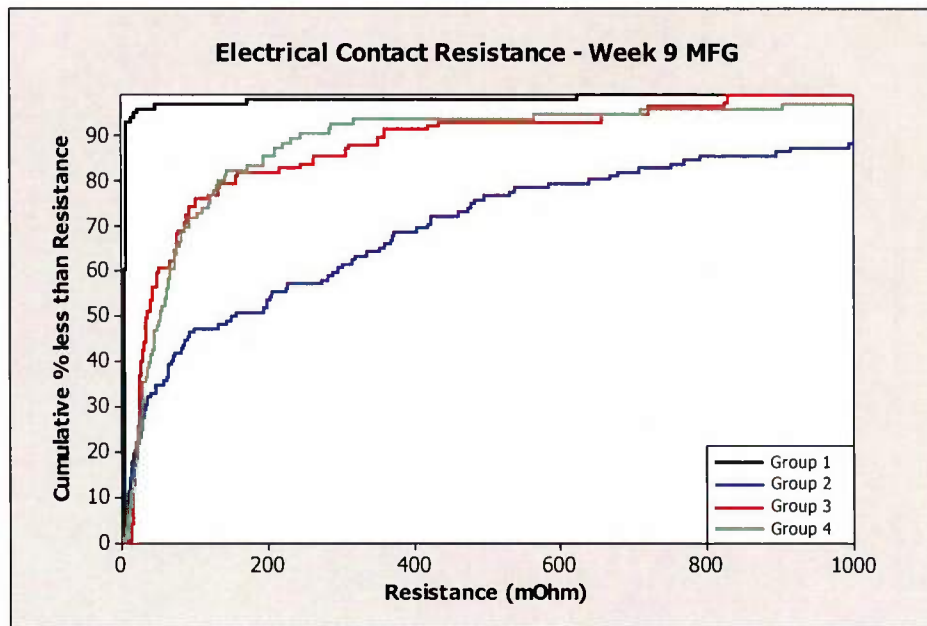


Figure 4-43. Electrical contact resistance data under a 200g load for the Au/Ni plated samples (Groups 1, 2, 3, and 4) after nine weeks of exposure to the Battelle Class II environment (MFG).

From Figure 4-44 it can be observed that the majority of the corrosion occurred within the first three weeks of aging for the Group 1 Au/Ni plated MFG samples as the electrical contact resistance data after three and nine weeks of aging are very close. In comparison, Figure 4-45 and Figure 4-46 shows that most of the corrosion for the Group 2 and 4 Au/Ni plated MFG samples occurred sometime between Week 3 and Week 9.

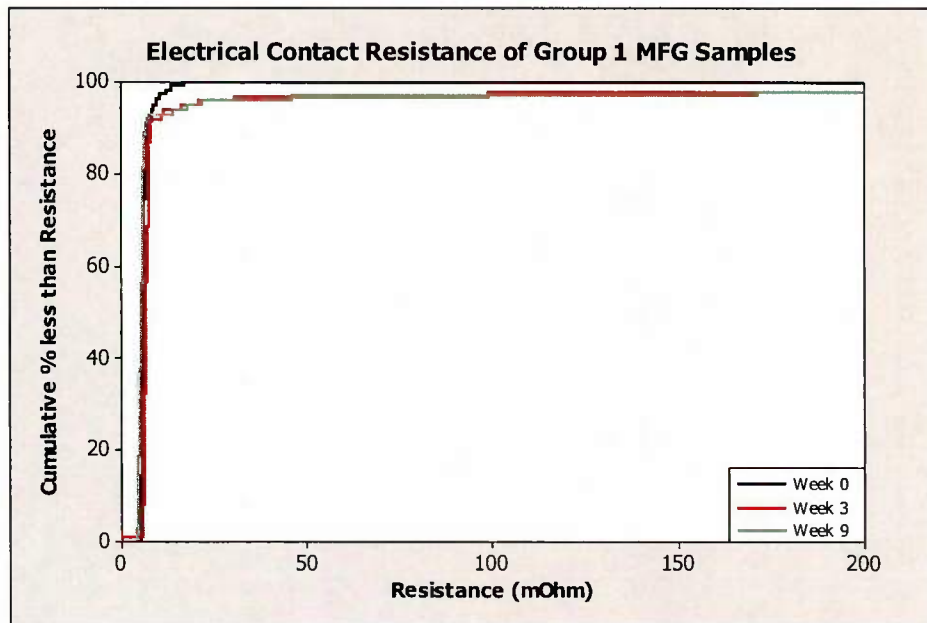


Figure 4-44. Electrical contact resistance data under a 200g load for the Au/Ni plated Group 1 samples as a function of aging time in the MFG environment.

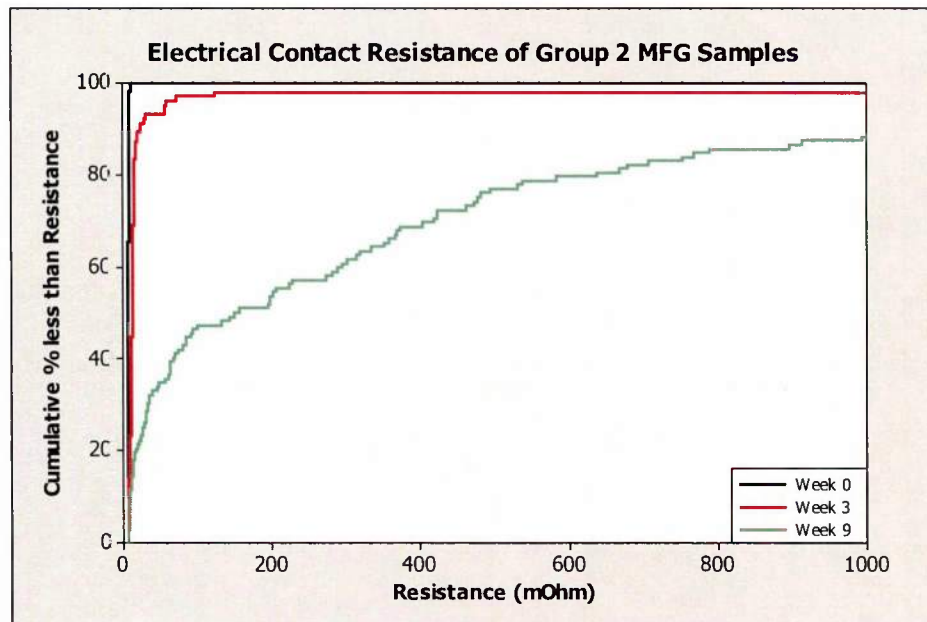


Figure 4-45. Electrical contact resistance data under a 200g load for the Au/Ni plated Group 2 samples as a function of aging time in the MFG environment.

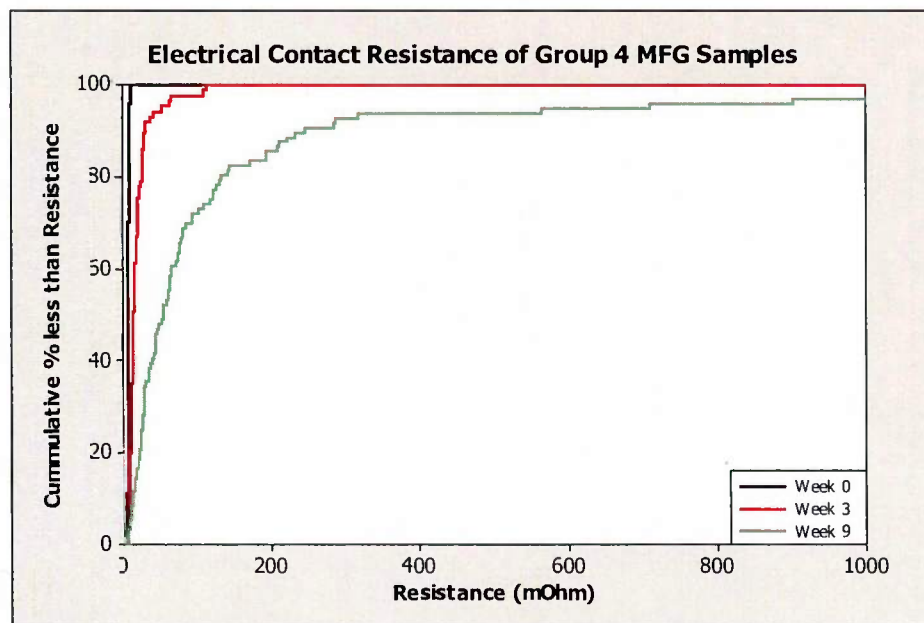


Figure 4-46. Electrical contact resistance data under a 200g load for the Au/Ni plated Group 4 samples as a function of aging time in the MFG environment.



The data collected from this research can be compared to similar experiments completed at Sandia National Laboratories (SNL) as shown in Figure 4-47. The current research results vary from the reported SNL data due to the fact that slightly different surface roughnesses were prepared for the initial samples, different coating thicknesses of gold plating, and the fact that the SNL data shown is for a Au plated sample with no Ni underlayer.

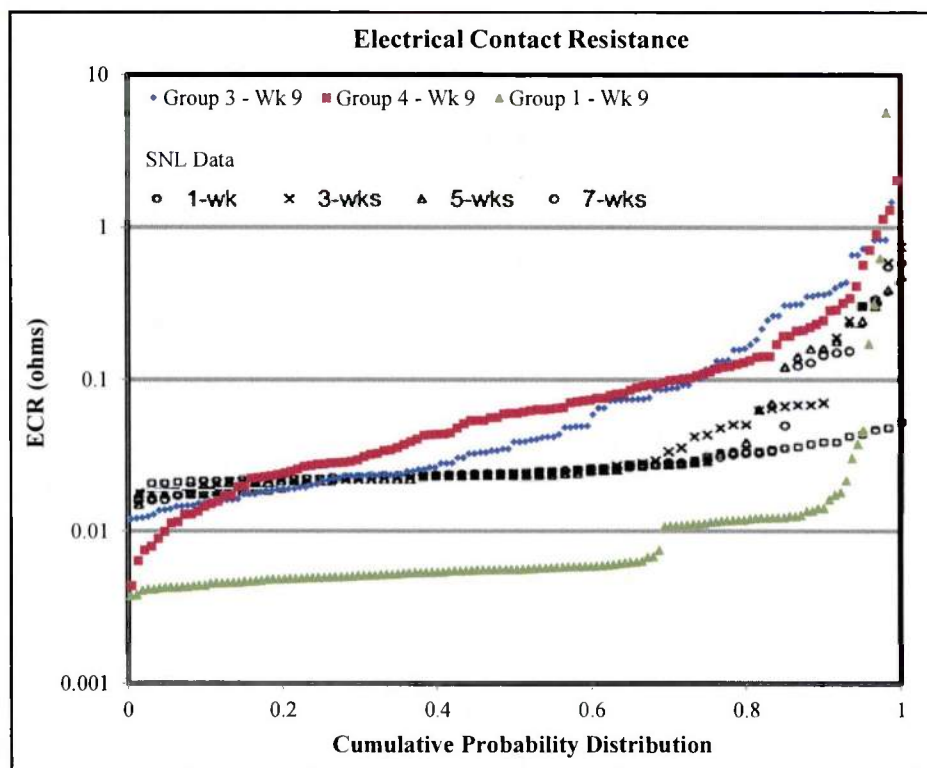


Figure 4-47. Electrical contact resistance data comparison between current research and data from Sandia (SNL). Source: Moffat et al. [52]. Note that the SNL data is for a Au plated copper sample with no Ni underlayer, thus the values vary to a degree.

In contrast to the Au/Ni plated samples, the Ni sputtered samples exposed to the MFG environment did not exhibit the same localized type of corrosion and change in electrical contact resistance. Instead, the absence of the a noble metal top plate allowed for the entire nickel surface to

react causing the observed changes in the electrical contact resistance to be more uniform across the surface, as shown in Figure 4-48.

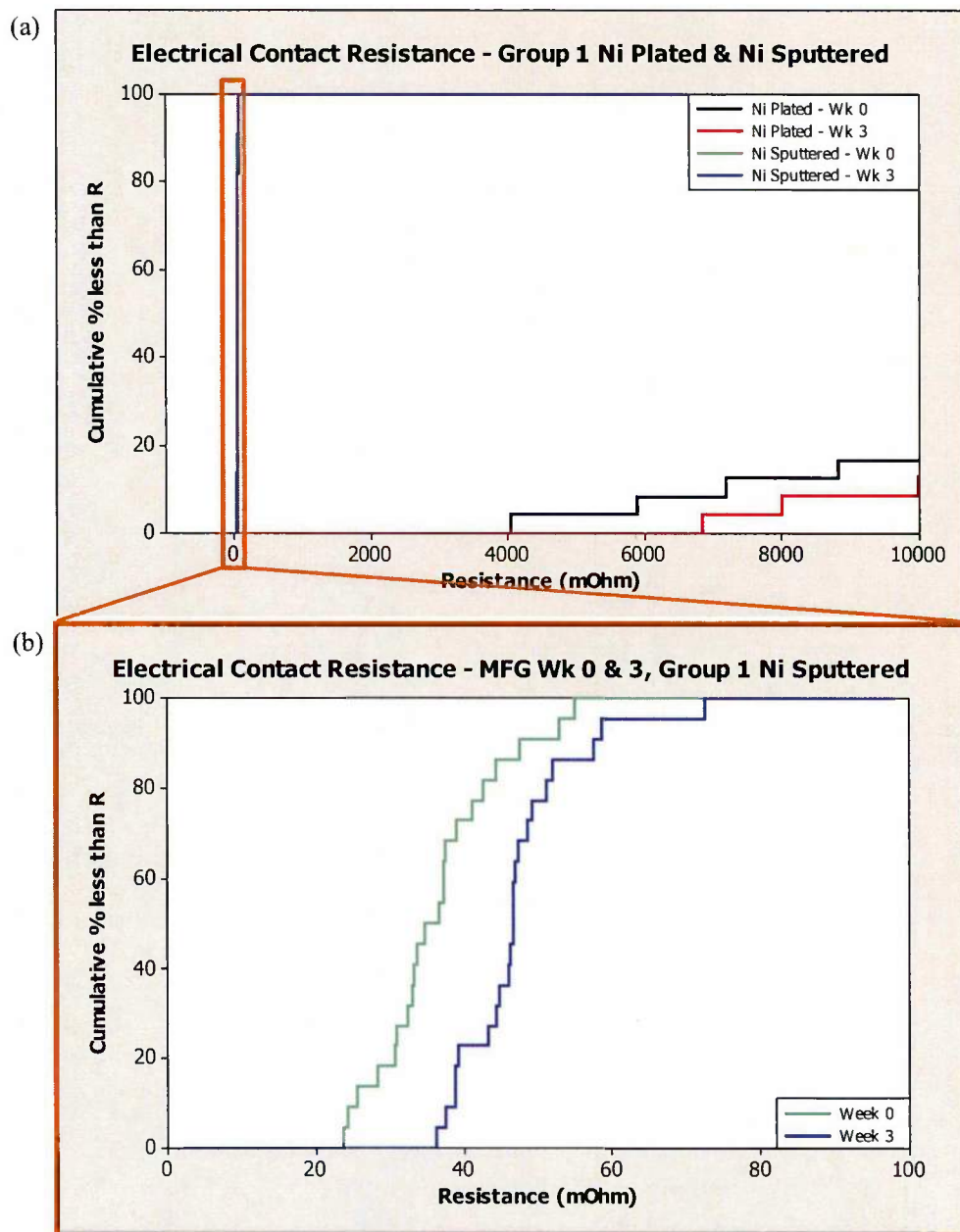


Figure 4-48. (a) Electrical contact resistance data for Ni plated and Ni sputtered Group 1 Week 0 and Week 3 samples and (b) close-up of (a) providing a better depiction of the changes in the electrical contact resistance for the Ni sputtered samples.

#### 4.2.2 Elevated Temperature and Relative Humidity (TRH) Aged Samples

The elevated temperature and relative humidity environment is the least aggressive of the three aging environments studied. Based on this fact, along with the knowledge that gold is very corrosion resistant, it was expected that there would not be a large change with aging in the elevated temperature and relative humidity environment.

##### 4.2.2.1 Surface Morphology

Little to no obvious changes were observed optically or in the SEM surface images of the TRH samples after aging as shown in Figure 4-49 through Figure 4-53. However, an increase in the surface roughness for the Au/Ni plated Group 1 aged samples was observed. The surface roughness for the rougher samples remained approximately constant, see Table 4-5.

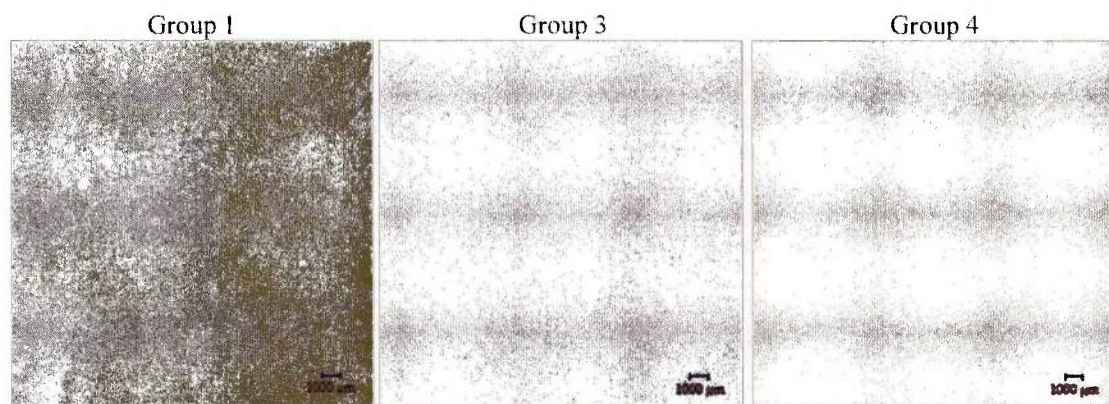


Figure 4-49. Optical surface mapping of Au/Ni plated TRH samples after nine weeks of aging. No noticeable changes in the surface are observed.



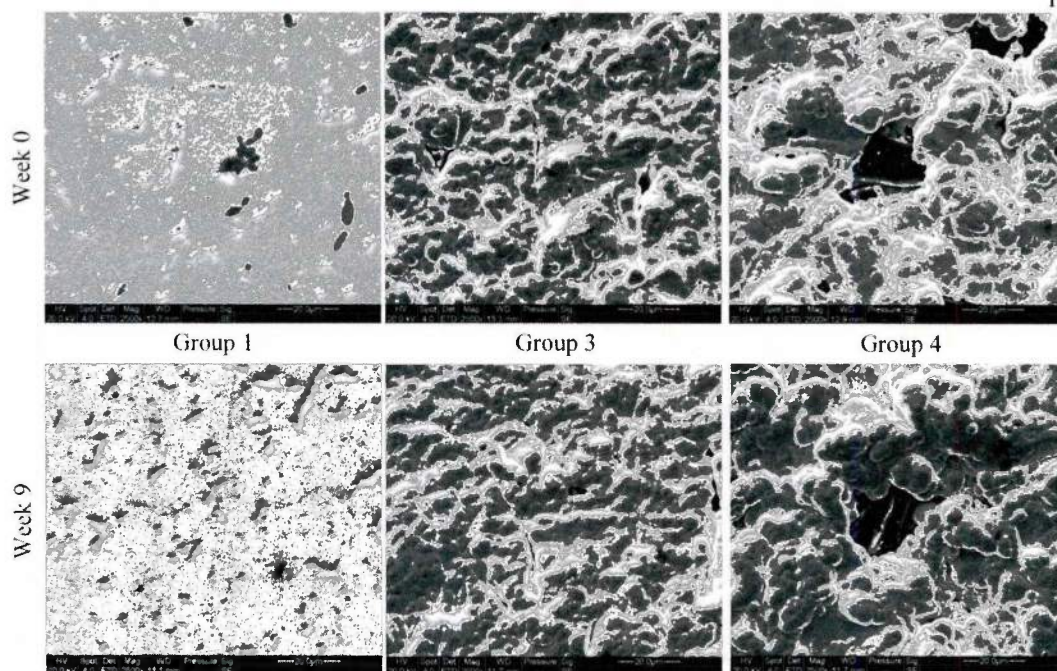


Figure 4-50. SEM images of the Au/Ni plated TRH samples before and after aging (i.e., Week 0 and Week 9). No obvious changes in the surface were observed.

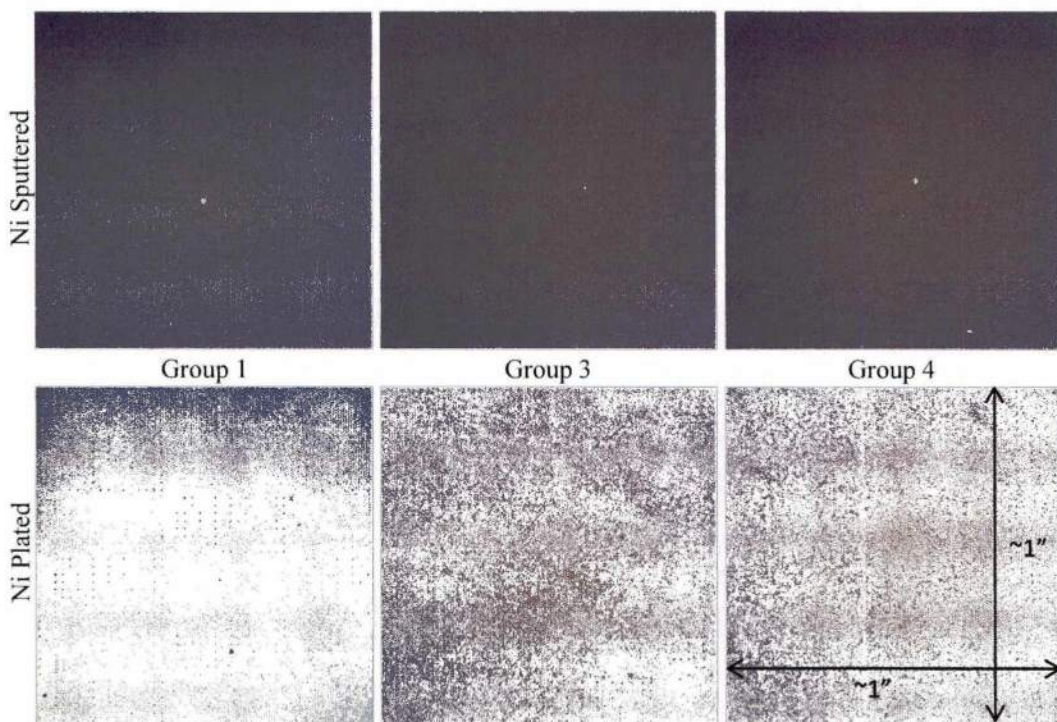


Figure 4-51. Optical images of the Ni plated and Ni sputtered TRH samples after nine weeks of aging. No noticeable changes in the surface are observed.

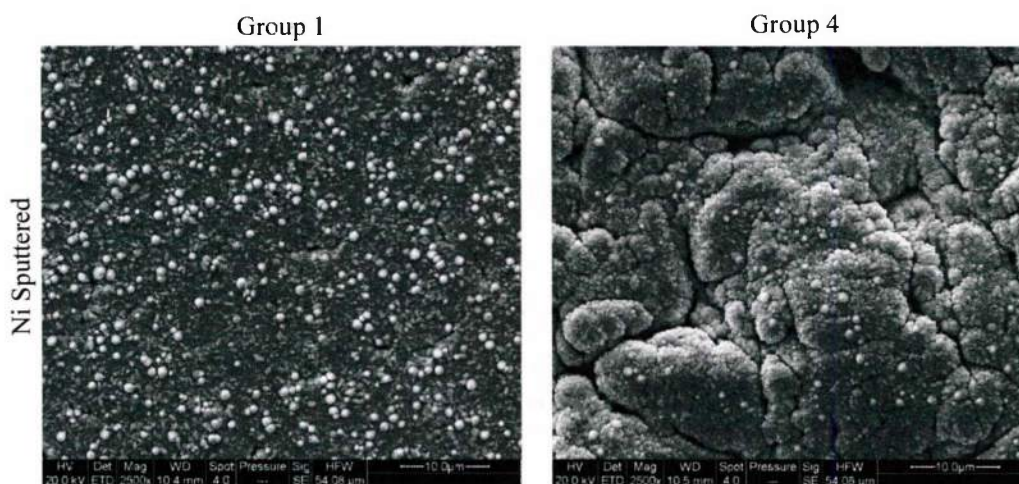


Figure 4-52. SEM images of the Ni sputtered Group 1 and 4 TRH samples after nine weeks of aging. No noticeable changes in the surface are observed.

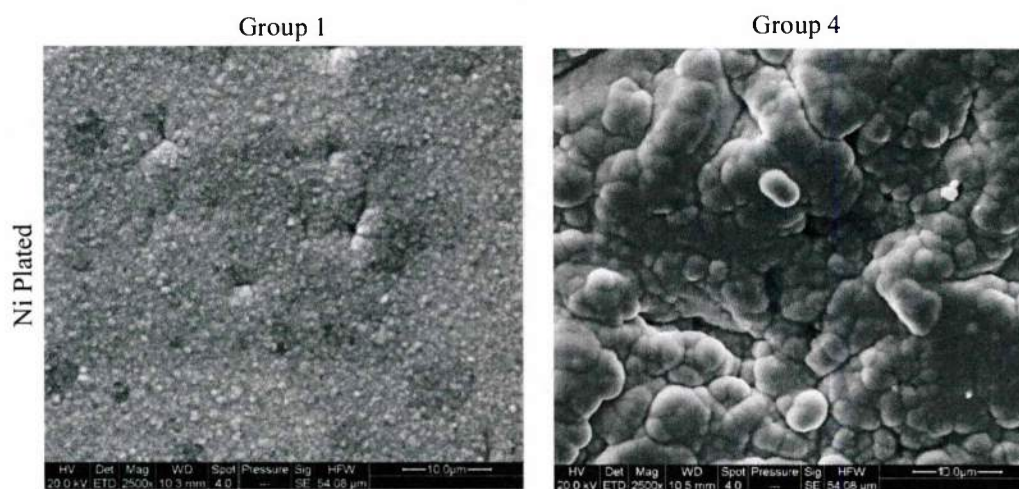


Figure 4-53. SEM images of the Ni plated Group 1 and 4 TRH samples after nine weeks of aging. No noticeable changes in the surface are observed.



Table 4-5. Optical profilometry results for the Group 1, 3, and 4 TRH Au/Ni plated samples listing the roughness before and after aging, as well as the percent difference.

Panel	$R_{a0}$ , $\mu\text{m}$	$R_{a9}$ , $\mu\text{m}$	$\Delta R_{a0-9}$ , $\mu\text{m}$
Group 1 - T/RH	$0.033 \pm 0.001$	$0.042 \pm 0.001$	0.009
Group 3 - T/RH	$0.843 \pm 0.038$	$0.872 \pm 0.016$	0.029
Group 4 - T/RH	$2.77 \pm 0.202$	$2.582 \pm 0.061$	-0.185

#### 4.2.2.2 Residual Stress

The x-ray diffraction results for the elevated temperature and relative humidity (TRH) samples showed little change in the residual stress as depicted in Figure 4-54. The magnitude of the residual stress in Group 3 and 4 samples appears to decrease to a degree, which may be a result of stress relaxation over time in the slightly elevated temperature environment. The residual stress for the Group 1 samples remains approximately constant.

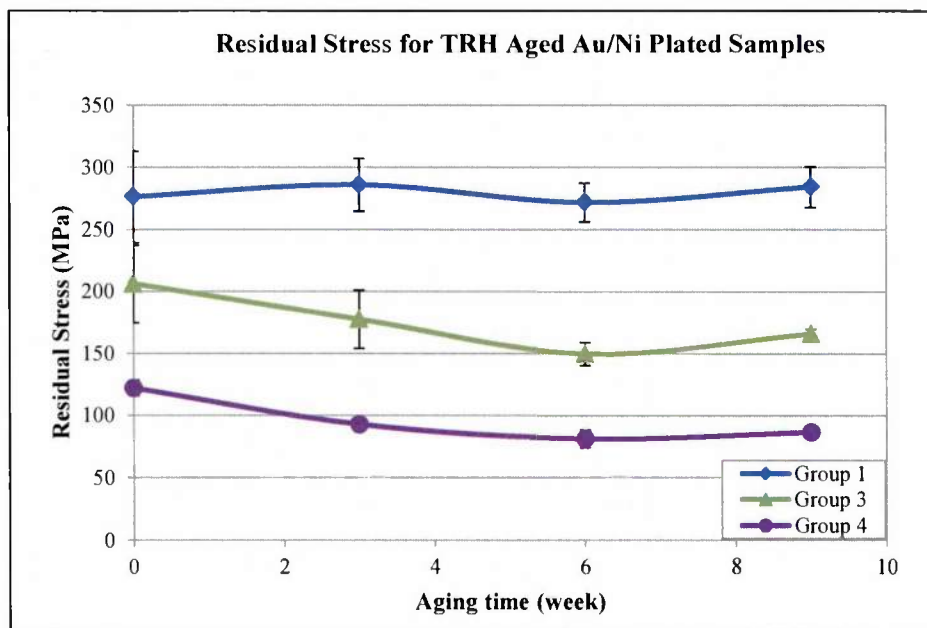


Figure 4-54. Residual stress in the gold coating for each of the elevated temperature and relative humidity (TRH) samples. Each point represents the averaged residual stress from the three duplicate samples.

#### 4.2.2.3 Electrical Contact Resistance

As expected, little to no statistically significant changes in the electrical contact resistance of the elevated temperature and relative humidity samples were observed (see Figure 4-55 through Figure 4-57). It can be noted that, particularly with the Group 4 data, there is a subset of data points with significantly higher resistances, though these data points are most likely due to the embedded grit in the surface rather than evidence of the formation of a corrosion product or surface film.

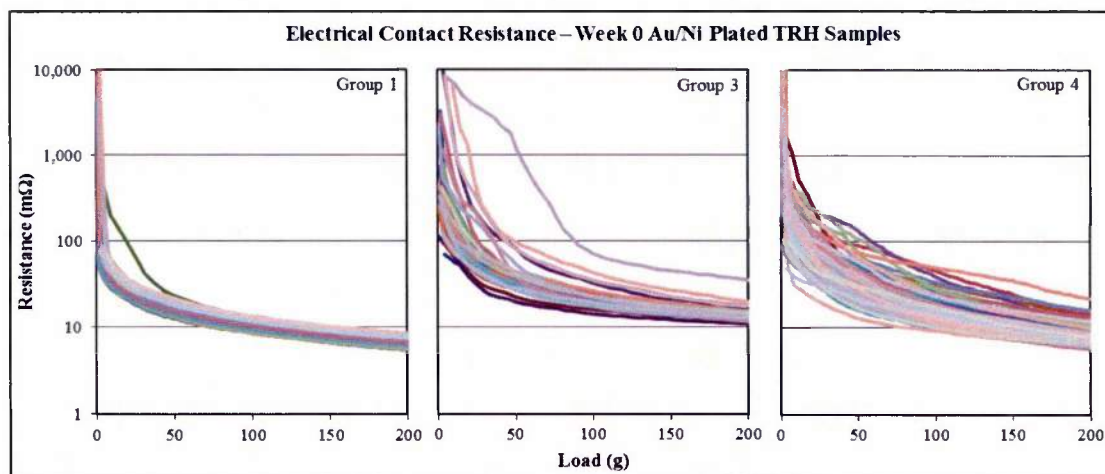


Figure 4-55. Week 0 ECR data for Group 1, 3, and 4 Au/Ni plated TRH samples as a function of load.

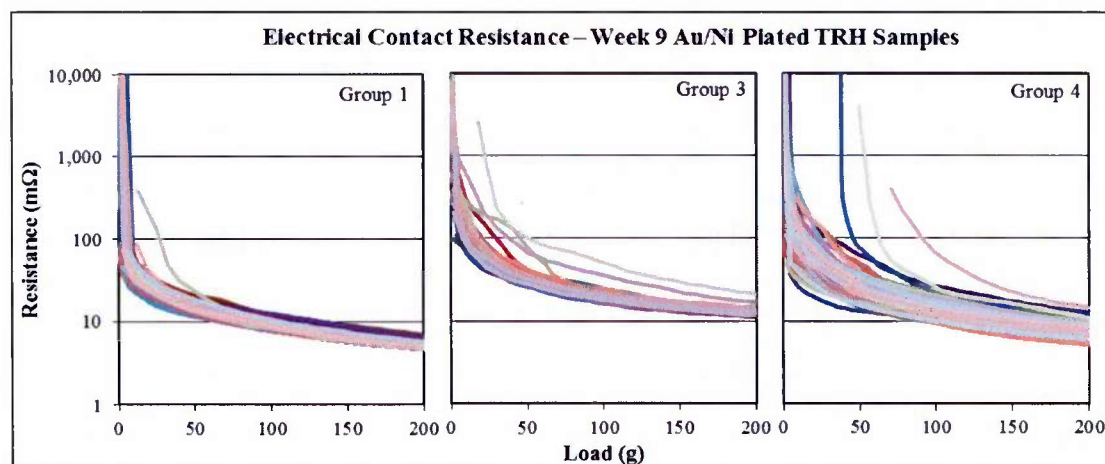


Figure 4-56. Week 9 ECR data for Group 1, 3, and 4 Au/Ni plated TRH samples as a function of load.

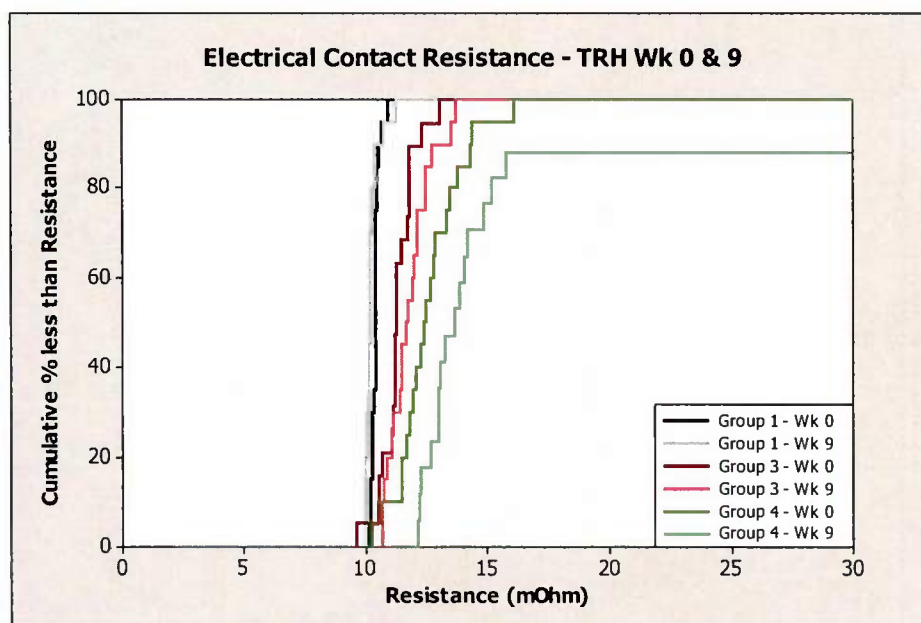


Figure 4-57. Electrical contact resistance data under a 200g load for the Au/Ni plated TRH as received and nine weeks aged samples.

#### 4.2.3 Thermal Cycled (TC) Aged Samples

Thermal cycle tests allow for an investigation into the effects of thermal expansion mismatch between the various materials, though in general this was not expected to be a significant issue, as all of the materials in our system are metals with relatively similar thermal expansion coefficients (discussed in more detail in Section 4.2.3.2).

##### 4.2.3.1 Surface Morphology

As with the TRH samples, little to no change was observed in the surface of the thermal cycled samples, as expected and shown in Figure 4-58 through Figure 4-61. The only exceptions were the Group 1 Au/Ni plated and Group 1 Ni plated samples. The Group 1 Au/Ni plated samples appear to become rougher with cycling, though the change is still within the standard deviation of the



original surface (see Figure 4-60 and Table 4-6). This was thought to be the result of buckling of the underlying nickel coating to relieve additional compressive stresses induced by the thermal aging.

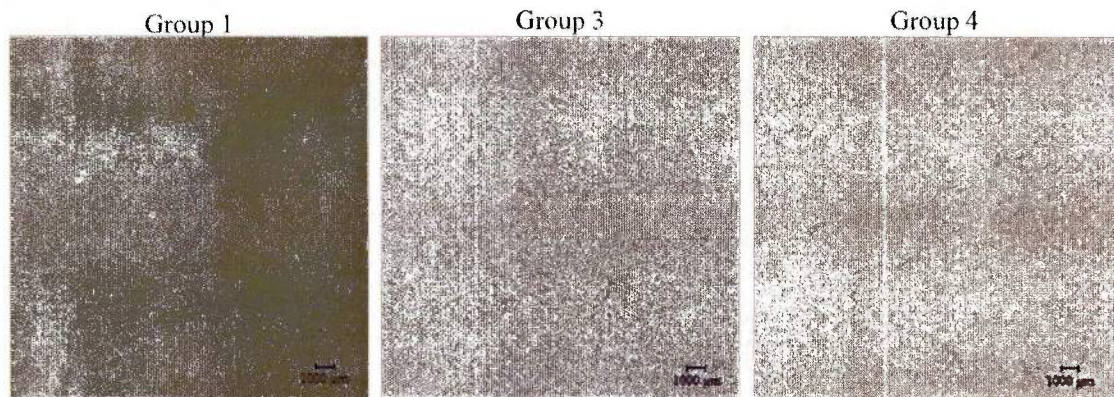


Figure 4-58. Optical surface mapping of Au/Ni plated TC samples after nine weeks of aging. No noticeable changes in the surface are observed.

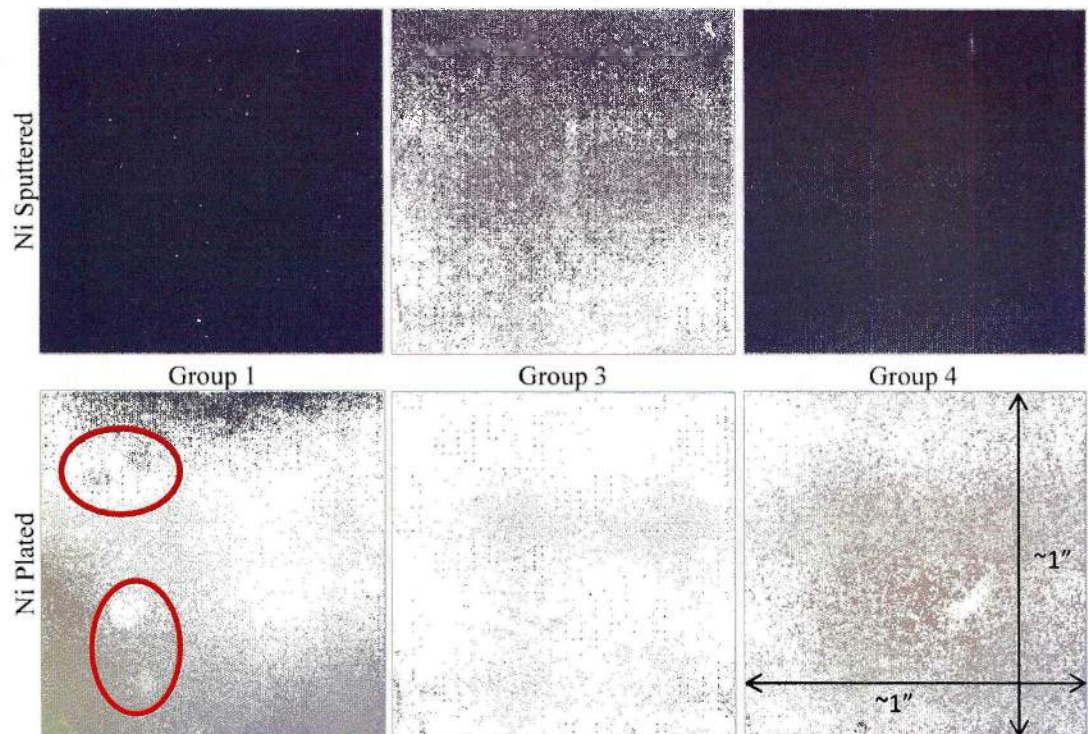


Figure 4-59. Optical images of Ni sputtered and Ni plated samples after nine weeks of thermal cycling.



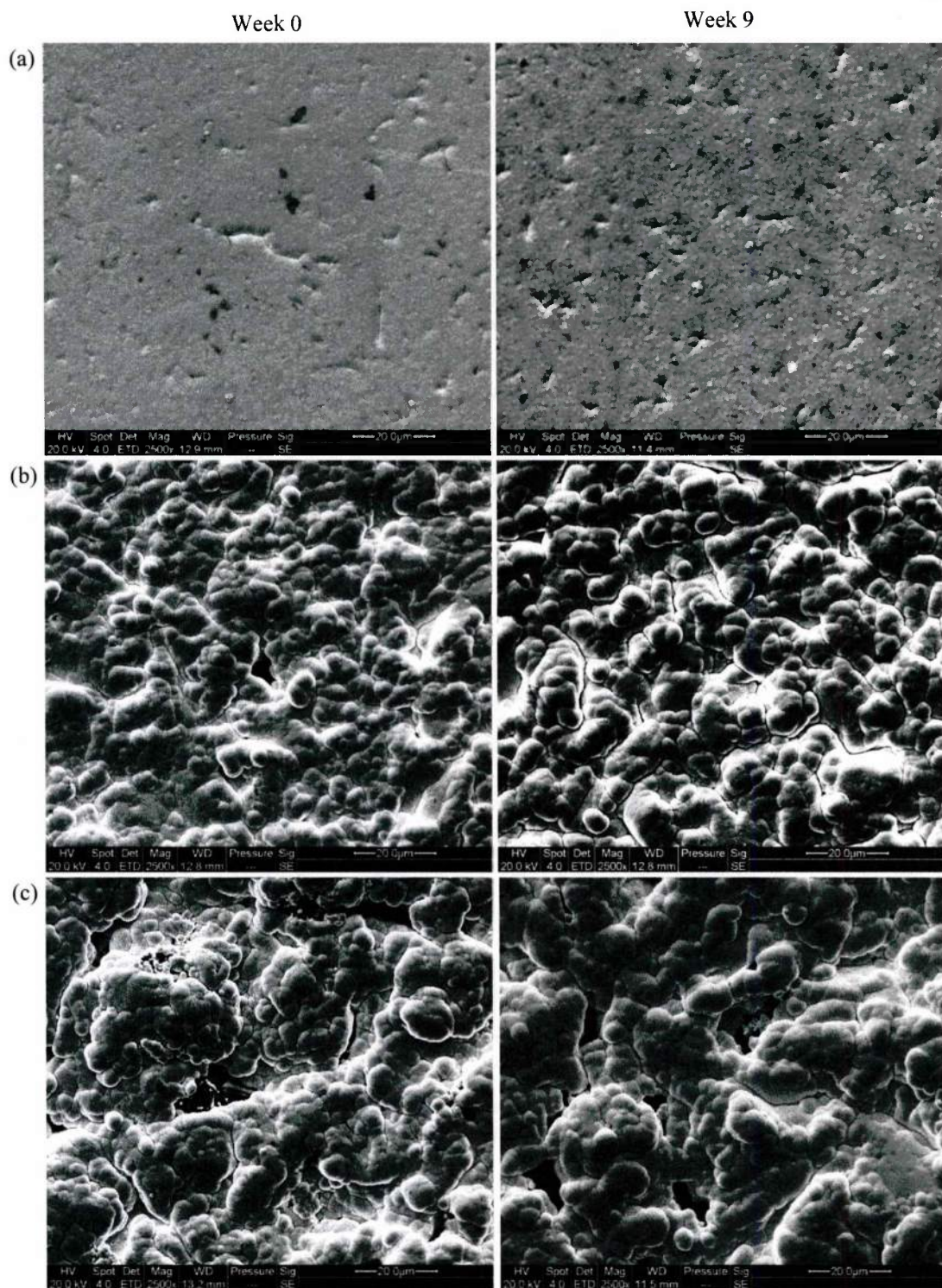


Figure 4-60. SEM surface images of Week 0 and Week 9 Au/Ni plated TC samples for (a) Group 1, (b) Group 3, and (c) Group 4.



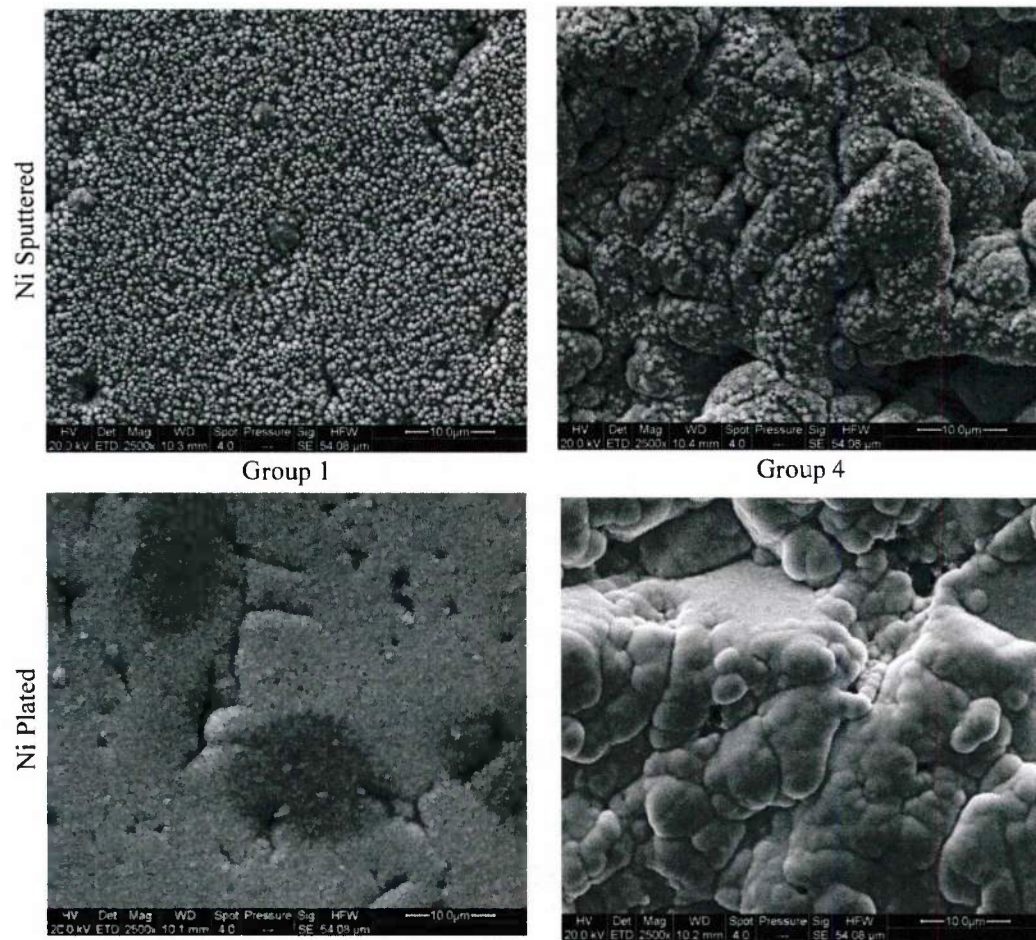


Figure 4-61. SEM surface images of Week 9 Ni plated and Ni sputtered Groups 1 and 4 TC samples.

Table 4-6. Optical profilometry results for the Group 1, 3, and 4 TC Au/Ni plated samples listing the surface roughness before and after aging, as well as the percent difference.

Panel	$R_{a0}$ , $\mu\text{m}$	$R_{a9}$ , $\mu\text{m}$	$\Delta R_{a0-9}$ , $\mu\text{m}$
Group 1 - TC	0.032 $\pm$ 0.003	0.034 $\pm$ 0.001	0.002
Group 3 - TC	0.893 $\pm$ 0.089	0.890 $\pm$ 0.092	-0.003
Group 4 - TC	2.87 $\pm$ 0.180	2.552 $\pm$ 0.147	-0.318

#### 4.2.3.2 Residual Stress

As previously mentioned, thermal cycling studies allow for an investigation into the effects of thermal expansion mismatch between the various materials. Table 4-7 lists the linear thermal expansion coefficients for the three metals utilized in this research. Of the three metals, nickel has the lowest thermal expansion coefficient and is located in between the two other materials. As such, the nickel is under an increased compressive stress while at the lower temperatures of the thermal cycle and a slightly more tensile stress when heated.

Table 4-7. Linear thermal expansion coefficients (for temperatures between roughly 20 °C and 300 °C) [3, 77].

Material	Thermal Expansion Coefficient ppm/°C
Oxygen-Free Copper	17.7
Nickel	13.3
Gold	14.2

If we look at the nickel layer without the additional gold layer on top (such as it is for the Ni plated and Ni sputtered samples), the residual stress in the nickel associated with thermal expansion during a cooling cycle (i.e., when the sample is cooled from 60 °C to -40 °C) could be calculated as:

$$\sigma_{\text{Ni}} = \frac{E_{\text{Ni}}}{1 - \nu_{\text{Ni}}} (\alpha_{\text{Cu}} - \alpha_{\text{Ni}}) (T_2 - T_1) = \frac{232 \text{ GPa}}{1 - 0.31} \frac{(17.7 - 13.3) \times 10^{-6}}{^{\circ}\text{C}} (-40 - 60)^{\circ}\text{C} = -148 \text{ MPa}$$

A stress of the same magnitude, but opposite sign (i.e., “positive” or tensile stresses), is associated with the nickel when the samples are heated. Repeating the same calculation, we can see that for gold on copper the thermally induced residual stress is only a third of what was calculated for nickel on copper.

$$\sigma_{Au} = \frac{E_{Au}}{1 - \nu_{Au}} (\alpha_{Cu} - \alpha_{Au})(T_2 - T_1) = \frac{79 \text{ GPa}}{1 - 0.42} \frac{(17.7 - 14.2) \times 10^{-6}}{^{\circ}\text{C}} (-40 - 60)^{\circ}\text{C} = -48 \text{ MPa}$$

As a subset of the samples for this research has gold plated on top of nickel on copper, the stress between the gold and nickel is also of importance. Using the same basic stress equation, the thermally induced residual stress in the gold associated with a gold on nickel system cooling from 60 °C to -40 °C is calculated below:

$$\sigma_{Au} = \frac{E_{Au}}{1 - \nu_{Au}} (\alpha_{Ni} - \alpha_{Au})(T_2 - T_1) = \frac{79 \text{ GPa}}{1 - 0.42} \frac{(13.3 - 14.2) \times 10^{-6}}{^{\circ}\text{C}} (-40 - 60)^{\circ}\text{C} = 12.3 \text{ MPa}$$

These stresses calculated above are not exact as they do not account for other variables, such as coating thickness and surface roughness, but they can provide an estimate as to the amount of residual stress induced by thermal cycling for the various coatings/materials systems.

As with the TRH samples, a slight decrease in the magnitude of the residual stress is observed in the Group 3 and 4 Au/Ni plated samples over the course of the aging study, see Figure 4-67. Again, time spent at elevated temperatures (60 °C for the TC samples) could have aided in stress relaxation of the coatings resulting in decreased residual stress values. The Group 1 TC Au/Ni plated samples, however, appear to have a more significant decrease in residual stress, particularly after the first three weeks of exposure.

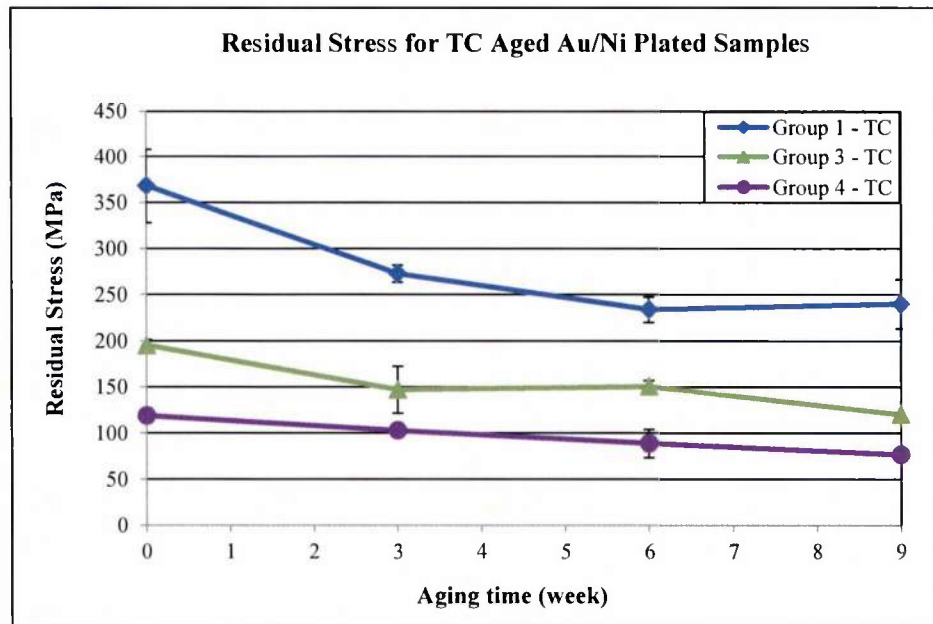


Figure 4-62. Residual stress in the gold coating for each of the thermal cycled (TC) samples. Each point represents the averaged residual stress from the three duplicate samples.

Recall from Section 4.1.4 that the residual stress for the Ni plated Group 1 samples was compressive. It is possible that with the added compressive stresses associated with the cooling portion of the thermal cycle that the nickel layer began to buckle in order to relieve the stress. This may account for the rougher appearance of the Group 1 samples after nine weeks of cycling.

#### 4.2.3.3 Electrical Contact Resistance

As with the residual stress, the larger change was observed in the electrical contact resistance of the Group 1 thermal cycled samples as compared to the Group 3 and 4 samples, see Figure 4-63 through Figure 4-65. The change in electrical contact resistance is on a much smaller scale for the thermal cycled samples, including Group 1, as compared to the MFG samples.

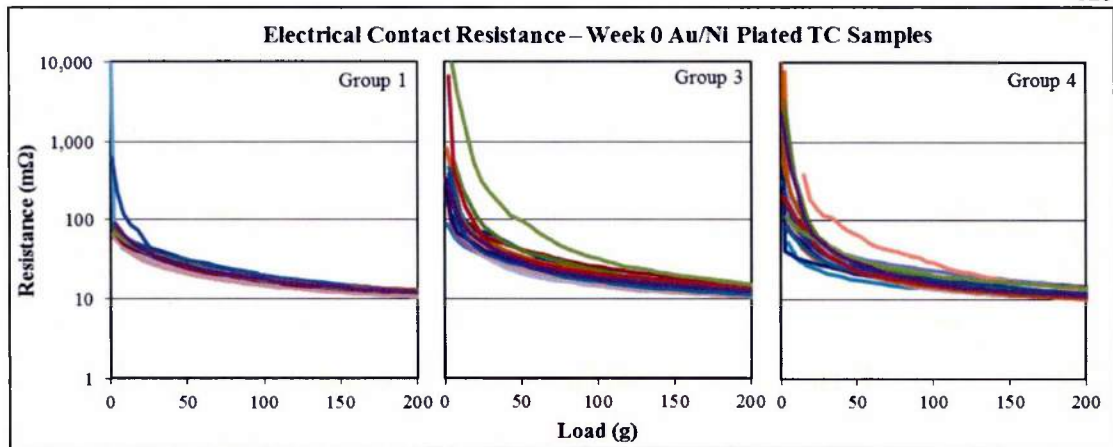


Figure 4-63. Electrical contact resistance data as a function of load for Group 1, 3, and 4 Au/Ni plated Week 0 TC samples.

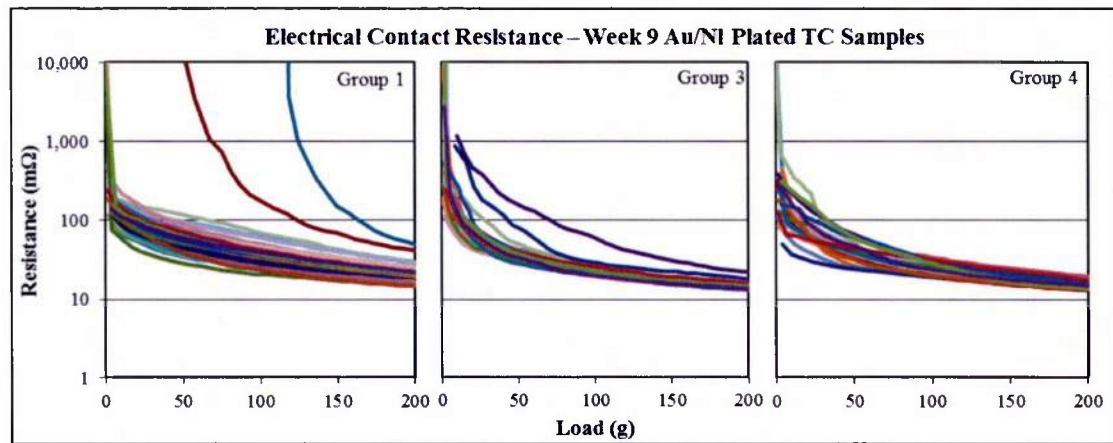


Figure 4-64. Electrical contact resistance data as a function of load for Group 1, 3, and 4 Au/Ni plated Week 9 TC samples.



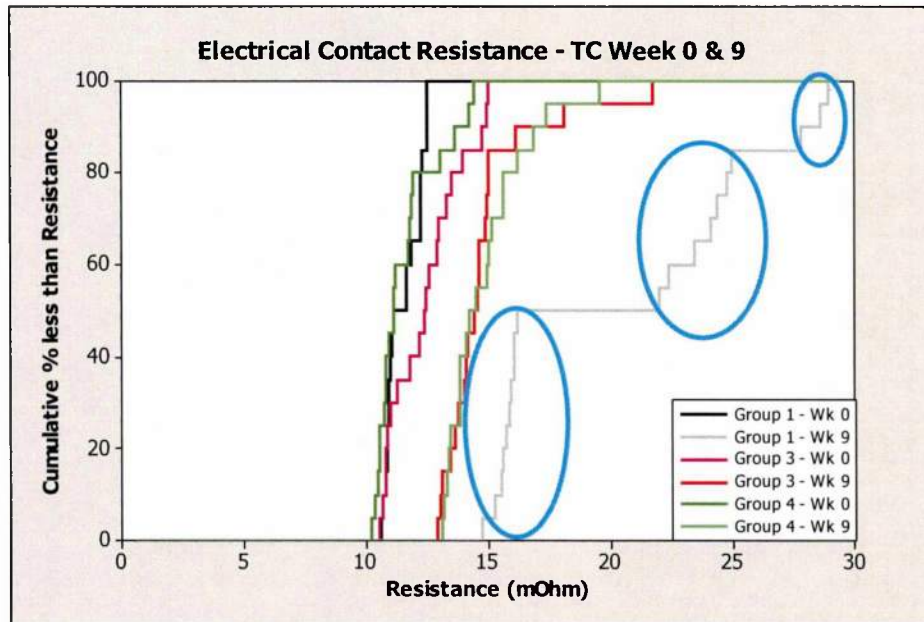


Figure 4-65. Electrical contact resistance data under a 200g load for the Au/Ni plated thermal cycled samples after nine weeks of cycling. Note that the Group 1 Week 9 data appears to be tri-modal.

From Figure 4-65 it appears that the electrical contact resistance data for the Group 1 Au/Ni plated samples after nine weeks of aging is “tri-modal”. Further investigation of this data revealed that each of the three sections of data were collected at different times resulting in potential additional aging effects influencing the resistance. Figure 4-66 shows the electrical contact resistance data as a function of load. Note that the data in each circled group corresponds to data collected on a specific day, as well as to the data circled in red in Figure 4-66.

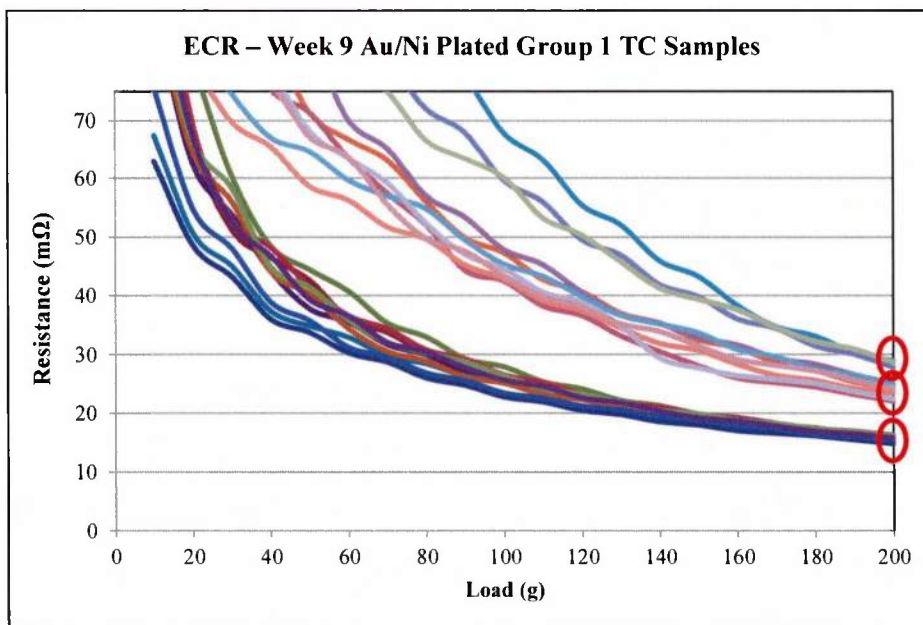


Figure 4-66. Electrical contact resistance data under a 200g load for the Au/Ni plated thermal cycled samples after nine weeks of cycling. Note that the Group 1 Week 9 data appears to be tri-modal.

#### 4.2.4 Aging Environment Effects on Surface Roughness

Up to this point the data presented has been compared within a single aging study (i.e., focusing on the effects of surface roughness/coating for a given environment). This section will provide more discussion regarding the effects of the aging environment for a given surface roughness group.

##### 4.2.4.1 Residual Stress

Figure 4-67 through Figure 4-69 show the residual stress data grouped based on surface roughness. From these figures it can be noted that for all of the Au/Ni plated samples, the residual stress either remained approximately constant or decreased with aging time. For each of the surface roughnesses, the largest change in residual stress occurred as a result of TC aging.

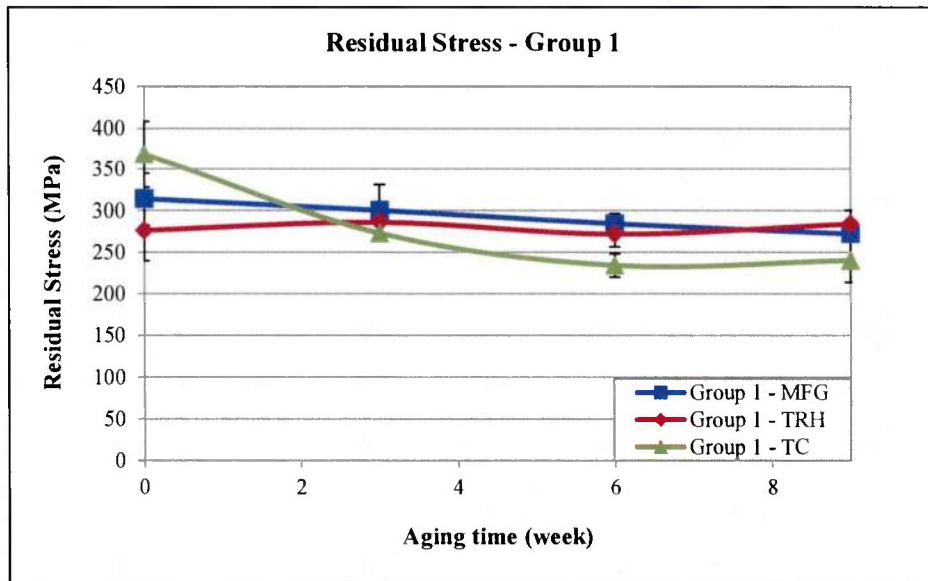


Figure 4-67. Residual stress data for all Group 1 Au/Ni plated samples. Note that the magnitude of the residual stress remains approximately constant/decreases slightly for the MFG and TRH aged samples, while decreasing more significantly for the TC aged samples.

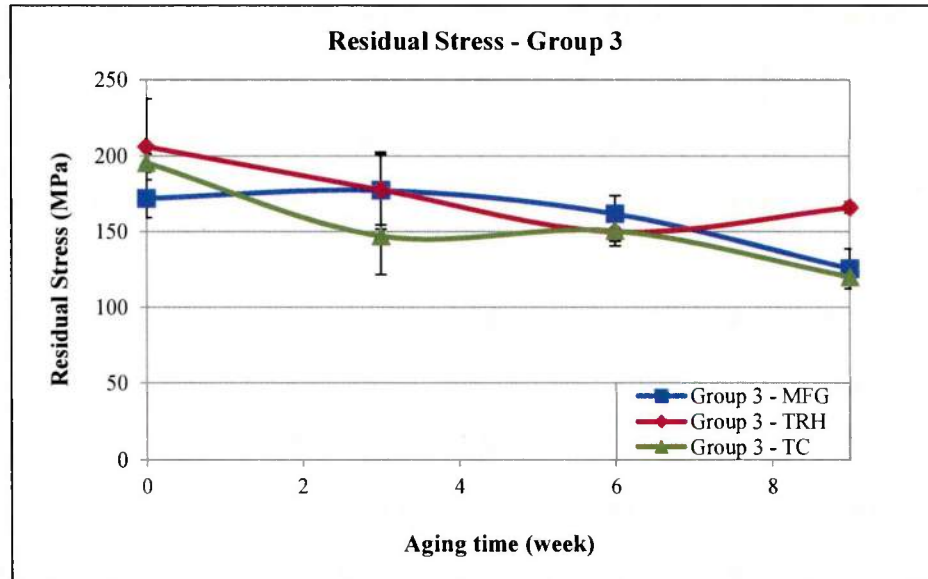


Figure 4-68. Residual stress data for all Group 3 Au/Ni plated samples. Note that the magnitude of the residual stress decreases slightly.

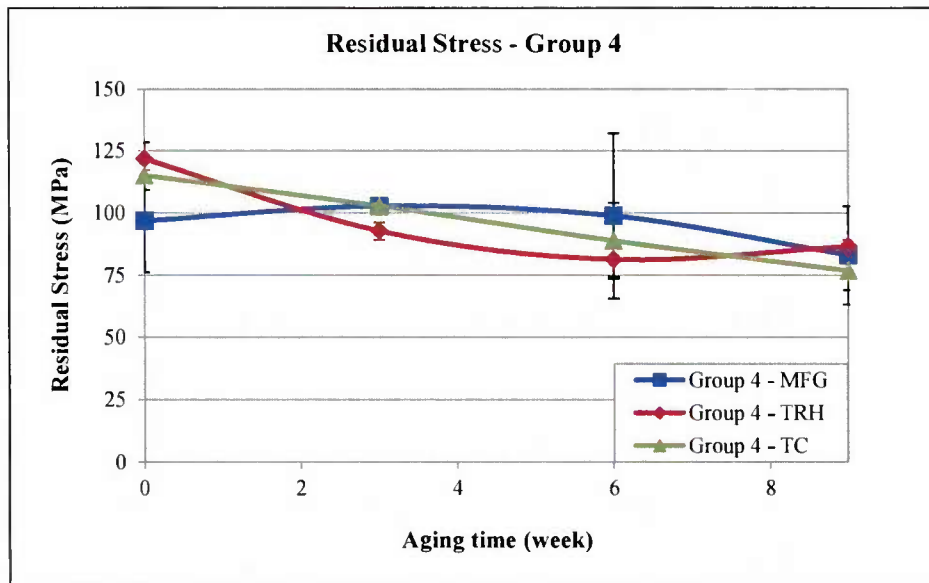


Figure 4-69. Residual stress data for all Group 4 Au/Ni plated samples. Note that the magnitude of the residual stress decreases slightly.

#### 4.2.4.2 Electrical Contact Resistance

Unlike with the residual stress, there is a more distinct difference between the mechanisms in which the electrical contact resistance changes with time based on the aging environment. As discussed previously, the Au/Ni plated samples undergo localized corrosion at defect sites via pore corrosion. As such, the changes in the surface are also localized meaning that the electrical contact resistance remains approximately the same for areas not corroded/covered with corrosion product, see Figure 4-70 for the Group 1 samples. For Groups 2, 3, and 4, the extent of corrosion was much larger resulting in a much larger percentage of the sample surface being covered in corrosion sites/products, as shown in Figure 4-71.

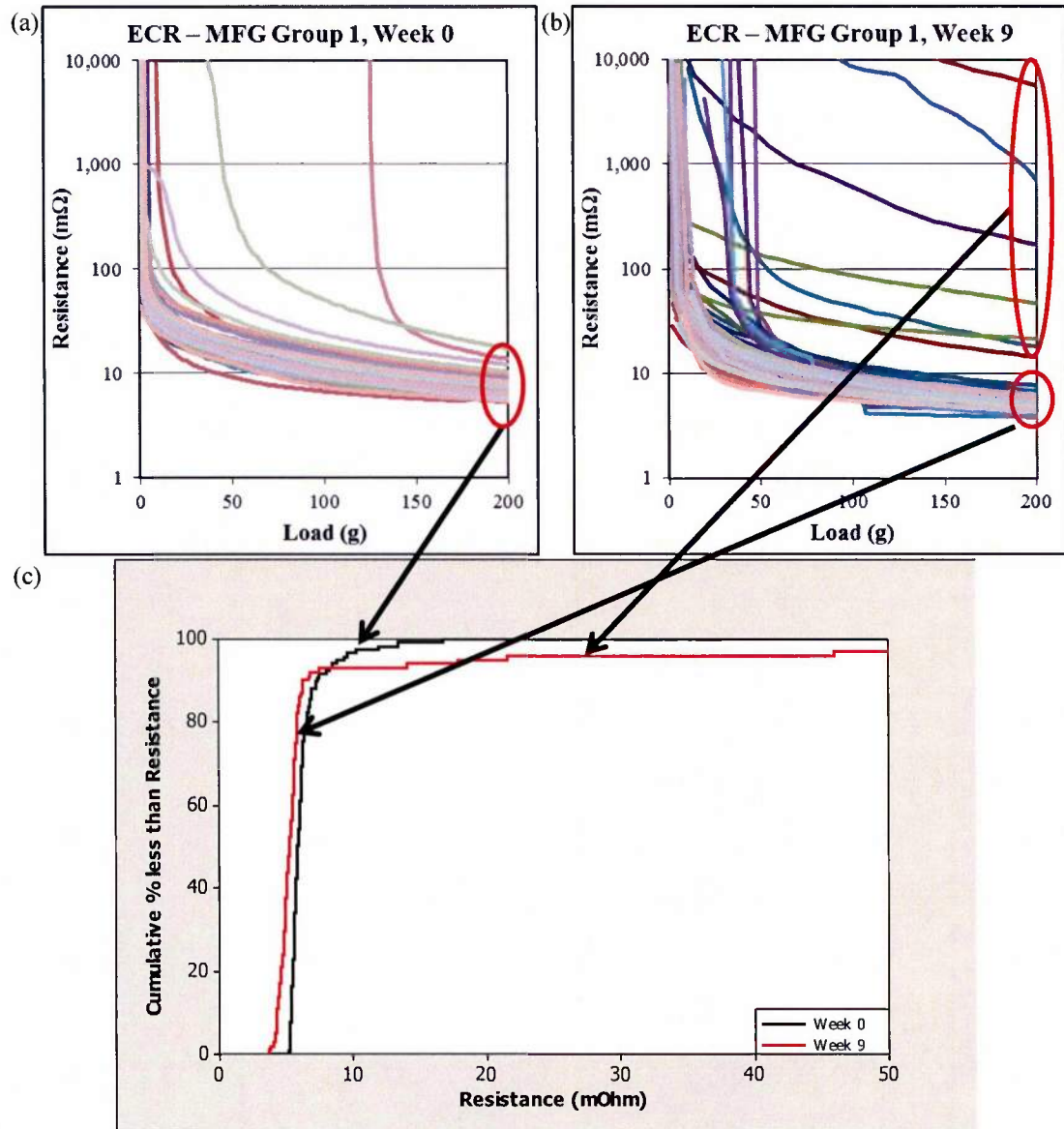


Figure 4-70. Electrical contact resistance data for Group 1 Au/Ni plated samples before and after aging in the MFG environment, showing the effect of localized corrosion in the data distributions for (a) ECR data as a function of load before aging (i.e., Week 0), (b) ECR data as a function of load after nine weeks of aging, and (c) CDF plot of ECR data under a load of 200g.



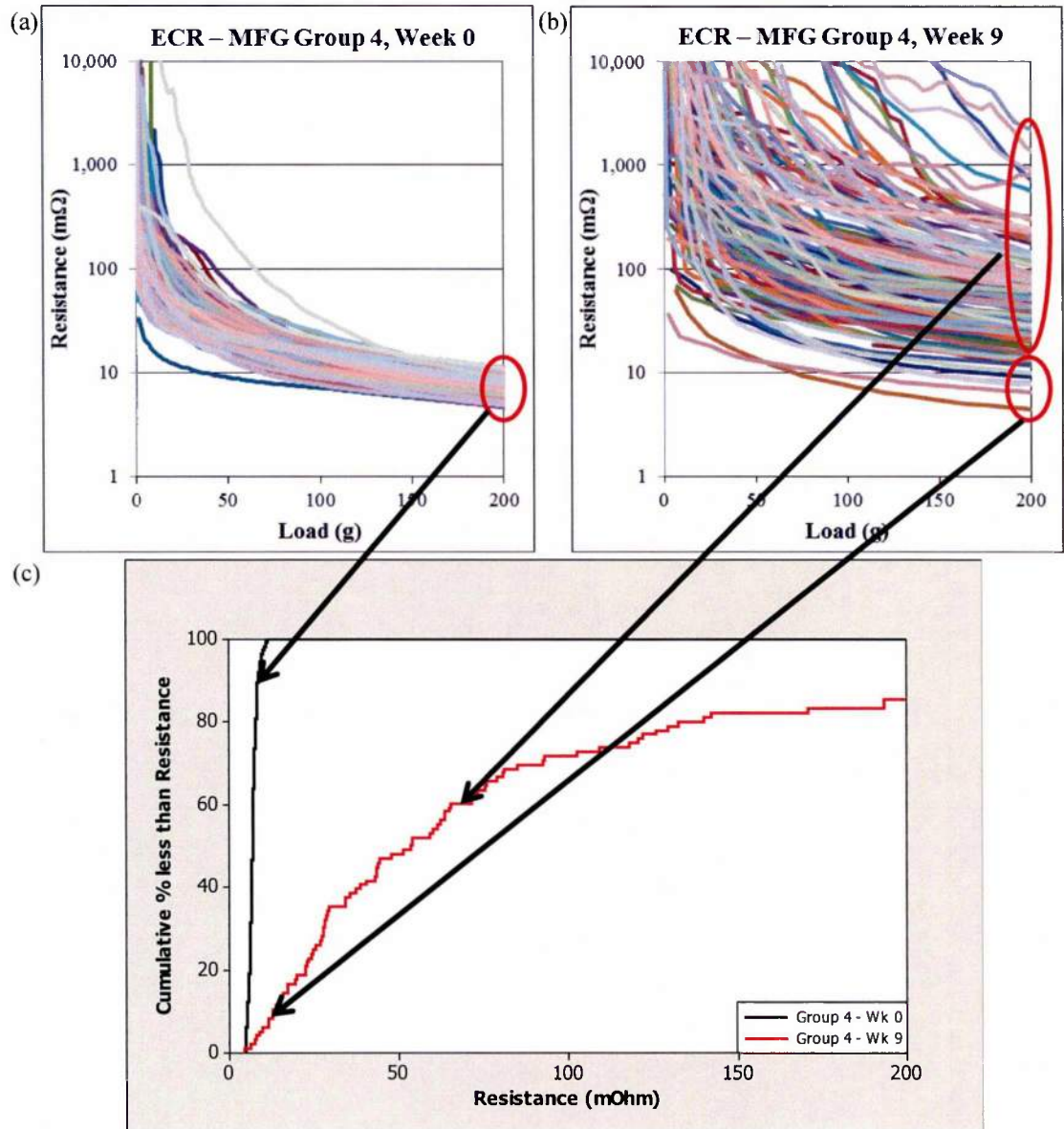


Figure 4-71. Electrical contact resistance data for Group 4 Au/Ni plated samples before and after aging in the MFG environment, showing the effect of extensive localized corrosion in the data distributions for (a) ECR data as a function of load before aging (i.e., Week 0), (b) ECR data as a function of load after nine weeks of aging, and (c) CDF plot of ECR data under a load of 200g.

When directly comparing the electrical contact resistance data for each of the surface roughness groups and aging environments, it can be observed that in most cases, the mixed flowing gas environment caused the largest change, as expected from the literature, see Figure 4-72 through

Figure 4-74. In addition, with the exception of Group 1 Au/Ni plated samples aging in either the TRH and TC environments results in little to no observed changes in the electrical contact resistance.

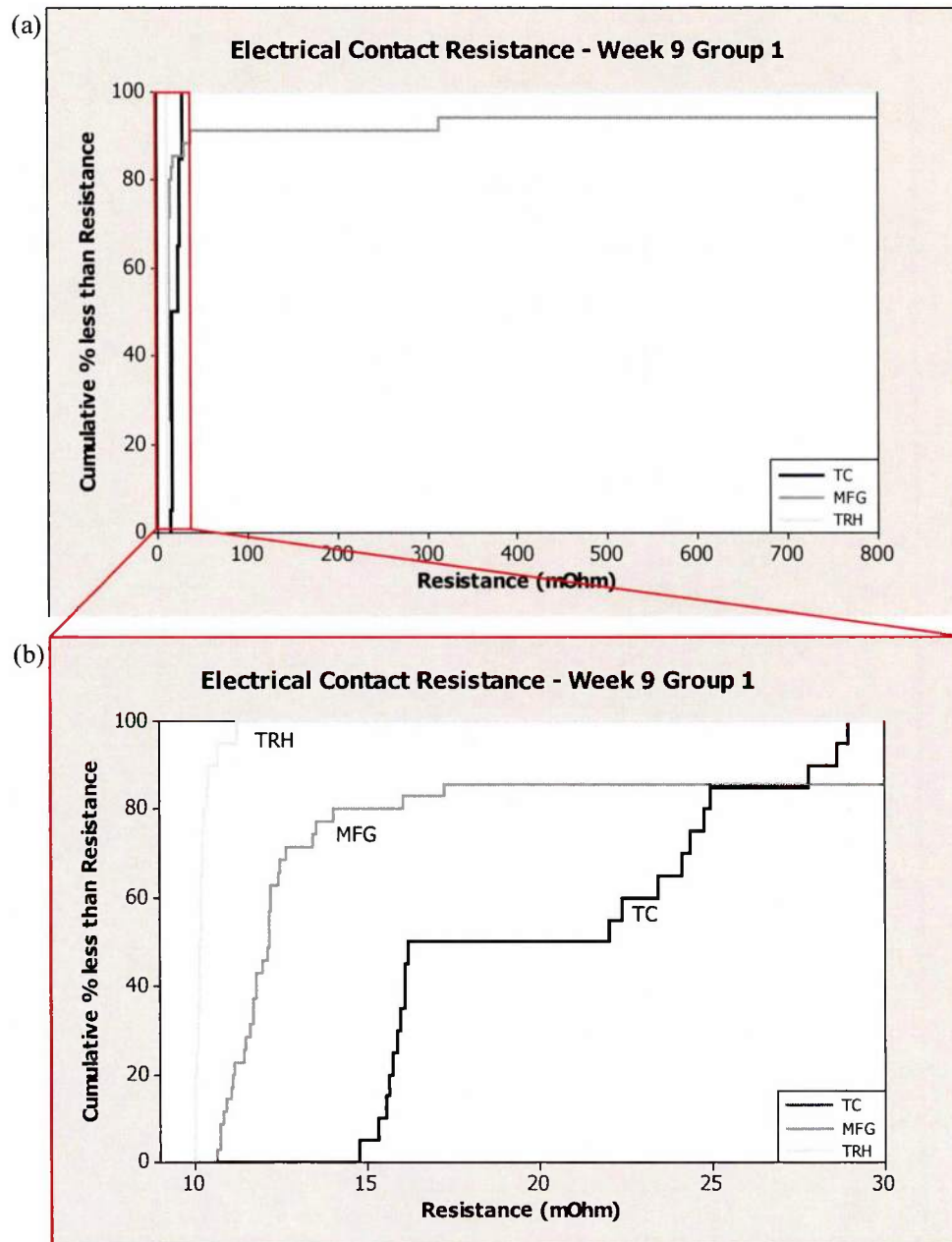


Figure 4-72. (a) Electrical contact resistance data for Week 9 Au/Ni plated Group 1 samples and (b) close-up of data in (a) showing the differences in ECR values as a function of the aging environment.

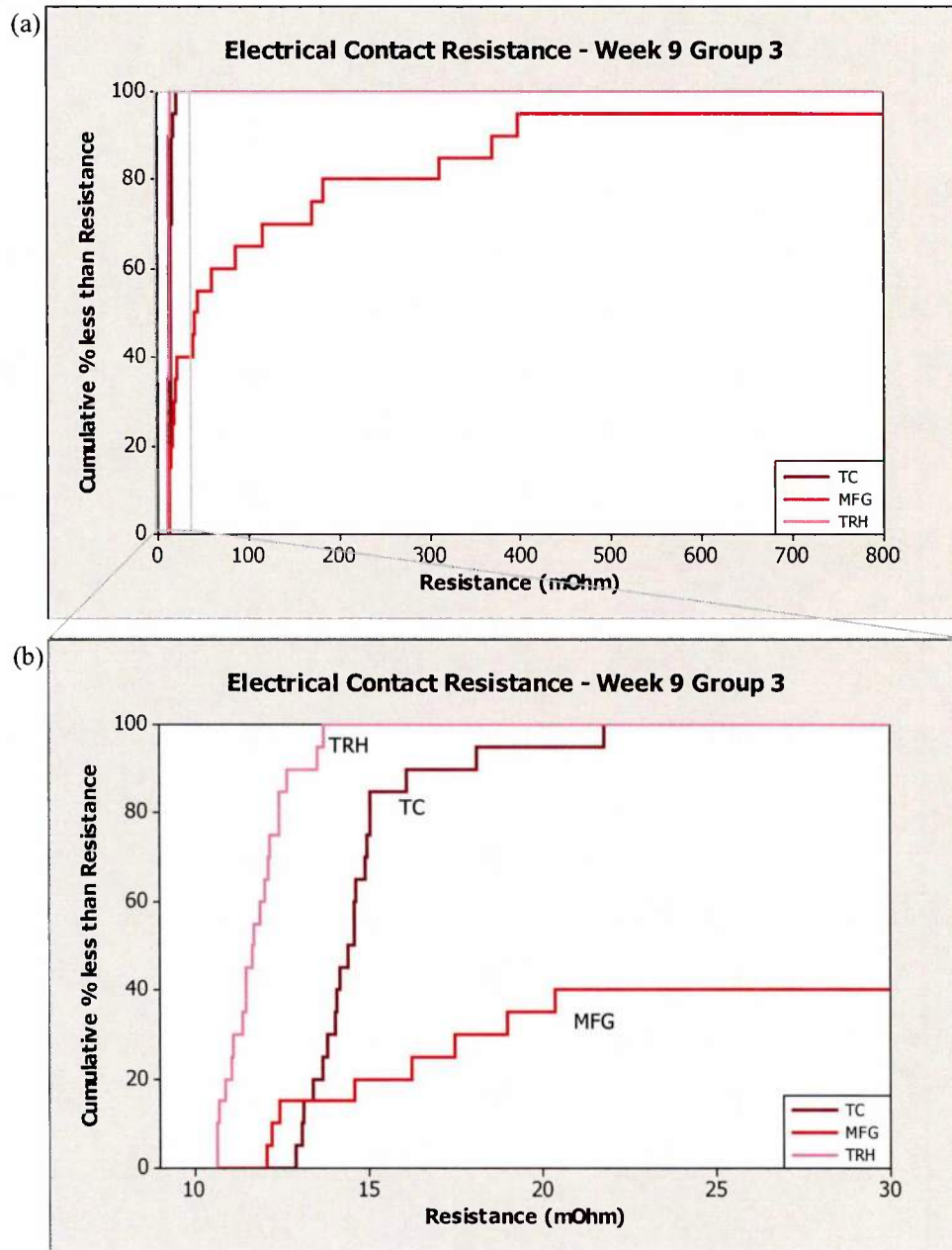


Figure 4-73. (a) Electrical contact resistance data for Week 9 Au/Ni plated Group 3 samples and (b) close-up of data in (a) showing the differences in ECR values as a function of the aging environment.

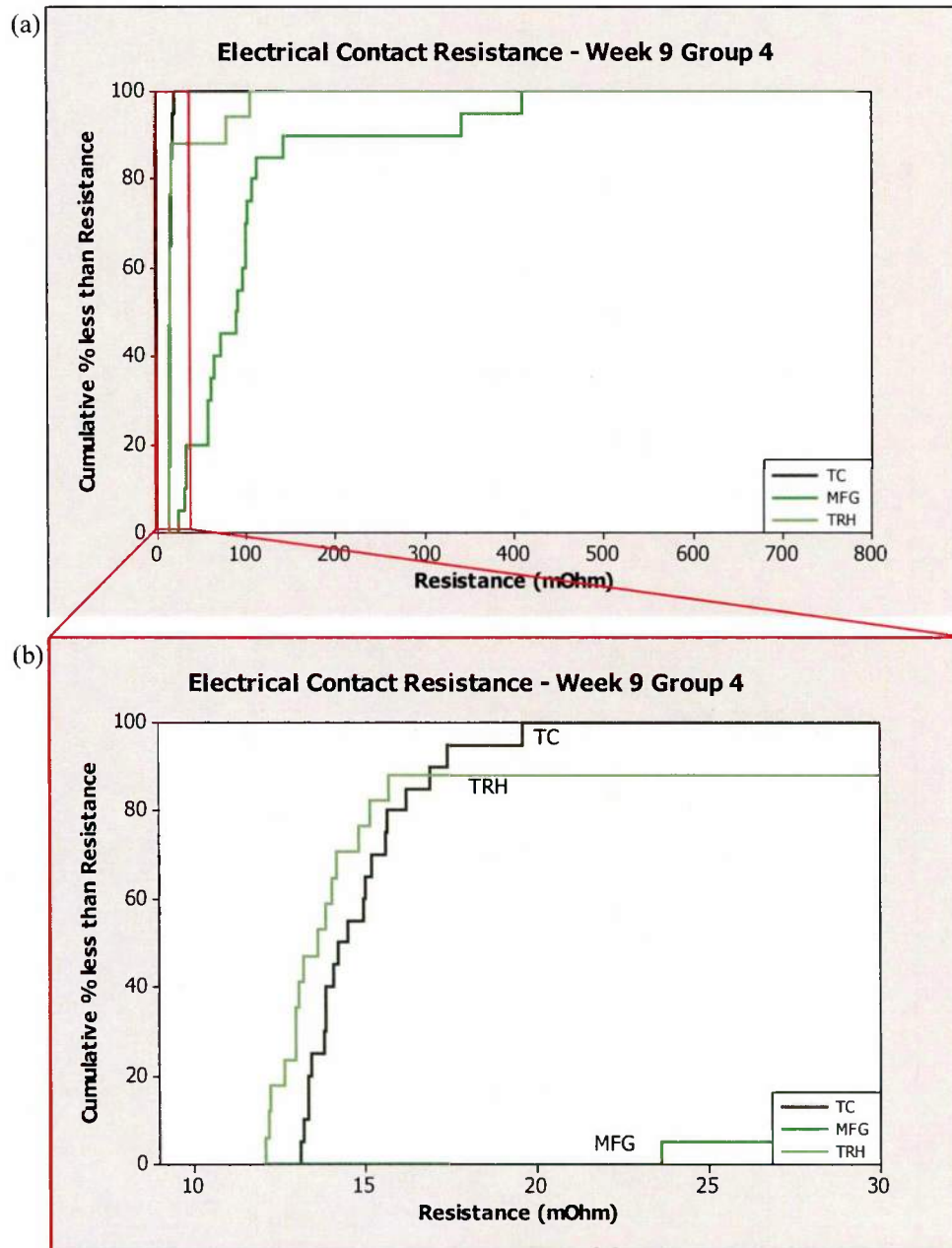


Figure 4-74. (a) Electrical contact resistance data for Week 9 Au/Ni plated Group 4 samples and (b) close-up of data in (a) showing the differences in ECR values as a function of the aging environment.

## **Chapter 5**

### **Conclusions and Future Work**

#### **5.1 Summary and Conclusions**

Electrical connectors using nickel and gold coated copper are commonly used in many applications, some of which have very high reliability requirements. The functionality of electrical connectors is typically determined by the electrical contact resistance. In addition, residual stresses present in a coating can either be beneficial or detrimental to the coating performance. As such, the effects of surface roughness and aging were investigated to determine their effects on the electrical contact resistance and residual stress in the coatings.

Associated work reported in the literature for aged connector materials focuses predominately on the electrical contact resistance with little to no investigation into residual stress. Likewise, the work on residual stress in similar coating systems report little data regarding the effects of aging and surface roughness. As such, this research helps to bridge the gap regarding the effects of aging and surface roughness on the electrical contact resistance and residual stress trends for electrical connector materials in representative aging environments.

The residual stress observed in the as received samples varied based on the surface roughness and coating system. For the electroplated samples (i.e., Au/Ni plated and Ni plated) the magnitude of the residual stress decreased with increasing surface roughness (i.e., the residual stress in the Au plated coating became less tensile, and the Ni plated coating became less compressive in nature). The residual stress in the Ni sputtered samples did not exhibit the same relationship between residual stress and surface roughness. Instead, the residual stress of the sputtered samples remained approximately constant regardless of the surface roughness. This could potentially be due to the



residual stresses associated with the sputtering process (i.e., the bombardment of particles and thermal stresses induced by cooling from 200 °C to room temperature) overshadowing the residual stresses resulting from varying degrees of surface roughness.

Upon aging, the magnitude of the residual stress present in the Au/Ni plated samples either remained approximately constant or decreased, depending on the surface roughness and aging environment. The largest observed change in residual stress occurred in the thermal cycled samples with reported changes on the order of 40-120 MPa (where Group 1 samples had the largest change of 100 – 120 MPa and Group 4 the smallest at 40 – 50 MPa). The MFG samples exhibited residual stress changes on the order of 15 – 50 MPa, again with the largest stress changes reported for the Group 1 samples followed by Groups 3 and 4. The smallest changes in residual stress were observed in the TRH aged samples. Residual stress values decreased on the order of 0 – 40 MPa. In contrast to the MFG and TC samples however, the larger changes in residual stress for the TRH samples were observed in the Group 4 samples. See Table 5-1 for a summary of the residual stress trends.

Table 5-1. Summary of trends in residual stress based on surface roughness and aging environment for the Au/Ni plated samples. Note that all residual stress numbers refer to the amount of decrease in tensile residual stress observed.

	Aging Environment	Group 1	Group 3	Group 4
$\Delta$ Residual Stress, MPa	MFG	~ 40 - 50	~ 40 - 50	~ 10 - 20
	TRH	~ 0 - 10	~ 15 - 30	~ 30 - 40
	TC	~ 100 - 120	~ 75 - 80	~ 60 - 70
% Reduction in Residual Stress	MFG	~ 12 - 16%	~ 21 - 26%	~ 9 - 18%
	TRH	~ 0 - 3%	~ 8 - 16%	~ 27 - 36%
	TC	~ 32 - 38%	~ 39 - 42%	~ 54 - 63%

The electrical contact resistance only displayed a slight shift (1 – 3 mΩ) based on the surface roughness prior to aging for the Au/Ni plated samples. After aging, however, more distinct changes were observed based on the surface roughness and aging environment. The MFG samples exhibited

localized changes due to the corrosion sites/products formed on the surface that dramatically increased the electrical contact resistance in those areas (some with resistances well over 1000 m $\Omega$ ). The TC samples exhibited a more macro-scale change (on the order of 2 – 20 m $\Omega$  depending on the roughness), as the aging mechanism does not involve changes only at a defect sites, but with the entire interface between materials. Little to no changes were observed in the TRH samples (0 – 3 m $\Omega$ ). See Table 5-2 for a summary of the electrical contact resistance trends.

Table 5-2. Summary of trends in electrical contact resistance values based on surface roughness and aging environment for the Au/Ni plated samples. Note that all ECR values refer to the increase in ECR observed.

	Aging Environment	Group 1	Group 3	Group 4
$\Delta ECR, m\Omega$	MFG	Localized areas with ECR increase > 1000		
	TRH	~ 0	~ 0 - 1	~ 1 - 3
	TC	~ 5 - 20	~ 3 - 5	~ 3 - 5

As a result of this research, it can be observed that the coating process, as well as the surface roughness and aging environment/time, can have a significant influence on the residual stress and electrical contact resistance of nickel and nickel/gold coated copper. In particular, the coating process and surface roughness have a substantial effect on the residual stress, while the aging environment/time has a smaller influence (at least at the macro-scale) for the selected materials/environments. In contrast, the aging environment (particularly the MFG environment) and exposure time exhibit a much more significant influence on the electrical contact resistance to varying degrees based on the surfaces roughness. In addition, care must be exercised when preparing substrate surfaces. The samples prepared for this research had a significant amount of embedded grit which can have a significant effect on the coating performance, though additional work would be needed to confirm the extent of influence for the residual stress and electrical contact resistance in particular.

## 5.2 Future Work

The original intent of this research was to investigate the effects of surface roughness and aging on the residual stress and electrical contact resistance for three sets of coupons, i.e., Au/Ni plated, Ni plated, and Ni sputtered. However, the scope of this project was narrowed to predominately focus on the Au/Ni plated samples with some supporting data from the Ni plated and Ni sputtered samples to use as comparisons. Additional work, including a more detailed examination of the Ni plated and Ni sputtered residual stress, coating thickness, surface morphology/corrosion density, electrical contact resistance, should be performed to further the understanding of surface roughness and aging effects on the nickel coatings. In addition, future studies should be completed to provide a more in depth understanding of the various mechanisms associated with the observed trends.

Small amounts of the Ni plated and Ni sputtered data were reported in Chapter 4 providing a comparison based on the coating material and coating process for the as received case. With additional examination of the samples, the Ni coatings can be compared to determine which type of nickel coating may be the better option for use as an underlayer to the gold (i.e., Ni plated under Au plated or Ni sputtered under Au plated).

## References

- [1] Abbott, W.H., "The development and performance characteristics of mixed flowing gas test environments", *IEEE Transactions on Components, Hybrids, and Manufacturing Technology*, 11(1), p 22-35, (1988).
- [2] Abbott, W.H. & Antler, M., "Connector contacts: Corrosion inhibiting surface treatments for gold-plated finishes", *Electrical Contacts Proceedings of the 41<sup>st</sup> IEEE Holm Conference on Electrical Contacts*, p 97-123, (1995).
- [3] Agilent Technologies, "Material expansion coefficients", Chapter 17 in Laser and optics user's manual, p 17-1 – 17-12, (2002).
- [4] Anderoglu, O., "Residual stress measurement using x-ray diffraction", Master's thesis, Texas A&M University, (2004).
- [5] Chang, S.A. et al., "High rate sputtering deposition of nickel using dc magnetron mode", *Journal of Vacuum Science and Technology A*, 4(3), p 413-416, (1986).
- [6] Enos, D., "Understanding the atmospheric degradation of noble metal-plated connector materials", *Corrosion*, 66(10), p 105003-1 – 105003-12, (2010).
- [7] Kulwanoski, G. et al., "Electrical contact failure mechanisms relevant to electronic packages", *Proceedings of the 37<sup>th</sup> IEEE Holm Conference on Electrical Contacts*, p 184-192, (1991).
- [8] Lille, H. et al., "Residual stresses in brush-plated gold coating", *JCPDS – International Centre for Diffraction Data*, p 320-327, (2009).
- [9] Lille, H. et al., "Investigation of residual stresses and some elastic properties of brush-plated gold and silver galvanic coatings", *Key Engineering Materials*, 527, p 125-130, (2013).
- [10] Meckel, B. B., & Bromley, E. I., *U.S. Patent No. 4,324,631*, Washington, DC: U.S. Patent and Trademark Office, (1982).
- [11] Reid, M. et al., "Study of mixed flowing gas exposure of copper", *Journal of the Electrochemical Society*, 155(4), p C147-C153, (2008).
- [12] Repper, J. et al., "Microstrain accumulation in multiphase superalloys", *JCPDS – International Centre for Diffraction Data*, p 732-738, (2009).
- [13] Sun, A. et al., "Pore corrosion model for gold-plated copper contacts", *IEEE Transactions on Components and Packaging Technologies*, 30(4), p 796-804, (2007).
- [14] Prevey, P., "X-ray diffraction: residual stress techniques", ASM handbook: Materials characterization, vol. 10, p 380-392, (1986).

- [15] Prevey, P., “Current applications of x-ray diffraction residual stress measurement”, Developments in materials characterization technologies (J. Friel & G. Van der Voort, Ed.), ASM International: Material Park, OH, p 103-110, (1996).
- [16] Withers, P.J. & Bhadeshia, H.K.D.H., “Overview: Residual stress part 1 – measurement techniques”, *Materials Science and Technology*, 17, p 355-365, (2001).
- [17] Withers, P.J. & Bhadeshia, H.K.D.H., “Overview: Residual stress part 2 – nature and origins”, *Materials Science and Technology*, 17, p 366-375, (2001).
- [18] Yang, S. et al., “Reliability assessment of land grid array sockets subjected to mixed flowing gas environment”, *IEEE Transactions on Reliability*, 58(4), p 634-640, (2009).
- [19] Ye, J. et al., “Electrochromic properties of Ni(V)Ox films deposited via reactive magnetron sputtering with a 8V-92Ni alloy target”, *Thin Solid Films*, 59, p 1578-1582, (2010).
- [20] Schajer, G.S. Ed., Practical Residual Stress Measurement Methods, Hoboken: Wiley, (2013).
- [21] Song, J. et al., “Corrosion protection of electrically conductive surfaces”, *Metals*, 2(4), p 450-477, (2012).
- [22] Oxford Vacuum Science, [http://www.oxford-vacuum.com/background/thin\\_film/sputtering.htm](http://www.oxford-vacuum.com/background/thin_film/sputtering.htm).
- [23] M. Vincent & Associates Ltd. Specialty Metals, [http://www.vincentmetals.com/C10100\\_Data.html](http://www.vincentmetals.com/C10100_Data.html).
- [24] Slade, P.G., Electrical Contacts: Principles and Applications, New York: Marcel Dekker, (1999).
- [25] Goodman, P., “Current and future uses of gold in electronics”, *Gold Bulletin*, 35(1), p 21-26, (2002).
- [26] Wolfe, D.E., “Advanced coating processing and properties”, Course lecture notes, Pennsylvania State University, (2013).
- [27] Chou, G.J.S., “New corrosion resistant plating to reduce gold consumption in connectors”, *IEEE 58th Holm Conference on Electrical Contacts*, (2012).
- [28] Fawakiri, M., “Investigation and growth of nickel coatings for electrical contact applications”, Master’s thesis, Linköping University, Sweden, (2009).
- [29] AMP Incorporated, “Golden rules: Guidelines for the use of gold on connector contacts”, Tyco Electronics Corporation, (2004).
- [30] *Standard guide for mixed flowing gas (MFG) tests for electrical contacts*, ASTM B845.
- [31] Smith, D.L., Thin-film deposition: Principles and Practice, New York: McGraw-Hill, Inc., (1995).
- [32] Di Bari, G.A., “Electrodeposition of nickel”, Chapter 3 in Modern Electroplating (5<sup>th</sup> ed., M. Schlesinger & M. Paunovic, ed.), Hoboken, NJ: John Wiley & Sons, Inc., p 79-114, (2010).



- [33] Kohl, P.A., "Electrodeposition of gold", Chapter 4 in Modern Electroplating (5<sup>th</sup> ed., M. Schlesinger & M. Paunovic, ed.), Hoboken, NJ: John Wiley & Sons, Inc., p 115-129, (2010).
- [34] Paunovic, M. et al., "Fundamental considerations", Chapter 1 in Modern Electroplating (5<sup>th</sup> ed., M. Schlesinger & M. Paunovic, ed.), Hoboken, NJ: John Wiley & Sons, Inc., p 1-31, (2010).
- [35] Paunovic, M & Schlesinger, M., Fundamentals of electrochemical deposition (2<sup>nd</sup> ed.), Hoboken, NJ: John Wiley & Sons, Inc., (2006).
- [36] Jones, D.A., Principles and prevention of corrosion, 2<sup>nd</sup> ed., Upper Saddle River, NJ: Prentice Hall, (1996).
- [37] Antler, M., "Materials, coatings, and platings", Chapter 7 in Electrical contacts: Principles and applications (P.G. Slade ed.), New York, NY: Marcel Dekker, p 403-432, (1999).
- [38] Misra, P. & Nagaraju, J., "Electrical contact resistance in thin ( $\leq 0.5 \mu\text{m}$ ) gold plated contacts: Effect of gold plating thickness", *IEEE Transactions on Components and Packaging Technologies*, 33(4), p 830-835, (2010).
- [39] Reade, <http://www.reade.com>.
- [40] Delpa, D. et al., "Sputter Deposition Processes". Chapter 5 in Handbook of deposition technologies for films and coatings (3<sup>rd</sup> ed., P. Martin ed.), Burlington, MA: William Andrew Publishing, p 253-296, (2010).
- [41] Adachi, H. et al., "Basic process of sputtering deposition", Chapter 5 in Handbook of sputter deposition technology (2<sup>nd</sup> ed, H. Adachi et al.), Boston, MA: William Andrew Publishing, p 295-359, (2012).
- [42] Rossnagel, S., "Sputtering and sputter deposition", Chapter 8 in Handbook of thin-film deposition processes and techniques: Principles, methods, equipment and applications (2<sup>nd</sup> ed, K. Seshan ed.), Norwich, NY: William Andrew Publishing, p 319-348, (2002).
- [43] Ohring, M., Materials science of thin films: Deposition and structure (2<sup>nd</sup> ed.), San Diego, CA: Academic Press, (2002).
- [44] Thornton, J. A., "The microstructure of sputter-deposited coatings", *Journal of Vacuum Science and Technology A*, 4(6), p 3059-3065, (1986).
- [45] Thornton, J. A., "Influence of apparatus geometry and deposition conditions on the structure and topography of thick sputtered coatings", *Journal of Vacuum Science and Technology*, 11(4), p 666-670, (1974).
- [46] Stelmack, L., "An introduction to ion beam coating deposition techniques", AVS Short Course Program: New England Chapter, Burlington, MA, (2004).
- [47] Marca Coating Technologies, LLC., [http://www.marcacoating.com/cm\\_metallizer.html](http://www.marcacoating.com/cm_metallizer.html).
- [48] Abbott, W.H., "Contact corrosion", Chapter 3 in Electrical contacts: Principles and applications (P.G. Slade ed), New York, NY: Marcel Dekker, p 89-112, (1999).

- [49] Timsit, R.S., "Electrical contact resistance: Fundamental principles". Chapter 1 in Electrical contacts: Principles and applications (P.G. Slade ed), New York, NY: Marcel Dekker, p 1-88, (1999).
- [50] Braunović, M., "Power connections", Chapter 4 in Electrical contacts: Principles and applications (P.G. Slade ed), New York, NY: Marcel Dekker, p 155-278, (1999).
- [51] Boyer, L., "Contact resistance calculations: Generalization of Greenwood's formula include interface films", *IEEE Transactions on Components and Packaging Technologies*, 24(1), p 50-58, (2001).
- [52] Moffat, H. et al., "Modeling pore corrosion in normally open gold-plated copper connectors", Sandia Report SAND2008-5737, Sandia National Laboratories, (2008).
- [53] Greenwood, J.A., "Constriction resistance and the real area of contact", *British Journal of Applied Physics*, 17, p 1621-1632, (1966).
- [54] Malucci, R.D., "Multispot model of contacts based on surface features". *Proceedings of the 36<sup>th</sup> IEEE Holm Conference on Electrical Contact*, p 625-634, (1990).
- [55] Malucci, R.D., "Dynamic model of stationary contacts based on random variations of surface features", *IEEE Transactions on Components, Hybrids, and Manufacturing Technology*, 15(3), p 339-347, (1992).
- [56] Malucci, R.D., "Making contact to aged surfaces", *IEEE Transactions on Components, Hybrids, and Manufacturing Technology*, 16(4), p 424-430, (1993).
- [57] Holm, R., Electrical Contact (4<sup>th</sup> ed.), New York, NY: Springer-Verlag, (1967).
- [58] Braithwaite, J. et al., "A modeling approach for predicting the effects of corrosion on electrical-circuit reliability", Sandia Report SAND2003-0359, Sandia National Laboratories, (2003).
- [59] Lee, A., "Low power commercial, automotive, and appliance connections". Chapter 5 in Electrical contacts: Principles and applications (P.G. Slade ed.), New York, NY: Marcel Dekker, p 279-308, (1999).
- [60] Glossbrenner, E.W., "Sliding contacts for instrumentation and control", Chapter 19 in Electrical contacts: Principles and applications (P.G. Slade ed.), New York, NY: Marcel Dekker, p 855-942, (1999).
- [61] Bock, E.M., Jr., "Low-level contact resistance characterization", *AMP journal of technology*, 3, p 64-68, (1993).
- [62] PANalytical, Highscore Plus software, Version 2.2c (2.2.3), (2007).
- [63] Cullity, B.D., Elements of x-ray diffraction, Reading, MA: Addison-Wesley Publishing Company, Inc., (1956).
- [64] Brundel, C.R. et al., ed., Encyclopedia of materials characterization, Boston, MA: Butterworth-Heinemann, (1992).

- [65] Faurie, D. et al., "Elastic anisotropy of polycrystalline Au films: Modeling and respective contributions of x-ray diffraction, nanoindentation and Brillouin light scattering", *Acta Materialia*, 58, p 4998-5008, (2010).
- [66] Peck, C.A., "Practical aspects of residual stress measurement by x-ray diffraction", *Proceedings of ASM Conference on Residual Stress – In Design, Process and Materials Selection*, p 7-9, (1987).
- [67] Oniciu, L. & Muresan, L., "Some fundamental aspects of levelling and brightening in metal electrodeposition", *Journal of Applied Electrochemistry*, 21, p 565-574, (1991).
- [68] Ferro-Ceramic Grinding, Inc., [www.ferroceramic.com](http://www.ferroceramic.com).
- [69] Holgate, S.A., Understanding solid state physics, Boca Raton, FL: CRC Press/ Taylor & Francis Group, p 115, (2010).
- [70] Takano, E. & Mano, K., "The failure mode and lifetime of static contacts". *IEEE Transactions on Parts, Materials and Packaging*, 4(2), p 51-55, (1968).
- [71] Antler, M., "Corrosion control and lubrication of plated noble metal connector contacts", *IEEE Transactions on Components, Packaging, and Manufacturing Technology – Part A*, 19(3), p 304-312, (1996).
- [72] Martens, R. & Pecht, M., "Effects and interactions of design parameters for gold-plated electric contacts", *Journal of Materials Science in Electronics*, 11, p 9209-218, (2000).
- [73] Abbott, W., "Corrosion of porous gold plating in field and laboratory environments", *Plating and Surface Engineering*, 74, p 72-75, (1987).
- [74] Abbott, W., "Recent studies of tarnish film creep", *Electrical Contacts*, p 117-121, (1978).
- [75] Center for Advanced Cycle Life Engineering (CALCE), "Mixed flowing gas testing introduction and CALCE MFG capabilities", University of Maryland.
- [76] Enos, D., *Materials Reliability (Organization 1818)*, Sandia National Laboratories, Albuquerque, NM.
- [77] James, J. D. et al., "A review of measurement techniques for thermal expansion coefficient of metals and alloys at elevated temperatures", *Measurement Science and Technology*, 12, p R1-R15, (2001).

## **Appendix**

### **Raw Data**

#### **Optical Profilometry**

Raw optical profilometry data (including the average surface roughness,  $R_a$ , root mean square roughness, RMS, and peak-to-valley values, PV) for the following sets of samples are included in Tables 0-1 through 0-7:

- Uncoated samples
- Unaged Au/Ni plated, Ni plated, and Ni sputtered samples
- MFG, TRH, and TC aged Au/Ni plated samples

Table A-1. Optical profilometry data for select samples prior to coating.

Optical Profilometry of Uncoated Panels																	
Objective:		50x		Field of View:		0.64 mm x 0.48mm		Time:		Week 0							
Zoom:		0.5x		Stitch % Overlap:		20		Averaged Scans:		3							
Group 1	Panel	Sample	R <sub>s</sub>	RMS	PV	Panel	Sample	R <sub>s</sub>	RMS	PV	Panel	Sample	R <sub>s</sub>	RMS	PV		
	N-13	1	0.055	0.113	3.82	N-14	1	0.059	0.143	10.53	N-15	1	0.048	0.106	3.99		
		2	0.067	0.125	3.47		2	0.050	0.111	6.88		2	0.057	0.118	4.13		
		3	0.074	0.137	3.85		3	0.053	0.111	3.44		3	0.048	0.107	3.78		
		4	0.067	0.132	4.07		4	0.070	0.139	4.47		4	0.054	0.116	3.81		
		5	0.071	0.133	4.32		5	0.066	0.130	4.16		5	0.042	0.097	4.17		
		6	0.050	0.102	4.35		6	0.056	0.113	3.82		6	0.043	0.094	4.10		
		7	0.046	0.098	3.73		7	0.051	0.105	4.70		7	0.044	0.092	3.73		
		8	0.071	0.133	3.99		8	0.052	0.104	3.77		8	0.060	0.117	---		
		9	0.061	0.124	5.51		9	0.055	0.113	5.11		9	0.047	0.133	6.27		
		10	0.063	0.123	4.15		10	0.058	0.118	4.07		10	0.050	0.103	3.50		
		11	0.056	0.116	3.97		11	0.056	0.113	4.19		11	0.053	0.107	3.83		
		12	0.060	0.120	4.11		12	0.060	0.118	4.32		12	0.051	0.105	4.15		
Average		0.062		0.121	4.11	Average		0.057		0.118	4.96	Average		0.050		0.108	4.13
Std Dev		0.009		0.012	0.50	Std Dev		0.006		0.013	1.97	Std Dev		0.006		0.012	0.74
Group 2	Panel	Sample	R <sub>s</sub>	μm RMS	μm PV	Panel	Sample	R <sub>s</sub>	μm RMS	μm PV	Panel	Sample	R <sub>s</sub>	μm RMS	μm PV		
	N-01	1	0.664	0.874	22.07	N-02	1	0.598	0.770	10.04	N-03	1	0.560	0.716	11.40		
		2	0.707	0.910	10.62		2	0.595	0.764	9.17		2	0.573	0.735	9.78		
		3	0.689	0.780	10.79		3	0.581	0.745	8.84		3	0.551	0.707	7.66		
		4	0.680	0.784	20.09		4	0.596	0.776	10.73		4	0.567	0.726	8.29		
		5	0.671	0.852	11.58		5	0.593	0.769	9.81		5	0.539	0.692	13.36		
		6	0.770	0.997	21.39		6	0.600	0.771	11.99		6	0.543	0.696	8.84		
		7	0.737	0.947	15.16		7	0.614	0.793	11.20		7	0.584	0.752	9.26		
		8	0.683	0.884	12.56		8	0.612	0.789	10.15		8	0.565	0.728	9.63		
		9	0.638	0.820	13.88		9	0.599	0.774	14.06		9	0.590	0.762	17.84		
		10	0.673	0.878	15.65		10	0.590	0.763	14.09		10	0.558	0.721	9.92		
		11	0.710	0.924	13.47		11	0.583	0.747	9.70		11	0.582	0.745	9.24		
		12	0.654	0.846	14.49		12	0.648	0.846	10.79		12	0.591	0.758	8.86		
Average		0.690		0.875	15.14	Average		0.601		0.776	10.88	Average		0.567		0.728	10.34
Std Dev		0.037		0.064	3.99	Std Dev		0.018		0.026	1.72	Std Dev		0.018		0.023	2.79



Table A-1 continued.

Table A-1 Continued.														
Group 3										Group 4				
Panel	Sample	$R_s$ , $\mu m$	RMS, $\mu m$	PV, $\mu m$	Panel	Sample	$R_s$ , $\mu m$	RMS, $\mu m$	PV, $\mu m$	Panel	Sample	$R_s$ , $\mu m$	RMS, $\mu m$	PV, $\mu m$
N-25	1	0.949	1.227	15.02	N-26	1	1.067	1.372	16.32	N-27	1	0.976	1.26	16.52
	2	0.900	1.163	15.79		2	1.040	1.348	16.98		2	0.965	1.254	14.45
	3	0.951	1.233	13.22		3	1.035	1.355	20.76		3	0.983	1.272	16.47
	4	0.968	1.258	17.91		4	1.082	1.401	16.71		4	0.994	1.291	16.90
	5	0.878	1.143	14.44		5	0.996	1.296	18.20		5	0.932	1.219	18.87
	6	0.922	1.245	19.91		6	0.892	1.168	16.29		6	0.87	1.143	14.96
	7	0.879	1.149	17.51		7	0.875	1.139	13.76		7	0.894	1.174	15.66
	8	0.875	1.144	13.41		8	0.948	1.226	13.54		8	0.928	1.212	20.17
	9	0.889	1.171	20.21		9	0.909	1.177	13.96		9	0.948	1.234	17.15
	10	0.854	1.146	18.43		10	0.867	1.146	17.55		10	0.875	1.16	21.19
	11	0.873	1.173	20.00		11	0.896	1.160	15.26		11	0.893	1.19	19.55
	12	0.855	1.160	21.88		12	0.950	1.235	17.55		12	0.919	1.214	16.61
Average		0.899	1.184	17.31	Average		0.963	1.252	16.41	Average		0.931	1.219	17.37
Std Dev		0.039	0.043	2.90	Std Dev		0.078	0.097	2.08	Std Dev		0.043	0.046	2.11
N-37	1	2.44	3.15	27.48	N-38	1	2.48	3.17	30.53	N-39	1	2.50	3.20	26.65
	2	2.47	3.14	27.23		2	2.50	3.17	26.70		2	2.62	3.36	31.07
	3	2.41	3.06	26.66		3	2.55	3.25	32.27		3	2.41	3.08	28.70
	4	2.54	3.19	26.29		4	2.50	3.15	26.32		4	2.65	3.41	31.68
	5	2.51	3.27	27.49		5	2.46	3.21	32.32		5	2.45	3.15	29.12
	6	2.47	3.16	26.10		6	2.54	3.38	35.48		6	2.54	3.27	30.69
	7	2.43	3.08	31.58		7	2.56	3.27	29.59		7	2.33	2.98	30.03
	8	2.47	3.12	24.11		8	2.52	3.20	28.31		8	2.52	3.27	31.05
	9	2.57	3.34	30.68		9	2.49	3.21	26.17		9	2.61	3.40	33.71
	10	2.53	3.22	35.11		10	2.72	3.14	27.84		10	2.37	3.07	28.33
	11	2.69	3.45	29.53		11	2.49	3.21	31.14		11	2.42	3.06	24.90
	12	2.78	3.55	39.03		12	2.51	3.23	31.17		12	2.43	3.14	31.21
Average		2.53	3.23	29.28	Average		2.53	3.22	29.82	Average		2.49	3.20	29.76
Std Dev		0.110	0.150	4.26	Std Dev		0.068	0.064	2.86	Std Dev		0.102	0.143	2.39

Table A-2. Optical profilometry data for unexposed Au/Ni plated samples.

Optical Profilometry of Au/Ni Plated Panels													
Objective: 50x Zoom: 0.5x				Field of View: 0.64 mm x 0.48mm Stitch % Overlap: 20				Time: Week 0 Averaged Scans: 3					
Panel	Sample	R <sub>a</sub> , µm	RMS, µm	PV, µm	Panel	Sample	R <sub>a</sub> , µm	RMS, µm	PV, µm	Panel	Sample	R <sub>a</sub> , µm	PV, µm
Group 1	N-14	1	0.039	0.057	3.38	N-18	1	0.033	0.049	N-22	1	0.031	1.99
		2	0.046	0.066	3.15		2	0.040	0.059		2	0.033	1.90
		3	0.043	0.062	3.06		3	0.036	0.055		3	0.033	1.89
		4	0.057	0.079	2.99		4	0.034	0.049		4	0.029	3.21
		5	0.047	0.068	2.43		5	0.032	0.049		5	0.031	1.78
		6	0.047	0.066	1.98		6	0.038	0.056		6	0.039	2.33
		7	0.051	0.073	2.39		7	0.038	0.058		7	0.038	1.89
		8	0.044	0.062	2.30		8	0.033	0.048		8	0.032	1.39
		9	0.042	0.061	2.08		9	0.034	0.052		9	0.027	1.49
		10	0.042	0.063	3.17		10	0.037	0.057		10	0.035	1.74
		11	0.044	0.063	1.62		11	0.034	0.051		11	0.038	3.11
		12	0.045	0.065	2.06		12	0.034	0.051		12	0.034	1.79
Average		0.046	0.065	2.55	Average		0.035	0.053	2.49	Average		0.033	2.04
Stand Deviation		0.005	0.006	0.58	Stand Deviation		0.002	0.004	1.16	Stand Deviation		0.004	0.57
Group 2	N-02	1	0.505	0.646	10.27	N-06	1	0.678	0.866	N-10	1	0.656	11.04
		2	0.485	0.625	11.11		2	0.583	0.745		2	0.614	10.08
		3	0.483	0.617	7.93		3	0.547	0.695		3	0.634	10.40
		4	0.695	0.999	11.44		4	0.510	0.649		4	0.630	10.83
		5	0.488	0.623	8.37		5	0.476	0.616		5	0.607	12.17
		6	0.512	0.657	8.09		6	0.528	0.677		6	0.616	10.60
		7	0.508	0.658	9.73		7	0.524	0.680		7	0.615	9.46
		8	0.544	0.699	9.18		8	0.505	0.650		8	0.606	12.29
		9	0.525	0.670	10.91		9	0.533	0.681		9	0.608	9.71
		10	0.486	0.626	10.11		10	0.554	0.713		10	0.651	14.21
		11	0.485	0.616	9.09		11	0.563	0.726		11	0.634	10.40
		12	0.506	0.649	9.34		12	0.540	0.694		12	0.629	11.41
Average		0.518	0.674	9.63	Average		0.545	0.699	10.29	Average		0.625	11.05
Stand Deviation		0.059	0.105	1.17	Stand Deviation		0.050	0.063	1.76	Stand Deviation		0.017	1.32

Table A-2 continued.

Table A-2 continued.														
Group 3					Group 4									
Panel	Sample	R <sub>a</sub> , μm	RMS, μm	PV, μm	Panel	Sample	R <sub>a</sub> , μm	RMS, μm	PV, μm	Panel	Sample	R <sub>a</sub> , μm	RMS, μm	PV, μm
N-26	1	1.030	1.35	16.97	N-30	1	0.946	1.24	20.32	N-34	1	0.799	1.07	17.05
	2	0.979	1.28	16.57		2	0.987	1.32	18.90		2	0.822	1.12	21.42
	3	0.962	1.26	16.41		3	0.926	1.20	16.18		3	0.765	1.04	20.33
	4	1.060	1.39	20.50		4	0.881	1.17	16.61		4	0.831	1.08	15.65
	5	0.899	1.18	19.50		5	0.846	1.13	19.39		5	0.836	1.12	20.24
	6	0.836	1.10	15.68		6	0.856	1.14	20.51		6	0.797	1.07	19.08
	7	0.845	1.12	16.55		7	0.877	1.18	21.09		7	0.837	1.11	17.11
	8	0.927	1.22	17.73		8	0.805	1.09	18.74		8	0.854	1.14	21.11
	9	0.863	1.13	16.41		9	0.846	1.12	18.26		9	0.881	1.16	16.66
	10	0.791	1.05	17.17		10	0.780	1.04	18.53		10	0.923	1.21	15.57
	11	0.858	1.13	16.54		11	0.815	1.11	21.42		11	0.939	1.23	14.14
	12	0.951	1.28	19.47		12	0.844	1.15	25.91		12	0.995	1.30	17.27
Average		0.917	1.21	17.46	Average		0.867	1.16	19.66	Average		0.856	1.14	17.97
Stand Deviation		0.082	0.106	1.53	Stand Deviation		0.061	0.073	2.55	Stand Deviation		0.067	0.076	2.40
N-38	1	2.62	3.35	32.10	N-42	1	2.70	3.48	37.92	N-46	1	2.63	3.46	36.56
	2	2.81	3.68	38.59		2	2.85	3.76	39.92		2	2.46	3.22	35.12
	3	2.85	3.74	39.18		3	2.61	3.44	38.07		3	2.84	3.71	36.92
	4	2.97	3.88	37.97		4	2.64	3.45	41.93		4	3.02	3.96	44.95
	5	2.54	3.34	31.41		5	2.78	3.62	37.26		5	2.53	3.24	28.89
	6	2.59	3.41	42.34		6	2.76	3.57	33.65		6	2.48	3.22	31.02
	7	3.04	4.12	43.46		7	2.50	3.23	31.41		7	2.81	3.64	42.69
	8	2.88	3.77	40.31		8	2.66	3.41	41.40		8	2.92	3.76	37.59
	9	2.60	3.46	49.54		9	2.67	3.47	39.38		9	2.44	3.20	33.31
	10	2.77	3.59	40.77		10	2.67	3.54	50.40		10	2.45	3.32	38.33
	11	2.95	3.87	41.81		11	2.59	3.40	34.07		11	2.73	3.52	33.97
	12	2.84	3.71	37.59		12	3.00	3.90	42.68		12	2.67	3.41	31.64
Average		2.79	3.66	39.59	Average		2.70	3.52	39.01	Average		2.67	3.47	35.92
Stand Deviation		0.17	0.24	4.85	Stand Deviation		0.13	0.18	4.99	Stand Deviation		0.20	0.25	4.67

Table A-3. Optical profilometry data for unexposed Ni plated samples.

Optical Profilometry of Ni Plated Panels																		
Objective: 50x		Field of View: 0.64 mm x 0.48mm				Time: Week 0		Averaged Scans: 3										
Zoom: 0.5x		Stitch % Overlap: 20																
Panel	Sample	R <sub>a</sub> , µm	RMS, µm	PV, µm	Panel	Sample	R <sub>a</sub> , µm	RMS, µm	PV, µm	Panel	Sample	R <sub>a</sub> , µm	RMS, µm	PV, µm				
Group 1	N-13	1	0.038	0.056	2.29	N-17	1	0.033	0.049	1.96	N-21	1	0.036	0.053	1.63			
		2	0.037	0.055	2.42		2	0.036	0.052	2.15		2	0.033	0.050	2.20			
		3	0.040	0.060	2.49		3	0.042	0.061	2.57		3	0.039	0.059	1.60			
		4	0.039	0.057	2.50		4	0.043	0.061	1.33		4	0.036	0.053	1.77			
		5	0.037	0.055	1.66		5	0.033	0.049	1.62		5	0.037	0.054	1.84			
		6	0.030	0.046	2.75		6	0.034	0.049	1.92		6	0.031	0.048	3.36			
		7	0.031	0.045	2.03		7	0.035	0.051	2.09		7	0.033	0.049	1.48			
		8	0.036	0.054	2.68		8	0.039	0.056	1.66		8	0.035	0.053	2.44			
		9	0.037	0.055	3.05		9	0.035	0.052	2.02		9	0.036	0.054	1.88			
		10	0.036	0.053	1.77		10	0.034	0.050	2.04		10	0.032	0.048	2.78			
		11	0.032	0.048	2.28		11	0.037	0.054	2.11		11	0.031	0.047	1.85			
		12	0.033	0.049	1.48		12	0.038	0.055	2.07		12	0.028	0.043	1.45			
Average		0.035	0.053	2.28	Average		0.037	0.053	1.96	Average		0.034	0.051	2.02				
Stand Deviation		0.003	0.005	0.47	Stand Deviation		0.003	0.004	0.31	Stand Deviation		0.003	0.004	0.58				
Group 2	N-01	1	0.511	0.661	8.09	N-05	1	0.543	0.707	11.02	N-09	1	0.453	0.580	9.12			
		2	0.503	0.649	10.33		2	0.544	0.693	9.07		2	0.458	0.581	7.99			
		3	0.504	0.684	20.73		3	0.616	0.843	11.38		3	0.293	0.384	10.60			
		4	0.607	0.931	12.09		4	0.520	0.668	9.69		4	0.460	0.582	6.06			
		5	0.538	0.693	12.84		5	0.555	0.790	11.55		5	0.371	0.482	9.13			
		6	0.608	0.783	13.99		6	0.518	0.658	8.35		6	0.462	0.589	9.24			
		7	0.589	0.762	12.14		7	0.500	0.637	8.72		7	0.434	0.552	7.78			
		8	0.518	0.657	7.18		8	0.453	0.582	9.65		8	0.346	0.462	9.85			
		9	0.551	0.709	9.80		9	0.454	0.579	7.65		9	0.445	0.564	7.40			
		10	0.617	0.792	10.62		10	0.455	0.584	9.17		10	0.455	0.580	9.45			
		11	0.579	0.743	9.13		11	0.443	0.564	6.68		11	0.443	0.563	7.13			
		12	0.538	0.686	9.23		12	0.414	0.526	6.27		12	0.466	0.591	6.69			
Average		0.555	0.729	11.35	Average		0.501	0.653	9.10	Average		0.424	0.543	8.37				
Stand Deviation		0.043	0.080	3.56	Stand Deviation		0.059	0.095	1.71	Stand Deviation		0.056	0.065	1.39				

Table A-3 continued.

Table A-3 continued.														
Group 3										Group 4				
Panel	Sample	R <sub>a</sub> , μm	RMS, μm	PV, μm	Panel	Sample	R <sub>a</sub> , μm	RMS, μm	PV, μm	Panel	Sample	R <sub>a</sub> , μm	RMS, μm	PV, μm
N-25	1	0.733	0.946	25.59	N-29	1	0.759	0.995	13.18	N-33	1	0.715	0.944	15.71
	2	0.691	0.890	11.12		2	0.733	0.960	17.18		2	0.709	0.924	13.46
	3	0.711	0.910	15.99		3	0.762	1.010	17.34		3	0.675	0.884	13.52
	4	0.774	1.030	24.95		4	0.736	0.950	13.57		4	0.693	0.900	16.63
	5	0.694	0.902	18.32		5	0.762	1.010	15.10		5	0.738	0.959	12.51
	6	0.834	1.150	14.85		6	0.717	0.940	20.65		6	0.709	0.931	13.29
	7	0.708	0.926	13.84		7	0.737	0.963	16.33		7	0.695	0.902	16.18
	8	0.668	0.874	16.44		8	0.778	1.040	16.94		8	0.714	0.952	18.64
	9	0.713	0.931	17.20		9	0.806	1.040	14.91		9	0.836	1.090	18.16
	10	0.691	0.908	13.57		10	0.756	0.980	12.95		10	0.812	1.060	22.96
	11	0.723	0.957	18.25		11	0.739	0.972	19.63		11	0.751	0.975	15.64
	12	0.648	0.847	13.61		12	0.679	0.894	11.56		12	0.770	1.010	19.32
Average		0.716	0.939	16.98	Average		0.747	0.980	15.78	Average		0.735	0.961	16.34
Stand Deviation		0.049	0.081	4.41	Stand Deviation		0.032	0.043	2.75	Stand Deviation		0.049	0.064	3.05
N-37	1	2.53	3.38	36.97	N-41	1	2.48	3.14	27.66	N-45	1	2.61	3.42	34.89
	2	2.60	3.42	37.43		2	2.51	3.27	32.51		2	2.30	3.04	38.34
	3	2.53	3.27	33.11		3	2.63	3.42	32.54		3	2.34	3.03	29.73
	4	2.31	2.97	27.13		4	2.76	3.67	41.13		4	2.45	3.26	37.16
	5	2.53	3.28	34.49		5	2.44	3.12	31.43		5	2.70	3.56	39.96
	6	2.59	3.37	43.02		6	2.59	3.39	32.58		6	2.53	3.32	35.97
	7	2.60	3.39	37.15		7	2.48	3.22	32.36		7	2.44	3.15	34.77
	8	2.51	3.21	29.86		8	2.70	3.54	44.05		8	2.56	3.32	34.71
	9	2.68	3.49	43.40		9	2.70	3.54	32.75		9	2.68	3.45	36.95
	10	2.66	3.44	33.18		10	2.60	3.30	29.11		10	2.50	3.16	35.49
	11	2.62	3.35	30.54		11	2.82	3.69	35.35		11	2.68	3.48	32.98
	12	2.67	3.37	35.70		12	2.60	3.40	43.52		12	2.71	3.57	38.49
Average		2.569	3.328	35.17	Average		2.609	3.392	34.58	Average		2.542	3.313	35.79
Stand Deviation		0.10	0.14	4.91	Stand Deviation		0.12	0.19	5.41	Stand Deviation		0.14	0.19	2.73



Table A-4. Optical profilometry data for all unexposed Ni sputtered samples.

Optical Profilometry of Ni Sputtered Panels																	
Objective: 50x		Field of View: 0.64 mm x 0.48mm				Time: Week 0											
Zoom: 0.5x		Stitch % Overlap: 20				Averaged Scans: 3											
Panel		Sample	R <sub>s</sub> , µm	RMS, µm	PV, µm	Panel		Sample	R <sub>s</sub> , µm	RMS, µm	PV, µm	Panel		Sample	R <sub>s</sub> , µm	RMS, µm	PV, µm
Group 1	N-19	1	0.047	0.070	2.78	N-23	1	0.197	0.266	9.39	N-16	1	0.054	0.079	4.91		
		2	0.056	0.084	2.76		2	0.187	0.253	9.36		2	0.066	0.082	3.31		
		3	0.061	0.089	4.33		3	0.197	0.273	11.98		3	0.065	0.096	3.48		
		4	0.052	0.080	2.71		4	0.194	0.261	9.62		4	0.052	0.076	3.07		
		5	0.053	0.079	2.77		5	0.189	0.253	6.41		5	0.066	0.099	2.77		
		6	0.065	0.096	2.96		6	0.208	0.284	9.81		6	0.082	0.120	5.71		
		7	0.067	0.099	3.54		7	0.199	0.269	9.85		7	0.091	0.132	4.52		
		8	0.062	0.094	3.58		8	0.201	0.285	9.41		8	0.067	0.101	7.03		
		9	0.051	0.078	3.94		9	0.207	0.397	18.14		9	0.065	0.098	4.33		
		10	0.061	0.092	3.25		10	0.210	0.287	10.03		10	0.087	0.127	4.53		
		11	0.056	0.084	2.74		11	0.201	0.295	14.53		11	0.090	0.131	3.86		
		12	0.050	0.079	4.82		12	0.189	0.254	11.03		12	0.075	0.117	3.95		
Average		0.057	0.085	3.35	Average		0.198	0.281	10.80	Average		0.072	0.105	4.29			
Stand Deviation		0.006	0.009	0.71	Stand Deviation		0.008	0.039	2.99	Stand Deviation		0.013	0.020	1.20			
Group 2	N-07	1	0.587	0.764	12.59	N-04	1	0.575	0.750	12.07	N-11	1	0.614	0.803	16.35		
		2	0.581	0.756	12.11		2	0.535	0.698	12.73		2	0.616	0.810	12.95		
		3	0.566	0.740	14.32		3	0.561	0.733	19.29		3	0.593	0.777	12.71		
		4	0.576	0.755	13.38		4	0.551	0.716	11.61		4	0.631	0.876	20.42		
		5	0.576	0.747	12.71		5	0.555	0.724	12.85		5	0.593	0.772	12.83		
		6	0.573	0.746	12.20		6	0.546	0.714	13.51		6	0.622	0.821	15.89		
		7	0.605	0.788	11.73		7	0.562	0.762	21.29		7	0.643	0.840	11.96		
		8	0.609	0.793	11.53		8	0.567	0.742	12.41		8	0.600	0.790	13.23		
		9	0.564	0.735	14.89		9	0.577	0.770	12.28		9	0.659	0.897	13.88		
		10	0.559	0.729	11.79		10	0.548	0.715	11.13		10	0.682	0.929	23.63		
		11	0.548	0.715	11.84		11	0.569	0.743	12.33		11	0.626	0.822	11.68		
		12	0.562	0.734	11.12		12	0.557	0.728	14.26		12	0.624	0.818	13.19		
Average		0.576	0.750	12.52	Average		0.559	0.733	13.81	Average		0.625	0.830	14.89			
Stand Deviation		0.018	0.023	1.15	Stand Deviation		0.012	0.021	3.16	Stand Deviation		0.026	0.048	3.67			

Table A-4 continued.

Table A-4 continued.														
Group 3										Group 4				
Panel	Sample	R <sub>s</sub> , μm	RMS, μm	PV, μm	Panel	Sample	R <sub>s</sub> , μm	RMS, μm	PV, μm	Panel	Sample	R <sub>s</sub> , μm	RMS, μm	PV, μm
N-31	1	0.830	1.12	20.48	N-35	1	0.834	1.12	25.31	N-28	1	0.883	1.20	20.71
	2	0.819	1.09	19.59		2	0.884	1.23	28.97		2	0.912	1.23	18.69
	3	0.824	1.10	19.28		3	0.852	1.16	23.97		3	0.937	1.26	18.80
	4	0.824	1.11	20.70		4	0.830	1.25	36.38		4	0.998	1.33	21.25
	5	0.815	1.10	21.83		5	0.846	1.14	18.38		5	0.834	1.11	18.16
	6	0.813	1.09	22.40		6	0.833	1.13	29.26		6	0.842	1.14	32.30
	7	0.841	1.13	18.41		7	0.857	1.15	20.72		7	0.845	1.12	20.30
	8	0.825	1.13	23.44		8	0.909	1.23	24.66		8	0.921	1.24	19.42
	9	0.906	1.21	19.07		9	1.020	1.38	21.47		9	0.817	1.10	23.29
	10	0.916	1.23	19.15		10	0.941	1.26	17.87		10	0.832	1.14	20.97
	11	0.854	1.14	17.14		11	0.979	1.32	16.33		11	0.840	1.12	21.88
	12	0.897	1.19	17.55		12	1.010	1.34	19.60		12	0.841	1.13	17.22
Average		0.847	1.14	19.92	Average		0.900	1.23	23.58	Average		0.875	1.18	21.08
Stand Deviation		0.038	0.048	1.92	Stand Deviation		0.071	0.088	5.80	Stand Deviation		0.055	0.074	3.92
N-43	1	2.64	3.37	30.10	N-40	1	2.62	3.42	34.28	N-47	1	2.70	3.52	38.42
	2	2.46	3.15	28.67		2	2.73	3.55	38.98		2	2.69	3.56	41.72
	3	2.58	3.30	28.93		3	2.64	3.38	32.85		3	2.62	3.41	34.21
	4	2.70	3.55	35.91		4	2.69	3.51	33.10		4	2.72	3.57	35.95
	5	2.58	3.35	31.65		5	2.48	3.21	29.97		5	2.58	3.36	32.76
	6	2.62	3.41	34.38		6	2.57	3.33	32.60		6	2.61	3.33	30.38
	7	2.52	3.25	30.92		7	2.64	3.41	31.78		7	2.70	3.55	36.63
	8	2.62	3.37	31.74		8	2.64	3.40	35.31		8	2.61	3.41	39.30
	9	2.66	3.43	29.86		9	2.49	3.21	35.88		9	2.73	3.52	31.18
	10	2.57	3.38	34.02		10	2.43	3.14	32.82		10	2.72	3.49	28.25
	11	2.52	3.29	32.12		11	2.66	3.49	35.56		11	2.70	3.50	32.01
	12	2.48	3.19	27.49		12	2.86	3.81	33.37		12	2.78	3.58	30.69
Average		2.58	3.34	31.32	Average		2.62	3.41	33.88	Average		2.68	3.48	34.29
Stand Deviation		0.073	0.11	2.52	Stand Deviation		0.118	0.18	2.32	Stand Deviation		0.061	0.09	4.13

Table A-5. Optical profilometry data for all MFG aged Au/Ni plated samples

Optical Profilometry of Coated Panels - MFG Aged															
Objective:		50x	Field of View:		0.64 mm x 0.48mm		Averaged Scans:		3		Coating:				
Zoom:		0.5x	Stitch % Overlap:		20		Ni/Au Plated								
	Week 3				Week 6				Week 9						
Panel	Sample	R <sub>a</sub> , µm	RMS, µm	PV, µm	Panel	Sample	R <sub>a</sub> , µm	RMS, µm	PV, µm	Panel	Sample	R <sub>a</sub> , µm	RMS, µm	PV, µm	
Group 1	N-14	2	0.061	0.095	3.49	N-14	3	0.054	0.083	2.28	N-14	4	0.071	0.101	2.85
		6	0.053	0.079	2.36		7	0.060	0.089	2.68		8	0.048	0.075	2.15
		10	0.052	0.080	2.06		11	0.054	0.081	2.02		12	0.071	0.106	5.34
	Average		0.055	0.085	2.63	Average		0.056	0.084	2.33	Average		0.063	0.094	3.45
Stand Deviation			0.005	0.009	0.75	Stand Deviation		0.003	0.004	0.33	Stand Deviation		0.013	0.017	1.68
Panel	Sample	R <sub>a</sub> , µm	RMS, µm	PV, µm	Panel	Sample	R <sub>a</sub> , µm	RMS, µm	PV, µm	Panel	Sample	R <sub>a</sub> , µm	RMS, µm	PV, µm	
Group 2	N-02	2	0.545	0.708	9.03	N-02	3	0.490	0.625	11.74	N-02	4	0.527	0.683	11.84
		6	0.529	0.680	15.22		7	0.498	0.632	10.77		8	0.530	0.683	11.13
		10	0.519	0.671	9.56		11	0.491	0.629	10.82		12	0.545	0.706	11.84
	Average		0.531	0.686	11.27	Average		0.493	0.629	11.11	Average		0.534	0.691	11.61
Stand Deviation			0.013	0.019	3.43	Stand Deviation		0.004	0.004	0.54	Stand Deviation		0.010	0.013	0.41
Panel	Sample	R <sub>a</sub> , µm	RMS, µm	PV, µm	Panel	Sample	R <sub>a</sub> , µm	RMS, µm	PV, µm	Panel	Sample	R <sub>a</sub> , µm	RMS, µm	PV, µm	
Group 3	N-26	2	0.980	1.28	18.34	N-26	3	0.935	1.22	16.15	N-26	4	1.006	1.32	16.78
		6	0.827	1.09	21.61		7	0.816	1.08	17.65		8	0.889	1.17	27.26
		10	0.806	1.08	23.96		11	0.854	1.13	21.19		12	0.946	1.25	19.28
	Average		0.871	1.152	21.30	Average		0.868	1.144	18.33	Average		0.947	1.243	21.11
Stand Deviation			0.095	0.114	2.82	Stand Deviation		0.061	0.074	2.59	Stand Deviation		0.059	0.076	5.47
Panel	Sample	R <sub>a</sub> , µm	RMS, µm	PV, µm	Panel	Sample	R <sub>a</sub> , µm	RMS, µm	PV, µm	Panel	Sample	R <sub>a</sub> , µm	RMS, µm	PV, µm	
Group 4	N-38	2	2.99	3.97	41.27	N-38	3	2.83	3.73	36.56	N-38	4	3.00	3.97	38.46
		6	2.54	3.34	33.55		7	2.73	3.61	37.29		8	2.74	3.56	39.53
		10	3.05	4.15	49.32		11	2.57	3.47	42.43		12	2.64	3.46	39.91
	Average		2.86	3.82	41.38	Average		2.71	3.61	38.76	Average		2.79	3.67	39.30
Stand Deviation			0.28	0.43	7.88	Stand Deviation		0.13	0.13	3.20	Stand Deviation		0.18	0.27	0.75

Table A-6. Optical profilometry data for all TRH aged Au/Ni plated samples

Optical Profilometry of Coated Panels - TRH Aged															
Objective:		50x		Field of View: 0.64 mm x 0.48mm			Averaged Scans: 3			Coating: Ni/Au Plated					
Zoom:		0.5x		Stitch % Overlap: 20											
Week 3					Week 6					Week 9					
Group 1	Panel	Sample	R <sub>a</sub> , µm	RMS, µm	PV, µm	Panel	Sample	R <sub>a</sub> , µm	RMS, µm	PV, µm	Panel	Sample	R <sub>a</sub> , µm	RMS, µm	PV, µm
	N-18	2	0.047	0.077	2.40	N-18	3	0.048	0.078	2.33	N-18	4	0.043	0.071	2.10
		6	0.054	0.087	2.97		7	0.052	0.082	3.24		8	0.042	0.070	3.02
		10	0.048	0.080	2.21		11	0.045	0.074	2.11		12	0.042	0.102	11.88
	Average		0.050	0.081	2.53	Average		0.048	0.078	2.56	Average		0.042	0.081	5.66
	Stand Deviation		0.004	0.005	0.40	Stand Deviation		0.004	0.004	0.60	Stand Deviation		0.001	0.018	5.40
Group 2	Panel	Sample	R <sub>a</sub> , µm	RMS, µm	PV, µm	Panel	Sample	R <sub>a</sub> , µm	RMS, µm	PV, µm	Panel	Sample	R <sub>a</sub> , µm	RMS, µm	PV, µm
	N-06	2	0.559	0.710	9.62	N-06	3	0.539	0.690	10.02	N-06	4	0.573	0.738	12.81
		6	0.522	0.669	9.25		7	0.521	0.666	17.74		8	0.489	0.628	8.11
		10	0.557	0.713	9.99		11	0.543	0.696	9.02		12	0.535	0.685	10.68
	Average		0.546	0.697	9.62	Average		0.534	0.684	12.26	Average		0.532	0.684	10.53
	Stand Deviation		0.021	0.025	0.37	Stand Deviation		0.012	0.016	4.77	Stand Deviation		0.042	0.055	2.35
Group 3	Panel	Sample	R <sub>a</sub> , µm	RMS, µm	PV, µm	Panel	Sample	R <sub>a</sub> , µm	RMS, µm	PV, µm	Panel	Sample	R <sub>a</sub> , µm	RMS, µm	PV, µm
	N-30	2	0.979	1.29	21.97	N-30	3	0.953	1.25	17.58	N-30	4	0.887	1.16	15.76
		6	0.851	1.13	21.39		7	0.834	1.12	17.69		8	0.874	1.20	22.75
		10	0.815	1.10	23.49		11	0.832	1.12	24.69		12	0.855	1.16	22.14
	Average		0.882	1.175	22.28	Average		0.873	1.162	19.98	Average		0.872	1.171	20.21
	Stand Deviation		0.086	0.099	1.08	Stand Deviation		0.069	0.073	4.07	Stand Deviation		0.016	0.021	3.87
Group 4	Panel	Sample	R <sub>a</sub> , µm	RMS, µm	PV, µm	Panel	Sample	R <sub>a</sub> , µm	RMS, µm	PV, µm	Panel	Sample	R <sub>a</sub> , µm	RMS, µm	PV, µm
	N-42	2	2.43	3.19	38.60	N-42	3	2.50	3.21	31.69	N-42	4	2.56	3.34	34.26
		6	2.64	3.44	38.89		7	2.61	3.36	33.96		8	2.65	3.46	38.87
		10	2.83	3.71	36.91		11	2.65	3.44	30.53		12	2.54	3.25	30.93
	Average		2.636	3.447	38.13	Average		2.59	3.33	32.06	Average		2.58	3.35	34.69
	Stand Deviation		0.200	0.259	1.07	Stand Deviation		0.07	0.12	1.74	Stand Deviation		0.06	0.11	3.99



Table A-7. Optical profilometry data for all TC aged Au/Ni plated samples

Optical Profilometry of Coated Panels - TC Aged															
Objective:		50x		Field of View:		0.64 mm x 0.48mm		Averaged Scans:		3		Ni/Au Plated			
Zoom:		0.5x		Stitch % Overlap:		20		Coating:							
		Week 3				Week 6				Week 9					
Group 1	Panel	Sample	R <sub>a</sub> , µm	RMS, µm	PV, µm	Panel	Sample	R <sub>a</sub> , µm	RMS, µm	PV, µm	Panel	Sample	R <sub>a</sub> , µm	RMS, µm	PV, µm
	N-22	2	0.043	0.064	2.20	N-22	3	0.038	0.059	2.10	N-22	4	0.034	0.052	2.51
		6	0.048	0.075	2.45		7	0.050	0.077	1.93		8	0.034	0.052	3.11
		10	0.045	0.070	3.75		11	0.046	0.071	2.84		12	0.033	0.054	4.26
Group 2	Average		0.045	0.070	2.80	Average		0.045	0.069	2.29	Average		0.034	0.053	3.29
	Stand Deviation		0.003	0.006	0.83	Stand Deviation		0.006	0.009	0.49	Stand Deviation		0.001	0.001	0.89
	Panel	Sample	R <sub>a</sub> , µm	RMS, µm	PV, µm	Panel	Sample	R <sub>a</sub> , µm	RMS, µm	PV, µm	Panel	Sample	R <sub>a</sub> , µm	RMS, µm	PV, µm
	N-10	2	0.606	0.783	13.97	N-10	3	0.587	0.753	12.99	N-10	4	0.632	0.811	10.91
Group 3		6	0.617	0.797	11.86		7	0.628	0.804	15.73		8	0.634	0.828	14.91
		10	0.612	0.784	13.13		11	0.620	0.798	11.50		12	0.643	0.837	20.30
	Average		0.612	0.788	12.99	Average		0.612	0.785	13.41	Average		0.636	0.825	15.37
	Stand Deviation		0.006	0.008	1.06	Stand Deviation		0.022	0.028	2.15	Stand Deviation		0.006	0.013	4.71
Group 4	Panel	Sample	R <sub>a</sub> , µm	RMS, µm	PV, µm	Panel	Sample	R <sub>a</sub> , µm	RMS, µm	PV, µm	Panel	Sample	R <sub>a</sub> , µm	RMS, µm	PV, µm
	N-34	2	0.813	1.11	18.38	N-34	3	0.794	1.07	18.02	N-34	4	0.850	1.12	17.88
		6	0.827	1.10	19.16		7	0.787	1.06	21.79		8	0.825	1.08	18.00
		10	0.931	1.23	24.49		11	0.992	1.32	28.76		12	0.995	1.29	19.58
Group 5	Average		0.857	1.142	20.68	Average		0.858	1.149	22.86	Average		0.890	1.164	18.49
	Stand Deviation		0.064	0.072	3.33	Stand Deviation		0.116	0.149	5.45	Stand Deviation		0.092	0.114	0.95
	Panel	Sample	R <sub>a</sub> , µm	RMS, µm	PV, µm	Panel	Sample	R <sub>a</sub> , µm	RMS, µm	PV, µm	Panel	Sample	R <sub>a</sub> , µm	RMS, µm	PV, µm
	N-46	2	2.76	3.58	32.47	N-46	3	2.70	3.55	45.52	N-46	4	2.56	3.32	50.19
Group 6		6	2.47	3.21	35.05		7	2.54	3.28	36.67		8	2.69	3.43	30.43
		10	2.56	3.44	37.15		11	2.70	3.54	40.94		12	2.40	3.07	27.83
	Average		2.60	3.41	34.89	Average		2.65	3.45	41.04	Average		2.55	3.27	36.15
	Stand Deviation		0.147	0.182	2.34	Stand Deviation		0.095	0.153	4.42	Stand Deviation		0.147	0.186	12.23



### **Distribution List**

- (a) Applied Research Laboratory  
The Pennsylvania State University  
Attn: Dr. Douglas E. Wolfe  
PO Box 30  
University Park, PA 16804  
Email: [dew125@arl.psu.edu](mailto:dew125@arl.psu.edu)
  
- (b) Defense Technical Information Center (DTIC)  
Attn: DTIC-BSC  
8725 John J. Kingman Road, Suite 0944  
Fort Belvoir, VA 22060-0944  
Email: [TR@dtic.mil](mailto:TR@dtic.mil)